



Theses and Dissertations

2009-07-14

Radiation and Convection Heat Transfer in Wildland Fire Environments

David J. Frankman
Brigham Young University - Provo

Follow this and additional works at: <https://scholarsarchive.byu.edu/etd>



Part of the [Mechanical Engineering Commons](#)

BYU ScholarsArchive Citation

Frankman, David J., "Radiation and Convection Heat Transfer in Wildland Fire Environments" (2009).
Theses and Dissertations. 1813.
<https://scholarsarchive.byu.edu/etd/1813>

This Dissertation is brought to you for free and open access by BYU ScholarsArchive. It has been accepted for inclusion in Theses and Dissertations by an authorized administrator of BYU ScholarsArchive. For more information, please contact scholarsarchive@byu.edu, ellen_amatangelo@byu.edu.

RADIATION AND CONVECTION HEAT TRANSFER
IN WILDLAND FIRE ENVIRONMENTS

by

David J. Frankman

A dissertation submitted to the faculty of
Brigham Young University
in partial fulfillment of the requirements for the degree of

Doctor of Philosophy

Department of Mechanical Engineering

Brigham Young University

August 2009

Copyright © 2009 David J. Frankman

All Rights Reserved

BRIGHAM YOUNG UNIVERSITY

GRADUATE COMMITTEE APPROVAL

of a dissertation submitted by

David J. Frankman

This dissertation has been read by each member of the following graduate committee and by majority vote has been found to be satisfactory.

Date

Brent W. Webb, Chair

Date

Matthew R. Jones

Date

Dale R. Tree

Date

Daniel Maynes

Date

Thomas H. Fletcher

BRIGHAM YOUNG UNIVERSITY

As chair of the candidate's graduate committee, I have read the dissertation of David J. Frankman in its final form and have found that (1) its format, citations, and bibliographical style are consistent and acceptable and fulfill university and department style requirements; (2) its illustrative materials including figures, tables, and charts are in place; and (3) the final manuscript is satisfactory to the graduate committee and is ready for submission to the university library.

Date

Brent W. Webb
Chair, Graduate Committee

Accepted for the Department

Larry L. Howell
Graduate Coordinator

Accepted for the College

Alan R. Parkinson
Dean, Ira A. Fulton College of Engineering
and Technology

ABSTRACT

RADIATION AND CONVECTION HEAT TRANSFER IN WILDLAND FIRE ENVIRONMENTS

David J. Frankman

Department of Mechanical Engineering

Doctor of Philosophy

Wildland fire research has been extensive and on going since before 1950. The motivation behind this research is to prevent loss of property and lives. In spite of this research, the heat transfer of fuel ignition and flame spread is not well understood. This dissertation seeks to fill gaps in this understanding through modeling and also by experimentation.

The effect of water vapor on the transmission of thermal radiation from the flame to the fuel was investigated. The Spectral Line Weighted-sum-of-gray-gases approach was adopted for treating the spectral nature of the radiation. The study reveals that water vapor has only a moderate effect even at 100 percent humidity.

Experiments were conducted wherein wood shavings and Ponderosa pine needles in quiescent air were subjected to an imposed radiant heat flux. The internal temperature of these particles was measured and compared to steady-state model predictions. Excel-

lent agreement was observed between the model predictions and the experimental data. Exercise of the model led to the conclusion that ignition of the fuel element by radiation heating alone is unlikely.

Time-resolved radiation and convection heat flux were measured in a series of experimental laboratory fires designed to explore heat transfer behavior during combustion of discontinuous fuel beds. Convection heat flux was shown to fluctuate between positive and negative values during flame engulfment, indicating the presence of alternating packets of hot combustion gas and cool ambient air within the flame. Rapid temporal fluctuations were observed in both radiation and convection. Spectral analysis revealed content at frequencies as high as 150 to 200 Hz.

Time-resolved radiation and convection heat flux histories were also collected on fourteen controlled burns and wildfires. The data reveal significant temporal fluctuations in both radiation and convection heat flux. Spectral analysis using a Fast Fourier Transform (FFT) revealed content as high as 100 Hz using data sets that were sampled at 500 Hz. The role of the higher frequency convective content in fuel thermal response was explored using a one-dimensional transient conduction model with a convective boundary condition. It was shown that high-frequency (*i.e.*, short-duration) convective pulses can lead to fine fuel ignition.

ACKNOWLEDGMENTS

I would like to give my appreciation to all those who have been the most influential in aiding me with this dissertation. First, my advisor, Brent W. Webb has always given me an astute evaluation of my work and sage advice when I have confronted road blocks in this research. Further, words cannot express my gratitude for his inspiration in knowing whether I need encouragement or stretching realism.

Bret Butler has also been useful in giving wise and humble advice and will continue to be an example to me of professionalism and tactful navigation of a sometimes political environment.

I also express appreciation to the Joint Fire Science Program and the U.S. Forest Service who have provided significant technical and financial support.

Finally, my wife Allyson has offered me her vote of confidence even when it was difficult to vote for myself. She joined my life when I was desperately in need of structure and love. This work would not have been completed without her.

TABLE OF CONTENTS

List of Tables.....	xiii
List of Figures.....	xv
1. Introduction.....	1
1.1. Problem Overview	2
1.2. General Literature Review	3
1.3. Objectives	10
1.4. Dissertation Organization	10
1.5. Summary.....	14
2. Influence of Absorption by Environmental Water Vapor on Radiation Transfer in Wildland Fires	15
2.1. Abstract.....	15
2.2. Introduction.....	16
2.3. Literature Review	16
2.4. Model	17
2.5. Results and Discussion	27
2.6. Conclusions.....	35
3. Fine Fuel Heating by Radiant Flux	37
3.1. Abstract.....	37
3.2. Introduction.....	38
3.3. Experiments	40
3.4. Model	46

3.5.	Model Parametric Study	51
3.6.	Conclusions.....	58
4.	Time-Resolved Radiation and Convection Heat Transfer in Combusting Discontinuous Fuel Beds.....	59
4.1.	Abstract.....	59
4.2.	Introduction.....	60
4.3.	Experimental Method	61
4.4.	Sensor Configuration	61
4.5.	Fuel Bed Assembly	68
4.6.	Results and Discussion	71
4.6.1.	Temporal Characteristics of Heat Flux	71
4.6.2.	Spectral Analysis	94
4.7.	Conclusions.....	96
5.	Convection and Radiation Heat Flux Data from Field Burns	99
5.1.	Abstract.....	99
5.2.	Introduction.....	99
5.3.	Measurement Procedure	101
5.4.	Results.....	109
5.4.1.	Fires Manifesting Frontal Flame Spread.....	109
5.4.2.	Fires Manifesting Non-frontal Flame Spread	120
5.4.3.	Discussion of Results	124
5.5.	Conclusions.....	132
6.	Fuel Response to Rapid Heating Fluctuations in Wildland Fires – Measurement and Analysis	133
6.1.	Abstract.....	133
6.2.	Introduction.....	133

6.3.	Measurement and Calibration Procedure.....	135
6.4.	Heat Flux Data Collection	137
6.5.	Model	152
6.6.	Model Predictions	157
6.7.	Conclusions.....	175
7.	Conclusions.....	177
8.	References.....	183
A.	Appendix A	189
A.1.	Description.....	189
A.2.	Code	189
B.	Appendix B	193
B.1.	Description.....	193
B.2.	Code	193
C.	Appendix C	203
C.1.	Description.....	203
C.2.	Solution.....	203

LIST OF TABLES

Table 2-1. Overall reduction in total radiative heat transfer incident on the fuel bed due to absorption by environmental water vapor.....	35
Table 3-1. Average fuel temperature and heat flux for all experiments	44
Table 4-1. Calculated flame spread rates for the experimental conditions investigated.	71
Table 5-1. Summary of fire conditions, radiation heat flux peaks and convection heat flux peaks (shaded areas represent non-ideal flame spread).....	108
Table 6-1. Peak radiation and convective heat flux resolved for the two burns as a function of sampling rate.	147

LIST OF FIGURES

Figure 2.1. Schematic illustration of configuration investigated.....	18
Figure 2.2. Detailed illustration of geometry and nomenclature for determination of volumetric exchange factor and local incident flux.....	22
Figure 2.3. a) Error between the volumetric exchange factor for $\kappa_k \rightarrow 0$ (for $K = 1$) and the corresponding classical radiation configuration factor, and b) variation in calculated volumetric exchange factor with number of integration points.....	26
Figure 2.4. Predicted local incident radiant flux along the fuel bed for the cases with and without water vapor absorption, $H = 1$ m, $L = 10$ m, $\phi = 90$ deg, and $T_f = 1000$ K.....	29
Figure 2.5. Effect of flame temperature on local incident radiant flux along the fuel bed for $H = 1$ m, $L = 10$ m, and $\phi = 90$ deg.....	30
Figure 2.6. Effect of flame length on local incident radiant flux along the fuel bed for $\phi = 90$ deg and $T_f = 1000$ K.....	31
Figure 2.7. Effect of flame angle on local incident radiant flux along the fuel bed for $H = 1$ m, $L = 10$ m, and $T_f = 1000$ K.....	32
Figure 2.8. Difference in local incident radiant flux due to water vapor absorption as a function of normalized position along the fuel bed for all cases studied.....	34
Figure 3.1. Experimental setup.....	40
Figure 3.2. Representative sample of experimentally measured timewise variation in heat flux and fuel temperature.....	43
Figure 3.3. Experimentally measured fuel temperature as a function of distance from plane burner for Ponderosa pine and small and large excelsior.....	45
Figure 3.4. Comparison between model predictions and experimental measurements of fuel temperature.....	50
Figure 3.5. Predicted relative contributions of radiation heating and cooling and natural convective cooling.....	50

Figure 3.6. Predicted fuel temperature as a function of incident radiation flux for different convective conditions. The ignition temperature indicated is the minimum temperature at which wood will ignite regardless of the heating arrangement (Babrauskas, 2003).	52
Figure 3.7. Sensitivity of predicted fuel temperature to plane burner temperature. The ignition temperature indicated is the minimum temperature at which wood will ignite regardless of the heating arrangement (Babrauskas, 2003).	54
Figure 3.8. Dependence of predicted fuel temperature on fuel diameter. The ignition temperature indicated is the minimum temperature at which wood will ignite regardless of the heating arrangement (Babrauskas, 2003).	56
Figure 3.9. Predicted distance from burner at which fuel ignition (Babrauskas, 2003) occurs as a function of burner temperature.	57
Figure 4.1. Schematic illustrations of a) sensor configuration with windowed sensor on the left and the non-windowed sensor on the right, and b) discontinuous fuel bed with each cylinder representing a fuel rod.	63
Figure 4.2. Measured radiation and convection characteristics for 0.61 m fuel rods and 0.20 m row spacing: (a) radiation and convection heat flux, (b) sensor temperatures, (c) fraction of time convective cooling and heating after flame arrival (time = 0 s), and (d) cumulative flux.	73
Figure 4.3. Comparison of the modeled heat flux experienced by the sensor and the fuel: a) Convective heating, and b) Convective cooling. Two different fuel particle diameters are represented.	76
Figure 4.4. Radiation and convection heat flux histories for experiments with the same conditions, 0.61 m fuel rod height and 0.15 m row spacing.	79
Figure 4.5. Comparison of the radiation and convection heat flux histories for two burns with the same fuel height (0.61 m) but with different row spacing (0.15 and 0.20 m).	80
Figure 4.6. Comparison of radiation and convection for two burns with the same fuel height (1.22 m) but with different row spacing (0.20 and 0.25 m).	84
Figure 4.7. Radiation and convection for two experiments with the same row spacing (0.20 m), but with different fuel heights (0.61 m and 1.22 m).	86
Figure 4.8. Photograph of fuel bed burned in the presence of wind at 2.2 m/s.	88
Figure 4.9. Two experiments with the same fuel height and row spacing, 0.61 m and 0.20 m respectively, one buoyancy-driven and the second wind-driven with a 2.2 m/s crossflow.	89

Figure 4.10. Heat flux histories for buoyancy- and wind-driven burns 0.61 m fuel with 0.20 m row spacing.....	92
Figure 4.11. Burn characteristics for 0.61 and 1.22 m height fuel plotted as a function of combustion zone position.	93
Figure 4.12. Power spectra for fluctuating convection and radiation heat flux: (a) buoyancy-driven experiment with 0.61 m fuel height and 0.15 m row spacing, (b) buoyancy-driven experiment with 0.61 m fuel height and 0.20 m row spacing, (c) buoyancy-driven experiment with 1.22 m fuel height and 0.20 m row spacing, and (d) wind-driven experiment with 0.61 m fuel height and 0.20 m row spacing.....	95
Figure 5.1. Sensor setup.....	102
Figure 5.2. Rombo Mountain fire data 28 th August 2007- Wind –none; Slope – 10 deg.; Fuel - grass and ponderosa pine needle cast. a - radiation and convection heat flux and fraction heating and cooling. b - sensor temperature.....	110
Figure 5.3. Rombo Mountain fire 29 August 2007 Wind –none; Slope -35 deg.; Fuel – grass, brush and ponderosa pine needle cast.....	113
Figure 5.4. (Top) Eglin Air Force Base 1 March 2008 Wind – 0.5-1 m/s; Slope – 0 deg.; Fuel - grass and longleaf pine (<i>Pinus palustris</i>) needle cast. 4 year southern rough, consumed fuel loading 0.38 kg/m ² . (bottom) Heat Flux data.....	115
Figure 5.5. Ichauway 3 March 2008 Wind – 0.5-1 m/s; Slope – 0 deg.; Fuel - grass and longleaf pine (<i>Pinus palustris</i>) needle cast. 1 year southern rough, consumed fuel loading 0.57 kg/m ² . (bottom) Heat Flux Data	116
Figure 5.6. Ichauway 5 March 2008 Wind – 0.5-1 m/s; Slope – 0 deg.; Fuel – grass and longleaf pine (<i>Pinus palustris</i>) needle cast, 1 year southern rough, consumed fuel loading 0.17 kg/m ² (bottom) Heat Flux Data	118
Figure 5.7. Ichauway 6 March 2008 (Burn 1) Wind – 0.5-1 m/s; Slope – 0 deg.; Fuel - grass and longleaf pine (<i>Pinus palustris</i>) needle cast, 2 year southern rough, consumed fuel loading 0.28 kg/m ²	119
Figure 5.8. Ichauway 6 March 2008 (Burn 2) Wind –none; Slope – 0 deg.; Fuel - grass and longleaf pine (<i>Pinus palustris</i>) needle cast, 1 year southern rough, consumed fuel loading unknown.	120
Figure 5.9. Rat Creek Fire 16 August 2007 – Wind –none; Slope - not measured but steep; Fuel - Lodgepole pine (<i>Pinus contorta</i>), grass and needle cast (bottom) Heat Flux Data	122

Figure 5.10. Mill creek crown fire 30 August 2007 Wind –none; Slope – 4 deg.; Fuel - Lodgepole pine (<i>Pinus contorta</i>), grass and needle cast. (bottom) Heat Flux Data.....	123
Figure 5.11. Eglin Air Force base 2 March 2008 Wind –0.5-1.5 m/s; Slope – 0 deg.; Fuel - grass and longleaf pine (<i>Pinus palustris</i>) needle cast, 1 year southern rough, consumed fuel loading 0.33 kg/m ²	125
Figure 5.12. Leadore; Wind – 0.5-1.5 m/s; Slope – unmeasured but present; Fuel – Sage brush (<i>Artemisia tridentata</i> subsp. <i>Wyomingensis</i>) and Grass.....	126
Figure 5.13. 1 s moving average radiant heat flux for all data sets	128
Figure 5.14. 1 s moving average convection heat flux for all data sets.....	129
Figure 5.15. Instantaneous cumulative radiation (top) and convection (bottom) heat flux for selected ground fires, brush fires and crown fires.	131
Figure 6.1. Photograph of flames passing over data collection setup.....	137
Figure 6.2. Heat flux and sensor temperature history for Sula, MT Burn 1.	138
Figure 6.3. Heat flux fluctuations in Sula, MT Burn 1. Figures b and c expand the time scale for one specific segment of the time series.....	140
Figure 6.4. Heat flux fluctuations in Sula, MT Burn 2. Figures b and c expand the time scale for one specific segment of the time series.....	141
Figure 6.5. Radiation and convection power spectra for both Sula, MT burns.	142
Figure 6.6. The effect of reducing sample rate on measured heat flux, Burn 1.....	145
Figure 6.7. The effect of reducing sample rate on measured heat flux, Burn 2.....	146
Figure 6.8. Cumulative convective and radiative heat flux histories for Burns 1 and 2 with different sample rates.....	149
Figure 6.9. 1 s moving average heat flux for Sula burns 1 and 2 radiation and convection.....	151
Figure 6.10. Fuel model schematic.	153
Figure 6.11. Model solution using for $R = 0.5$ and 1.0 mm using the thermophysical properties of fir, $T_{max} = 1600$ K, wind velocity = 5 m/s.....	159
Figure 6.12. Dimensionless predicted surface and centerline temperatures for $Bi = 0.1, 1, \text{ and } 10$	163

Figure 6.13. Dimensionless predicted surface and centerline temperatures, and temperature differences at $Bi = 0.2, 0.4, 0.6$ and 0.8	164
Figure 6.14. Dimensionless predicted surface and centerline temperatures, and temperature differences at $Bi = 2, 4, 6, 8, 15$ and 30	165
Figure 6.15. Relationship between predicted dimensionless ignition time and Biot number for a range of ambient temperature magnitudes.	168
Figure 6.16. Relationship between predicted dimensionless ignition frequency and Biot number for a range of ambient temperature magnitudes.	170
Figure 6.17. Predicted surface and centerline temperature histories of a 1mm Douglas Fir cylindrical particle under 3 imposed heat fluxes a) 100 kW/m^2 b) 200 kW/m^2 and c) 300 kW/m^2	172
Figure 6.18. Relationship between predicted dimensionless ignition frequency and dimensionless heat flux (q^*).	174

1. Introduction

Each year millions of acres of wildland are consumed by wildfires (NIFC, 2009) and the U.S. government spends over \$1 billion annually in suppressing them (GAO, 2009). Annual cost associated with damage to crops and property is estimated to be nearly \$800 million (NOAA, 2009). Between 1990 and 2006, 310 people lost their lives fighting wildfires (NWCG, 2009). With the increase in the number of people moving to the urban/wildland interface, the incidence of fire, risks to life and property, and cost of suppression are likely to increase. Given the financial costs and death toll associated with wildfires, there is a clear need to better understand fire behavior and to develop the capability of predicting fire spread in these complex environments. Understanding the mechanisms of convective and radiative heat transfer involved in the heating and subsequent ignition of fuel is critical to that effort.

Once the mechanisms of heat transfer in wildfires are better understood, the current underlying assumptions to fire prediction models can be modified to increase the accuracy of fire behavior prediction. If one can accurately predict how fast and where a fire will spread, proper warnings can be issued, lives can be saved, and the fire can be more effectively suppressed.

1.1. Problem Overview

The relative contribution of radiation and convection in a wildland fire depend in a complex way on the prevailing wind speed, fuel distribution, buoyancy-induced in-drafts, relative humidity, *etc.* As a result of this complexity, there is much that is not understood about heat transfer in wildland fires. In spite of these complexities, heat transfer in fires can be viewed in an elementary way by describing what an individual fuel particle experiences as it is heated, ignites, and combusts. A fuel particle may experience both radiation and convection heat transfer before ignition in a forest fire environment. The flame front irradiates the unburned fuel ahead of it. The radiant preheating of the fuel has the potential, depending on conditions, to drive water vapor and volatiles from the fuel. When the flames arrive at an unburned fuel particle, the particle is exposed to the convective influence of the flames as well as continued radiative influence. The transient nature of the flame provides a complex convective and radiative heat transfer environment. When modeling this environment, assumptions are required to formulate a tractable model and obtain solutions. However, the validity of these assumptions is difficult to determine because the mechanisms of the heat transfer have not yet been fully explored. This work seeks to provide meaningful experimental data in both controlled laboratory and wildland fire environments which can shed light on the heat transfer behavior during wildland fire spread. Particular emphasis is placed in the study on the characterization of the relative contributions of radiation and convection heat transfer in wildfire scenarios. Further, the mechanism of fuel particle heating to ignition temperature is explored in considerable detail.

1.2. General Literature Review

The relative roles of radiation and convection on flame spread have been an area of interest for some time (Anderson, 1969). Experiments to better understand wildland fire behavior have been undertaken since the 1940's. A few of the more influential studies are summarized in this section.

Fons (1946) developed an semi-empirical expression to predict the rate of flame spread through a homogenous fuel bed. The Nusselt number for quantifying particle convective heating was calculated using an experimentally derived relation for forced convection past a cylinder. The radiation heat transfer was assumed to be gray, constant, and independent of flame shape for all particles adjacent to the flame, and zero elsewhere. Experiments were conducted in a wind tunnel with a 1.83 m square cross section. The fuel beds were 1.22 m by either 2.44 or 3.66 m. The fuel used was either Ponderosa pine (*Pinus ponderosa*) needles layered 0.051 m deep or Ponderosa pine twigs evenly spaced. When twigs were used, three experiments were conducted with samples of nominal diameters 0.0032, 0.0048 or 0.0064 m. Once the parameter of interest was determined, rate of flame spread was predicted and compared to experimental fires with good success.

Hottel *et al.* (1965) exposed a bed of shredded newspaper or computer card punchings to irradiation to determine its effect on rate of flame spread. The irradiation was generated using electrically heated nichrome wires 3.17 cm above the fuel bed. It was shown that irradiation caused as much as a 200 percent increase in flame rate of spread when the wires were heated such that the fuel intercepted nearly 580 W of energy per meter of flame front length. A set of predictive equations governing flame spread

was developed. Four variations in assumptions were explored to determine if radiation and heat loss from the fuel could be more accurately accounted for. This appears to have been the first attempt to use radiation view factors for the calculation of flame radiation to the fuel.

Albini (1967) developed an early physics-based model to predict fire spread by assuming that the various stages in forest combustion can be described by intermittent steps. The steps included preheating (including outgassing from pyrolysis), intermittent ignition of gasses from preheating pyrolysis, attachment of flame to fuel, and steady burning after attachment. By assuming that each step requires a calculable amount of time, a dimensionless spread-rate was derived.

Thomas (1967) describes experiments conducted to better understand fire spread. Flame height was correlated with flame depth of the burning zone under a variety of fuel and ambient conditions. Through this work it was postulated that buoyancy-driven fires spread as a result of radiation heat transfer from the combusting fuel, and wind-driven fires occur primarily as a result of radiation heat transfer from the flames which are described as “thick.”

In an attempt to better understand the relative role of radiation and convection on flame spread, Van Wagner (1967) developed a model with a simplified view factor for describing the radiation transfer, and tested it against the spread rate of an experimental Red pine (*Pinus resinosa*) needle bed. Flame angles (measured between the fuel bed and the flame) between 25 and 90 in 5 degree increments were studied. The flame angles were generated by tilting the fuel bed which was 1.22 m long and 0.76 m wide with a depth of 0.05 m. Spot measurements of flame radiation were recorded, but no explana-

tion of the method of measurement used was offered. In the model, radiation was assumed to be described by a blackbody radiation flux multiplied by a factor to account for flame angle. Convection heat transfer was not considered.

Anderson (1968) measured the total (convective plus radiative) heat flux using a thermopile sensor in fuel beds of Ponderosa Pine (*Pinus ponderosa*), Western White Pine (*Pinus monticola*), and Lodgepole Pine (*Pinus contorta*) needles. K-type thermocouples were used to determine the flame temperature. The radiant heat flux was extrapolated by using view factor radiation transfer relations and flame photographs with a 1 s exposure time. Some of these same experiments were later used to verify a model that was developed (Anderson, 1969). In this model configuration factors for both the combustion zone and the flame were calculated. Flame convection was determined by using a Nusselt number derived for burning liquid pool fires.

Anderson (1969) developed a simple mathematical model which included both radiation and convection heat transfer. The model was compared to experimental results reported, and it was concluded that radiation accounted for no more than 40 percent of the energy required to maintain the observed rate of spread.

Pagni and Peterson (1972) developed a model to describe flame and ember radiation, surface and internal convection, turbulent diffusion of flame eddies and gas-phase conduction as heat transfer terms. The model development and analysis led to four conclusions: 1) Under ambient flow conditions, flame radiation is the dominant heat transfer mechanism with contributions from ember radiation and gas phase conduction; 2) In most non-zero ambient flow velocities, convection is dominant with significant contributions from flame radiation; 3) Energy from turbulent flame eddies appears to be negligible in

most cases; 4) Energy absorbed by pyrolysis before ignition appears to be negligible. The model was tested with beds of Western White pine (*Pinus monticola*) and Ponderosa pine (*Pinus ponderosa*). After neglecting internal convection (convection within the fuel layer) and changing the fuel thickness within the model (such that the modeled situation deviated from the experimental conditions on which the model was based), good qualitative agreement was reached.

Hirano *et al.* (1974) measured the spread rate of fire on a sheet of paper placed between two electrical resistance heater planes in an effort to better understand the effects of radiation on flame spread. Temperature and spread rate were measured. The study revealed that hot gases were only present a short distance from the flame front. Furthermore, the increase in spread rate ascribed to the irradiation from the electrical resistance heater planes was attributed primarily to the increase in temperature of the unburned fuel, rather than changes in flow patterns generated by buoyancy.

Konev (1977) measured radiant heat flux with a bed of Scots pine needles (*Pinus sylvestris*) using thermocouples in a copper cylinder with a black exposed end and insulated sides. The magnitude of radiation heat transfer was also estimated by artificially blackening (painting) the fuel and measuring the temperature. Through this the fraction of total heat transfer required for ignition by radiation was estimated to be between 8 percent for a nearly dying fire, and 37 percent under more vigorous flame conditions.

Albini (1985) developed a one-dimensional model for radiation-driven flame spread in an infinitely deep fuel bed. The model assumes that the fuel particles are randomly oriented, isothermal and radiatively black. This model was extended (Albini, 1986) to include radiation emission and convective cooling of the fuel particles, and it

was shown that the model could predict the experimental shape of the combustion interface when free parameters were adjusted to match the spread rate.

Albini and Stocks (1986) compared nine experimental wind-aided crown fires in Jack pine (*Pinus banksiana*) stands to a model developed by Albini (1985). Eight of the fires were used to determine empirical parameters within the model, and experimentally measured data from the ninth fire was used to determine if the model could predict the spread rate. The discrete ordinates method was used to solve the radiative transfer equation and the flame was assumed to be black and planar. The air separating the flame and fuel was assumed to be fully transparent and the fuel bed was assumed to be semi-transparent. The temperature distribution along the fuel bed was iteratively determined. Convection was neglected. The model predicts spread rates with rms errors between 0.034 m/s and 0.037 m/s, and a maximum absolute error of 0.06 m/s. Observed spread rates ranged from 0.179 m/s and 0.455 m/s.

De Mestre *et al.* (1989) developed more sophisticated modeling techniques to describe both the solid and gaseous components of the flame and fuel system and measured temperature distribution in front of the flame spreading across a pine needle bed. Comparing observed and calculated rate of flame spread with radiation as the only heat transfer mechanism resulted in a predicted spread rate thirteen times that which was observed. This was corrected by adding a convective cooling term. Convective heating was not included in the model.

Butler (1993) used both narrow-angle and hemispherical radiometry to measure radiant flux from laboratory fires using poplar (*Populus tremuloides*) excelsior and ponderosa pine (*Pinus ponderosa*) needles under a wide range of conditions (wind speed and

humidity). The data show that flame irradiation is a strong function of flame geometry (length and angle) and fuel conditions.

Cheney (1995) observed the flame spread in grass fires in Australia. It was shown that the time required for the fires to reach a steady rate of spread was dependent on the frequency of changes in wind direction.

Wotton *et al.* (1996) used narrow-angle radiometers to measure the vertical intensity profile from the flames of a burning bed of pine needles. It was shown that the flame intensity was highest at the base and lowest at the tip of the flame. A later study (Wotton *et al.*, 1999) also conducted a series of controlled burns on a pine plantation where the effect of fire front width on flame spread rate was determined. Total hemispherical radiation measurements were collected as described by Butler (1993) at different distances from the ignition point and at a height of 0.25 m from the ground. It was shown that fire front width had some effect on the spread rate until the flame front obtained a width of 2 m.

Morvan *et al.* (2000) developed a model to study the propagation of a surface fire in the forest. This model included some of the reaction chemistry associated with the combustion of wood. The results of the model reveal that the rate of spread is primarily controlled by radiation heat transfer.

Data from a comprehensive set of crown fire experiments in Northwest Territories of Canada were published by Butler *et al.* (2004). Temperatures using K-type thermocouples and radiant heat flux measurements using narrow angle radiometers were collected at heights of 3.1, 6.2, 9.2, 12.3, and 13.8 m above the ground and into the canopy. The radiometers featured a 40 ms response time (25 Hz frequency response), but were

sampled at 1 Hz. The calibrated range of the radiometers (due to blackbody calibration limit) was limited to 200 kW/m^2 , but the same calibrations were used to collect data nearly as high as 300 kW/m^2 . Peak measured air temperatures exceeded 1330°C and the maximum heat flux recorded in the upper third of the canopy was 290 kW/m^2 . Blackbody temperatures were calculated using the narrow angle radiometer heat flux measurements by use of the Stefan-Boltzman law. These calculated temperatures were then compared to thermocouple-based temperature measurements. It was shown that estimates of fireline intensity were in error for all but the 9.2 m height, indicating that fireline intensity estimates based on thermocouple temperatures may result in an underestimation of radiant intensity.

Knight and Sullivan (2004) developed a model to predict radiation intensity from flames. The flames are modeled as a semitransparent triangular prism whereas traditional flame radiation models assumed that the flames are blackbody radiators.

Sardoy *et al.* (2007) developed a model for the spread of firebrands, which are burning embers transported on the buoyant plume of the fire. These firebrands are carried ahead of the flame front by wind to start new fires and can potentially cross fire breaks. The model predicts the distance that firebrands are able to travel ahead of the flame front.

Although wildfires have been extensively studied, there are still large gaps in fire behavior knowledge. No work has been completed to determine the effect of environmental water vapor on the attenuation of radiation between the flames and the fuel, or to determine if radiation-only preheating to ignition is possible. To the knowledge of the author, no direct, simultaneous measurement of radiant and convective heat flux exists in

the archival literature. In fact, few field measurements of heat flux have been reported (Packham and Pompe, 1971; Butler *et al.*, 2004; Morandini *et al.*, 2006; Silvani and Morandini, 2009). Of these field measurements, no investigation of the partitioning between radiation and convection has been reported. Further, there has been no characterization of the time-resolved character of the heat flux, including its frequency content. This dissertation describes work designed to help address these deficiencies in the understanding of heat transfer behavior in wildland fires.

1.3. Objectives

Clearly, there is much that still needs to be done to understand heat transfer in forest fires. As pointed out in the foregoing section, there are deficiencies in understanding attenuation of radiation heat transfer due to water vapor, radiation-induced particle ignition, partitioning of radiation and convection in the laboratory and the field, as well as their temporal fluctuation characteristics and frequency content. This work seeks to fill the void which exists in these areas by modeling and by experimentation. All of the models included in this dissertation were developed by the author. All of the experimental data reported here were collected by the author with the exception of those in Chapter 3, which were conducted by Bret W. Butler and Don J. Latham at the US Forest Service Fire Sciences Laboratory in Missoula, Montana.

1.4. Dissertation Organization

This work is presented in five chapters, each covering a different aspect of heat transfer in simulated or field-based wildland fires. Each chapter is presented as a pub-

lishable stand-alone work. A general literature search comprehensively summarizing the body of work related to wildland fires has been presented in this chapter. Each chapter will present its own more study-specific literature review. The content of the chapters is described generally as follows:

Chapter 2: Influence of Absorption by Environmental Water Vapor on Radiation Transfer in Wildland Fires

Thermal radiation emission from a simulated black flame surface to a fuel bed is analyzed by a ray-tracing technique, tracking emission from points along the flame to locations along the fuel bed while accounting for absorption by environmental water vapor in the intervening medium. The Spectral Line Weighted-sum-of-gray-gases approach was adopted for treating the spectral nature of the radiation. The flame and fuel bed for the simulations are modeled two-dimensionally with the flame being one-tenth as long as the fuel bed. Flame heights of 1 and 10 m were explored, and the angle between the flame and the fuel bed was specified to be either 60 or 90 degrees. Simulated flame temperatures of 1000 K and 1500 K were investigated. The study reveals that water vapor at 100 percent humidity will reduce the incident radiation at the base of a 1000 K flame by 9 percent for a 1 m flame and 16 percent for a 10 m flame oriented normal to the fuel bed. Radiation from an angled flame (oriented at 60 degrees from the fuel bed) experiences slightly less attenuation from water vapor than the 90-deg flame. Further, local attenuation of the hotter flame (1500 K) from environmental water vapor is higher than for the 1000 K flame. The relative effect of the water vapor attenuation is increased with distance from the flame base.

Chapter 3: Fine Fuel Heating by Radiant Flux

Experiments were conducted wherein wood shavings and Ponderosa pine needles in quiescent air were subjected to a steady radiation heat flux from a planar ceramic burner. The internal temperature of these particles was measured using fine diameter (0.076 mm diameter) type K thermocouples. A narrow angle radiometer was used to determine the heat flux generated by the burner. A model was developed to predict the steady-state temperature of a cylindrical particle with an imposed radiation heat flux under both quiescent air (buoyancy-induced cooling) and windy (forced convection cooling) conditions. Excellent agreement was observed between the model predictions and the experimental data. Parametric studies using the validated model explore the effect of burner (flame) temperature and distance, fuel size, and wind speed. It is concluded that ignition of the fuel element by radiation heating alone is unlikely. While it may occur in a quiescent environment, it is speculated as unlikely due to intense buoyant in-draft induced by the combustion.

Chapter 4: Time-Resolved Radiation and Convection Heat Transfer in Combusting Discontinuous Fuel Beds

Time-resolved radiation and convection heat flux was measured in a series of experimental fires designed to explore heat transfer behavior during combustion of discontinuous fuel beds. Fuel spacing and height were varied for both buoyancy-driven and wind-driven combustion. Peak radiation heat fluxes as high as 130 kW/m^2 were recorded. Convection heat flux manifested significant temporal fluctuations and peaks were recorded at 90 kW/m^2 . Radiation flux had the effect of heating the fuel before flame arrival. Both positive (heating) and negative (cooling) convective heat transfer occurred

before flame arrival. Surprisingly, the convection could also be positive or negative after flame arrival indicating that even when engulfed in flames there were packets of cooler air moving across the sensor. In nearly all cases, short-duration convective heating pulses appear to precede the full onset of combustion, suggesting that convective heating may be critical as an ignition source. Rapid temporal fluctuations were observed in both radiation and convection, and spectral analysis revealed spectral content at frequencies as high as 70 Hz under buoyant flow conditions and 150 to 200 Hz under the influence of wind.

Chapter 5: Convection and Radiation Heat Flux Data from Field Burns

Very little heat flux data have been collected in actively spreading wildfires or controlled burns. Time-resolved radiation and convection heat flux data sets were collected under a variety of fuel and ambient conditions including two crown fires and three brush fires. It was shown that convective heat flux is composed of brief/intense peaks whereas radiation heat flux increases and decreases nearly monotonically with the approach, arrival and departure of the flame front.

Chapter 6: Fuel Response to Rapid Heating Fluctuations in Wildland Fires – Measurement and Analysis

Time-resolved radiation and convection heat flux histories were collected on a controlled wildland burn at a sampling frequency of 500 Hz. The data reveal relatively modest temporal fluctuations in the radiation heat flux. However, short-duration peaks in convective heat flux were observed. Frequency content in the radiant flux as high as 20 Hz and in the convection heat flux up to 100 Hz was revealed by a Fast Fourier Trans-

form of the time-series signals. The effect of sampling frequency on measured convective and radiative heat flux is explored, and it is asserted that sampling frequencies below 50 Hz and 120Hz in previous measurements may be insufficient to fully resolve temporal fluctuations in radiation and convection heat flux, respectively. The role of the higher frequency convective content in fuel thermal response is explored using a one-dimensional transient conduction model with a convective boundary condition. It is shown that high-frequency (*i.e.*, short-duration) convective pulses can lead to fine fuel ignition.

1.5. Summary

This work seeks to contribute in a significant way to the body of work on heat transfer in forest fires. It will shed light on engineering modeling techniques in the wild-fire research community, report measurements of time-resolved radiation and convection heat transfer phenomena which have previously gone unmeasured, and it will comprehensively study the relative interplay between radiation and convection and their role in fuel ignition.

2. Influence of Absorption by Environmental Water Vapor on Radiation Transfer in Wildland Fires

2.1. Abstract

Thermal radiation emission from a simulated black flame surface to a fuel bed is analyzed by a ray-tracing technique, tracking emission from points along the flame to locations along the fuel bed while accounting for absorption by environmental water vapor in the intervening medium. The Spectral Line Weighted-sum-of-gray-gases approach was adopted for treating the spectral nature of the radiation. The flame and fuel bed for the simulations are modeled two-dimensionally with the flame being one-tenth as long as the fuel bed. Flame heights of 1 and 10 m were explored, and the angle between the flame and the fuel bed was specified to be either 60 or 90 degrees. Simulated flame temperatures of 1000 K and 1500 K were investigated. The study reveals that water vapor at 100 percent humidity will reduce the incident radiation at the base of a 1000 K flame by 9 percent for a 1 m flame and 16 percent for a 10 m flame oriented normal to the fuel bed. Radiation from an angled flame (oriented at 60 degrees from the fuel bed) experiences slightly less attenuation from water vapor than the 90-deg flame. Further, local attenuation of the hotter flame (1500 K) from environmental water vapor is higher than for the 1000 K flame. The relative effect of the water vapor attenuation is increased with distance from the flame base.

2.2. Introduction

It is understood that thermal radiation transfer plays a significant role in wildland fire spread (De Mestre et al., 1989). High temperatures in gaseous and particulate products of combustion result in significant radiation transfer to the unburned fuel ahead of advancing flames. Attenuation of flame radiation can occur from smoke and combustion products that are entrained in the intervening air between flame and fuel. This mechanism for attenuation of flame radiation is a complex function of fuel, flame, wind, and other environmental conditions. It is also recognized that environmental water vapor may be a mechanism for attenuation of flame radiation. The magnitude of this influence has been a question among wildland fire scientists for some time, but has not been heretofore characterized. This paper explores the attenuation of radiation from flame to fuel bed by environmental water vapor in the intervening medium.

2.3. Literature Review

Wildland fire spread has been modeled using a variety of approaches. Some models attempt to conserve energy generally without separating convection from radiation heat transfer. Still others attempt to model radiation and convection separately (Weber, 1991). Those which do model the radiation transfer invoke varied approximations in the radiation submodels. Fons (1946) treats the radiation transfer in an approximate fashion by assuming that a fixed fraction of combustion energy comes from radiation. Emmons (1964) assumes radiation is attenuated with distance from the flame by an exponential relationship. Hottel *et al.* (1965) were the first to model the flame shape, introducing radiation configuration factor relations which quantify the fraction of radiation

emitted by one surface that is incident on another. One model considered radiation heat transfer from a planar flame to a planar fuel bed; the other used a relation that accounted for radiation attenuation through the fuel bed using an exponential factor. Albini (1967) formulated an approach that employed the same radiation sub-model as Hottel *et al.*, considering radiation as the dominant heat transfer mechanism. Thomas (1967) proposed that radiation from the flame was insignificant in comparison to radiation through the porous fuel bed. Other models were introduced using the same radiation configuration factor relations to track radiation transfer from flame to fuel until Cekirge (1978) introduced a formulation that could account for a circular flame front. Albini (1985) first introduced a solution to the Radiative Transfer Equation (RTE), the integro-differential equation governing transport of radiative energy. The RTE was solved using the discrete ordinates method, but no volumetric effects in the fuel, flame, or the intervening medium were included.

To the authors' knowledge, no prior study has explored the effect of attenuation of radiation between flame and fuel bed by environmental water vapor. This paper investigates this mechanism for attenuation of flame radiation by modeling the spectral emission from flame to fuel, accounting for the absorption by environmental water vapor.

2.4. Model

Consider a planar flame of length H and characterized by uniform temperature T_f advancing along a horizontal fuel bed, as shown in Figure 2.1. The length of the fuel bed L is specified arbitrarily in this study to be ten times the flame length, $L/H = 10$. Incident flame radiation beyond this point is negligible. The angle between flame and fuel

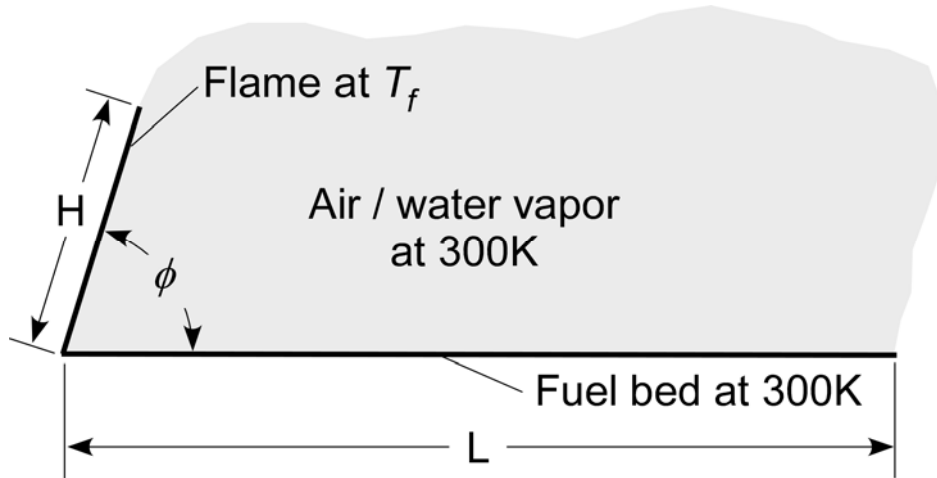


Figure 2.1. Schematic illustration of configuration investigated.

bed is specified to be ϕ . Simulations were conducted with and without environmental water vapor in the air separating the flame from the fuel bed. It is assumed that the intervening medium (air/H₂O vapor) and the fuel bed are at a uniform temperature of 300 K. It should be clearly stated that attenuation by entrained combustion products (ash, H₂O, CO₂, soot, *etc.*) is not considered here. Attenuation of flame radiation from such products will dominate any effects by environmental water vapor. Rather, the purpose of this study is to characterize only the effects of water vapor.

Absorption of radiation is governed by the Beer's Law (Modest, 2003) which states

$$I_{\eta}(s) = I_{\eta_0} e^{-\kappa_{\eta}(s-s_0)} \quad (2-1)$$

Equation (2-1) indicates that the spectral radiation intensity of magnitude I_{η_0} incident on a radiatively absorbing medium and propagating in a particular direction is attenuated ex-

ponentially with distance s from the point of incidence s_o along this direction by the factor $e^{-\kappa_\eta(s-s_o)}$, where κ_η is the volumetric absorption coefficient.

As indicated by the subscript η , Eq. (2-1) is a spectral relation; the radiative intensity I_η , incident radiation intensity $I_{\eta o}$, and absorption coefficient κ_η vary with wavenumber (or wavelength). While significant absorption may occur in some regions of the spectrum, others are transparent to radiative transfer. For gases capable of volumetric absorption in the infrared spectrum, the spectral absorption coefficient is characterized by vibration-rotation bands. For water vapor, the principal absorption bands are centered at wavenumbers 3760 and 1600 cm^{-1} (wavelengths of 2.7 and 6.3 μm , respectively). Within each absorption band, thousands of narrow absorption lines exist, with strong absorption of radiation within each narrow line. Several hundred thousand absorption lines are associated with the two principal vibration-rotation bands for water vapor. The absorption strength of each line is a function of the temperature and partial pressure of water vapor. The challenges associated with rigorously modeling mathematically the attenuation of flame radiation by water vapor are significant. The spectral emission characteristics of the flame is a strong function of fuel type, humidity, water content, wind conditions, *etc.* Further, as described herein, absorption of flame radiation by the environmental water vapor occurs within the hundreds of thousands of extremely narrow spectral lines within both infrared vibration-rotation bands. In this study, the flame is characterized as a planar surface whose spectral emission of radiation can be taken to be that of a blackbody at the flame temperature T_f .

Radiation transfer within a black enclosure with non-gray medium was formulated by Hottel and Sarofim (1967) for application to combustion chambers. The total

radiative flux emitted by black surface i which is incident on surface j may be expressed generally as

$$q_{i \rightarrow j} = \int_0^{\infty} \int_{A_i} \int_{A_j} e^{-\kappa_{\eta} s} \frac{\cos \theta_i \cos \theta_j}{\pi s^2} dA_i dA_j E_{bi, \eta} d\eta \quad (2-2)$$

Equation (2-2) is a triple integration over wavenumber (η), the area of the emitting surface (A_i), and the incident surface (A_j). The double integration over area is required to track the radiant emission from a location on surface i that arrives at all possible locations on surface j . This tracking must be done for all points of radiation emission on surface i . The geometric term $\cos \theta_i \cos \theta_j / \pi s^2$ accounts for the varying field of view for differential elements on surface i and surface j , separated by a distance s . $E_{bi, \eta}$ is the spectral blackbody emission from surface i , described by the Planck blackbody radiation spectral distribution at the temperature of surface i . The exponential term $e^{-\kappa_{\eta} s}$ in Eq. (2-2) accounts for absorption of radiation by the intervening medium of spectral absorption coefficient κ_{η} according to Beer's Law. Integrating over the spectrum as in the development of the classical weighted-sum-of-gray-gases model (Modest, 2003), it can be shown that the radiative flux emitted by surface i which is incident on surface j is

$$q_{i \rightarrow j} = \int_0^{\infty} (\overline{s_i s_j})_{\eta} E_{bi, \eta} d\eta \quad (2-3)$$

where $(\overline{s_i s_j})_\eta$ is the spectral volumetric exchange factor, expressed as

$$(\overline{s_i s_j})_\eta = \int_{A_i} \int_{A_j} e^{-\kappa_\eta s} \frac{\cos \theta_i \cos \theta_j}{\pi s^2} dA_i dA_j \quad (2-4)$$

The dependence of both the volumetric exchange factor defined in Eq. (2-4), and the total radiant flux, Eq. (2-3), on wavenumber is evident. Because of the complex spectral variation in the absorption coefficient of water vapor, the Spectral Line Weighted-sum-of-gray-gases (SLW) model (Denison and Webb, 1993a; 1993b) was used to account for its spectral absorption characteristics. The SLW model has been shown to yield accuracy approaching that of computationally intensive line-by-line integrations for a small fraction of the computational cost. Rather than calculate the absorption of flame radiation by integrating on a line-by-line basis over the hundreds of thousands of lines using the Beer's Law, the SLW model specifies several discrete values of the absorption coefficient κ_k (called gray gas absorption coefficients), determines the total radiation source spectral content corresponding to each discrete value of κ_k (characterized by gray gas weights w_k), and sums (or integrates) the total radiation from a blackbody source over the total number K of discrete gray gas absorption coefficients specified. The integration over a few carefully chosen values of the gray gas absorption coefficient thus takes the place of spectral integration over wavelength in the traditional line-by-line method.

The integration of Eq. (2-4) is used to evaluate the radiant flux from one finite area A_i to another A_j . As shown in Figure 2.2, θ_i and θ_j are the angles between the normal vector to each surface and the line joining the differential elements on surfaces i and j , respectively, and s is the distance between the two endpoints of the joining line. In order

to determine the variation of local incident flux along the fuel bed, the fuel was divided into small but finite spatial strips running parallel to the shared flame/fuel edge, as shown in Figure 2.2. The incident flux on the fuel was then calculated according to Eq. (2-4) for each strip.

Invoking the Spectral Line Weighted-sum-of-gray-gases model, the total (spectrally integrated) radiative flux leaving the planar flame surface and arriving at an arbitrary spatial strip j along the fuel bed may be shown to be the sum of radiative contributions from all gray gases:

$$q_{flame \rightarrow fuel, j} = E_{b, flame} \sum_k^K (\overline{s_{flame} s_{fuel, j}})_k w_k \quad (2-5)$$

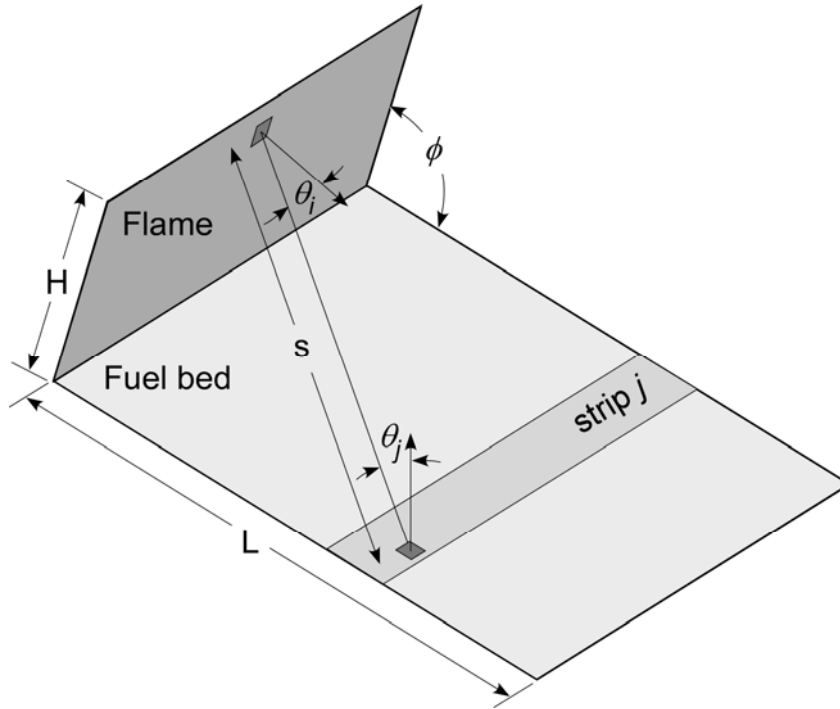


Figure 2.2. Detailed illustration of geometry and nomenclature for determination of volumetric exchange factor and local incident flux.

where $q_{flame \rightarrow fuel,j}$ is the total (spectrally integrated) incident radiation flux emitted by the flame which arrives at (is incident on) strip j along the fuel bed, $E_{b,flame}$ is the total blackbody radiation flux emitted by the flame at temperature T_f , $(\overline{s_{flame} s_{fuel,j}})_k$ is the volumetric exchange factor for radiant transfer from the flame to spatial strip j corresponding to gray gas coefficient κ_k , and w_k is the gray gas weight associated with each gray gas absorption coefficient κ_k . Once the discrete gray gas absorption coefficients κ_k are specified, the corresponding gray gas weights w_k are determined by evaluating the area under the Planck spectral blackbody radiation distribution $E_{b,flame,\eta}$ where the gray gas absorption coefficient prevails for the gas specie in question (water vapor in this case) (Denison and Webb, 1993b). The gray gas weights sum to unity, $\sum_k^K w_k = 1$. Increasing the number of gray gases employed improves the accuracy of the predictions. In this study, $K = 20$ gray gases were used in Eq. (2-5). Further increases in the number of gray gases yielded no appreciable change in the solution.

Because the closed-form integration of Eq. (2-4) to evaluate the volumetric exchange factor for each gray gas, $(\overline{s_{flame} s_{fuel,j}})_k$, is generally not possible for general cases involving radiation attenuation in the intervening medium, the expression was evaluated using numerical integration. Referring again to Figure 2.2, the approach followed here tracks radiation emitted from specified locations along the planar flame to destination strip j along the fuel bed. A reduction of two-dimensional flame and fuel surfaces (shown in Figure 2.2) to the one-dimensional variation in incident flux along the fuel suggested in Figure 2.1 is not forthcoming in the integration of Eq. (2-4). Consequently, two-dimensional flame and fuel bed surfaces were used in the numerical integration as

shown. The lateral extent of the flame and fuel surfaces was then sequentially increased in exploratory simulations to determine the dimension large enough to yield the one-dimensional variation in radiative flux along the fuel bed illustrated in Figure 2.1. The lateral dimension required to achieve predictions independent of end effects was twenty times the flame height for all configurations. The surfaces of both flame and fuel were discretized in two directions for numerical evaluation of the integrals in Eq. (2-4). The multiple spatial strips along the fuel bed were clustered near the base of the flame in order to accurately resolve the steep gradient of incident radiant flux with position along the fuel. Each strip j was subsequently discretized into smaller differential elements used to evaluate the integrals in Eq. (2-4). The numerical integration procedure sweeps through differential area elements on the fuel bed and on each strip of the flame, evaluating the local angles θ_i and θ_j for each of the elements and the corresponding distance s separating the two differential elements in question. The solution thus determines the fraction of radiation emitted by a given element on the flame that is incident on its destination element along the fuel after attenuation by the water vapor in the intervening medium. This accounting must be done for all elements on the flame. The double integration must be performed for the volumetric exchange factor corresponding to each gray gas. Thereafter, the summation over all K gray gases in Eq. (2-4) is carried out to determine the total radiative flux.

The volumetric exchange factor $\left(\overline{s_{flame} s_{fuel,j}}\right)_k$ presented above is identical to the classical configuration factor $F_{i,j}$ (used for predicting radiative exchange between diffuse surfaces in the absence of a radiatively participating intervening medium), with the exception of the exponential absorption term, $e^{-\kappa_k s}$. Analytical expressions for the radia-

tive configuration factor F_{ij} for commonly encountered surface-to-surface exchange configurations are tabulated in the literature (Siegel and Howell, 2002). The accuracy of the evaluation of the volumetric exchange factor can therefore be verified by comparing the numerical integration of Eq. (2-4) for the transparent intervening medium case ($\kappa_k \rightarrow 0$) to published analytical expressions for the radiation configuration factor between surfaces with adjoining edges and included angle ϕ . Figure 2.3a illustrates the error between the numerically evaluated volumetric exchange factor $(\overline{s_{flame} s_{fuel,j}})_k$ for $\kappa_k \rightarrow 0$ and the corresponding classical radiation configuration factor F_{ij} (Siegel and Howell, 2002) for radiative transport from the entire flame surface to a 10-cm long element at the base of the fuel bed as a function of number of points used in the numerical integration. Both $\phi = 60$ and 90 degree flame configurations for a flame length $H = 1$ m are shown. Radiative exchange between the flame and the small segment at the base was selected for this validation exercise because it is the most rigorous accuracy test of the numerical integration. It is for this configuration that the numerical evaluation of the exchange and configuration factors incur the greatest error. As expected, Figure 2.3a shows that the error decreases as the number of integration points increases. The difference between numerical integration and analytical result is less than 1 percent for a surface discretization employing more than 10^{11} integration points for both flame angle configurations. This favorable comparison for the limiting case $\kappa_k \rightarrow 0$ demonstrates the accuracy of the numerical integration of Eq. (2-4), if only for the transparent intervening medium case.

While the data of Figure 2.3a constitute evidence that the numerical integration is accurate for the transparent-medium scenario, there is still some uncertainty that with the inclusion of the exponential attenuation term $e^{-\kappa_k s}$, the solution may not be convergent.

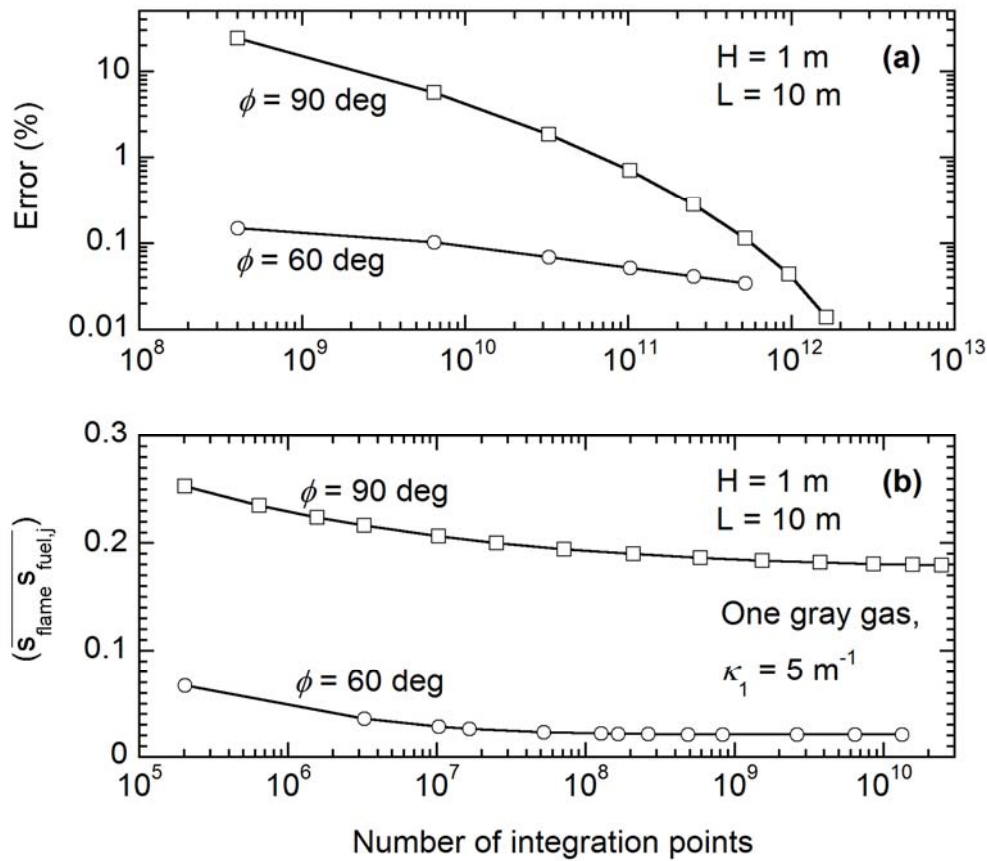


Figure 2.3. a) Error between the volumetric exchange factor for $\kappa_k \rightarrow 0$ (for $K = 1$) and the corresponding classical radiation configuration factor, and b) variation in calculated volumetric exchange factor with number of integration points.

Therefore, a study was undertaken to demonstrate that a convergent solution, independent of the number of points in the numerical integration, was achieved for the case of finite attenuation ($\kappa_k \neq 0$). Figure 2.3b illustrates the variation in calculated volumetric exchange factor $(\overline{s_{flame} s_{fuel,j}})_k$ between the flame and a fuel bed surface strip near the base of the flame for a single gray gas ($K = 1$) of gray gas absorption coefficient $\kappa_1 = 5 \text{ m}^{-1}$, with the number of points in the numerical integration for both the normally oriented and angled flame configurations. This value of the gray gas absorption coefficient used in the exercise is in the mid-range of the coefficients used in the simulations reported hereafter

in the results. The figure reveals that the value of $\left(\overline{s_{flame} s_{fuel,j}}\right)_k$ returned by the numerical integration is unchanging beyond 10^{10} integration points for both flame angles studied. Further, to insure that this choice produced a solution free of round-off error in addition to a solution independent of the number of integration points, all variables associated with the numerical integration were increased in computer precision to confirm that the answer remained the same. It was found that increasing the computer precision (to the so-called “long double” precision) yielded no change in eight significant figures over the double precision results used in all predictions shown hereafter. The results suggest a convergent solution, lending confidence in the accuracy of the volumetric exchange factor for finite gray gas absorption coefficient.

Based on the results of the validation exercise illustrated in Figure 2.3, 10^{11} integration points were used in all simulations reported here. The prediction of incident flux variation along the fuel bed for a given set of conditions was computationally intensive. The calculation of the volumetric exchange factor for each gray gas for all strips on the fuel bed required approximately 12 hours of computation time. This computation was performed for each of the 20 gray gases. In practice, $\left(\overline{s_{flame} s_{fuel,j}}\right)_k$ was evaluated for all gray gases simultaneously using parallel computing, after which the summation of Eq. (5) was performed to determine the local radiant flux incident on the fuel. A sample program used to calculate $\left(\overline{s_{flame} s_{fuel,j}}\right)_k$ is in the appendix.

2.5. Results and Discussion

Simulations were conducted for two flame heights, $H = 1$ and 10 m, with corresponding fuel bed lengths of $L = 10$ and 100 m, respectively. Included flame angles ϕ of

60 and 90 degrees were explored. Two flame temperatures were investigated, $T_f = 1000$ and 1500 K, bounding the reasonable nominal range of flame temperatures in wildland fires (Butler *et al.*, 2004). All simulations were conducted with and without environmental water vapor in the intervening medium between flame and fuel bed. For those predictions including water vapor, a uniform mole fraction of 3.5 percent H_2O was imposed, corresponding approximately to a relative humidity of 100 percent at a temperature of 300 K. This represents the upper bound on the influence of environmental water vapor on radiation attenuation in wildland fires.

Figure 2.4 illustrates the variation in predicted local incident radiant flux with position along the fuel bed for a 1 m long flame ($H = 1$ m) under normal flame conditions ($\phi = 90$ deg) for a flame temperature $T_f = 1000$ K. Two cases are shown, with and without the effect of radiation attenuation by 3.5 percent environmental water vapor. The trends for both cases are qualitatively similar. As expected, the highest flux incident on the fuel bed is at the base of the flame, where the flame is viewed most intensely by the fuel bed. The local radiant flux drops dramatically with increasing distance along the fuel bed. As expected, the influence of water vapor is to attenuate the radiation incident on the fuel bed. At the base of the flame where the radiant flux is the highest, the environmental water vapor reduces the flux incident on the fuel bed by approximately 9 percent. Also plotted in Figure 2.4 is the difference in local incident radiant flux due to water vapor, expressed as a local percentage difference relative to the otherwise identical case with no absorption. The fractional influence of water vapor is lowest near the base of the flame (9 percent), and increases with increasing distance along the fuel bed. This may be explained by the increasing absorbing path length through which emission from the flame

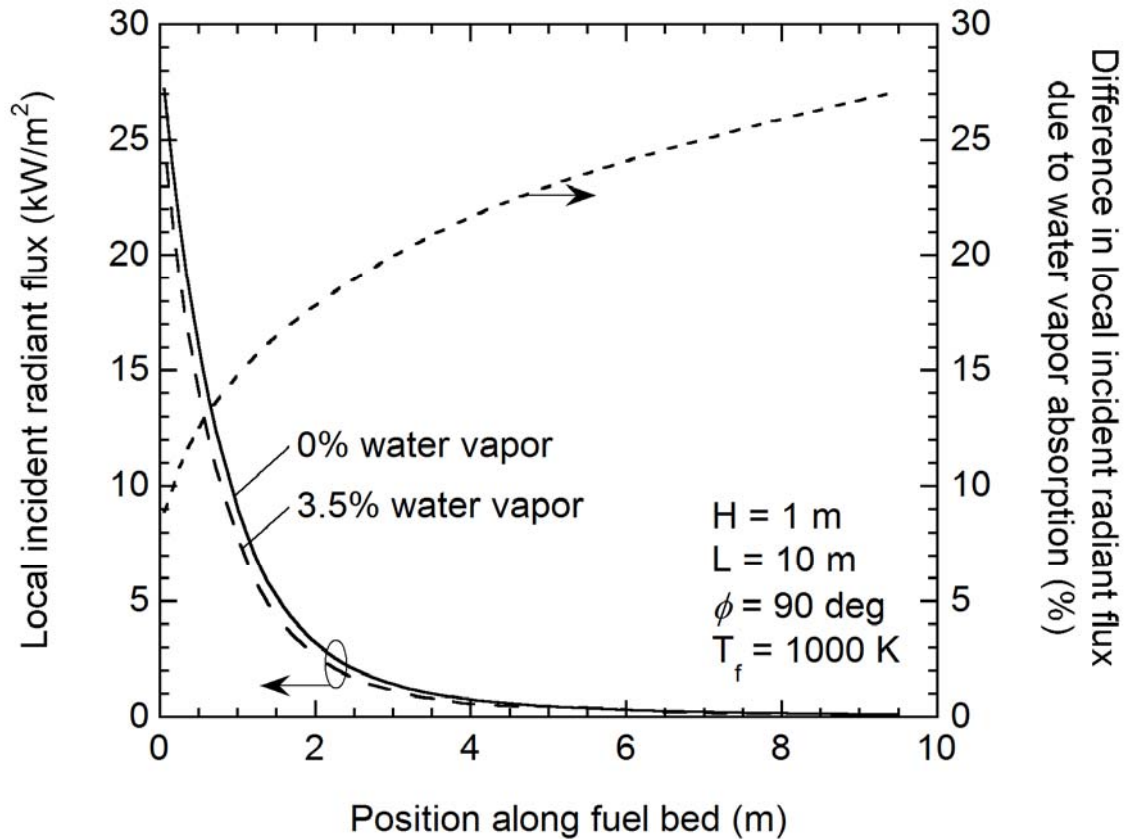


Figure 2.4. Predicted local incident radiant flux along the fuel bed for the cases with and without water vapor absorption, $H = 1$ m, $L = 10$ m, $\phi = 90$ deg, and $T_f = 1000$ K.

must pass for fuel bed locations farther from the flame base.

It should be recognized that although the fractional influence is higher farther from the flame, the incident flux decreases rapidly in this direction. Thus, the incident flux is lowest in regions where the percentage influence is highest. The data of Figure 2.4 are used as benchmark against which the parametric effect of varying flame temperature, flame height, and flame angle will be explored in sections to follow.

The effect of varying flame temperature is illustrated in Figure 2.5 for the 1 m, normal flame configuration ($\phi = 90$ deg). Predictions for two flame temperatures are pre-

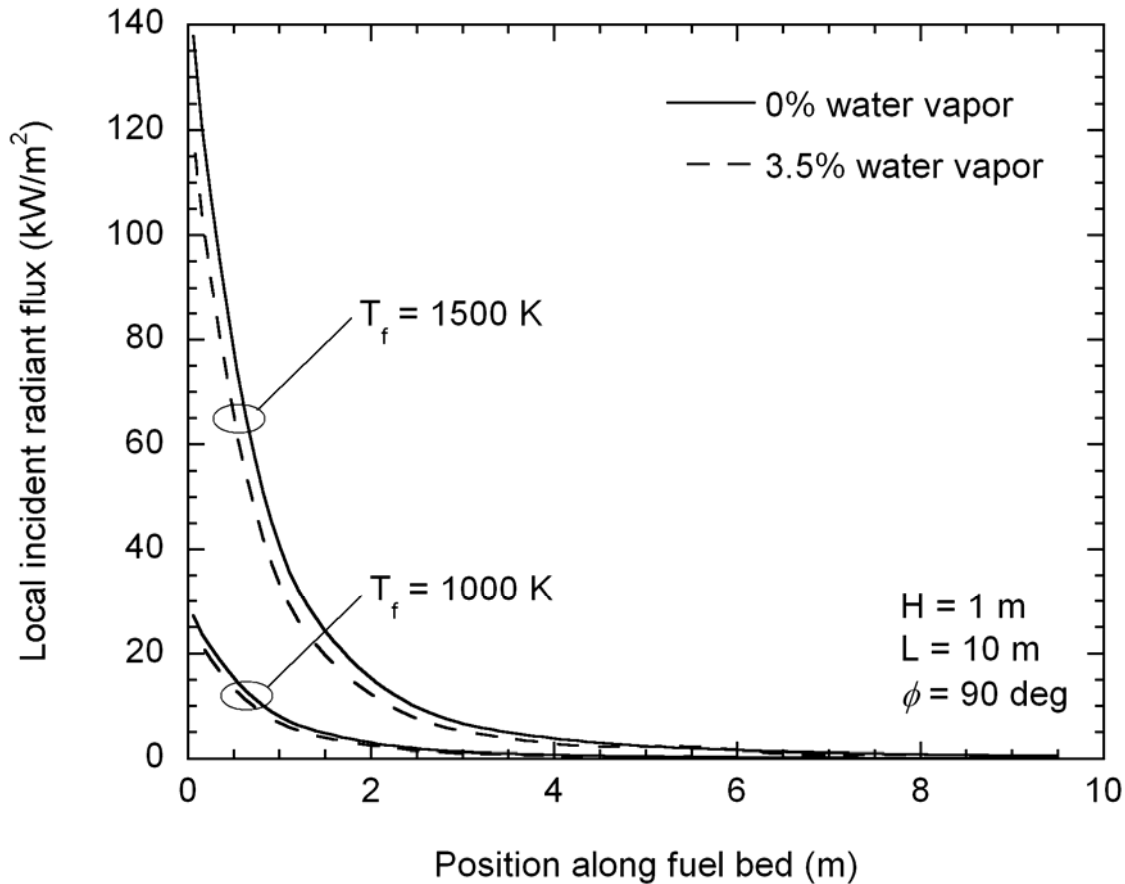


Figure 2.5. Effect of flame temperature on local incident radiant flux along the fuel bed for $H = 1$ m, $L = 10$ m, and $\phi = 90$ deg.

sented, $T_f = 1000$ and 1500 K. As expected, the magnitude of the incident flux is considerably higher for the hotter flame. The predictions reveal that the incident radiation at the base of the 1500 K flame is attenuated by water vapor an amount 13 percent relative to the case with no H_2O , compared to 9 percent for the 1000 K flame. The greater influence of water vapor at higher T_f is due to the fact that the spectral emission from the hotter flame is concentrated more heavily in the spectral regions corresponding to the two primary infrared absorption bands of water vapor. It may be concluded that a hotter

flame scenario results in greater attenuation by environmental water vapor than is experienced by a relatively cooler flame.

The effect of flame length is shown in Figure 2.6, where local incident flux predictions for $H = 1$ and 10 m (with $L = 10$ and 100 m, respectively) are plotted for the normal flame configuration with $T_f = 1000$ K. The differences in flux magnitude very near the base of the flame are not significantly different for the two different flame length simulations.

This is not surprising, since the region near the flame base “sees” little of the flame beyond the 1 m length, and is therefore exposed to nearly the same radiative environment in both cases. Farther from the flame base along the fuel bed, however, the lon-

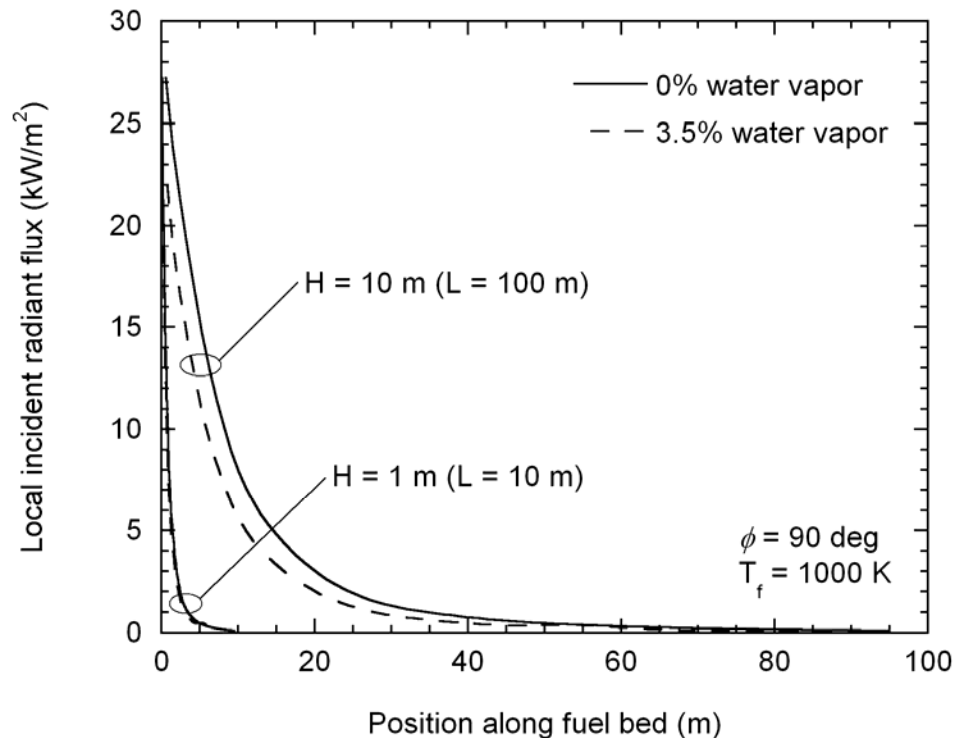


Figure 2.6. Effect of flame length on local incident radiant flux along the fuel bed for $\phi = 90$ deg and $T_f = 1000$ K.

ger flame yields higher incident flux magnitudes produced by the effect of the additional flame length for $H = 10$ m. It appears that attenuation of radiation by water vapor is more significant for the longer flame. This may be explained by the fact that radiation from the longer flame must, on average, traverse greater distance of absorbing medium before reaching the fuel bed.

Figure 2.7 illustrates the influence of flame angle on the incident radiant flux for the 1 m flame, $T_f = 1000$ K. Relative to the normal flame configuration ($\phi = 90$ deg), the radiative flux is substantially higher for the angled flame. As the flame angle decreases from $\phi = 90$ deg, it occupies a greater field of view for all locations along the fuel bed. In other words, the fuel bed “sees” the flame more prominently for angled flame conditions,

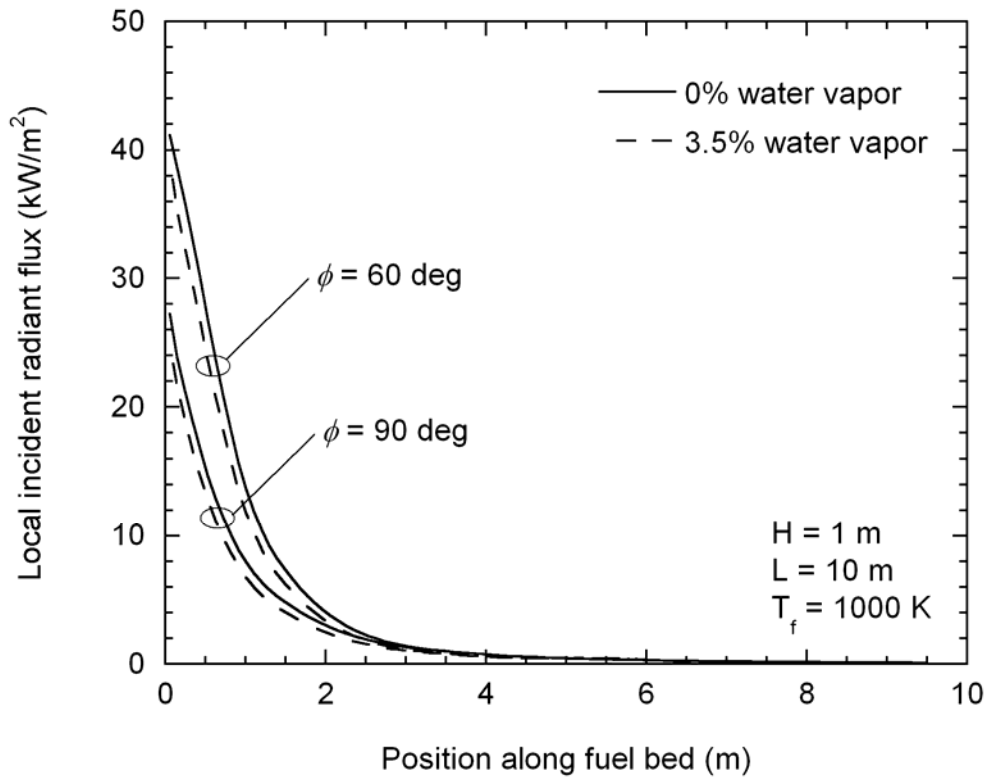


Figure 2.7. Effect of flame angle on local incident radiant flux along the fuel bed for $H = 1$ m, $L = 10$ m, and $T_f = 1000$ K.

resulting in high incident radiant flux. While not evident in the figure, the fractional decrease in incident flux due to absorption by water vapor is reduced for the angled flame. Whereas the reduction in incident flux at the base of the flame for the $\phi = 90$ deg case was 9 percent, the flux is reduced there by only 5 percent for the $\phi = 60$ deg case. Again, this may be explained by the fact that the average path length for radiation between flame and fuel bed is smaller for $\phi < 60$ deg. Consequently, there is less attenuation by water vapor.

The local influence of flame radiation absorption by water vapor for the cases presented in the foregoing sections is summarized in Figure 2.8. As was done in Figure 2.4, the effect of absorption by water vapor is expressed in Figure 2.8 as a local percentage difference relative to the otherwise identical case with no absorption. To facilitate the presentation of data for both flame lengths studied, the data are plotted as a function of normalized position along the fuel bed, x/L , where x is the coordinate along the fuel bed measured from the base of the flame. For all cases the fractional influence is lowest near the base of the flame, and increases with increasing distance along the fuel bed.

It should be recognized, however, that although the fractional influence is higher farther from the flame, Figure 2.4 - Figure 2.7 indicate that the local incident flux decreases rapidly in this direction. Thus, the flux is lowest in regions where the percentage influence is highest. It is again observed that the relative effect of water vapor absorption is greater for increasing flame temperature, flame length, and inclination angle. As outlined previously, this is explained by the greater average path-length through which the flame radiation must pass before arriving at the fuel bed for these scenarios.

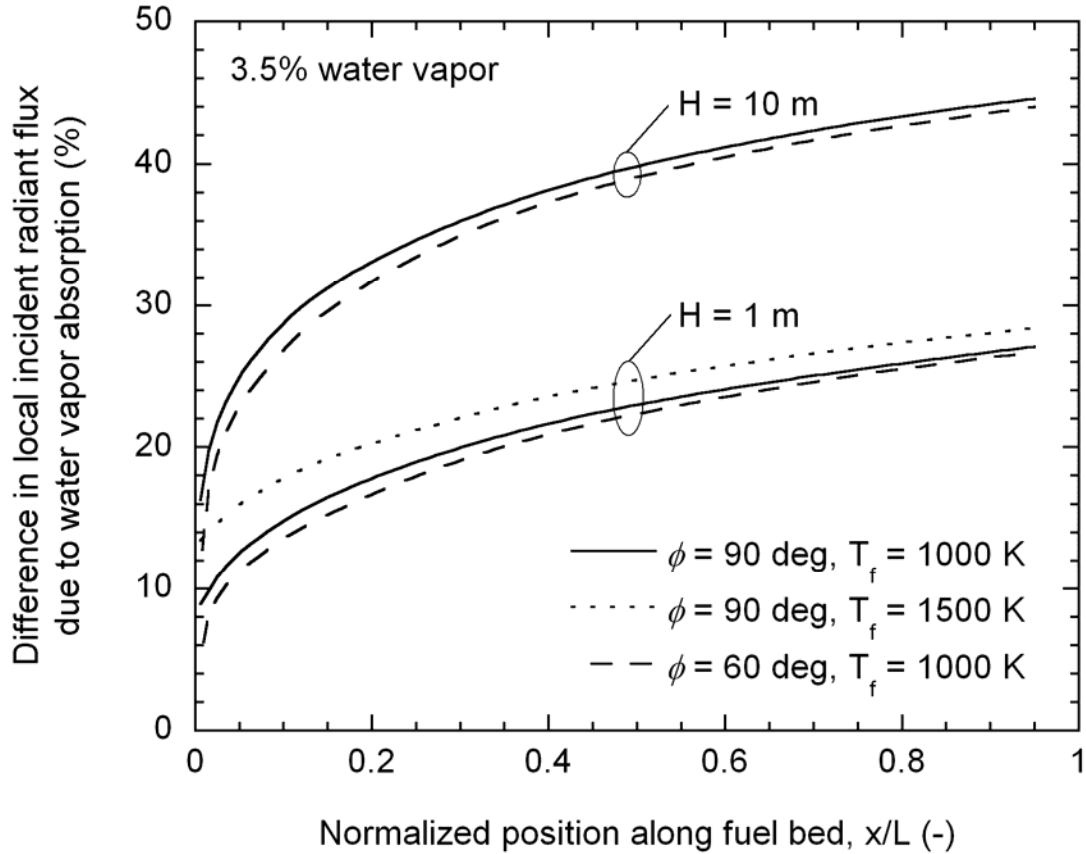


Figure 2.8. Difference in local incident radiant flux due to water vapor absorption as a function of normalized position along the fuel bed for all cases studied.

The foregoing sections have presented the effect of absorption by environmental water vapor on the *local* radiative flux incident on the fuel bed. Of interest is the aggregate effect of radiation absorption by water vapor on the overall heat transfer to the fuel, found by summing the local incident flux spatially over the entire fuel bed area:

$$Q_{flame \rightarrow fuel} = \sum_j q_{flame \rightarrow fuel, j} A_j \quad (2-6)$$

Here, $Q_{flame \rightarrow fuel}$ is the total radiant heat transfer (as opposed to local heat *flux*) emitted by the flame that is incident on the entire fuel bed. The results of the calculation of Eq.

(2-6) are found in Table 2-1 for all of the cases explored, again expressed as a percentage difference relative to an otherwise identical case with no H₂O absorption.

Table 2-1. Overall reduction in total radiative heat transfer incident on the fuel bed due to absorption by environmental water vapor.

	$\phi = 90$ deg $T_f = 1000$ K	$\phi = 90$ deg $T_f = 1500$ K	$\phi = 60$ deg $T_f = 1000$ K
$H = 1$ m ($L = 10$ m):	13.5 percent	16.7 percent	11.9 percent
$H = 10$ m ($L = 100$ m):	26.7 percent		25.1 percent

The general trends illustrated by Figure 2.8 are confirmed by the tabulated results. For the range of parameters investigated here, the attenuation of flame radiation by environmental water vapor affects the total heat transfer to the fuel bed by an amount ranging from 11.9 percent to 26.7 percent. As observed and explained previously, the overall influence of environmental water vapor is less important for lower-temperature flames and for angled flames. While its effect is modest (but perhaps non-negligible) for small flames, it can become quite significant for larger flames.

2.6. Conclusions

Predictions have been made for radiative transfer from black, isothermal, planar flame to a black fuel bed maintained at 300 K. The effect of flame inclination, flame temperature, and flame length were explored for cases with and without absorption by environmental water vapor in the intervening air (at 300 K). From these simulations one can see that, depending on the conditions, water vapor has a modest but non-negligible

effect on the radiative transfer from flame to fuel. The effect is more pronounced for larger flames at higher flame temperatures. The influence of water vapor on attenuation of radiation is reduced for angled flames.

3. Fine Fuel Heating by Radiant Flux

3.1. Abstract

Experiments were conducted wherein wood shavings and Ponderosa pine needles in quiescent air were subjected to a steady radiation heat flux from a planar ceramic burner. The internal temperature of these particles was measured using fine diameter (0.076 mm diameter) type K thermocouples. A narrow angle radiometer was used to determine the heat flux generated by the burner. A model was developed to predict the steady-state temperature of a cylindrical particle with an imposed radiation heat flux under both quiescent air (buoyancy-induced cooling) and windy (forced convection cooling) conditions. Excellent agreement was observed between the model predictions and the experimental data. Parametric studies using the validated model explore the effect of burner (flame) temperature and distance, fuel size, and wind speed. It is concluded that ignition of the fuel element by radiation heating alone is unlikely. While it may occur in a quiescent environment, it is speculated as unlikely due to intense buoyant in-draft induced by the combustion.

3.2. Introduction

Radiation and convection heat transfer have complimentary roles in wildland fire spread (Anderson, 1969). Intense radiative transfer from the flame preheats fuel ahead of the flame front, while convection transfer brings hot combustion products into intimate contact with fuel particles. Their relative contributions depend in a complex way on the local environment and fuel properties. The balance between radiation and convection is not well understood. Some prior work has experimentally determined that only radiation contributes to fuel preheating (Telisin, 1973; Albin, 1985), whereas others include both radiation and convection as significant heat transfer mechanisms in fire spread (Anderson, 1969; Asensio and Ferragut, 2002). A detailed understanding of the relative contributions of radiative and convective transfer in wildland fires is critical to the understanding of the ignition phenomenon. This work seeks to add insight in this area.

Several previous studies have explored the contributions of radiative and convective heat transfer in wildland fire phenomena. Simms (1963) investigated the total irradiation required on a wood fuel sample to achieve pilot ignition. Pilot ignition time was correlated with incident radiant flux, and a critical incident heat flux of 13 kW/m^2 was determined where, in a prescribed time (10 min) the wood would ignite. Van Wagner (1967) concluded that radiation is the dominant preheating mechanism in the fuel ignition process through a series of pine needle bed fire spread experiments. A subsequent study defined temperature thresholds above which cellulosic materials would ignite (Anderson, 1969). Anderson conducted experiments in which it was determined that radiation contributed no more than 40 percent of the energy required for ignition. Pagni (1972) conducted a series of experiments designed to determine when radiation was dominant and

when convection was dominant. It was shown that under no-wind ambient conditions, radiation was dominant and in wind-aided flame spread convection was dominant. Teli-sin (1973) developed a radiation-driven fire model that included an extinction distance equal to the mean free path within the fuel. This model did not agree well with experimental results reported. Hirano and Sato (1974) showed in an experimental study of combusting paper that hot gases existed only very near the flame. The pine needle litter experiment of Konev and Sukhinin (1977) revealed that a steadily spreading fire contributes approximately 37 percent of the energy for ignition and 8 percent for a nearly extinguished flame. Albini (1985) developed a wildland fire model which rigorously solved the governing equation of radiative transfer, neglecting convective transfer completely. The model was subsequently modified to include fuel cooling by natural convection (Albini, 1986). However, the model did not include convective pre-heating of the fuel. Weber (1991) identified radiation heat transfer as the dominant heat transfer mode in the forest fires through a simple analytical model, and expressed the need for a “short-range” heat transfer mechanism for fires in still air. Dupuy (2000) used experiments to verify multiple radiation driven models to determine if radiation alone can describe experimental results when it is considered as the dominant heat transfer mechanism in flame spread. It was concluded that a radiation-dominant model could not account for experimental observations. Butler *et al* (2004) reports direct measurements of energy transfer in full scale crown fires. The data suggest that radiative heating can account for the bulk of the particle heating ahead of the flaming front, but that immediately prior to ignition convective heating is significant and possibly required for ignition.

The survey of literature presented in the forgoing paragraphs indicates that there remains considerable uncertainty regarding the relative roles of radiation and convection heat transfer in combustion of wildland fuel. This paper presents both experimental and analytical work seeking to explore the preheating mechanism of fine fuels in a controlled environment. The work identifies parameters affecting radiation and convection heat transfer to fine fuels before flame arrival and explores conditions leading to fine fuel ignition.

3.3. Experiments

A series of experiments was conducted by Don Latham and Bret Butler at the US Forest Service Fire Sciences Laboratory. In these experiments, fine fuel samples were subjected to an imposed radiant heat flux in a quiescent-air environment, and their

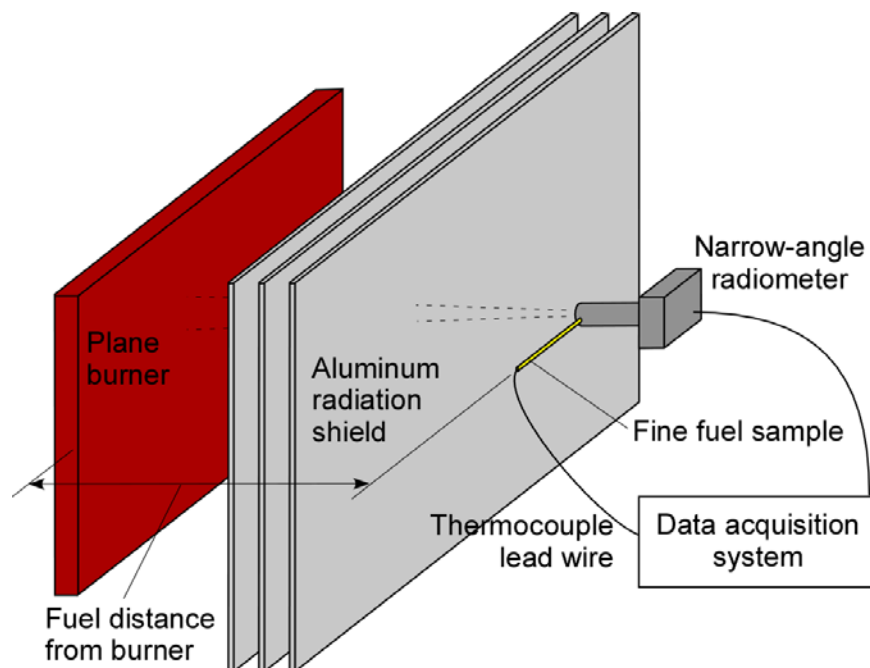


Figure 3.1. Experimental setup

steady-state temperature recorded as a function of distance from the heat source, as shown schematically in Figure 3.1. Fuel samples were prepared of two sizes of shavings of aspen (*Populus tremuloides*) termed small and large excelsior, and Ponderosa pine (*Pinus ponderosa*) needles 5 cm long. Neither the excelsior nor the pine needles have a round cross section. The excelsior has a rectangular cross section whereas the Ponderosa pine needle cross sections have 3 sides, two flat sides with a subtended angle of 120 degrees and the third side curved. The cross-sectional shape of the Ponderosa pine needles are such that, if flat sides are placed adjacent to flat sides, three needles will form a cylindrical fascicle (Wykoff, 2002). Because the cross section of the fuels used in this experiment were not round, the hydraulic diameter (Munson *et al.*, 2002) was used. The hydraulic diameter of the small and large excelsior, and Ponderosa pine fuel samples were measured as 0.44, 1.29, and 0.70 mm, respectively.

Small-bead (0.076 mm dia) type K thermocouples were pressed into the back (non-burner-exposed) surface of the fine and coarse excelsior samples, and the lead wires were threaded through the interior of the Ponderosa pine needles in order to measure the interior temperature of the fuel. The thermocouple beads were thus embedded in the fuel, and not exposed directly to the irradiation from the ceramic burner. The fuel samples were dried to 6 percent fuel moisture in a 297 K environment with a 20 percent relative humidity. A fuel sample of a given composition and size was mounted horizontally with thermocouple lead wires drawn away behind the fuel sample. The sample was positioned along the centerline of the burner at distances of 0.15, 0.25, 0.35, and 0.45 m from the burner surface. Thermocouple and narrow angle radiometer data were acquired using a multi-channel data acquisition system. As shown schematically in Figure 3.1, the radi-

ometer was positioned beside the fuel sample such that it could not interfere with the flow of air around the sample.

The experiments were performed in a large room free of drafts from the movement of persons or operation of exhaust fans. The radiant flux was provided by a propane-fired rectangular ceramic plane burner of dimensions 0.15 x 0.23 m. Once the fuel sample with the thermocouples was positioned properly, the burner was lit and allowed to stabilize for 2 to 3 minutes. A radiation shield (consisting of three 30 cm by 30 cm square aluminum sheets separated by 2 cm each) between the fuel and burner was then quickly removed, exposing the fuel to the radiation from the burner. Temperature data from the thermocouple was sampled at a rate of 10 Hz. A narrow angle radiometer described elsewhere (Butler, 1993) was positioned beside the fuel to determine the radiant heat flux emitted by the ceramic plane burner and incident on the fuel samples, and heat flux data were collected simultaneous to the temperature data. The collection angle of the radiometer was 4.5 degrees (Butler, 1993). Figure 3.2 illustrates a representative history of fuel temperature and irradiation for a Ponderosa pine needle sample. The temporal fuel temperature and irradiation data were averaged over the typical 2 - 2.5 minute sample period. The averaged temperature and standard deviations are included in Table 3-1 for all experiments. The data show that the temporal fluctuations in measured temperature are quite small, but generally increase at positions closer to the ceramic burner. The error associated with the averaged steady-state temperature was determined using a student's *t*-distribution. The average temperature measurements are accurate to within ± 5.4 K with 95% confidence.

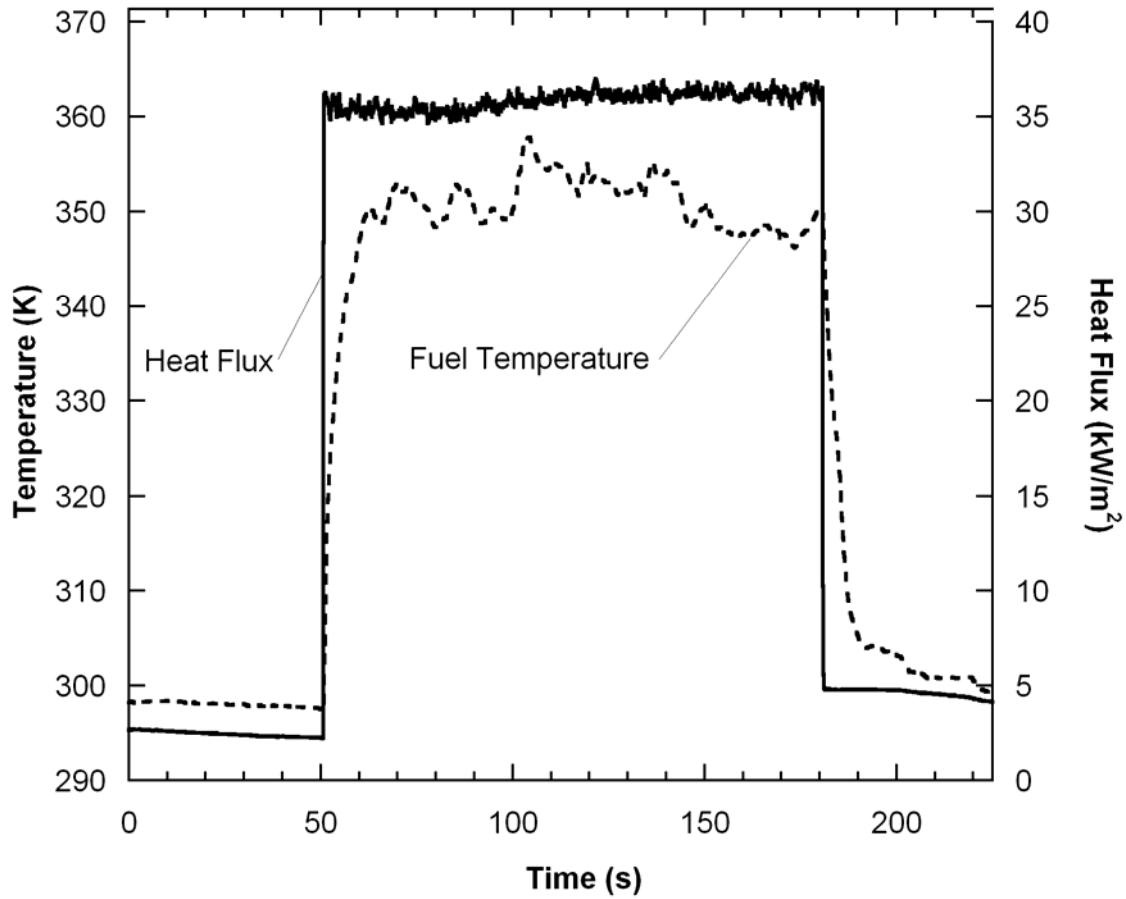


Figure 3.2. Representative sample of experimentally measured timewise variation in heat flux and fuel temperature.

Figure 3.3 shows the experimentally measured average fuel temperature as a function of distance for the three fuels investigated. The experimental uncertainty for each experiment is shown graphically using error bars. Multiple tests at the same experimental conditions and location relative to the burner are shown as separate data points, and reveal the data to be very repeatable. The data show that, as expected, the highest fuel temperatures are experienced by samples near the burner, with temperatures reaching 400 K for the large excelsior fuel samples at a distance of 0.15 m from the burner plane. Fuel temperature is seen to decrease with increasing distance from the burner. At 0.45 m from

Table 3-1. Average fuel temperature and heat flux for all experiments

	Distance From Burner (m)	Experimental Repetition #	Average Fuel Temp. (K)	Fuel Temp. Stdev (kW/m ²)	Heat Flux (kW/m ²)	Heat Flux Stdev (kW/m ²)
Small Excelsior	15	1	364.4	2.6	39.3	0.8
	15	2	363.4	4.5	40.6	0.7
	15	3	364.3	3.0	38.2	0.8
	25	1	329.5	1.6	37.7	0.8
	25	2	331.0	2.2	38.0	0.4
	25	3	331.4	3.2	37.4	0.4
	35	1	326.0	2.5	34.4	0.7
	35	2	326.0	1.9	34.8	0.4
	35	3	325.1	2.3	34.1	0.4
	45	1	309.6	1.2	35.1	0.6
	45	2	310.5	1.2	35.1	0.5
	45	3	310.3	1.0	34.5	0.4
Large Excelsior	15	1	401.5	7.1	37.4	0.6
	15	2	399.5	7.5	37.3	0.9
	15	3	402.1	6.9	36.5	0.8
	25	1	353.8	3.4	35.7	1.5
	25	2	347.9	3.2	35.9	0.5
	25	3	350.9	4.3	35.6	0.5
	35	1	335.5	1.9	32.9	0.4
	35	2	334.9	1.2	32.8	0.5
	35	3	333.6	3.3	33.3	0.6
	45	1	322.5	1.3	33.2	0.3
	45	2	323.5	1.8	33.0	0.3
	45	3	323.5	2.7	32.8	0.7
Ponderosa Pine	15	1	390.9	1.9	38.3	0.9
	15	2	390.5	2.8	37.8	0.7
	15	3	390.4	1.7	37.1	0.9
	25	1	349.3	4.1	36.6	0.5
	25	2	351.7	4.6	36.2	0.5
	25	3	351.0	2.6	35.9	0.8
	35	1	328.6	1.1	33.4	0.5
	35	2	329.2	2.6	33.3	0.3
	35	3	330.4	2.3	33.1	0.5
	45	1	318.3	1.1	34.2	0.5
	45	2	319.3	1.4	34.6	0.3
	45	3	320.6	1.4	34.0	0.3

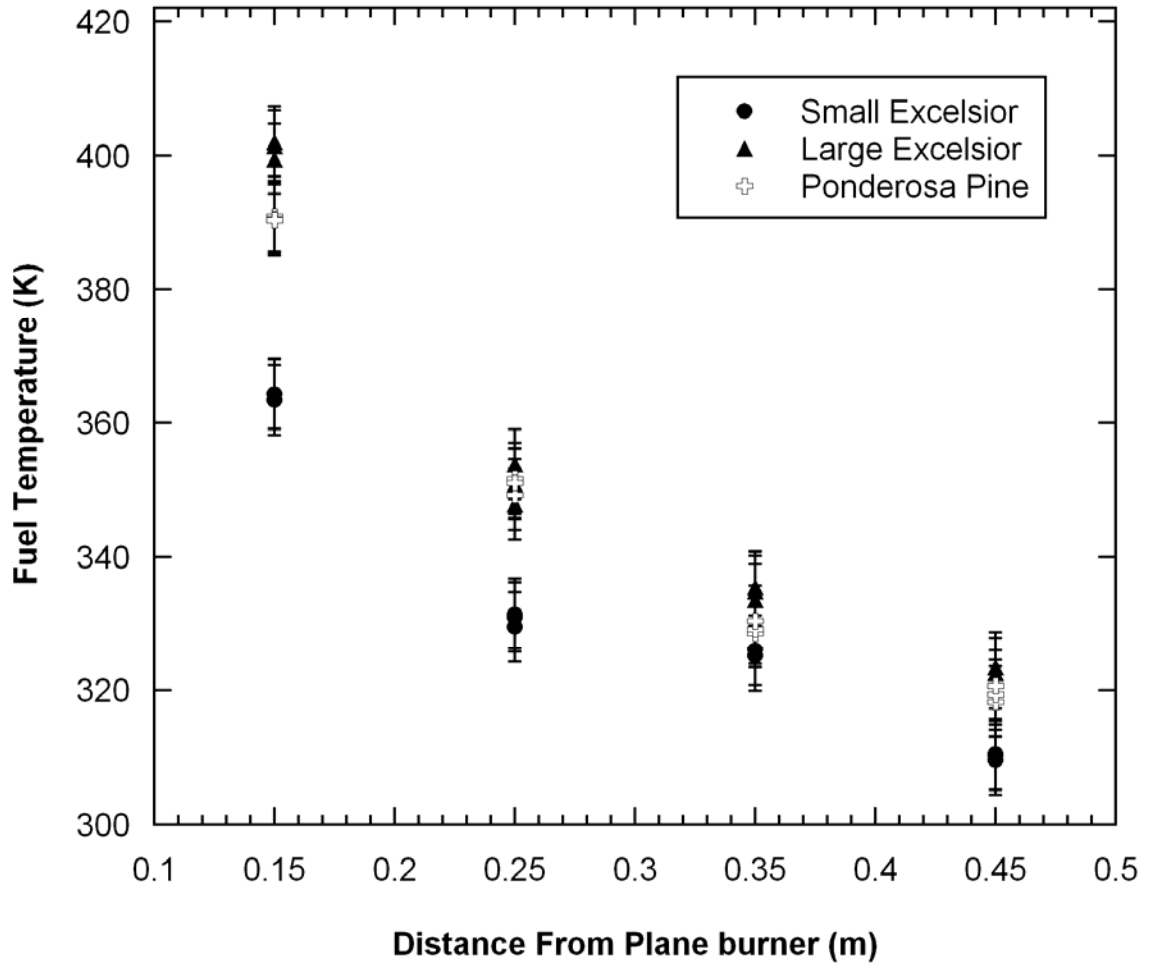


Figure 3.3. Experimentally measured fuel temperature as a function of distance from plane burner for Ponderosa pine and small and large excelsior

the burner plane the fuel temperatures are nominally at or below 320 K. Smaller fuel results in lower temperatures at a given separation distance, seen by comparing the large and small excelsior samples. This is due to the smaller capture area for radiative transfer incident on the fuel sample. The Ponderosa pine samples exhibit temperatures which lie generally between the two excelsior sample sizes at all separation distances.

3.4. Model

A mathematical model of the energy transfer for an individual fuel particle was developed. The model assumed a small fuel element of cylindrical cross-section with known diameter suspended in quiescent air. The fuel particle is heated by exposure to irradiation from a radiatively black heat source of finite size and known temperature T_b , and is cooled by convective and radiative loss to the ambient air and surroundings at temperature $T_\infty = 293$ K. The particle is located at a specified distance from the burner surface and is allowed to reach a steady-state temperature. It should be mentioned that energy transfer to the particle through convection once the fuel element enters the natural convection boundary layer at the front of the rectangular plane burner is possible. The thickness of the boundary layer was evaluated using the similarity solution of Ostrach (1953) for the free convection boundary layer on a vertical heated rectangular plane. The analysis indicated that the thickness of the boundary layer along the burner plane was approximately 0.03 m. Therefore, the boundary layer at the front of the ceramic planar burner was not considered in the model. It should be further mentioned that desiccation and devolatilization were not considered in the model. As mentioned previously, the fuel samples used in the experimental work were dried prior to testing. The range of temperatures at which devolatilization occurs is found in the literature. Susott (1980) showed that volatile generation begins at a temperature of 463 K (190°C), with maximum mass release at 623 K (350°C) in Ponderosa pine needles. Stamm (1964) suggests that thermal degradation occurs at temperatures as low as 498 K, but that substantial degradation does not occur until 523 K, which is the minimum ignition temperature indicated by Babrauskas (2003). Thus, at elevated temperatures where the model would be significantly

affected by devolatilization, the ignition temperature would perhaps be reached. Further, desiccation and devolatilization represent energy absorption phenomena that would result in actual fuel temperatures lower than those predicted. Predictions may therefore be considered to represent an upper limit on fuel temperature.

A steady-state energy balance performed on the fuel element yields

$$q_{rad,gain} = q_{conv} + q_{rad,loss} \quad (3-1)$$

where $q_{rad,gain}$ is the total radiation heat transfer emitted by the plane burner and absorbed by the particle, q_{conv} is the convective energy loss due to buoyancy- or forced convection-driven flow generated around the particle, and $q_{rad,loss}$ is the total radiation emitted by the fuel particle to the surroundings. The emissivity of carbon-based woody materials is very high (Incropera *et al.*, 2007), and is assumed here to be unity for the fuel samples studied.

The medium separating the fuel elements from the burner is assumed to be volumetrically non-participating, and therefore the burner-fuel radiation exchange is purely a surface phenomenon. Radiation transfer between the two surfaces may thus be treated using the radiation exchange factor (Siegel and Howell, 2002). Because the fuel element is much smaller than the burner, the radiation exchange factor from a finite rectangular area (burner) to a differential element (fuel) was used, with the projected area of the cylindrical fuel element employed as the area of the differential element. Radiation exchange is accounted for between both sides of the differential fuel element and the surroundings, as well as between the front side of the fuel and burner.

In addition to radiant loss to a cooler environment, the model also accounts for convective cooling of the fuel element. In treating the convection transfer, the fuel was

considered to be a horizontal cylinder exposed to either natural convective cooling characteristic of quiescent air, or forced convection cooling as would arise from wind motion. The convection heat transfer coefficient was determined from empirical correlations for both the buoyancy-driven (Churchill and Chu, 1975) and forced convection-driven (Churchill and Bernstein, 1977) cooling scenarios. The thermophysical properties used in conjunction with this correlation were interpolated from property tables (Incropera *et al.*, 2007).

Under these assumptions, the energy balance of Eq. (3-1) becomes

$$A_{fp} F_{fb} \sigma (T_b^4 - T_f^4) = h A_f (T_f - T_\infty) + A_{fp} \sigma (1 - F_{fb}) (T_f^4 - T_\infty^4) \quad (3-2)$$

where T_f is the temperature of the fuel, A_{fp} is the projected area of the fuel, F_{fb} is the radiative exchange factor from the fuel to the burner, σ is the Stefan-Boltzman constant, T_b is the temperature of the burner, h is the convection coefficient, A_f is the circumferential area of the fuel, and T_∞ is the temperature of both the ambient air and the radiative surroundings.

Equation (3-2) is non-linear in the unknown fuel temperature, T_f . The radiation exchange factor F_{fb} depends on the burner-fuel separation distance, and the heat transfer coefficient is an implicit function of the fuel temperature through properties evaluated at the film temperature $(T_f + T_\infty)/2$. The imposed temperature of the rectangular plane burner was determined by calculating the blackbody temperature corresponding to the magnitude of the incident flux measured experimentally by the narrow angle radiometer using the Stefan-Boltzmann law. The fuel temperature governed by the energy balance of Eq. (3-2) was determined iteratively for each fuel element position. A fuel temperature was

guessed, substituted into the fourth-order temperature terms in Eq. (3-2), and the first-order fuel temperature in the convective cooling portion of the equation was solved. The guess was then modified by systematically adjusting it a fraction of the difference between the initial guess and that solved. Convergence was declared when Eq. (3-2) was satisfied to within 0.01 percent. In practice, the fuel element was positioned far from the burner (beginning with a burner-element separation distance of 1 m). Once the solution to Eq. (3-2) for T_f was determined for this position, the distance between the burner and the fuel was reduced and the converged temperature corresponding to the previous separation distance was used as the initial guess for the new position. This procedure was followed until the location nearest the burner was reached. The program used for the calculation of the steady state temperature of the fuel is included in the appendix.

Model predictions are compared to the experimental data presented previously in Figure 3.4, where the fuel temperature is plotted as a function of distance from the burner for the three fuel samples investigated experimentally. Quiescent air in the laboratory environment was assumed, and therefore, buoyancy-driven cooling of the fuel was imposed. The figure reveals excellent agreement between model prediction and the experimental results with regard to dependence on burner-fuel separation distance, fuel type and fuel size. The maximum difference between predicted fuel temperature and that measured experimentally is 6 K, and the agreement between prediction and experiment is within ± 2 K for the majority of cases. The excellent agreement lends confidence to the model's ability to predict the thermal response of fine fuel exposed to radiative heating.

Figure 3.5 illustrates the relative magnitude of fuel element heat loss/gain for a case in which the fuel diameter specified in the simulation was an average of those studi-

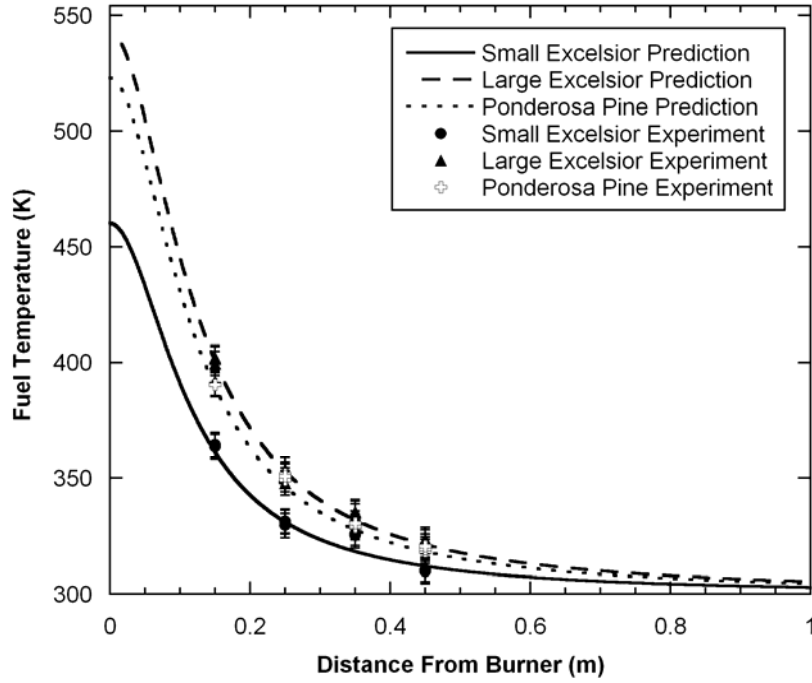


Figure 3.4. Comparison between model predictions and experimental measurements of fuel temperature.

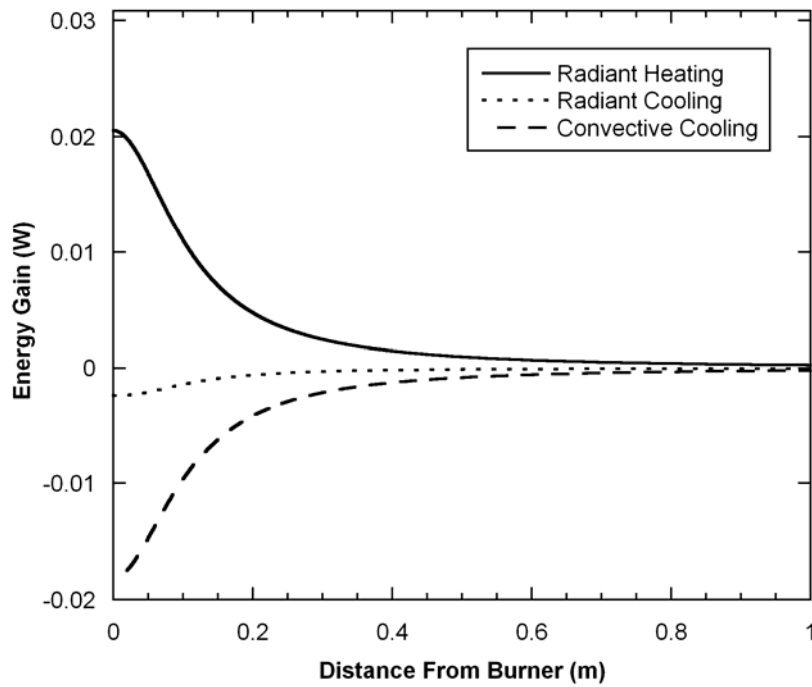


Figure 3.5. Predicted relative contributions of radiation heating and cooling and natural convective cooling.

ed experimentally (0.8 mm), and the blackbody burner temperature imposed was calculated from an average of the experimental narrow angle radiometer measurements (890 K). Of course, at steady-state the sum of all heat transfer mechanisms is identically zero at all burner-fuel element separation distances. The results of Figure 3.5 show that radiation gain is high near the burner and decreases as the distance between the burner and the fuel increases. The peak heat gain to the particle for these conditions is 20 mW. It is apparent that the vast majority of fuel particle cooling occurs by convection rather than radiation transfer, with radiation transfer accounting for no more than 13 percent of the total heat loss from the heated particle. Thus, in relative terms the temperature of the fuel is not high enough to produce significant radiative emission, but it is high enough to generate a rather significant natural convection current around the fuel particle.

3.5. Model Parametric Study

The model developed and validated in the foregoing section was exercised to explore the effects of fuel diameter, burner size and temperature, and incident radiant flux on fuel element thermal behavior. This parametric study is undertaken both to explore the physics of the fuel heating phenomenon, and to identify, if possible, the role of radiation heating in ignition of the fuel particles.

The fuel temperature predictive model has been validated by comparison with experimental data collected in a quiescent air environment. In an effort to better understand the range of temperatures a fuel element might experience under different convective environmental conditions, the model was extended to a forced convective cooling scenario. As stated previously, the magnitude of the forced convective cooling was determined us-

ing the empirical correlation for the heat transfer coefficient of Churchill and Chu (1977) for forced convection from a horizontal cylinder. This was done for wind speeds of 1, 3, and 5 m/s (11 mi/hr). Figure 3.6 illustrates the dependence of predicted fuel element temperature on incident radiant flux for the natural and forced convection conditions investigated. The predictions of Figure 3.6 are for the limiting case of an infinitely large burner (*i.e.*, vanishing separation distance between burner and fuel element). It should be noted that experimental measurements in field burns (see chapter 4) reveal ground fire

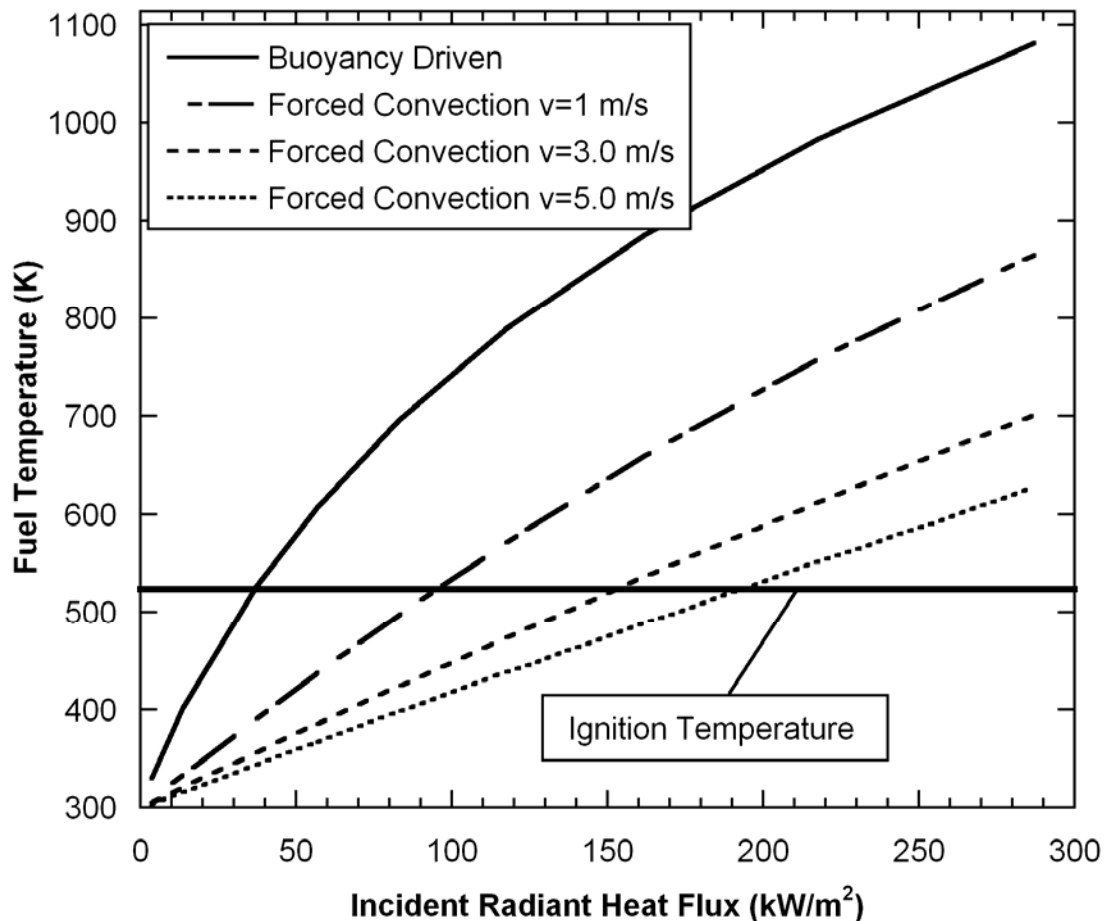


Figure 3.6. Predicted fuel temperature as a function of incident radiation flux for different convective conditions. The ignition temperature indicated is the minimum temperature at which wood will ignite regardless of the heating arrangement (Babrauskas, 2003).

average peak heat fluxes to be 200 kW/m^2 with a maximum of 290 kW/m^2 in a crown peak radiant heat fluxes to be between 50 and 150 kW/m^2 , with flux levels in crown fires to be between 200 and 300 kW/m^2 . This is confirmed by Butler *et al.* (2004) who report fire. The ignition temperature line in Figure 3.6 indicates the minimum fuel temperature, 523 K , at which ignition is suggested to occur (Babrauskas, 2003). Thus, for a given fuel cooling condition (buoyancy- or wind-driven cooling), the incident radiant flux at which the predicted fuel temperature reaches the fuel ignition point is that flux which will result in combustion. The figure illustrates the significant difference that exists between buoyancy-driven cooling and that which results from forced flow. Differences in predicted fuel temperature for the buoyancy-driven cooling and the forced flow at a wind speed of 1 m/s exceed 200 K at incident radiant fluxes above 100 kW/m^2 . As expected, increases in wind speed result in lower predicted fuel temperature. As expected, the figure reveals that fuel reaches the ignition temperature at lower incident radiant heat flux as the forced convection wind speed is reduced. The limiting buoyancy-driven fuel cooling condition reveals that ignition may be reached for an incident radiant flux as low as 50 kW/m^2 . It should be noted, however, that in the wildland fire environment a quiescent condition is unlikely to prevail. Significant buoyancy-driven in-drafts are present at the flame front, which draw cool ambient air into the flame front as oxygen is consumed in the combustion and high-temperature combustion products rise. The magnitude of the wind speed in such in-drafts will, of course, be a complex function of the flame environment. Field measurements by Butler (2003) suggest that air velocities of 1 to 10 m/s are common in naturally spreading crown fires with significantly higher transient gusts.

Considering the potential for relatively strong in-drafts the results of Figure 3.6 suggest that radiant heating alone may be insufficient to cause ignition of the fuel.

Figure 3.7 shows the predicted fuel temperature plotted as a function of burner (flame) temperature for burner-fuel element spacings ranging from 0 to 0.3 m. These simulations are for the limiting case of buoyancy-driven convective cooling of the fuel element with a radiating plane burner of the size used in the experiments (0.15 m x 0.23 m). As expected, Figure 3.7 shows that increasing the temperature of the plane burner results in an increase in the temperature of the fuel. Also not unexpected is the fact that

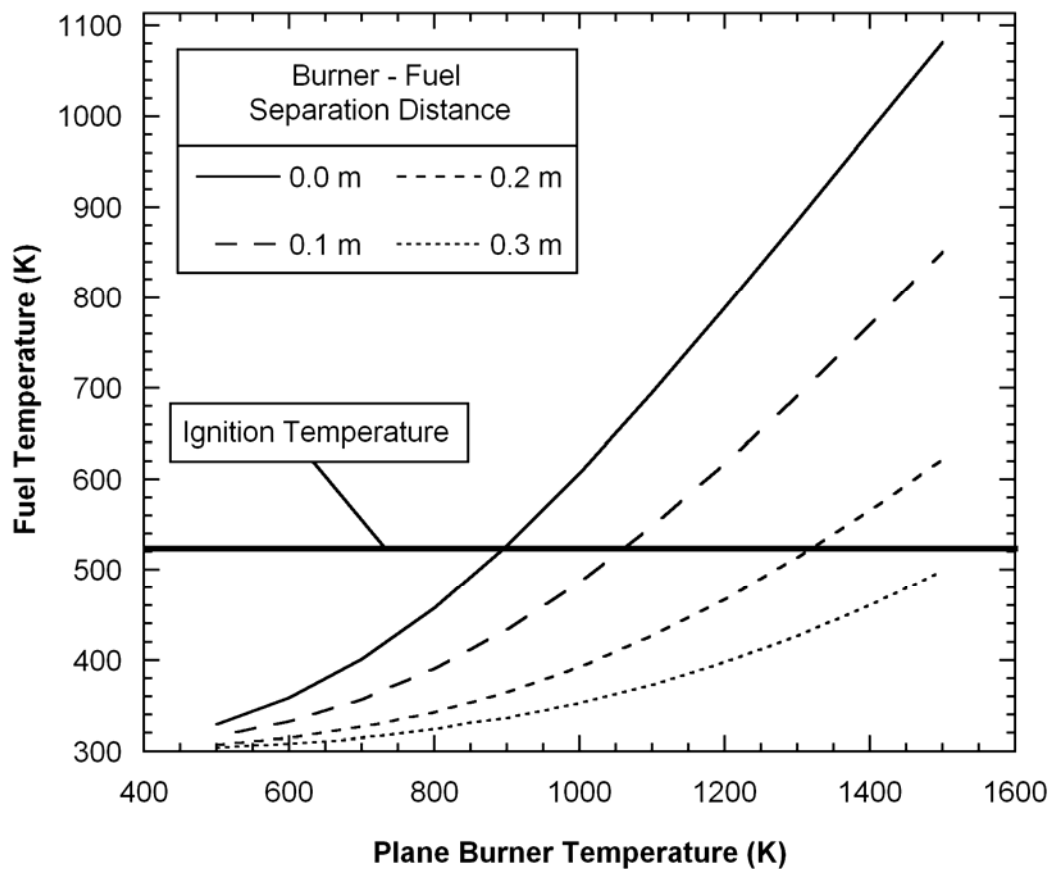


Figure 3.7. Sensitivity of predicted fuel temperature to plane burner temperature. The ignition temperature indicated is the minimum temperature at which wood will ignite regardless of the heating arrangement (Babrauskas, 2003).

this increase is not as pronounced as the burner-fuel separation distance increases. For a burner of finite size, increasing separation distance between burner and fuel element results in reduced incident radiation flux on the particle. Again shown in Figure 3.7 is the accepted minimum fuel ignition temperature (Babrauskas, 2003). For the finite burner explored here, only fuel particles nearest the flame and subjected to irradiation from a higher temperature source are prone to reach the ignition temperature by radiant heating. In the limit of a large flame (*i.e.*, vanishing separation distance from the burner) and for optically thick flames, the burner temperature and radiant flux incident on the fuel particle may be related through Stefan-Boltzman law. In this limiting case, the predictions reveal that a flame temperature of nominally 900 K is required for fuel ignition.

The dependence of predicted fuel temperature on fuel element diameter is illustrated in Figure 3.8 for a burner temperature of 890 K and natural convection cooling of the fuel element at four different burner-fuel separation distances. The average of the blackbody temperatures are determined from the narrow angle radiometer flux measurements in the experiments. Increasing the fuel diameter results in an increase in fuel temperature at all distances. Fuel temperature is quite sensitive to fuel diameter for very small fuel elements, more particularly near the burner. The fuel temperature is observed to be less sensitive to diameter as the diameter increases. Relative to the ignition temperature indicated in the figure, and for the conditions of the prediction, ignition due to radiant heating appears likely only for larger diameter fuel elements very near the burner surface. Fuel element diameters less than 0.7 mm are unlikely to ignite due to radiant heating alone.

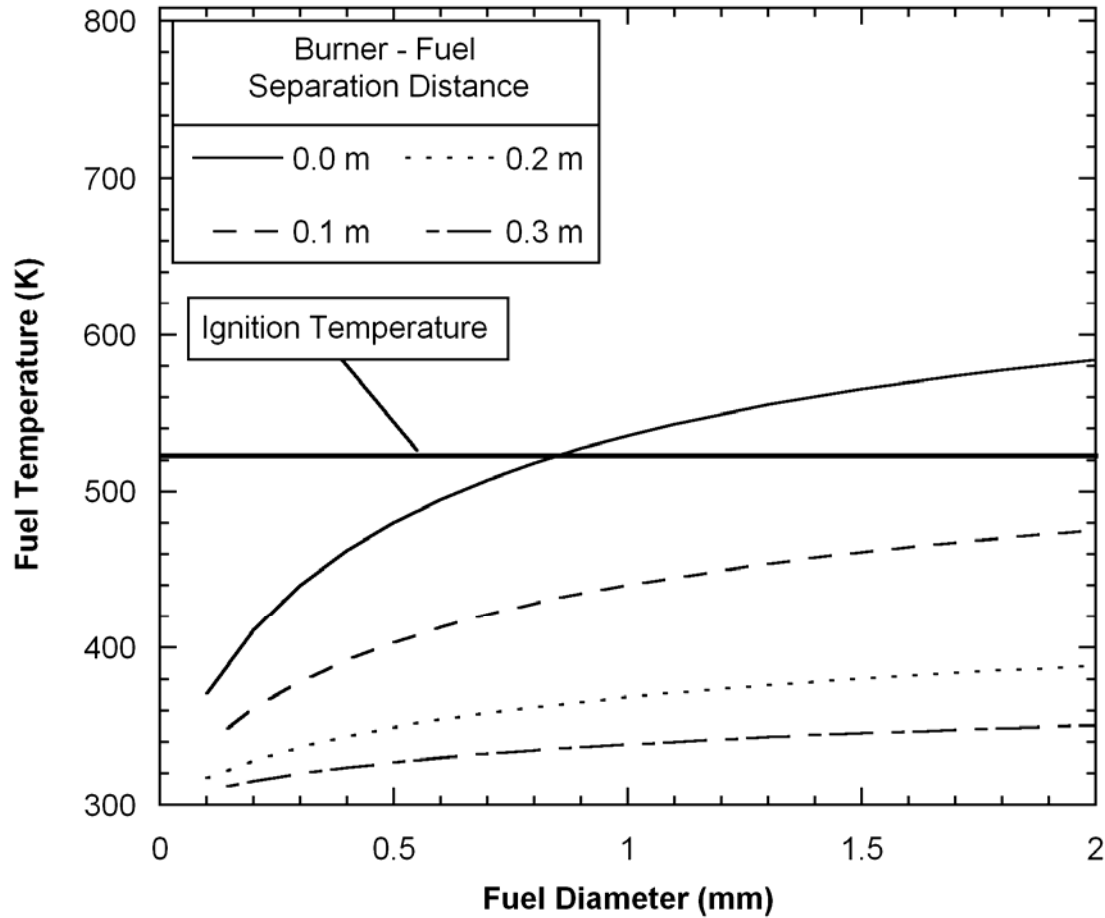


Figure 3.8. Dependence of predicted fuel temperature on fuel diameter. The ignition temperature indicated is the minimum temperature at which wood will ignite regardless of the heating arrangement (Babrauskas, 2003).

Figure 3.9 shows the distance at which the fuel reaches 523 K, the minimum ignition temperature indicated by Babrauskas (2003), as a function of burner temperature for a range of fuel diameters. Both natural convection fuel cooling and forced convection cooling with a velocity of 1 m/s are represented here. It is seen that even a moderate air velocity drastically changes the distance at which fuel may ignite by radiation only. In addition, air velocities higher than 1 m/s will ignite only at unrealistically high burner temperatures. Again, it appears that while particle ignition may occur due to radiation

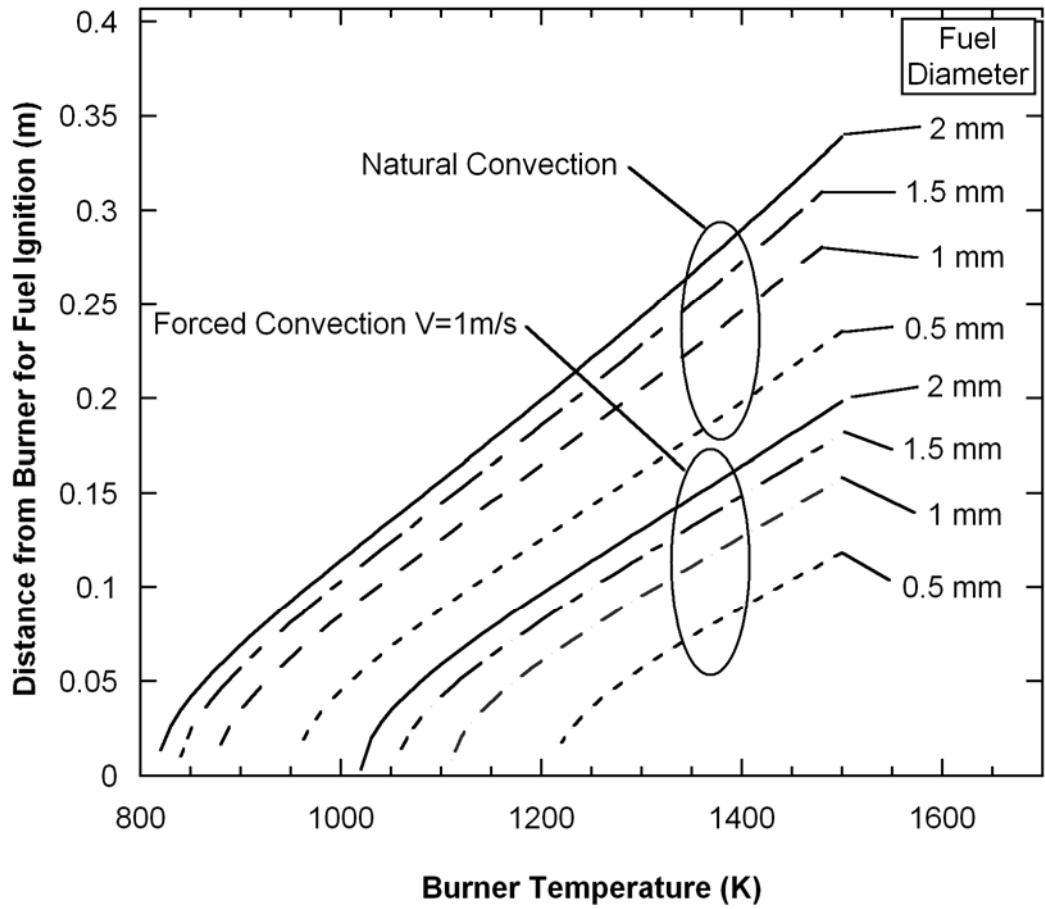


Figure 3.9. Predicted distance from burner at which fuel ignition (Babrauskas, 2003) occurs as a function of burner temperature.

transfer, it is likely to occur only under the most extreme of circumstances, namely, very low ambient air velocity or very high irradiation. However, this general observation applies only to scenarios where the flame is much larger than the fuel. By way of reminder, it is emphasized that as the fuel approaches the ignition temperature, desiccation and devolatilization would result in energy losses which are not accounted for here. However, these energy transfer mechanisms result in further reductions in temperature, and strengthen the general conclusions.

3.6. Conclusions

A model has been developed to predict the steady-state temperature of fine fuels subject to irradiation from a burner of known size and temperature. The model was validated by comparison with experimental data gathered for poplar excelsior of two sizes, and Ponderosa pine needles. The model presented here accurately predicts the heat transfer of fine fuels with an incident radiant flux cooled by radiant emission and natural convection. Parametric results with the model seem to suggest that ignition by radiant heating alone is unlikely.

4. Time-Resolved Radiation and Convection Heat Transfer in Combusting Discontinuous Fuel Beds

4.1. Abstract

Time-resolved radiation and convection heat flux was measured in a series of experimental fires designed to explore heat transfer behavior during combustion of discontinuous fuel beds. Fuel spacing and height were varied for both buoyancy-driven and wind-driven combustion. Peak radiation heat fluxes as high as 130 kW/m^2 were recorded. Convection heat flux manifested significant temporal fluctuations and peaks were recorded at 90 kW/m^2 . Radiation flux had the effect of heating the fuel before flame arrival. Both positive (heating) and negative (cooling) convective heat transfer occurred before flame arrival. Surprisingly, the convection could also be positive or negative after flame arrival indicating that even when engulfed in flames there were packets of cooler air moving across the sensor. In nearly all cases, short-duration convective heating pulses appear to precede the full onset of combustion, suggesting that convective heating may be critical as an ignition source. Rapid temporal fluctuations were observed in both radiation and convection, and spectral analysis revealed spectral content at frequencies as high as 70 Hz under buoyant flow conditions and 150 to 200 Hz under the influence of wind.

4.2. Introduction

Radiation and convection heat transfer have complimentary roles in wildland fire spread (Anderson, 1969). Radiative transfer from the flame may preheat fuel ahead of the flame front, while convective transfer brings hot combustion products into intimate contact with fuel particles. Their relative contributions depend in a complex way on the prevailing wind speed, fuel distribution, buoyancy-induced in-drafts, *etc.*

A variety of measurements have been collected from fire experiments including but not limited to flame spread rate (Fons, 1946; Hottel *et al.*, 1965; Catchpole *et al.*, 1998), high speed photography to determine flame shape (Anderson, 1968), and flame temperature (Anderson, 1968; De Mestre *et al.*, 1989). Various experimental methods have been used to measure the radiation heat transfer. Konev and Sukhinin (1977) used a copper cylinder with a blackened end along with a thermocouple to measure radiation heat flux. Butler (1993) used both narrow-angle and hemispherical radiometers to measure radiant flux from laboratory fires of poplar excelsior and ponderosa needles under a wide range of conditions (wind and humidity). These data show that flame irradiation is a strong function of flame geometry (length and angle) and fuel conditions.

Laboratory fuel configurations are largely limited to packed fuel beds composed of a variety of different fuel types (Fons, 1946; Hottel *et al.*, 1965; Van Wagner, 1967; Anderson, 1968; Pagni, 1972; Konev and Sukhinin, 1977; De Mestre *et al.*, 1989; Butler, 1993; Catchpole *et al.*, 1993; Catchpole *et al.*, 1998; Santoni *et al.*, 1999; Dupuy, 2000). Fuel arrays composed of generally homogeneous randomly oriented fuel elements have been shown to provide nominally consistent fire behavior and repeatability. However,

the mechanism by which flame spreads across a gap from one fuel element to another is not well understood.

To the knowledge of the authors, no direct/simultaneous measurement of radiation and convection in wildland fires has been reported in the archival literature. Further, the temporal dynamics of the convective and radiative flux have gone unexplored in previous studies. This work seeks to fill this void in understanding through analysis of results from laboratory experiments.

4.3. Experimental Method

The primary focus of this effort is to 1) develop a technique for determining experimentally the partitioning between convective and radiative flux in deep fuel beds consisting of fine wood shavings designed to simulate the discrete fuel spacing found in naturally occurring forest vegetation, 2) measure the temporal dynamics of the convective and radiative flux in this environment, and 3) determine the frequency content of convection and radiation heat flux in flame spread. These characterizations are sought under different fuel bed configurations, and under both buoyancy- and wind-driven burn conditions.

4.4. Sensor Configuration

A two-sensor configuration was used to measure radiation and convection. The sensors were Vatell HFM 7 heat flux micro-sensors. These sensors are 6 mm in diameter, are coated with a highly absorbent coating ($\varepsilon = 0.94$), and possess a 300 μs response time (frequency response > 3000 Hz) (Vatell, 2007). The sensors are equipped with both

a thermopile heat flux gage and a resistance temperature sensor and the voltage from both must be recorded to measure the heat flux. Thus, the dual-sensor configuration requires that two voltages be recorded. Each sensor was mounted in a thick walled aluminum cylindrical sensor housings shown in Figure 4.1a. The mass of the sensor housings are meant to act as heat sinks and thus minimize temperature rise and associated radiant emission loss. The sensor housings have a 3.8 cm diameter. The sensors face the same direction and are separated by 5.7 cm. One sensor has a 0.5 mm thick sapphire window mounted over it, whereas the other sensor is left exposed. The windowed sensor has a 0.5 mm air gap between the sensor face and the window. In this way, the non-windowed sensor gathers total heat transfer whereas the windowed sensor gathers only radiant energy (after some loss in transmission through the window). Sapphire was used due to its favorable transmission characteristics (transmission range $0.3 \mu\text{m} \sim 5 \mu\text{m}$) and durability. A Vatell Amp 6 amplifier was used to amplify the output of the heat flux micro-sensors which have a voltage output in the μV range. Once the sensor signals were amplified, the voltages were simultaneously sampled at either 50 Hz or 500 Hz using a National Instruments Daqpad 6015 data acquisition system, which has a 16 bit analog-to-digital output resolution. The Daqpad 6015 was connected to the USB port on a laptop computer and the data were downloaded and stored on the internal hard drive.

In order to accomplish the aim of this study, the radiative and convective flux was determined using the calibrated, measured heat flux of the dual Vatell sensors. The analysis to separate radiation and convection using the two-sensor configuration is outlined below.

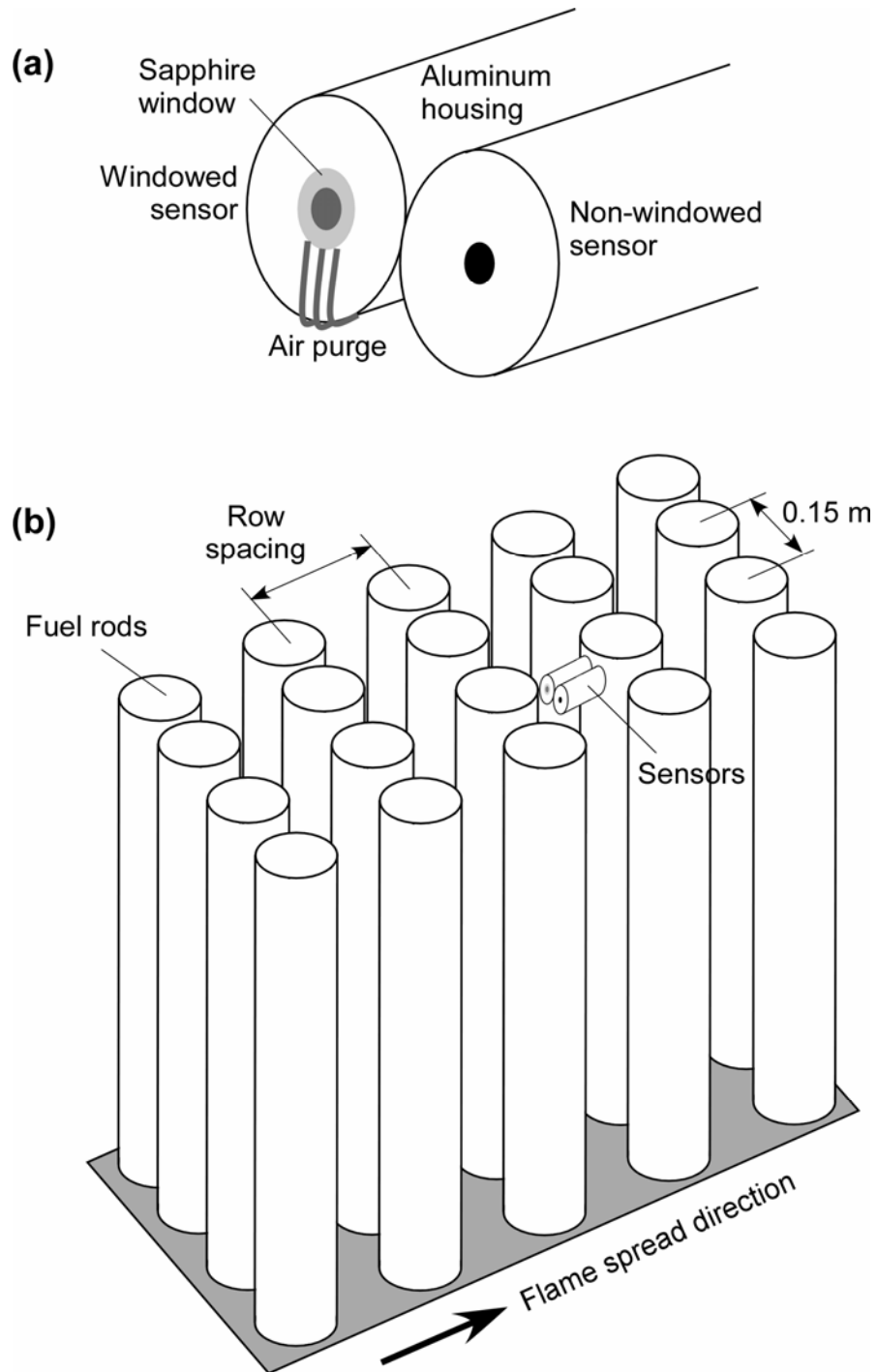


Figure 4.1. Schematic illustrations of a) sensor configuration with windowed sensor on the left and the non-windowed sensor on the right, and b) discontinuous fuel bed with each cylinder representing a fuel rod.

The heat flux sensors are calibrated by the manufacturer in a blackbody cavity environment, such that the radiant flux incident on the sensor is known as a function of the imposed blackbody cavity temperature. The calibration thus yields the incident radiant flux, $q''_{rad,inc}$, if the sensor is in a radiation-only environment:

$$q''_{cal} = q''_{rad,inc} \quad (4-1)$$

Only heat flux absorbed by the sensor, q''_{abs} , results in a voltage response, and the absorbed heat flux is a fraction of the incident flux, the scaling factor being the emissivity, ε :

$$q''_{abs} = \varepsilon q''_{rad,inc} \quad (4-2)$$

The difference between the absorbed flux and the incident radiant flux increases with decreasing sensor emissivity; if the sensor emissivity were unity, the absorbed flux would equal the incident radiant flux. If the sensor is exposed to convective heating or cooling, the sensor calibration will yield a flux magnitude higher than that actually experienced by the sensor, in a factor equal to the emissivity. Thus, the actual combined convective and radiative flux is always less than or equal to the value indicated by the sensor calibration.

Equations (4-1) and (4-2) are general expressions for sensors exposed to convective and radiative modes of heat transfer acting in a combined fashion or independently. The absorbed flux which results in sensor response voltage is related to either the convective, radiative, or combined flux. The non-windowed sensor used in the experiments reported here responds to both radiation and convection heat transfer, while the windowed sensor is not exposed to convective transfer. The heat flux absorbed by the windowed

sensor, $q''_{abs,w}$, is equal to the radiant heat flux incident on the outside of the window, $q''_{rad,inc}$, scaled by the emissivity and the effective window transmittance, τ :

$$q''_{abs,w} = \tau \varepsilon q''_{rad,inc} \quad (4-3)$$

Here it is assumed that the radiant flux incident on both the non-windowed sensor and the outside surface of the sapphire window (of the windowed sensor) are identical. The effective transmittance of the sapphire window was experimentally measured by igniting 400 g of excelsior strands 1 m from the sensors. This distance was selected to insure that no buoyancy-driven flow from the flame would come into contact with the sensors. Thus, both sensors (non-windowed and windowed) were exposed to the same radiation-only environment. Voltage data were collected for both windowed and non-windowed sensors in this configuration, the calibration fluxes were determined for both sensors ($q''_{cal,w}$ and $q''_{cal,nw}$), and the effective transmittance was determined by calculating the time-average of the ratio of the two magnitudes:

$$\tau = average \left(\frac{q''_{cal,w}}{q''_{cal,nw}} \right) \quad (4-4)$$

Using this method, the value of τ was determined to be 0.62. This value is derived from the mean of over 2000 measurements taken over 40 s, but due to instrument precision there is some uncertainty. A student's t -confidence interval gives 90 percent probability that the true mean lies between 0.57 and 0.67. Calculating the effective transmittance of the sapphire window allows for the determination of the radiation flux incident on the sensor array.

Substituting Eq. (4-2) into Eq. (4-3), and solving for the radiation incident on the outside of the sapphire window yields

$$q''_{rad,inc} = q''_{cal,w} / \tau \quad (4-5)$$

The heat flux absorbed by the non-windowed sensor is the sum of the incident radiant flux that is absorbed and the convective flux:

$$q''_{abs,nw} = \varepsilon q''_{rad,inc} + q''_{conv} \quad (4-6)$$

where q''_{conv} is the convective heat flux. Substituting Eqs. (4-2) and (4-5) into Eq. (4-6) yields

$$\varepsilon q''_{cal,nw} = \left(\varepsilon q''_{cal,w} / \tau \right) + q''_{conv} \quad (4-7)$$

Solving Eq. (4-7) for the convective heat flux yields

$$q''_{conv} = \varepsilon \left(q''_{cal,nw} - q''_{cal,w} / \tau \right) \quad (4-8)$$

The incident radiation and convection flux can be calculated from Eq. (4-5) and Eq. (4-8), respectively, as a function of the calibration heat flux determined from measurements using the non-windowed and windowed sensors. The convective heat flux values calculated in Eq. (4-8) are a strong function of the geometry of the sensor housing and should not be interpreted as what a fuel particle with a dissimilar geometry might experience. Despite this limitation, the data provide valuable information regarding the partitioning of convective and radiative flux in a wildland fire environment.

Because the fire environment is laden with particulate combustion products, the sapphire window could become fouled with products of incomplete combustion. Therefore, the window was continuously purged with dried and filtered compressed air. One of the underlying assumptions of the analysis presented previously is that the two sensors are experiencing the same radiative flux environment. This requires that the sensors be positioned physically as close to each other as possible. However, there was risk that the air purge system would interfere with the non-windowed sensor. For this reason, the experimental setup was tested by activating and deactivating the purge air while the sensors were engulfed in excelsior flames to verify that when the purge air was active, the non-windowed sensor signal remained unperturbed. Through these tests, the purge air was determined to be both strong enough to keep the window clean and weak enough to ensure that the adjacent non-windowed sensor signal remained unaffected.

With each successive experiment, the exposed sensor experienced fouling by products of incomplete combustion from the fire. It was desired to test for any change in sensor calibration due to the fouling. Several tests were conducted wherein an unfouled sensor was used to measure the sensor's response in a calibrated blackbody cavity. The sensor was then exposed to poplar excelsior flames with visible fouling resulting from the exposure. The fouled sensor was again inserted into the blackbody cavity and the heat flux measured. This process was repeated until a very thick coating on the sensor was achieved. The final coating was sufficiently thick that the sensor housing, which was constructed of aluminum, completely lost its metallic luster and the housing and sensor took on a color of dark brown /black. The results of this test revealed that the combustion product coating did not appreciably change the sensor response; the sensor signal in un-

fouled and fouled state was nearly identical when exposed to the same blackbody cavity environment. It must be acknowledged that the coating could change the frequency response of the sensor. In order to minimize this, the sensors were periodically cleaned, recoated, and re-calibrated by the manufacturer. Whatever effect the fouling had on the response of the sensor was not observed in the blackbody tests or any other of the numerous experiments conducted.

The measurement uncertainty associated with the sensor setup was characterized by sampling noise in a fuel bed before the fuel was ignited. The voltages corresponding to each sensor were recorded and subsequently converted to corresponding values of radiation and convection heat flux. A total of 600 points were sampled, and the precision error associated with this test is estimated to be $\pm 0.32 \text{ kW/m}^2$ for radiation, and $\pm 0.34 \text{ kW/m}^2$ for convection with 99 percent confidence. The bias error associated with these measurements is minimized by adjusting the voltage output of the sensors after amplification to a mean of zero when the sensors have reached thermal equilibrium with the burn chamber.

4.5. Fuel Bed Assembly

As mentioned previously, most experimental fires directed at simulating wildland flames consist of a thin bed of continuous fuel (Fons, 1946; Van Wagner, 1967; Pagni, 1972; Telisin, 1973; Konev and Sukhinin, 1977; De Mestre *et al.*, 1989; Butler, 1993; Catchpole *et al.*, 1998). These continuous fuel experiments certainly have merit in that they create a steadily spreading flame front, thus removing variability from the experiment. However, they likely do not accurately represent most wildfire environments in

which fuel is distributed in discrete elements or clumps. It is of interest to simulate less continuous fuels. This was accomplished by wrapping shredded aspen (*Populus tremuloides*) heart wood (commonly termed excelsior) around a steel rod, thus creating a roughly cylindrical “fuel rod” with a diameter of approximately 0.1 m. The height of the fuel rods was either 0.61 m or 1.22 m. 120 g (± 4 g) of fuel was wrapped on the 0.61 m high fuel rods, and that amount was doubled for the 1.22 m high fuel rods. The fuel rods were then arranged laterally in rows of four with a 0.15 m distance between the centers of adjacent fuel rods in each row, as shown schematically in Figure 4.1b. This spacing was chosen so the fuel rods would be close enough to insure that the entire row would ignite rather than the ignition of each fuel rod in the row occurring separately. The spacing between rows was varied from 0.15, 0.20 or 0.25 m (fuel rod center-to-center spacing). In this way the fire intensity of each experiment could be varied. A spacing of 0.15, 0.20 and 0.25 m corresponds, respectively, to a fuel loading of 5.3, 4.0, and 3.2 kg/m² for the 0.61 m fuel rods, and 10.6, 8.0, and 6.4 kg/m² for the 1.22 m fuel rods. The flame intensity was influenced not only by changing the fuel height and spacing but also by introducing forced flow of air simulating wind-driven combustion conditions.

The excelsior was conditioned at 291 K and 35 percent relative humidity for eight hours. The heat flux sensors were placed downstream of the flame spread direction so that a steady rate of spread could be achieved before the flame arrived at the sensors. The sensors were faced toward the oncoming flames and were positioned at a height of 0.53 m from the floor of the fuel bed for all experiments. This placed the sensors near the top of the 0.61 m high fuel rods, and near the middle of the 1.22 m high fuel rods. The sensor leads were routed behind the sensors and out of the fuel bed to the data acquisition

system. A digital video camera oriented to give a side view of the sensors created a visual record of each experiment, and documented flame impingement on the sensor face and other combustion events. An LED was also placed within the view of the camera. Once data acquisition began, the LED was triggered and the voltage was recorded by the data acquisition system. In this way the visual combustion events could be synchronized with the recorded heat flux data.

Fuel particle moisture was measured by drying samples of the fuel collected immediately prior to each experiment in an oven at 90°C for at least eight hours, and comparing pre- and post-drying weight. The average fuel moisture level for all experiments was 7.5 percent, and the range was 6.9 percent to 8.3 percent on an oven-dried mass basis.

The flame spread rate (in rows/s) was calculated by reviewing the videographic record of each burn, and measuring the time between ignition of adjacent fuel rows. The known fuel row spacing was then used to calculate the flame spread rate [m/s]. The flame spread rates calculated for all rows in a given experiment were averaged to characterize the spread rate for that experimental condition.

Once the fuel bed was assembled and conditioned, the experiment commenced by spraying approximately 40 cc of ethanol on the lower 5 cm of the first row of fuel and then igniting it. The ethanol ensured that the entire base of the first row ignited at the same time. Experiments were conducted both in a wind tunnel and in a quiescent environment. The total length of the fuel bed was 1.22 m in the experiments conducted in the quiescent environment, and as many rows of fuel rods were mounted as could be accommodated for a given row spacing. The fuel bed length was 6.1 m long in the wind tunnel

experiments to permit establishment of steady flaming in the wind-assisted combustion environment. The burn chamber used to conduct buoyancy-driven experiments was 20.1 m high with a floor that was 13.4 m square. The wind tunnel has a test section that is 7.5 m long in the streamwise direction, 3 m wide and 3 m high. Catchpole *et al.* (1998) provide additional details about the facility.

Table 4-1 shows a summary of experimental conditions investigated, and spread rates calculated from the videographic record of each experiment.

Table 4-1. Calculated flame spread rates for the experimental conditions investigated.

Fuel Height	Row Spacing	Condition	Spread Rate
0.61 m	0.15 m	Buoyancy-driven	0.016 m/s (0.11 rows/s)
	0.20 m	Buoyancy-driven	0.012 m/s (0.060 rows/s)
	0.20 m	Wind-driven	0.080 m/s (0.40 rows/s)
1.22 m	0.20 m	Buoyancy-driven	0.017 m/s (0.080 rows/s)
	0.25 m	Buoyancy-driven	0.018 m/s (0.070 rows/s)

4.6. Results and Discussion

4.6.1. Temporal Characteristics of Heat Flux

A plot of the representative measured radiation and convection flux history from these experiments is shown in Figure 4.2. These data come from a buoyancy-driven flow experiment with 0.61 m high fuel rods and 0.20 m row spacing. The sampling rate used for this experiment was 50 Hz. The general features of the combustion behavior will be discussed here.

The time-series flux data of Figure 4.2a reveal that both the radiation and convection heat flux are nominally zero initially. Radiative heating is detected well ahead of the

convective flux, evidenced by the rise in radiative heat flux 45 s earlier than the non-zero convective heat flux detected. The videographic record of the experiment revealed that when the sensor is engulfed in flames the convection heat flux manifests an abrupt and significant rise with peaks indicating intense heating. This sharp rise in convective flux will hereafter be arbitrarily assigned a time of zero. The data of Figure 4.2a manifest local maxima in radiation heat flux at -63, -43, -25 and -5 s. The time elapsed between the peak of one local maximum to the next (~20 s) corresponds nominally to the elapsed time between observation of a sustained flame on one fuel row and its establishment on the next row. As will be demonstrated later, this apparent periodicity in the radiation flux is observed only in experiments characterized by sufficiently large fuel rod row spacing to cause the ignition and combustion to occur as relatively discrete events. The sensors experience convective cooling in this configuration 25 to 30 s before the sensors are engulfed in flames. This convective cooling is a result of radiative preheating of the sensors prior to the arrival of the flame and buoyancy-induced in-draft of cool air. This cooling trend prior to onset of combustion is interrupted by discrete heating events in the time period nominally 5 s prior to ignition. However, the negative convective heat flux is not observed in all experiments.

The inset panel of Figure 4.2a shows an expanded time scale for a 2.5-s period around ignition. The convective and radiative flux data were collected in this experiment at 50 Hz. The panel illustrates short convective pulses preceding the full combustion event. These pulses may be intermittent flame bursts sweeping past the sensors, and suggest that convection of combustion products are a mechanism for ignition. At time 0 s a significant rise in the convective flux reaching a magnitude of approximately 60 kW/m^2

is observed. This peak is of short duration, however, and the convective flux drops to a near-zero value followed by heat flux excursions reaching magnitudes of 10 – 20 kW/m².

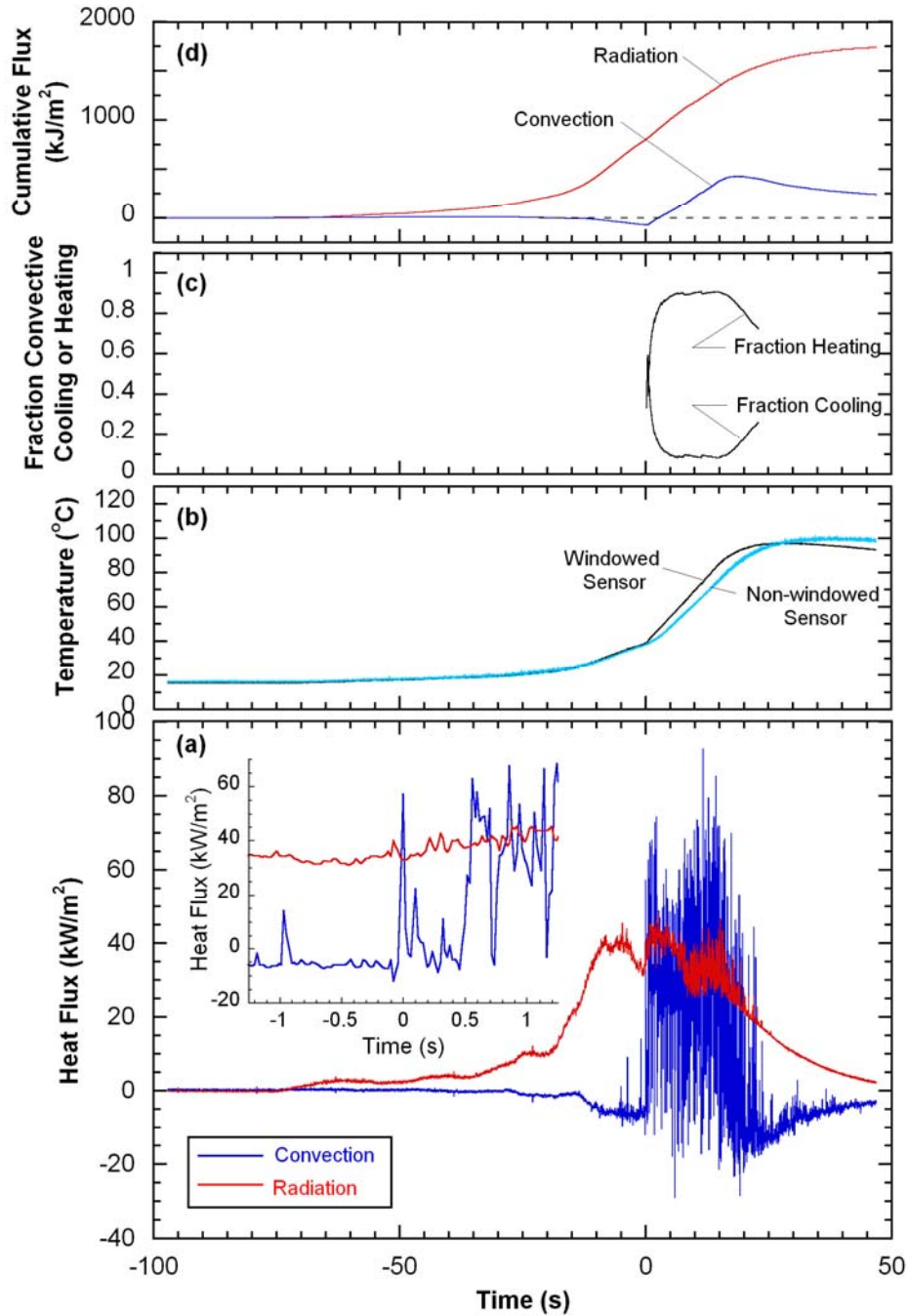


Figure 4.2. Measured radiation and convection characteristics for 0.61 m fuel rods and 0.20 m row spacing: (a) radiation and convection heat flux, (b) sensor temperatures, (c) fraction of time convective cooling and heating after flame arrival (time = 0 s), and (d) cumulative flux.

The inset panel illustrates clearly the rapid temporal fluctuations of convective heating, with strong pulses followed by abrupt drops in the flux occurring on a time scale of the order of 0.02 - 0.05 s. These fluctuations are believed due to pockets of alternately hot combustion products and cool ambient air sweeping past the sensors.

The radiation heat flux transients in Figure 4.2a peak at nearly 50 kW/m^2 , while the maximum in the convection heat flux transients are nearly 90 kW/m^2 . The radiative flux rises nearly monotonically, with relatively small temporal fluctuations in its magnitude through the combustion event. This may suggest that the flame is relatively optically thick, such that any local temporal fluctuations in flame temperature and emitting constituents are compensated by flaming combustion elsewhere, and do not appreciably affect the radiation flux history. By contrast, after the arrival of the flame, the temporal fluctuations in convection heat flux become rapid and dramatic, ranging between -30 and 90 kW/m^2 . As observed previously, these fluctuations suggest the existence of alternating packets of hot combustion gas and cold ambient air while the sensors are engulfed in flames. The fluctuations occur at relatively high frequency, considerably higher than has been contemplated in wildland fire environments.

The temperature history of both heat flux sensors is shown in Figure 4.2b. The sensor temperature data reveal a rise corresponding to the onset of the radiation heating. The sensors' temperature increases monotonically through the combustion event, reaching a maximum for this test of approximately 100°C . This is representative of all tests; the maximum sensor temperature observed in all experiments was 120°C . It may be argued that relative to the high-temperature combustion gases, the sensors are very nearly at ambient temperature. Further, the maximum temperature of the sensors results in a

radiant heat loss from the sensors of less than 1.1 kW/m^2 , which is no more than 2 percent of the 50 kW/m^2 peak radiation flux. It must again be candidly acknowledged that the convective flux reported here cannot be interpreted as the convective flux experienced by the fuel elements. Convective heating/cooling is a strong function of both object geometry and temperature. The convective flux reported here is that flux which is experienced by the sensor and housing from which the convective flux is extracted. The difference between the measured convective heat flux and that experienced by the fuel was quantified by modeling the heat transfer experienced by the sensor and that by a simulated fine fuel element under identical conditions. The parameters of the study were intentionally chosen to be the most extreme to reflect a worst case scenario of convective cooling or heating. The sensor is assumed to be subject to direct impingement of hot combustion or cool ambient air of known freestream velocity. The fuel is assumed to be cylindrical and experiencing a cross flow at a freestream velocity identical to that which the sensor experiences in direct impingement. Accepted empirical correlations for impingement (Jakob, 1949) and cylinder crossflow (Churchill and Bernstein, 1977) heat transfer were taken from the literature. The results of the study are shown in Figure 4.3. Figure 4.3a shows the convective heat flux when the fuel and the sensor are heated, and Figure 4.3b shows the convective heat flux when the sensors are being cooled. The temperature of the sensors and the fuel are assumed to be at their minimum possible value, 300 K, during heating. During cooling, the sensors and fuel are assumed to be at their maximum possible values. These maximum values are 423 K for the sensor, and the nominal ignition temperature for the fuel, 523 K (Babrauskas, 2003). These temperatures were chosen to simulate the most extreme heating or cooling conditions.

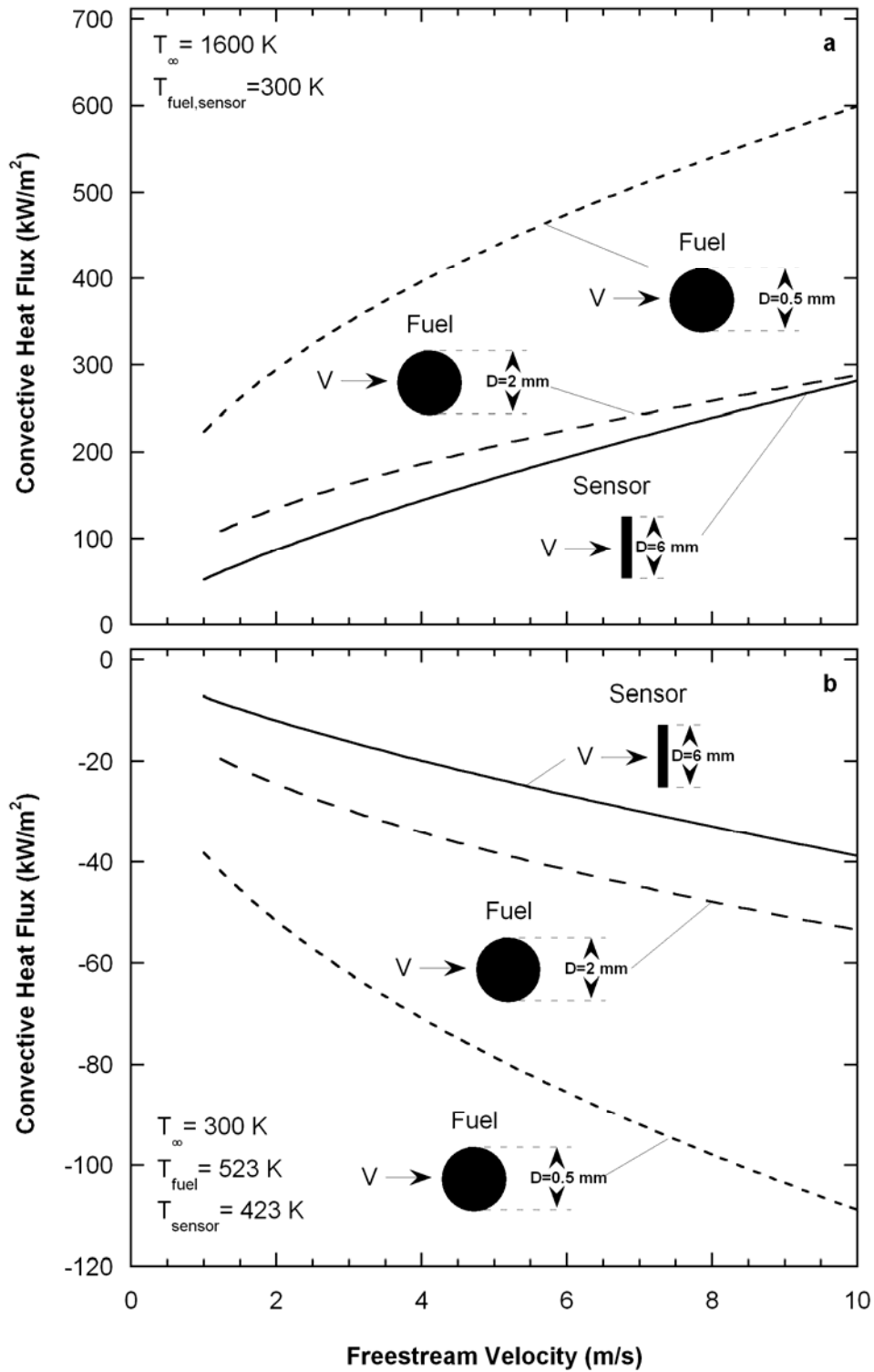


Figure 4.3. Comparison of the modeled heat flux experienced by the sensor and the fuel: a) Convective heating, and b) Convective cooling. Two different fuel particle diameters are represented.

shows that even under these extreme conditions, the absolute heat flux magnitude measured by the sensor is always below that which would be experienced by a fine fuel particle in both heating and cooling. The modeled difference in heat flux magnitude experienced by sensor and fuel can reach over 200%, with the difference increasing with smaller diameter fuels. These trends were verified for fine fuels of diameter as large as 3 mm. It is thus concluded that fine fuels experience a more extreme heat flux magnitude than that which is measured using the sensors employed in the experiments.

Figure 4.2c illustrates the running fraction of time during the combustion event that the convective heat flux exceeds 1 kW/m^2 and falls below -1 kW/m^2 , termed “fraction heating” and “fraction cooling,” respectively. These are computed beginning at flame arrival (time = 0 s). This temporal fraction of convective cooling/heating is determined by accumulating the number of data points above and below the convective flux threshold in the time record. This parameter is presented to characterize both positive (heating) and negative (cooling) fluctuations in the convective flux history. The data of Figure 4.2c reveal that the convective transients heat the sensors approximately 75 - 90 percent of the time during the event. Quite surprisingly, the sensors are exposed to cooler gases (cooler than the sensor temperature) presumably from the ambient air 10 to 25 percent of the burn event, resulting in negative convective flux. These data highlight the intense fluctuating nature of combustion, and the corresponding rapid transients of positive and negative excursions in the convective flux.

The burn event of Figure 4.2a, defined loosely as the time from first indication of radiation flux to that corresponding to a return to zero-flux conditions, is of duration approximately 120 s. The actual combustion event during which flame engulfs the fuel rod

on which the sensors are mounted lasts between 20 and 25 s. After the combustion event, both radiation and convective flux decay to zero as the hot fuel bed cools and the embers burn out, and the sensors cool to ambient temperature. While the non-zero radiation flux which prevails following the combustion event is indicative of clear exposure to a hot radiating environment, the decay in negative convective flux which occurs at approximately 22 s is reflective of the thermal mass of the sensor and sensor housing, which cool while exposed to ambient air.

Figure 4.2d illustrates the cumulative behavior of the radiative and convective heat flux experienced by the sensors. These data are calculated from the time-resolved heat flux by integrating the data of Figure 4.2a with respect to time. In practice, this was done by numerical integration of the convective and radiative heat flux time series. Determination of the cumulative flux permits characterization of the total radiative and convective heat load on the sensors. The data reveal that the cumulative radiative flux rises slowly and quite modestly prior to flame arrival. Consistent with the convective cooling noted in the temporally resolved flux data of Figure 4.2a, the cumulative convective flux drops below zero prior to flame arrival, rises to a peak after onset of combustion, and falls due to cooling of the heated sensor/housing following the combustion event. The magnitude of the cumulative radiation flux is four to five times that of the convective flux for this experimental condition. It is interesting to note that despite the dominance of radiation heat transfer indicated in Figure 4.2d, the time series data suggest that ignition is convectively driven.

While the flames by nature are highly turbulent, the experiments are quite repeatable. Figure 4.4 shows the measured radiation and convection flux for three separate ex-

periments with nominally identical conditions, 0.61 m high fuel rods and 0.15 m row spacing. While variations in radiative and convective flux magnitude are clearly evident, the general features of the burn are similar in all three repeated tests. Examination of data for repeated test results for other fuel rod spacings, fuel heights, and experiments with the addition of wind were all similarly repeatable. Hereafter, a single representative data set from repeated tests at identical experimental conditions will be presented for analysis and discussion. Three parameters were varied in the laboratory experiments which have the potential to influence the intensity of the experiments. These include fuel row spacing, fuel height, and ambient air speed (wind or no wind).

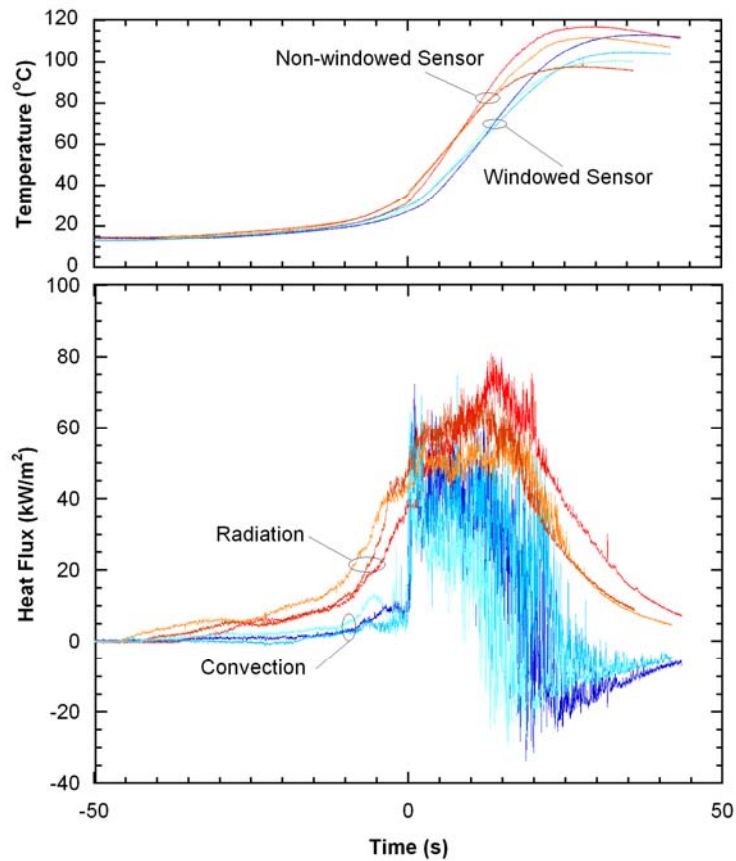


Figure 4.4. Radiation and convection heat flux histories for experiments with the same conditions, 0.61 m fuel rod height and 0.15 m row spacing.

Figure 4.5 shows a comparison of the radiation and convection flux histories for two burns with the same fuel height (0.61 m) but with different row spacing, 0.15 and 0.20 m. In the experiment with 0.20 m row spacing, radiation heating is detected 75 s before flame arrival, whereas the radiation is detected at -37 s in the experiment with the closer 0.15 m spacing. This can be explained principally by the difference in fire spread rate for the two experiments. As summarized in Table 4-1, the spread rate for the 0.15 m

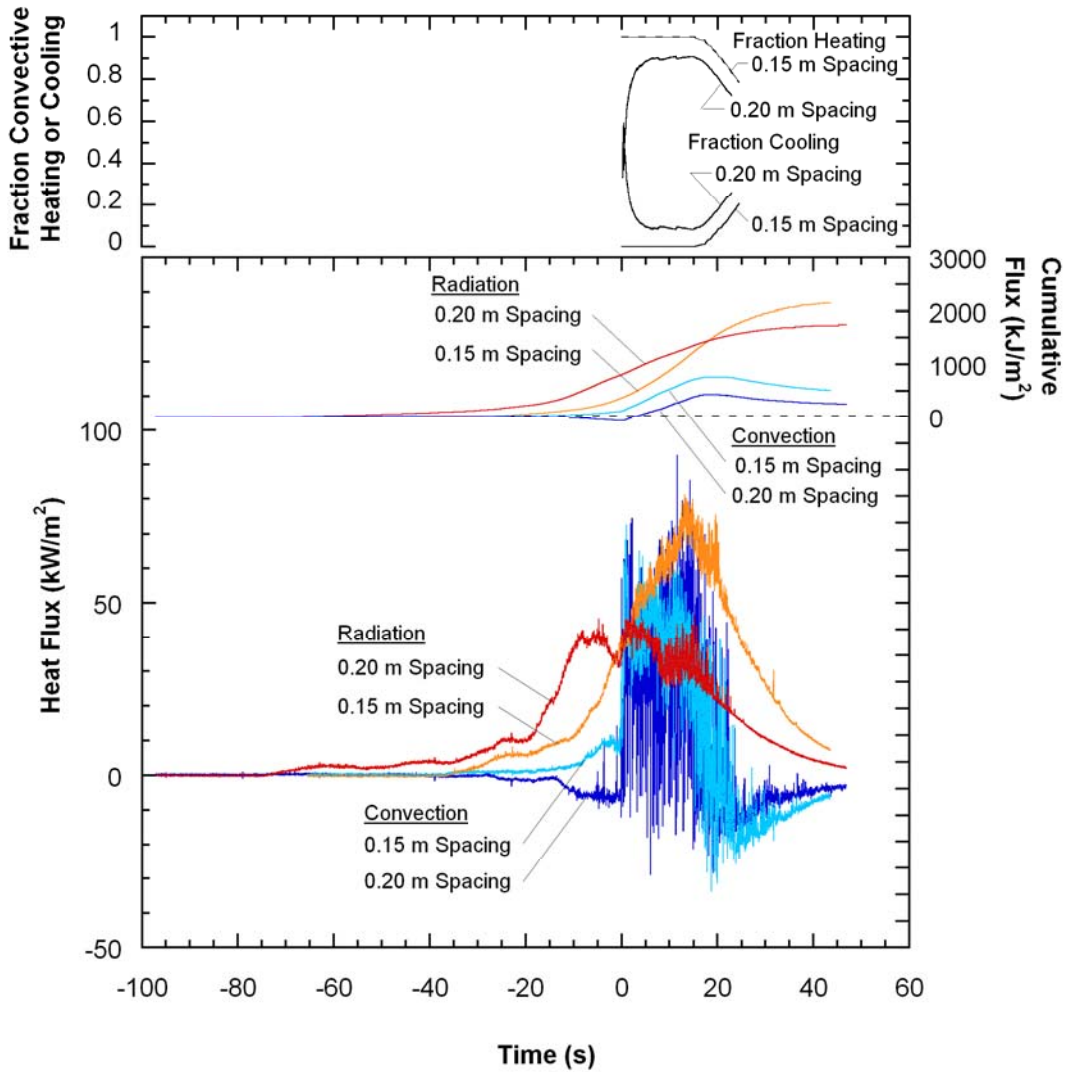


Figure 4.5. Comparison of the radiation and convection heat flux histories for two burns with the same fuel height (0.61 m) but with different row spacing (0.15 and 0.20 m).

and 0.20 m spacing experiments was determined to be 0.016 m/s and 0.012 m/s, respectively. The elapsed time between the first detection of radiation flux and flames overtaking the sensors will be significantly smaller when the spread rate is higher. The convection flux in the 0.15 m row spacing experiment is positive before flame arrival and is first detected at nominally the same time as the radiation heating in that experiment, although it does not reach significant magnitude until -15 to -10 s (10 to 15 s prior to flame arrival). By contrast, the convection flux in the 0.20 m spacing experiment is negative before flame arrival and is not detected until -30 s, well after the radiation was detected at -75 s. The negative convective flux prior to flame arrival observed only in the 0.20 m row spacing can be explained by the ability of ambient air in-drafts to penetrate the fuel bed in the larger 0.20 m spacing experiment. As observed previously, the generally negative convective flow is interrupted by several discrete but very short positive fluctuations nominally 5 - 10 s prior to ignition. More compact fuel beds apparently have the effect of suppressing ambient air flow prior to flame arrival. After the arrival of the flame, the convective heat flux experiences significant temporal fluctuations for both row spacings.

The cumulative flux data of Figure 4.5 reveal an initially negative convective flux load for the 0.20 m spacing configuration corresponding to the pre-flame convective cooling noted previously. By contrast, the 0.15 m spacing exhibits steady rise. The cumulative convective flux data for both fuel row spacing configurations indicate a maximum, followed by a slight decrease before leveling off. The peak and subsequent drop in the convective flux load is the result of post-flame convective cooling of the sensors. The cumulative radiative flux for the 0.20 m spacing configuration rises earlier, consistent with the radiative pre-heating observed in the time series data. As stated previously, the

larger fuel row spacing allows greater visibility of the approaching flame. Despite the delayed rise in radiative cumulative flux, the 0.15 m row spacing exhibits a larger final magnitude. It is clear that this (0.15 spacing configuration) results in higher total radiation transfer to the sensors than the 0.20 m spacing. This is not unsurprising, given the more intense flame that results from the denser fuel bed. Finally, the data show that the total convective heating appears to be nominally 20 - 25 percent of the radiative heating.

While the peak magnitudes in convective flux seen in Figure 4.5 are approximately equal for both row spacings, the amplitude (minimum-to-maximum excursions) of the fluctuations are considerably greater in the 0.20 m row spacing test. The fluctuations in convective flux are smaller in the 0.15 m spacing experiment. This suggests that the denser fuel bed (0.15 m row spacing) suppresses the penetration of cool ambient air into the fuel after flame arrival as well. This is illustrated by the fraction of time that the convection is cooling the sensors, which is plotted in the upper panel of Figure 4.5. In the 0.15 m row spacing experiment, the fraction of time that the sensors are convectively cooled (by ambient air) remains zero for the first 15 s of combustion, indicating purely convective heating through the initial stages of the burn event. By contrast, finite convective cooling is experienced in the 0.20 m test condition experiment throughout the event. This indicates the strong temporal fluctuations in convective flux, even dropping below the zero-flux level, suggestive of packets of ambient air intermittently sweeping past the sensors for the 0.20 m row spacing condition. It may be concluded that temporal fluctuations in convective flux exhibit greater amplitude as spacing between fuel rods increases due to the greater opportunity for ambient air to penetrate the bed.

Figure 4.5 shows that the peak radiative flux in the 0.15 m row spacing experiment is nearly twice that of the 0.20 m spacing test, and the peak is somewhat delayed in time as well. The 0.15 m row spacing configuration results in a more intense flame and correspondingly higher radiation flux. The time delay to peak radiation flux for the 0.15 m row spacing is perhaps due to a denser fuel bed obscuring the sensor view of approaching flame. The radiation flux for the 0.20 m row spacing experiment reaches its maximum value 10 s prior to flame arrival. Multiple maxima in radiation flux seen in the 0.20 m row spacing configuration, and explained as temporal periodicity in the ignition/combustion of upstream fuel rods, are not observed in the 0.15 m row spacing data. Again, this is because the more dense fuel bed burns more continuously, as opposed to the more discrete combustion character of the larger-row-spacing fuel beds.

Figure 4.6 illustrates the convection and radiation heat flux data for two experiments with the large fuel height (1.22 m), but with different row spacing, 0.20 m and 0.25 m. Recall that the heat flux sensors are positioned at the same vertical location for both the 0.61 m and 1.22 m fuel rod height. Thus, flames above the fuel bed in the 1.22 m fuel rod height configuration cannot be “viewed” as readily by the sensor as in the 0.61 m fuel height experiments. The data presented in Figure 4.6 show general trends similar to those observed data in Figure 4.5. The peak radiation flux is higher for the smaller fuel rod row spacing (0.20 m), temporal fluctuations in the convective flux are characterized by higher amplitude for larger row spacing (0.25 m), negative convective flux prior to flame arrival is observed only for larger fuel row spacing. Further, as illustrated in the inset panel showing the convective flux for the time period 4 s before the full onset of flaming, short-duration convective heating pulses are also observed shortly before igni-

tion for both experimental configurations. There are, however, differences in the data of Figure 4.6 worth noting. First, radiation heat transfer is detected at the same time before the arrival of the flame (-53 s) for both experiments. Second, there are no local radiation maxima corresponding to discrete combustion events prior to the arrival of the flame in Figure 4.6. Finally, the radiation flux rises and peaks for the 0.20 m spacing experiment

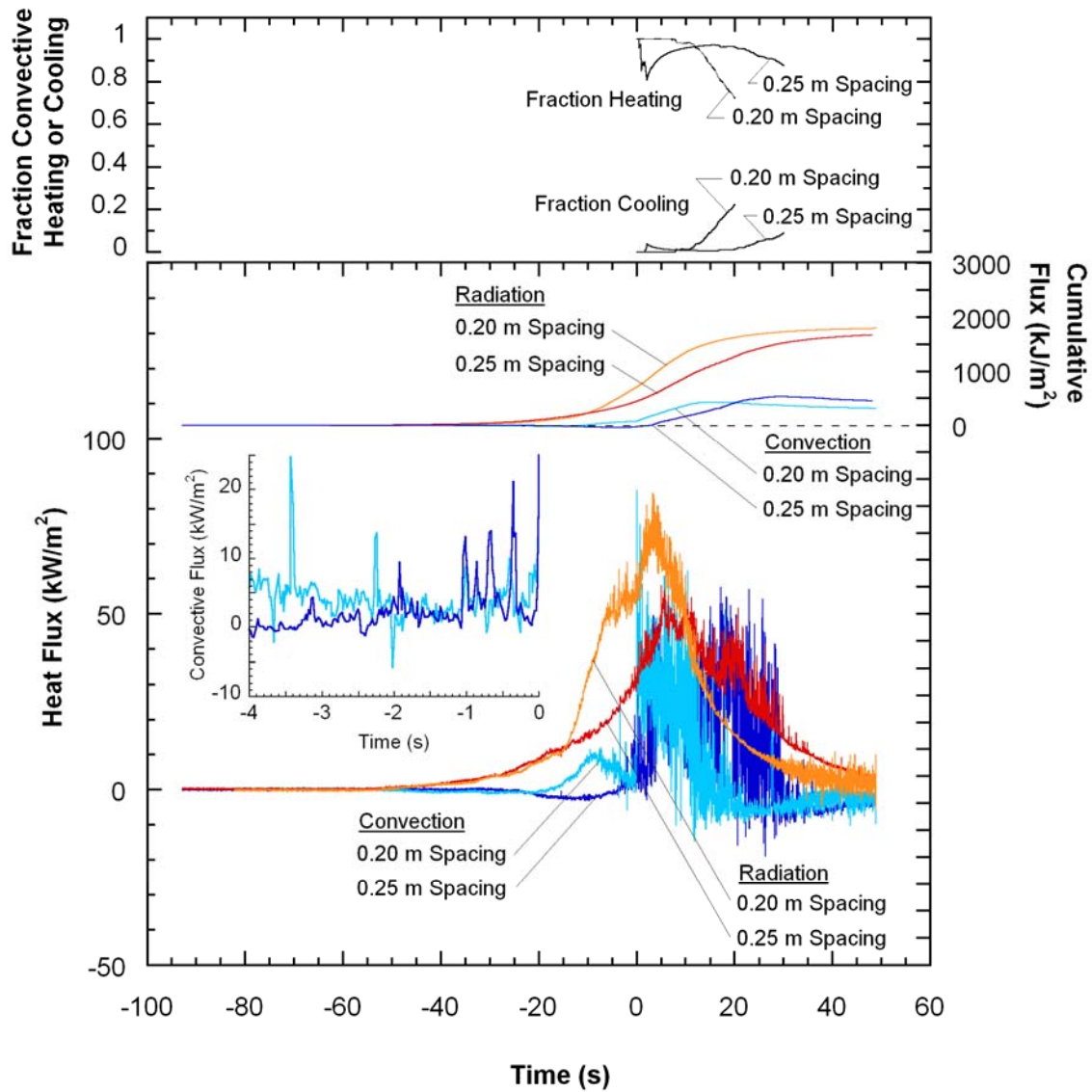


Figure 4.6. Comparison of radiation and convection for two burns with the same fuel height (1.22 m) but with different row spacing (0.20 and 0.25 m).

prior to the 0.25 m spacing data. All of these differences may be explained by the fact that the sensors' view of the flames above the fuel bed is obscured by the fuel directly in front of the sensors for the taller fuel rods. Further, it appears that more dense fuel beds have greater fuel loads and therefore result in higher flame intensity and associated radiation flux, but lower amplitude temporal fluctuations in convective flux. This is again illustrated in the fraction convectively heating/cooling data plotted in the upper panel of Figure 4.6. The sensors in the 0.20 m spacing experiment are convectively heated for the first 10 s, and the heating in the 0.25 m spacing experiment is delayed and prevails over shorter time during the event. Convective cooling occurs in both experimental configurations only after the initial combustion event has passed.

The cumulative convective flux data for the experimental configurations displayed in Figure 4.6 for a fuel height of 1.22 m are similar to those seen for the shorter 0.61 m fuel height of Figure 4.5, with the exception that the cumulative flux for the larger row spacing (0.25 m) ultimately exceeds that observed in the smaller row spacing (0.20 m). It appears that the convective heat load on the sensors is greater for the smaller fuel row spacing at large fuel heights. Moreover, the radiative flux for the larger fuel heights exhibits a higher cumulative magnitude throughout the burn event for the smaller row spacing. It is interesting to note that a comparison of the cumulative radiative flux data of Figure 4.5 and Figure 4.6 reveals that the 0.61 m fuel height, 0.15 m row spacing configuration exhibits a larger maximum cumulative flux (2200 kJ/m^2) than the 1.22 m fuel height, 0.20 m row spacing condition (1700 kJ/m^2) despite the significantly higher fuel loading in the larger fuel height test. The effect of fuel height on cumulative flux at the different fuel heights for the same row spacing will be shown later.

Figure 4.7 illustrates the effect of fuel rod height on the heat transfer behavior. This figure compares flux histories for two experiments with the same row spacing of 0.20 m, but with different fuel heights (0.61 m and 1.22 m). The 1.22 m high fuel rod configuration has both twice as much fuel to burn per unit area and a faster spread rate (see Table 4-1), and thus exhibits the more intense combustion. This is seen in the significantly higher peak radiation flux for the 1.22 m high fuel rod configuration. In the

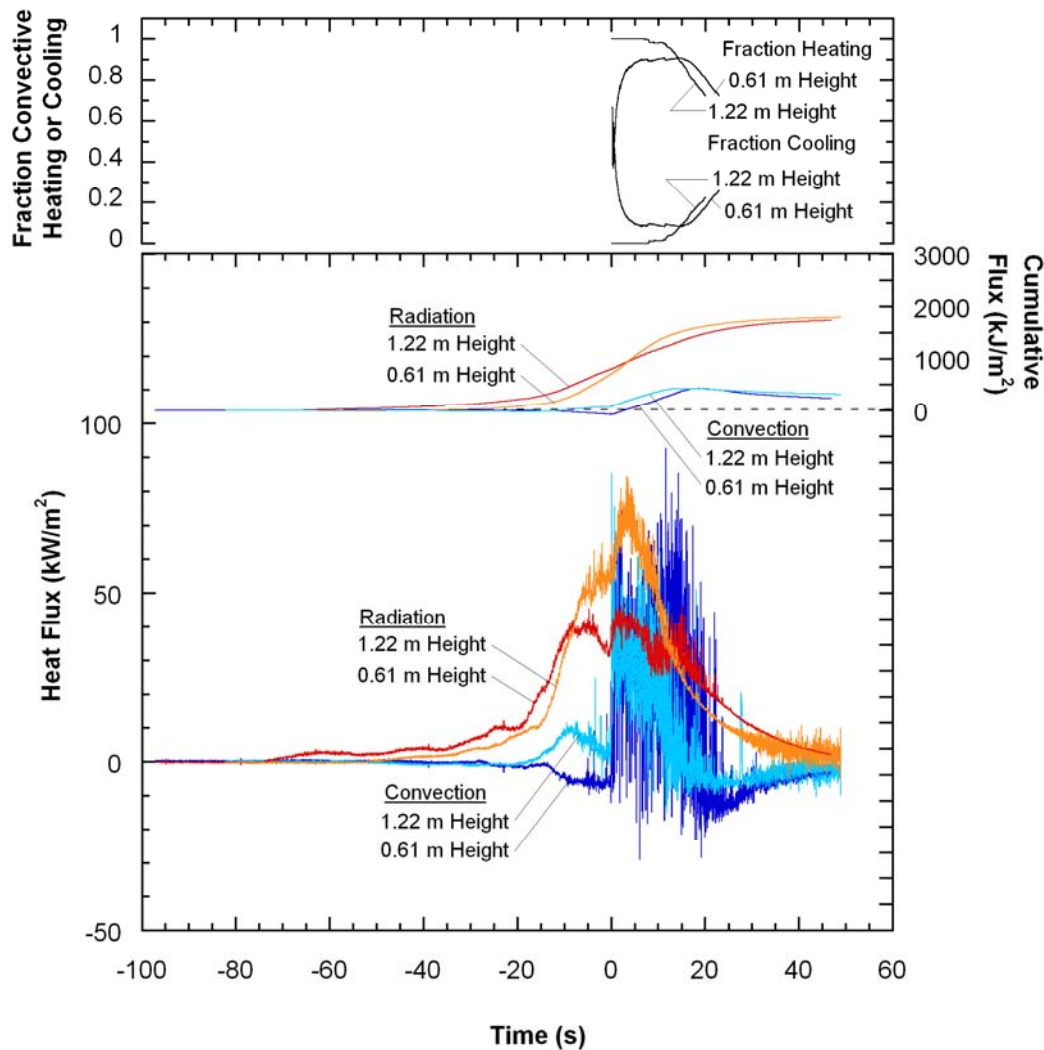


Figure 4.7. Radiation and convection for two experiments with the same row spacing (0.20 m), but with different fuel heights (0.61 m and 1.22 m).

lower-intensity 0.61 m high fuel rod experiment, the radiation flux is detected well ahead of the flame front with local maxima seen in the data corresponding to discrete combustion events of upstream fuel rods mentioned previously, all of which can be explained by the difference in spread rate summarized in Table 4-1 for the two experiments. Further, the convection heat flux is negative before flame arrival with the exception of the short duration positive convective pulses. The higher-intensity 1.22 m high fuel rod experiment shows no local maxima in radiation and exhibits a positive heat flux just before flame arrival. After flame arrival the 0.61 m high fuel rod experiment shows a lower radiation heat flux peak and lower-amplitude temporal fluctuations in the convective heat flux. Convective flux data for both experimental configurations exhibit the short-duration heating pulses prior to full-onset combustion that has been observed previously. These pulses may well be a mechanism for flames “jumping” from one fuel rod to the next.

The cumulative convective and radiative flux levels are not significantly different for the two different fuel heights shown in Figure 4.7. The cumulative radiative flux for the smaller (0.61 m) fuel height rises more slowly than the larger (1.22 m) height, but the peak magnitude is slightly higher for the 0.61 m height configuration, this despite the fact that the fuel density (per square foot of burn plot area) is twice as high in the 1.22 m fuel height test.

As described previously, the effect of wind-driven combustion was investigated by performing experiments in a wind tunnel (Figure 4.8). The fuel bed for the wind-driven burn test was longer (6 m) than the buoyancy experiments to allow the fuel to reach a steady rate of spread before reaching the sensors. The forced air flow has the eff-



Figure 4.8. Photograph of fuel bed burned in the presence of wind at 2.2 m/s.

ect of inclining the flame such that the flame extends above the fuel bed well ahead of the fuel rod combustion zone.

Figure 4.9 shows temporal heat flux behavior from two experiments with the same row spacing (0.20 m) and fuel height (0.61 m), where one experiment was conducted in a quiescent environment and the other burned with a 2.2 m/s wind. The measured peak sensor temperature (not shown) was lowered from 100°C in the buoyancy-driven burns to 45°C for the wind-driven configuration. Figure 4.9 shows quite clearly that peak radiation flux in the wind-driven burn data is more than twice that of the buoyancy-driven configuration. Radiation is detected in the buoyancy-driven experiment well ahead of flame arrival, whereas its influence is delayed in the wind-assisted combustion. Both the wind-driven and buoyancy-driven experiments exhibit convective cooling before flame arrival. However, it appears that very strong, short-duration convective

pulses occur in the 5 s prior to ignition for both configurations, illustrated more clearly in the inset panel of Figure 4.9 showing a 5-s period. The short-duration pulses are not as apparent in the wind-driven data; this configuration exhibits a more gradual transition to the strongly fluctuating flux condition characteristic of full combustion.

Figure 4.9 suggests that the wind-driven experiment is affected more by entrained ambient (cool) air than does the buoyancy-driven experiment, giving rise to both the neg-

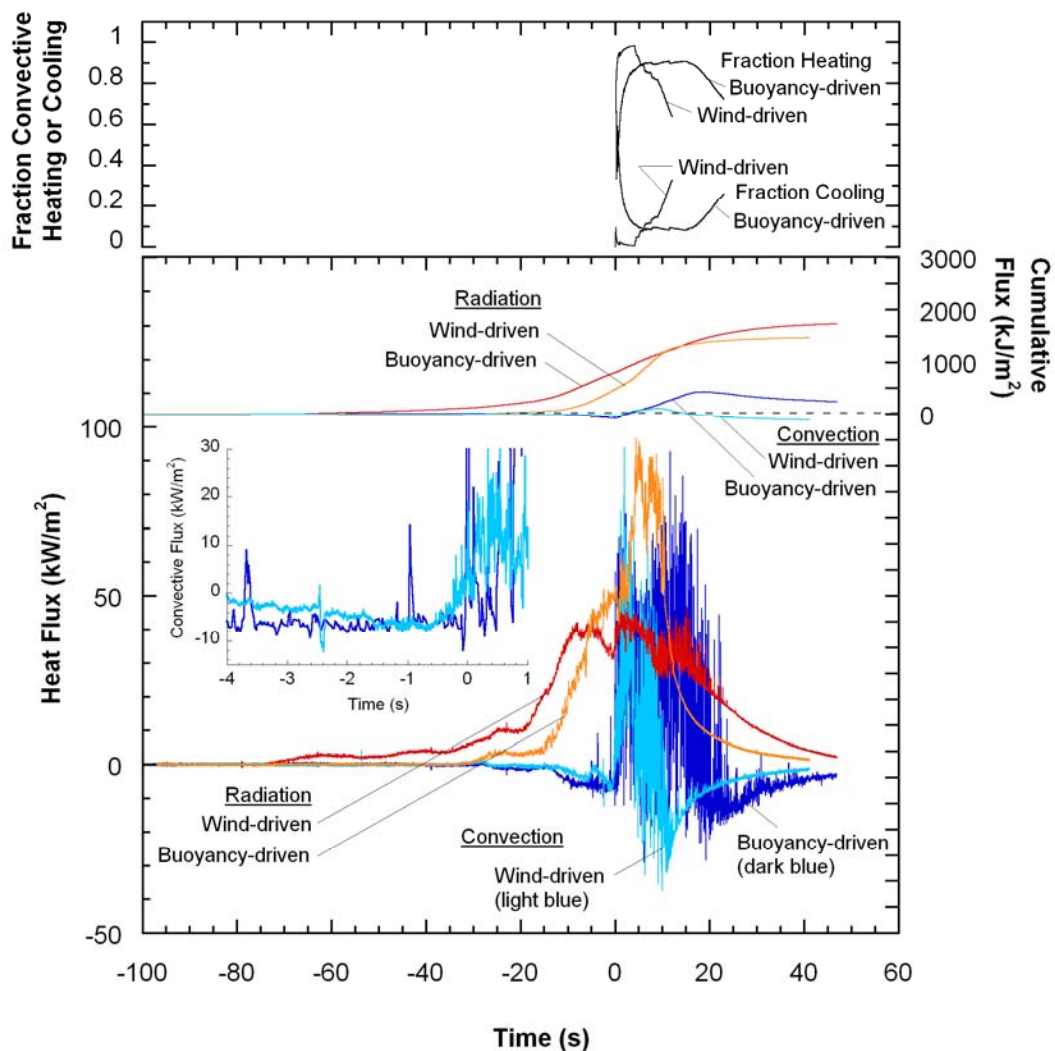


Figure 4.9. Two experiments with the same fuel height and row spacing, 0.61 m and 0.20 m respectively, one buoyancy-driven and the second wind-driven with a 2.2 m/s crossflow.

ative heat flux before flame arrival and the lower sensor temperature observed. The transients in convective heat flux exhibit peak magnitudes exceeding 90 kW/m^2 for both the buoyancy-driven and the wind-driven experiments. However, the wind-driven convective flux is characterized by smaller maximum-to-minimum excursions in the temporal fluctuations than the buoyancy-driven burn. This is illustrated by the fraction of convection heating/cooling data plotted in the upper panel of Figure 4.9. As the flame arrives, there is little convective cooling in the wind-driven experiment, whereas considerable negative convective flux is evident after flame arrival in the buoyancy-driven experiment. It may be suggested that the forced flow provides greater oxygen for combustion and suppresses large-amplitude convective fluctuations. Despite the effective delivery of oxygen in the wind-driven experiment, the cumulative radiative and convective flux levels are consistently higher in the buoyancy-driven burn configuration. Indeed, the cumulative convective flux is positive only for a small portion of the wind-driven burn, indicating much more convective cooling of the sensors.

As seen in Table 4-1, the rate of flame spread varies quite substantially among the different burn conditions. This is particularly noticeable in the data of Figure 4.9, where the flow-induced angling of the flame may have more significant influence on the heat flux than in the buoyancy-driven burn, but is not clearly reflected in the figure or data. The flame spread rate of the two experimental conditions is so different that it is difficult to determine if the radiation detected by the sensors at -30 s originates from the flames above the fuel bed or from the fuel bed itself. It is instructive to register the flux detected by the sensors to the location from which the flame originates measured by row number upstream of the sensor location. The temporal behavior of the different burn configura-

tions was normalized by plotting the convective and radiative heat flux histories as a function of the combustion zone position (fuel row), determined from the fuel row-based flame spread rate rather than elapsed time. This permits interpretation of the combustion history in terms of the flame front location (not flames above the fuel bed). Figure 4.10 reproduces the data of Figure 4.9 comparing buoyancy- and wind-driven burn conditions with the flux histories plotted as a function of combustion zone position rather than time. A different wind-driven data set is represented because better video footage was taken in order to determine a proper fuel row flame spread rate. Row zero represents the fuel row where the sensors are located, and a row number of -1 represents the combustion of the row immediately upstream (relative to flame spread) of the sensors. Note that the spread rate for the wind-driven burn (0.080 m/s) is 6 - 7 times that of the buoyancy-driven experiment (0.012 m/s). Figure 4.10 shows that the radiation heat flux in the wind-driven experiment is detected when the flame is 16 rows upstream of the sensor location. With 15 unignited rows of fuel between the sensor and the burning fuel, it is unlikely that the radiation detected by the sensor originates from the fuel bed. Rather, the sensor is viewing the flames extending above the fuel bed downstream of the combustion zone. While it is true that radiation is detected from the flames, the magnitude of this radiation remains below 5 kW/m^2 until the sixth fuel row upstream of the sensor is ignited. Prior to this, the sensors are exposed to relatively weak, intermittent flames visible above the fuel bed. As the flame moves nearer the sensor location, the flame is more intense and occupies a greater portion of the sensor's hemispherical field of view.

Figure 4.11 reproduces the data of Figure 4.7, plotted as a function of combustion zone position (in rows) rather than time. Both experiments feature the same row spacing

(0.20 m) but with differing fuel rod heights, 0.61 m and 1.22 m. Radiation heating is detected when the flame reaches the same nominal upstream location (expressed in rows) for both experiments. Recall that the sensors are located vertically near the middle of the fuel rod height for the 1.22 m fuel beds and near the top of the fuel bed for the 0.61 m fuel rod. Thus, the view of the flames is restricted in the deeper 1.22 m fuel beds. Given

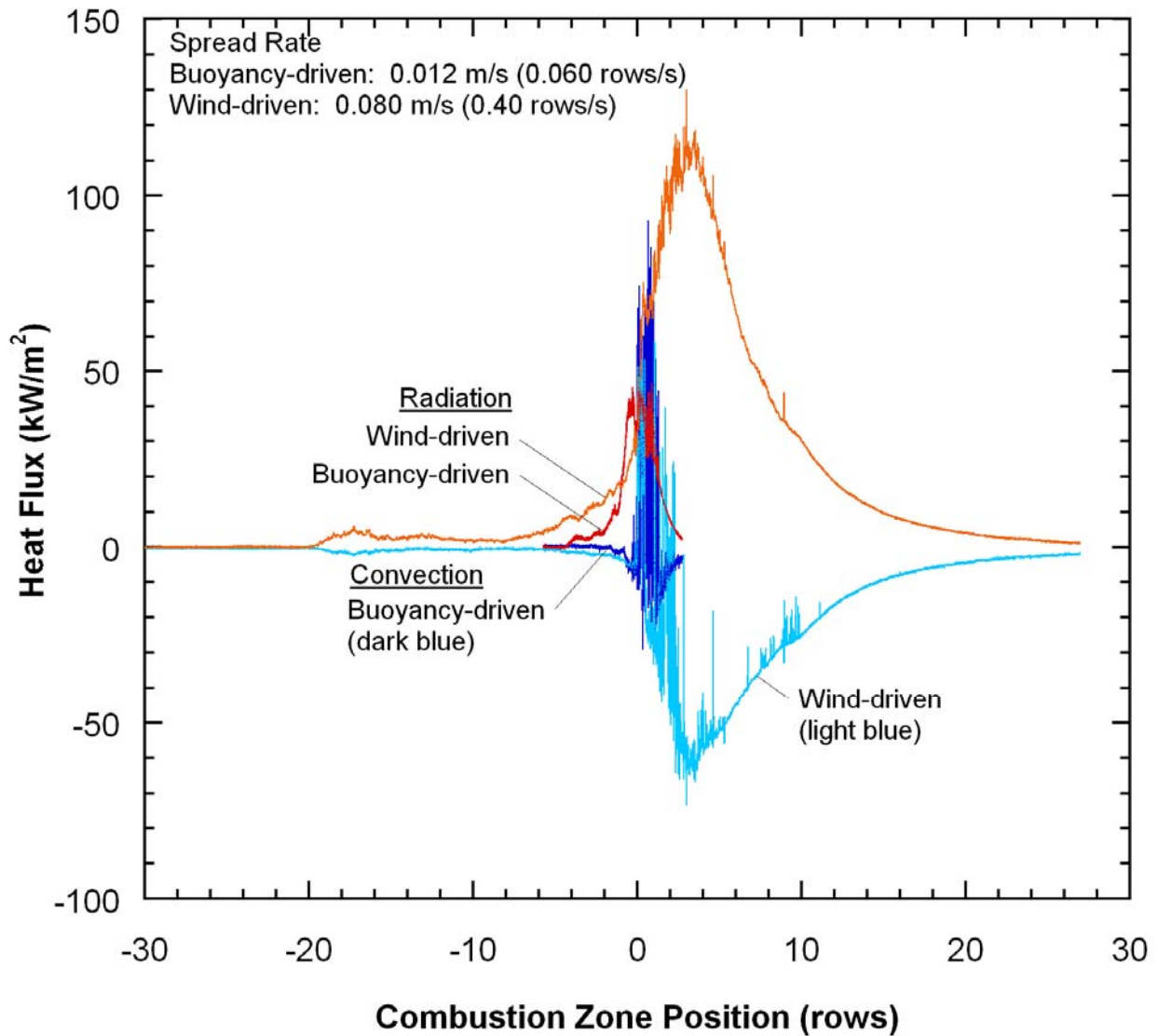


Figure 4.10. Heat flux histories for buoyancy- and wind-driven burns 0.61 m fuel with 0.20 m row spacing.

that the sensors detect radiation heat flux at the same combustion zone location for both experiments, and further, that the sensors can view the flames in the 0.61 m fuel rod height experiment and not the 1.22 m fuel rod height experiment, would seem to suggest that flame radiation (from flames extending above the fuel) in buoyancy driven experiment is low. Both sets of data exhibit the short-duration convective heating pulses

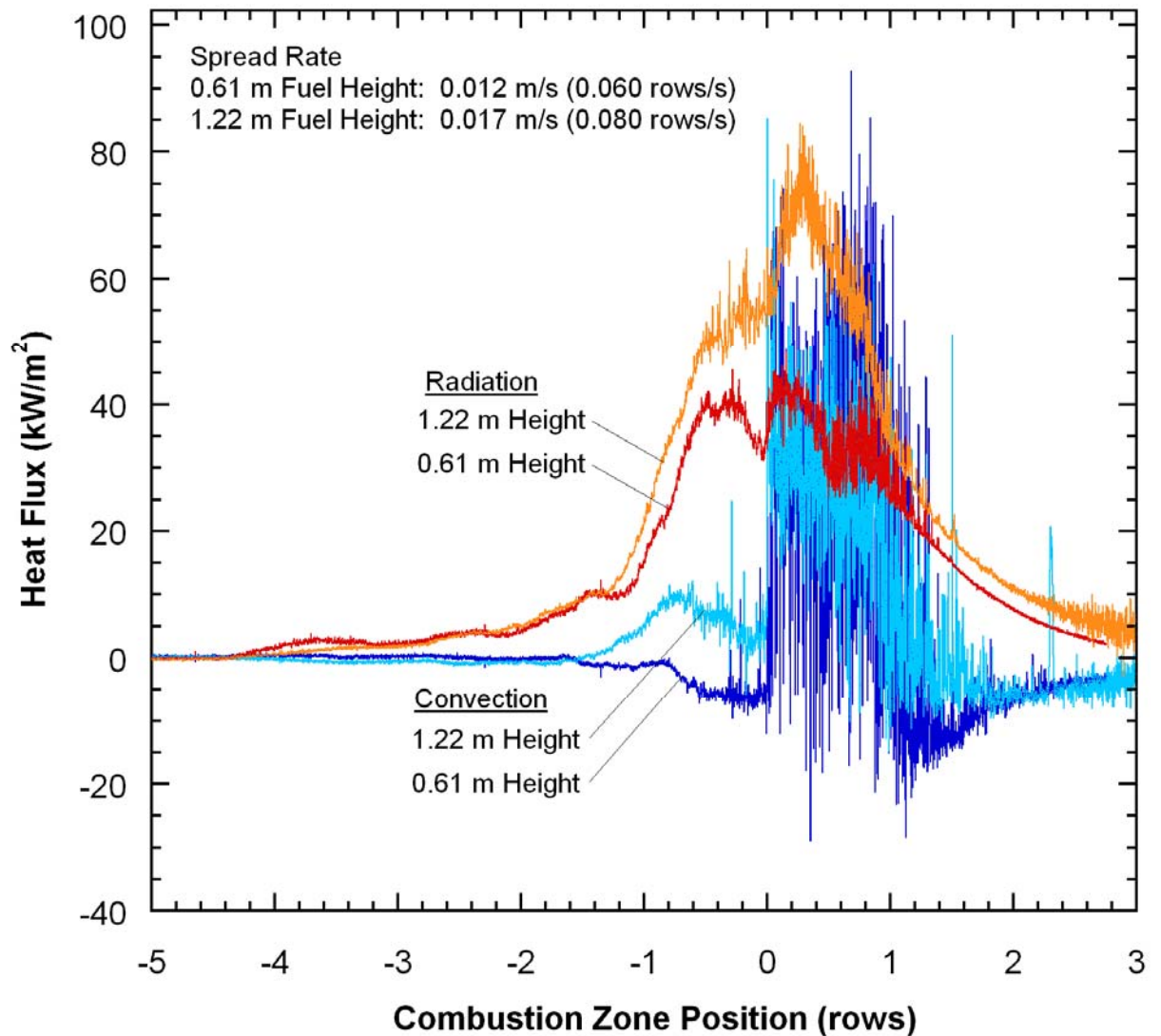


Figure 4.11. Burn characteristics for 0.61 and 1.22 m height fuel plotted as a function of combustion zone position.

immediately prior to ignition, and both are seen to occur when the combustion zone is within a half-row of the sensor location. This further supports the conclusion that the convective heating pulses provide the pilot ignition mechanism for flame spread from one row to the next.

From the aforementioned plots, it is suggested that convective heating or cooling is significantly lower in magnitude than the energy delivered through radiant energy transfer prior to ignition. However, there are indicators that intermediate very short-duration convective heating pulses occur immediately in the few seconds preceding ignition, suggesting that intermittent flame presence may be critical, possibly as a pilot ignition source.

4.6.2. Spectral Analysis

In an effort to characterize the difference in temporal fluctuation intensity between radiation and convection heat flux under different experimental conditions, the frequency content of the time series data in experiments where the flux was sampled at 500 Hz was determined by the use of a Fast Fourier Transform (FFT). The data processed in the FFT included the time period beginning with any non-zero radiative/convective flux and ending with the conclusion of the post-flame cooling period. Figure 4.12 shows the heat flux power spectrum for radiative and convective flux data collected at four different experimental conditions. The noise floor can be identified by the frequency at which the power spectrum ceases to change.

Figure 4.12a presents data from a buoyancy-driven experiment with a 0.61 m fuel height and a 0.15 m row spacing. The data of Figure 4.12b are also from a buoyancy-

driven experiment but with a 0.61 m fuel height and a 0.20 m row spacing. Figure 4.12c is again from a buoyancy-driven experiment but with a 1.22 m fuel height and a 0.20 m row spacing. Finally, Figure 4.12d is from a wind-driven experiment with a 0.61 m fuel height and a 0.20 m row spacing.

It is interesting to note that the power spectrum for both radiation and convection heat flux exhibits magnitudes that exceed the noise floor at frequencies as high as 30 – 70

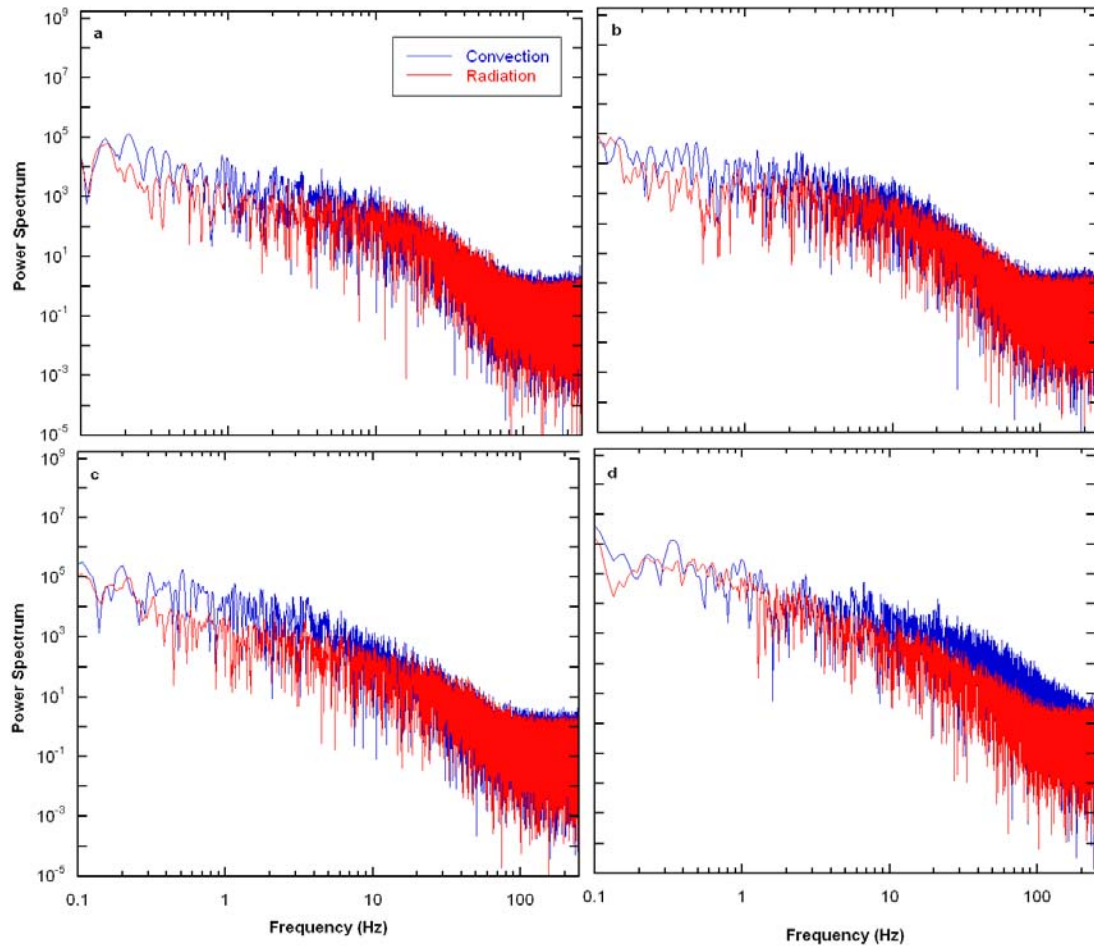


Figure 4.12. Power spectra for fluctuating convection and radiation heat flux: (a) buoyancy-driven experiment with 0.61 m fuel height and 0.15 m row spacing, (b) buoyancy-driven experiment with 0.61 m fuel height and 0.20 m row spacing, (c) buoyancy-driven experiment with 1.22 m fuel height and 0.20 m row spacing, and (d) wind-driven experiment with 0.61 m fuel height and 0.20 m row spacing.

Hz, depending on experimental condition. This suggests that fuel particles are exposed to temporal fluctuations in radiative and convective heating which are much more rapid than has been previously documented in the literature. The low-frequency (< 0.1 Hz) content of the radiation flux is uniformly stronger than that of the convective flux, consistent with the time-series plots presented previously where radiation transfer was seen to be more steady in time. On the other hand, all cases show that convection exhibits greater power at higher frequencies, suggesting convection transfer is more strongly governed by turbulent fluctuations in such flames. Radiation and convection transfer do not exhibit significant frequency content beyond 50 to 70 Hz in the buoyancy-driven experiments (a-c). However, the wind-driven experiment (Figure 4.12d) displays significant spectral content in convection and radiation heat flux to 200 and 100 Hz, respectively. This is perhaps the result of increased turbulence induced by the forced flow. While these data reveal that rather high frequencies do exist in these laboratory scale fires, it is unknown just how fuel particles may react to fluctuations in heat flux at these frequencies. Clearly more study must be undertaken to understand the significance.

4.7. Conclusions

This study reports experimental measurements of time-resolved convective and radiative heat flux in discrete fuel beds designed to simulate natural fuels present in wild-land fires. The influence of fuel row spacing and height on heat transfer characteristics were investigated for both buoyancy- and wind-driven flow. The results show the effect of discrete combustion characteristics of fuel rows on radiation pre-heating. Whereas radiation transfer is felt long before flame arrival, the convective heating occurs abruptly

when the combustion occurs. Convective cooling is evident during intervals of radiative pre-heating prior to flame arrival, and during high-amplitude turbulent fluctuations after flame arrival. Turbulent temporal fluctuations in convective flux are more rapid than previously documented, with content at frequencies as high as 70 Hz for buoyancy-driven flames, and 150 to 200 Hz for wind-assisted flames. Temporal fluctuations in the radiative flux are confined more principally to low frequencies. Total energy contributed by convection seems to be about 25 percent of that contributed by radiant energy transfer. Successively stronger convective heating pulses are exhibited immediately prior to ignition in nearly all cases, suggesting that convective energy transport may be critical to the flame “jumping” across discrete fuel gaps. These results have direct application to current efforts within wildland fire science to develop and evaluate new multidimensional numerical models describing the heating, pyrolysis, ignition, and spread of wildland fires.

5. Convection and Radiation Heat Flux Data from Field Burns

5.1. Abstract

Very little heat flux data have been collected in actively spreading wildfires or controlled burns. Time-resolved radiation and convection heat flux data sets were collected under a variety of fuel and ambient conditions including two crown fires and three brush fires. It is shown that convective heat flux is composed of brief/intense peaks whereas radiation heat flux increases and decreases nearly monotonically with the approach, arrival and departure of the flame front.

5.2. Introduction

Radiation and convection heat transfer have complimentary roles in wildland fire spread (Anderson, 1969; Yedinak *et al.*, 2006; Anderson, 2009). In order to accurately predict the behavior of forest fires, a better understanding of how these heat transfer modes interact is vital. Some measurements have been taken in an effort to facilitate this understanding.

Packham and Pompe (1971) measured radiant heat flux from a fire in Australian forest lands. The fires were set on slash material and the radiant heat flux was measured

using a vertical King radiometer (King, 1961) featuring a 10 s time response. Photographs of the flame were taken and used to estimate the view factor of the sensor to the flame. It was concluded that the radiant heat flux level was 100 kW/m^2 at the flame and 57 kW/m^2 at a distance of 7.6 m from the fire.

Butler *et al.* (2004) presented temporally resolved radiant heat flux measurements taken from a Boreal forest crown fire at various heights. The fuel was primarily composed of jack pine (*Pinus banksiana*) with an understory of black spruce (*Picea mariana*). A Gordon gauge (Gordon, 1960) with a response time of 0.05 s was used to measure the heat flux at a sample rate of 1 Hz. Measured peak radiant heat fluxes averaged 200 kW/m^2 with a maximum value of 290 kW/m^2 .

Morandini *et al.* (2006) measured time-resolved radiant heat fluxes at 5, 10 and 15 m from the flame front on a test fire in south Corsica (France). The fuel consisted of tall and dense Mediterranean shrubs. While the authors report that both total and radiant heat fluxes were measured, the sensors were not close enough to the flames to experience any convection. The radiant heat flux was measured using Captec® sensors (Santoni *et al.*, 2006) which have a 0.05 s response time. The radiant heat flux was sampled at 100 Hz, apparently exceeding the response time of the sensors. Radiant heat fluxes measured in this study ranged between 7 and 8 kW/m^2 .

Silvani and Morandini (2009) measured time-resolved radiant and total heat fluxes in four experiments conducted in southern France. The fuels consisted of pine needles, oak branches, oak and arbutus branches and broom. These data were sampled using Medtherm® 64 sensors at 1 Hz. The response time of these sensors is nominally 250 ms

at heat flux levels below 341 kW/m². Peak radiation heat flux values of 50 kW/m² and a total heat flux peak of 110 kW/m² were reported.

While these works have contributed significantly to the field, there is still much that is not understood with regard to the convective and radiative heat transfer in wildland fires. This study seeks to add to the body of work by presenting measurements of time-resolved convection and radiation heat fluxes in wildland fire scenarios using sensors with a high response time for a variety of fuel environments. In an effort to provide a comprehensive set of data for the different wildfire conditions explored, information characterizing the fuel and ambient environmental conditions is presented for each burn. It is believed that the data stand in their own as a contribution to the wildland fire science community.

5.3. Measurement Procedure

The goals of this study were met by placing a sensor package that could withstand the rigors of the environment in the path of flame spread in both controlled burns and wildfires. Both radiation and convection heat transfer data were collected using high frequency response sensors employed at high sampling rates. The paragraphs to follow will detail the instrumentation, experimental procedure, and data analysis techniques.

A two-sensor configuration was used to measure both radiation and convection heat flux. The sensors used were Vatell HFM 7 heat flux micro-sensors. These sensors were 6 mm in diameter, coated with a highly absorbent coating ($\varepsilon = 0.94$), and featured a 300 μ s response time (frequency response > 3000 Hz) (Vatell, 2007). The sensors were equipped with both a thermopile heat flux gage and a resistance temperature sensor, and

the voltage from both must be recorded to measure the heat flux. Thus, the dual-sensor configuration required that four voltages be acquired. Each sensor was mounted in a thick walled rectangular aluminum housing (0.05 m square cross-section) shown in Figure 5.1. The mass of the sensor housing was meant to act as a heat sink and thus minimize temperature rise and associated radiant emission loss.

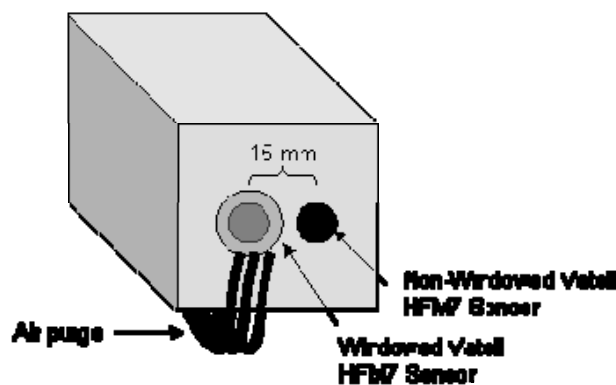


Figure 5.1. Sensor setup

The sensors face the same direction and were separated by 0.015 m. One sensor had a 0.5 mm thick sapphire window mounted over it, whereas the other sensor was left exposed. The windowed sensor had a 0.5 mm air gap between the sensor face and the window. In this way, the non-windowed sensor gathered total (convective plus radiative) heat transfer whereas the windowed sensor gathered only radiant energy (after some quantified loss in transmission through the window). Sapphire was used due to its favorable transmission characteristics (transmission range $0.3 \mu\text{m} \sim 5 \mu\text{m}$) and durability. A Vatell Amp 6 amplifier was used to amplify the output of the heat flux micro-sensors

which have a voltage output in the μV range. Once the sensor signals were amplified, the voltages were simultaneously sampled at a frequency between 5 Hz and 100 Hz using a Campbell Scientific CR1000. The analog-to-digital resolution of the cr1000 was 13 bits. Initially, memory restrictions required a sample rate of 5 Hz. However, the addition of a Campbell Scientific CFM100 memory extender module to the CR1000 allowed the use of a 2 Gb data card and the sample rate was extended as high as 100 Hz.

The amplifiers and datalogger were housed in an aluminum box below the sensors. The aluminum box and the rear of the sensor housing were thermally insulated by mineral wool sandwiched by two layers of fire shelter material.

The sensor package was placed in the expected path of the fire and the data were collected as the flame passed over the sensor package. After fire managers determined that it was safe, the sensor package was retrieved and the data were downloaded to a laptop computer. The voltages recorded by the datalogger were then converted to heat fluxes using the calibration provided by the manufacturer and separated into radiation and convection using the analysis which follows.

The heat flux sensors were calibrated by the manufacturer in a blackbody cavity environment, such that the radiant flux incident on the sensor was known as a function of the imposed blackbody cavity temperature. The calibration thus yields the incident radiant flux, $q''_{rad,inc}$, if the sensor is in a radiation-only environment:

$$q''_{cal} = q''_{rad,inc} \quad (5-1)$$

Only heat flux absorbed by the sensor, q''_{abs} , results in a voltage response, and the absorbed heat flux is a fraction of the incident flux, the scaling factor being the emissivity,

ε .

$$q''_{abs} = \varepsilon q''_{rad,inc} \quad (5-2)$$

The difference between the absorbed flux and the incident radiant flux increases with decreasing sensor emissivity; if the sensor emissivity were unity, the absorbed flux would equal the incident radiant flux. If the sensor is exposed to convective heating or cooling, the sensor calibration will yield a flux magnitude higher than that actually experienced by the sensor, in a factor equal to the emissivity. Thus, the actual combined convective and radiative flux is always less than or equal to the value indicated by the sensor calibration.

Equations (5-1) and (5-2) are general expressions for sensors exposed to convective and radiative modes of heat transfer acting in a combined fashion or independently. The absorbed flux which results in sensor response voltage is related to either the convective, radiative, or combined flux. The non-windowed sensor used in the experiments reported here responds to both radiation and convection heat transfer, while the windowed sensor is not exposed to convective transfer. The heat flux absorbed by the windowed sensor, $q''_{abs,w}$, is equal to the radiant heat flux incident on the outside of the window, $q''_{rad,inc}$, scaled by the emissivity and the effective window transmittance, τ :

$$q''_{abs,w} = \tau \varepsilon q''_{rad,inc} \quad (5-3)$$

Here it is assumed that the radiant flux incident on both the non-windowed sensor and the outside surface of the sapphire window (of the windowed sensor) are identical. The effective transmittance of the sapphire window was experimentally measured by igniting 400 g of excelsior strands 1 m from the sensors. This distance was selected to insure that no hot buoyancy-driven flow from the flame would come into contact with the sensors. Thus, both sensors (non-windowed and windowed) were exposed to the same radiation-

only environment. Voltage data were collected for both windowed and non-windowed sensors in this configuration, the calibration fluxes were determined for both sensors ($q''_{cal,w}$ and $q''_{cal,nw}$), and the effective transmittance was determined by calculating the time-average of the ratio of the two magnitudes:

$$\tau = average \left(\frac{q''_{cal,w}}{q''_{cal,nw}} \right) \quad (5-4)$$

Using this method, the value of τ was determined to be 0.62. This value is derived from the mean of over 2000 measurements taken over 40 s, but due to instrument precision there is some uncertainty. A student's t -confidence interval gives 90 percent probability that the true mean lies between 0.57 and 0.67. Calculating the effective transmittance of the sapphire window allows for the determination of the radiation flux incident on the sensor array.

Substituting Eq. (5-2) into Eq. (5-3), and solving for the radiation incident on the outside of the sapphire window yields

$$q''_{rad,inc} = q''_{cal,w} / \tau \quad (5-5)$$

The heat flux absorbed by the non-windowed sensor is the sum of the incident radiant flux that is absorbed and the convective flux:

$$q''_{abs,nw} = \varepsilon q''_{rad,inc} + q''_{conv} \quad (5-6)$$

where q''_{conv} is the convective heat flux. Substituting Eqs. (5-2) and (5-5) into Eq. (5-6) yields

$$\varepsilon q''_{cal,nw} = \left(\varepsilon q''_{cal,w} / \tau \right) + q''_{conv} \quad (5-7)$$

Solving Eq. (5-7) for the convective heat flux yields

$$q''_{conv} = \varepsilon(q''_{cal,mw} - q''_{cal,w}/\tau) \quad (5-8)$$

The incident radiation and convection flux can be calculated from Eq. (5-5) and Eq. (5-8), respectively, as a function of the calibration heat flux determined from measurements using the non-windowed and windowed sensors. The convective heat flux values calculated in Eq. (5-8) are a strong function of the geometry of the sensor housing and should not be interpreted as what a fuel particle with a dissimilar geometry might experience. Despite this limitation, the data provide valuable information regarding the partitioning of convective and radiative flux in a wildland fire environment.

Because the fire environment is laden with particulate combustion products, the sapphire window was at risk to become fouled with products of incomplete combustion. Therefore, the window was continuously purged with two small battery-powered air pumps. One of the underlying assumptions of the analysis presented previously is that the two sensors are experiencing the same radiative flux environment. This requires that the sensors be positioned physically as close to each other as possible. However, there was risk that the air purge system would interfere with the non-windowed sensor. For this reason, the setup was tested by activating and deactivating the purge air while the sensors were exposed to excelsior flames to verify that when the purge air was active, the non-windowed sensor signal remained unperturbed. Through these tests, the purge air was determined to be both strong enough to keep the window clean and weak enough to ensure that the adjacent non-windowed sensor signal remained unaffected.

The battery powered pumps were buried, and the sensor package was placed on top of the pumps to protect them from the hot combustion gases. The air pumps were not

placed with the amplifiers and data loggers in order to prevent vibrations from affecting voltage measurements. Copper tubing was used to route the purge air from behind the sensor to the windowed sensor face.

The measurement uncertainty associated with the sensor setup was characterized by sampling noise before fire passed over the sensors. The voltages corresponding to each sensor were recorded and subsequently converted to corresponding values of radiation and convection heat flux. A total of 500 points were sampled, and the precision error associated with this test is estimated to be $\pm 0.17 \text{ kW/m}^2$ for radiation, and $\pm 0.13 \text{ kW/m}^2$ for convection with 99 percent confidence. The bias error associated with these measurements is minimized by adjusting the voltage output of the sensors at thermal equilibrium after amplification to a mean of zero.

Before the sensor package was positioned, the wind direction and slope (if any) were observed and the package was oriented facing the most likely direction of flame approach. Heat flux-activated videorecorders were trained on the instrumentation package. These cameras are described in Jimenez *et al.* (2007). In this way, the flame spread could be observed visually and compared to the radiation and convection heat flux data.

The flame spread toward the sensors roughly 60 percent of the tests. The flame spread laterally across the sensors for the remainder of the tests with the exception of one test where the flames spread directly toward the rear of the sensor package. There is one data set reported here that was neither observed nor filmed and thus the spread direction was indeterminate.

Data were taken under a variety of conditions. Table 5-1 shows a summary of the conditions, location and limited results of each data set. In total, twelve sets of heat flux

data were taken. Two data sets were taken on the Rombo Mountain fire in August 2007. The fuels in both of these burns consisted of mixed grasses and ponderosa pine (*Pinus ponderosa*) needle cast. The second burn also included some brush. Six data sets were taken in the Florida panhandle and southern Georgia. The intensity of these fires varied, but the fuels consisted primarily of longleaf pine (*Pinus palustris*) needle cast and mixed grasses. Fuel loading data were collected for five of six of the controlled burns in Florida and Georgia. Data were also captured from two crown fires in Montana, both in mature

Table 5-1. Summary of fire conditions, radiation heat flux peaks and convection heat flux peaks (shaded areas represent non-ideal flame spread)

Fire Name/ Date	Time of Day	Ground, Brush, Crown	Fuel*	Slope/ Wind	Flame Spread	Sample Rate (Hz)	1 s Moving Average Rad. Peak (kW/m ²)	Rad. Peak (kW/m ²)	Consumed Fuel Loading	Location/ elevation	Aspect
Rombo/ 28 Aug 07	1130	Ground	gr/pp nc	10°/none	Frontal	5 Hz	18.5	20**	Not Measured	N45.79417 W114.1350/ 1920m	NW
Rombo/ 29 Aug 07	1220	Brush	gr/br/pp nc	35°/none	Frontal	5 Hz	105.3	130**	Not Measured	N45.80144 W114.13649/ 1950m	S
Eglin AFB/ 1 Mar 08	0900	Ground	gr/lp nc/br	0°/ 0.5-1 m/s	Frontal	50 Hz	63.4	75	0.38 kg/m ²	N30.527639 W86.728139/ 40m	N/A
Ichawway/ 3 Mar 08	1330	Ground	gr/lp nc	0°/ 0.5-1 m/s	Frontal	50 Hz	77.1	115	0.28 kg/m ²	N31.201222 W84.443139/ 45m	N/A
Ichawway/ 5 Mar 08	1020	Ground	gr/lp nc	0°/ 0.5-1 m/s	Frontal	100 Hz	64.0	105	0.17 kg/m ²	N31.245833 W84.395333/ 50m	N/A
Ichawway/ 6 Mar 08 Burn 1	0920	Ground	gr/lp nc	0°/ 0.5-1 m/s	Frontal	100 Hz	64.1	90	0.57 kg/m ²	N31.249000 W84.479583/ 45m	N/A
Ichawway/ 6 Mar 08 Burn 2	1340	Ground	gr/lp nc	0°/ 0.5-1 m/s	Frontal	50 Hz	35.4	59	Not Measured	N31.249000 W84.479583/ 45m	N/A
Rat Creek/ 16 Aug 07	1320	Crown	gr/lp/lp nc	15°/none	Unkwn.	5 Hz	262.8	300**	Not Measured	N45.67907 W113.74894/ 2290m	SE
Mill Creek/ 30 Aug 07	1420	Crown	gr/lp/lp nc	<4°/none	Lateral	5 Hz	178.9	189**	Not Measured	N46.46460 W113.50946/ 1770m	E
Eglin AFB/ 2 Mar 08	1100	Ground	gr/lp nc	0°/ 0.5-1 m/s	Lateral	50 Hz	18.9	24	0.33 kg/m ²	N30.653028 W86.288639/ 65m	N/A
Leadore/ 20 May 08 Burn 1	0930	Brush	gr/sb	10°/ 0.5-1.5m/s shifting	Lateral	100 Hz	97.0	120	Not Measured	N44.81833 W113.29324/ 2315m	N
Leadore/ 20 May 08 Burn 2	1150	Brush	gr/sb	10°/ 0.5-1.5m/s shifting	Lateral	100 Hz	110.7	132	Not Measured	N44.81833 W113.29324/ 2315m	N

*gr=grass, pp=Ponderosa pine (*Pinus ponderosa*), lp=lodgepole, nc=needle cast, llp=long leaf pine (*Pinus palustris*), br=brush, sb=sage brush (*Artemisia tridentata* subsp. *Wyomingensis*)

** Values may be suspect due to sample rate

Lodgepole pine (*Pinus contorta*) forests with mixed grass ground cover. There were also two data sets taken in a sagebrush (*Artemisia tridentata* subsp. *Wyomingensis*) ecosystem just inside the Montana border near Leadore, Idaho. The details of these fires (both conditions and heat flux data) are discussed in detail below, grouped by fire spread direction relative to the sensor orientation. Once the details have been discussed some limited comparisons will be made between burns.

5.4. Results

5.4.1. Fires Manifesting Frontal Flame Spread

The first data set from the Rombo Mountain wildfire was taken on the morning of the 28 August 2007. The photograph in Figure 5.2 illustrates the data collection site photographically (N45.79417 W114.13509, 1920 m, northwest aspect, nominally 30 percent (10 degrees) slope) as well as the heat flux data. The fuels primarily consisted of mixed grasses and Ponderosa Pine (*Pinus ponderosa*) needle cast.

Figure 5.2a presents the radiation and convection flux data from the location shown in the photograph of Figure 5.2. These data were collected at 5 Hz. Radiation and convection both begin with a value of 0 kW/m². The sensors are engulfed in flames when the convection heat flux rises dramatically between 150 and 200 s into the burn. The radiation flux exhibits a peak of 20 kW/m². The convection fluctuates dramatically between 22 and -5 kW/m². Negative convective heat flux values can be explained by the presence of cool air surrounding the sensor after the sensor has been heated by positive radiant or convective heat flux. The radiation flux does not exhibit the significant fluctuations of the convection flux because radiation is sampled from the entire hemisphere

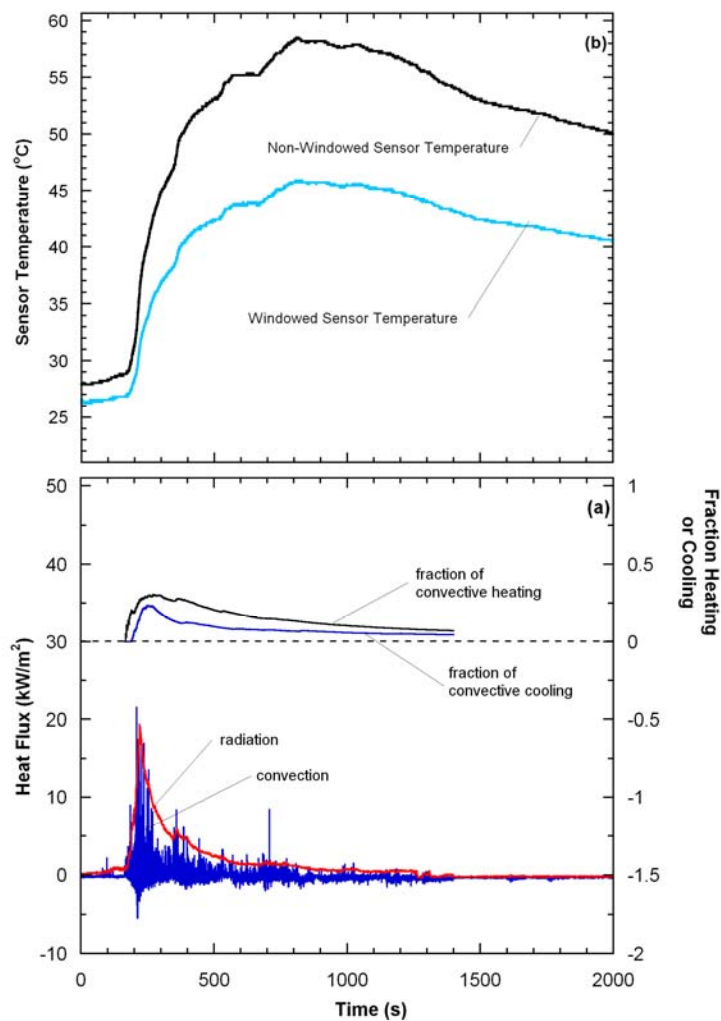


Figure 5.2. Rombo Mountain fire data 28th August 2007- Wind –none; Slope – 10 deg.; Fuel - grass and ponderosa pine needle cast. a - radiation and convection heat flux and fraction heating and cooling. b - sensor temperature.

viewed by the sensors, whereas convection is a local phenomenon. Thus, local fluctuations in flame conditions affect convection, but radiation samples multiple fluctuations of various magnitudes simultaneously and the integrated net effect leads to a relatively consistent heat flux. Strong convective fluctuations are characteristic to all the data sets included in this work.

Figure 5.2a also shows the fraction of time the convective flux exceeds 1 kW/m^2 (termed “fraction heating”) and falls below -1 kW/m^2 (termed “fraction cooling”), beginning at an arbitrarily assigned time when it was determined that the convection event had commenced. This parameter was devised in an attempt to characterize the positive and negative temporal fluctuations in convective flux, corresponding, respectively, to convective heating and cooling. This metric will be used to analyze all the heat flux data that were recorded under frontal flame spread conditions. Both the convective heating and cooling fractions peak within the first 100 s of the event, after which they both decline as the intensity of the combustion event subsides and the convection flux is predominantly zero.

Figure 5.2b shows the measured temperature history of both the windowed and the non-windowed sensors. The temperature rise of both sensors was no more than 30°C above ambient, which is typical of all the field burns. The temperature rise of the sensors is considered insignificant when compared to the combustion temperatures experienced in wildfires. The maximum sensor temperature of 58°C gives rise to a radiation emission error of no more than 0.68 kW/m^2 . Thus, it was concluded that the insulation was sufficient to prevent significant errors in the measurement.

A second set of heat flux data was taken on the Rombo Mountain fire at midday on 29 August 2007 (N45.80144 W114.13649, 1950 m elevation, south aspect, 45 percent (20 degrees) slope), and is shown in Figure 5.3. These data were also collected at 5 Hz. This fire also spread upslope and was significantly more intense than the fire whose data were presented in Figure 5.2.

The increased fire intensity can be primarily attributed to the presence of brush, a deeper bed of ponderosa pine needle cast, and a much steeper slope. No wind was observed during the burn. Radiation is detected from the oncoming flames 30 s before the flames arrive at the sensors. The air which is being drawn downslope into the flames convectively cools the sensors as they are heated by the radiation heat flux emitted from the flame. The flame arrives when the convection heat flux rises sharply at approximately 145 s. The convection heat flux shows a peak of 94 kW/m^2 and fluctuates, reaching values as low as -25 kW/m^2 . The radiation heat flux peaks at 130 kW/m^2 and fluctuates between 40 and 130 kW/m^2 .

Figure 5.3 also shows the fraction of time the convective flux is above 1 kW/m^2 and below -1 kW/m^2 . Initially, the amount of convective cooling drops as the flames arrive. Interestingly, the fraction of convective cooling rises as the heating fraction drops while the radiation and convection heat flux data appear to show that the flames are still vigorous. As the combustion event concludes, the sensor is exposed to relatively cooler air and the convective cooling fraction rises. The photograph included in Figure 5.4 was taken before a controlled burn on Eglin Air Force base in northern Florida on the morning of 1 March 2008 (N 30.527639° W 86.728139°, 40 m elevation, slope 0 degrees, 4 year southern rough). The term “southern rough” is used by fire managers to indicate

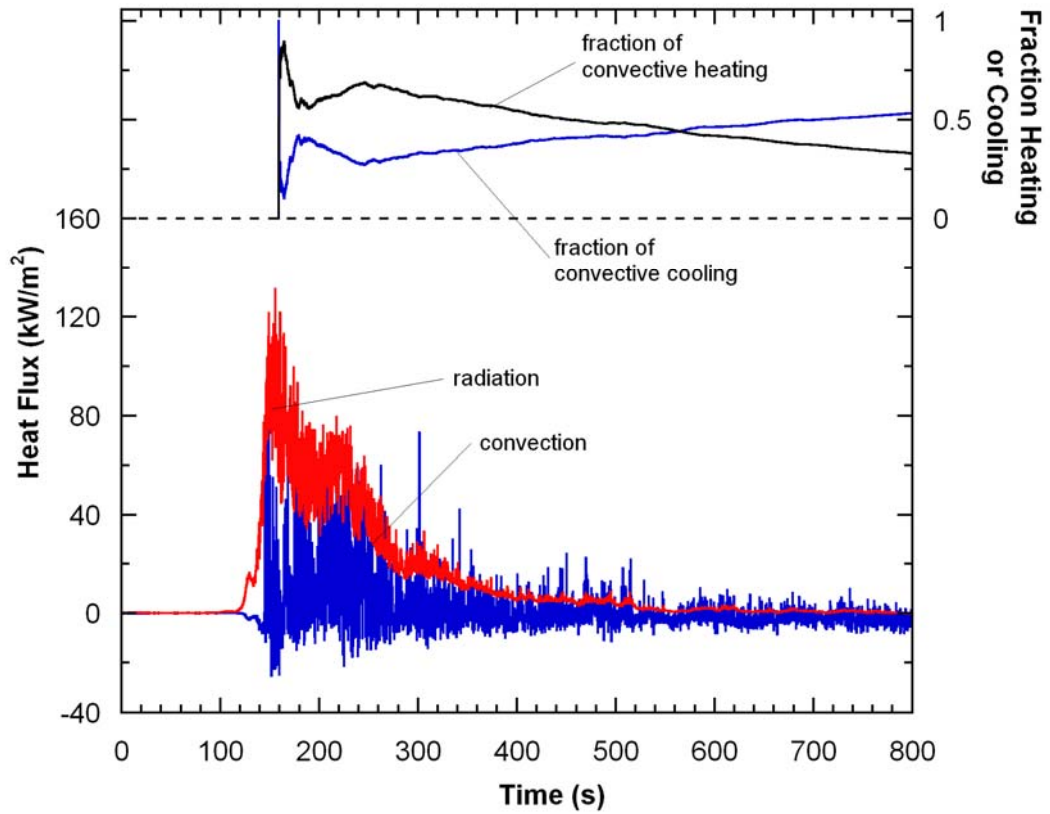


Figure 5.3. Rombo Mountain fire 29 August 2007 Wind –none; Slope -35 deg.; Fuel – grass, brush and ponderosa pine needle cast

how many years have elapsed since the site had been burned. As a reminder, the fuel bed consisted primarily of mixed grasses and Longleaf Pine (*Pinus palustris*) needle cast. Some brush was also present. The ground was flat and level, and there was a 0.5 - 1 m/s wind blowing toward the sensors. The consumed fuel loading was 0.38 kg/m².

Radiation and convection heat flux data from the site burn shown photographically in Figure 5.4 are presented in the bottom panel of Figure 5.4. These data were collected at 50 Hz. The radiation and convection peaks were, respectively, 75 kW/m² and 60 kW/m². Some of the convective peaks were quite brief, again owing to alternating packets of cold and hot air/combustion products. Figure 5.4 (bottom) also shows convective cooling/heating fraction plots. Convective heating occurs nominally 51 percent of the time and convective cooling occurs 13 percent of the time.

Data were collected from four controlled burns on the Joseph W. Jones ecological preserve owned by the Coca Cola Corporation in southern Georgia. The first burn (N 31.201222° W 84.443139° 45 m elevation, flat, 1 year southern rough) occurred on 3 March 2008. Figure 5.5 (top) shows a photograph of the fuel conditions on the day of the controlled burn, which had a consumed fuel loading of 0.57 kg/m². Again, the fuel bed consisted primarily of mixed grasses and Longleaf Pine (*Pinus palustris*) needle cast. There was no slope and a 0.5 - 1 m/s wind was observed blowing toward the sensor face.

The data had radiation and convection heat flux peaks at nearly the same level, 115 and 107 kW/m², respectively (shown in Figure 5.5, bottom panel). The intensity of this fire is manifested in the intensity of fluctuations on both the radiation and convection heat fluxes as well as the relatively high peak fluxes. The fraction heating/cooling plot included in Figure 5.5 show that convective heating prevails 76 percent of the time and

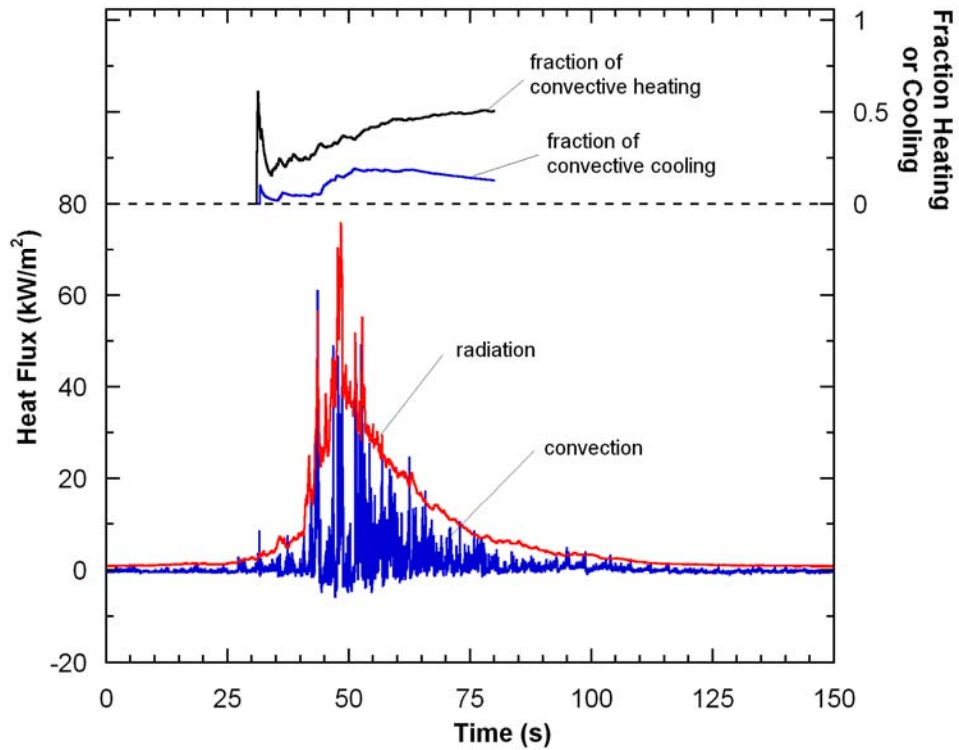


Figure 5.4. (Top) Eglin Air Force Base 1 March 2008 Wind – 0.5-1 m/s; Slope – 0 deg.; Fuel - grass and longleaf pine (*Pinus palustris*) needle cast. 4 year southern rough, consumed fuel loading 0.38 kg/m². (bottom) Heat Flux data

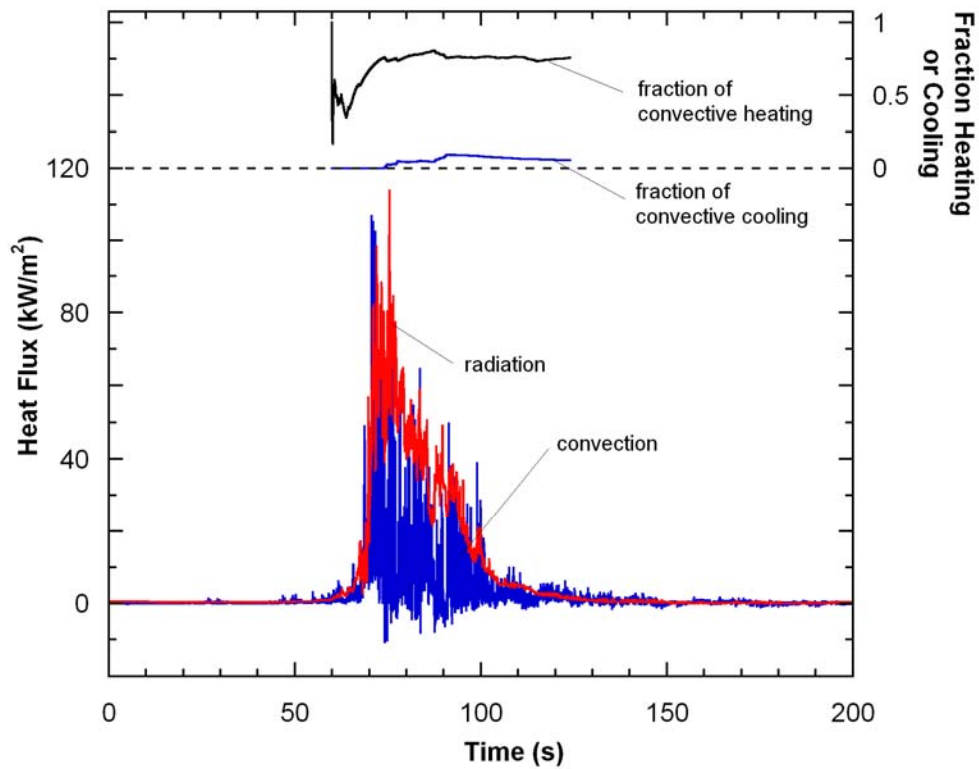


Figure 5.5. Ichauway 3 March 2008 Wind – 0.5-1 m/s; Slope – 0 deg.; Fuel - grass and longleaf pine (*Pinus palustris*) needle cast. 1 year southern rough, consumed fuel loading 0.57 kg/m². (bottom) Heat Flux Data

cooling prevails only 5 percent of the time. A photograph of the fuel conditions before the controlled burn (N 31.245833°, W 84.395333°, altitude 50 m, slope 0 degrees, 1 year southern rough) on the morning of the 5 March 2008 is shown in Figure 5.6. Again, the fuel bed consisted primarily of grass and Longleaf Pine (*Pinus palustris*) needle cast and the consumed fuel loading was 0.17 kg/m². There was no slope and only a 0.5 - 1 m/s wind was blowing toward the sensor face.

The radiation and convection heat flux data (taken at 100 Hz) are shown in Figure 5.6 (bottom panel). This fire also spread vigorously as evidenced by the relatively high radiative and convective heat flux peak values of 105 and 100 kW/m², respectively. The fraction heating/cooling plots included in Figure 5.6 show that the convection event heated 54 percent of the time and cooled 17 percent of the time.

The data shown in Figure 5.7 were collected on the morning of 6 March, 2008 at a controlled burn (N 31.249000°, W 84.479583°, 45 m altitude, slope 0 degrees, 2 year southern rough) similar to that of Figure 5.5, with the exception that there was more brush present. The consumed fuel loading was 0.28 kg/m². These data were sampled at 100 Hz. The convection peak heat flux of 140 kW/m² was far greater than the radiation heat flux peak of 90 kW/m². The fraction heating/cooling plots included in Figure 5.7 show that the convection heated 44 percent of the time and cooled 14 percent of the time.

Figure 5.8 shows heat flux data collected in the afternoon of the same day with similar fuel density to the conditions of Figure 5.7. These data were collected at a sampling rate of 50 Hz. The wind had subsided. Once again, convective peaks are very brief. The peak heat flux was 82 kW/m² in convection and 59 kW/m² in radiation. The

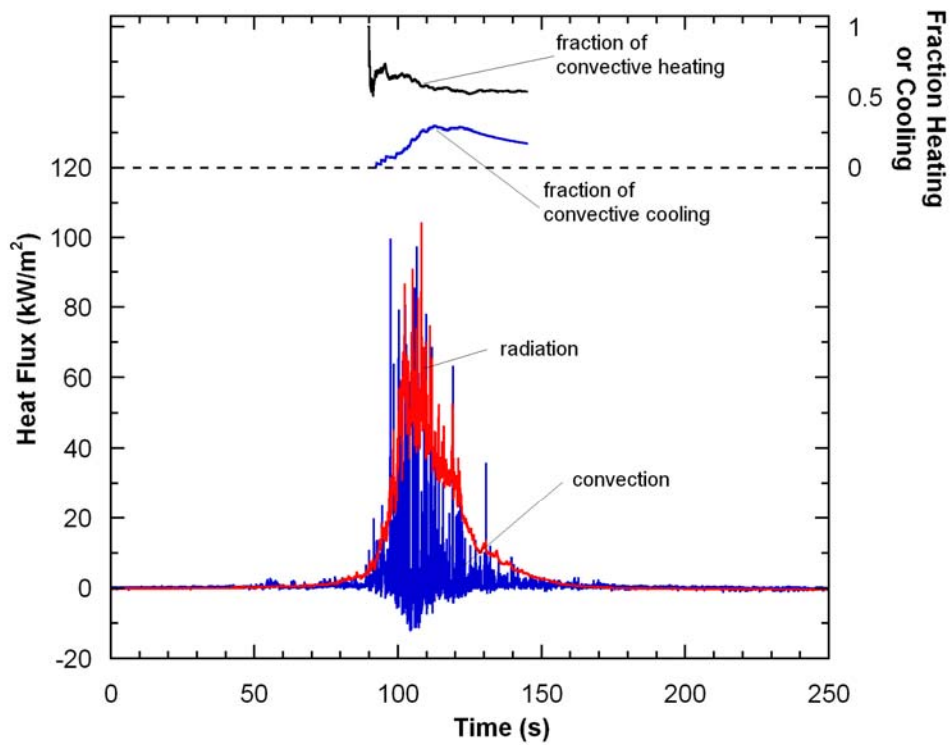


Figure 5.6. Ichauway 5 March 2008 Wind – 0.5-1 m/s; Slope – 0 deg.; Fuel – grass and longleaf pine (*Pinus palustris*) needle cast, 1 year southern rough, consumed fuel loading 0.17 kg/m² (bottom) Heat Flux Data

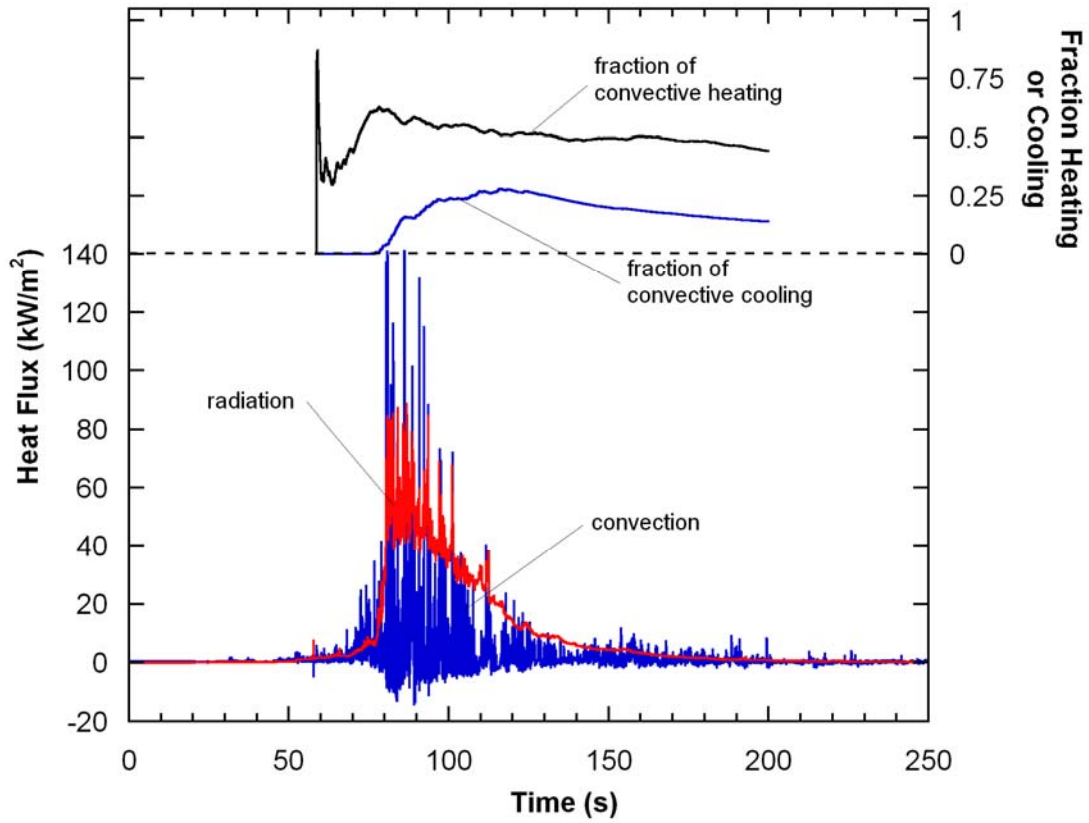


Figure 5.7. Ichauway 6 March 2008 (Burn 1) Wind – 0.5-1 m/s; Slope – 0 deg.; Fuel - grass and longleaf pine (*Pinus palustris*) needle cast, 2 year southern rough, consumed fuel loading 0.28 kg/m².

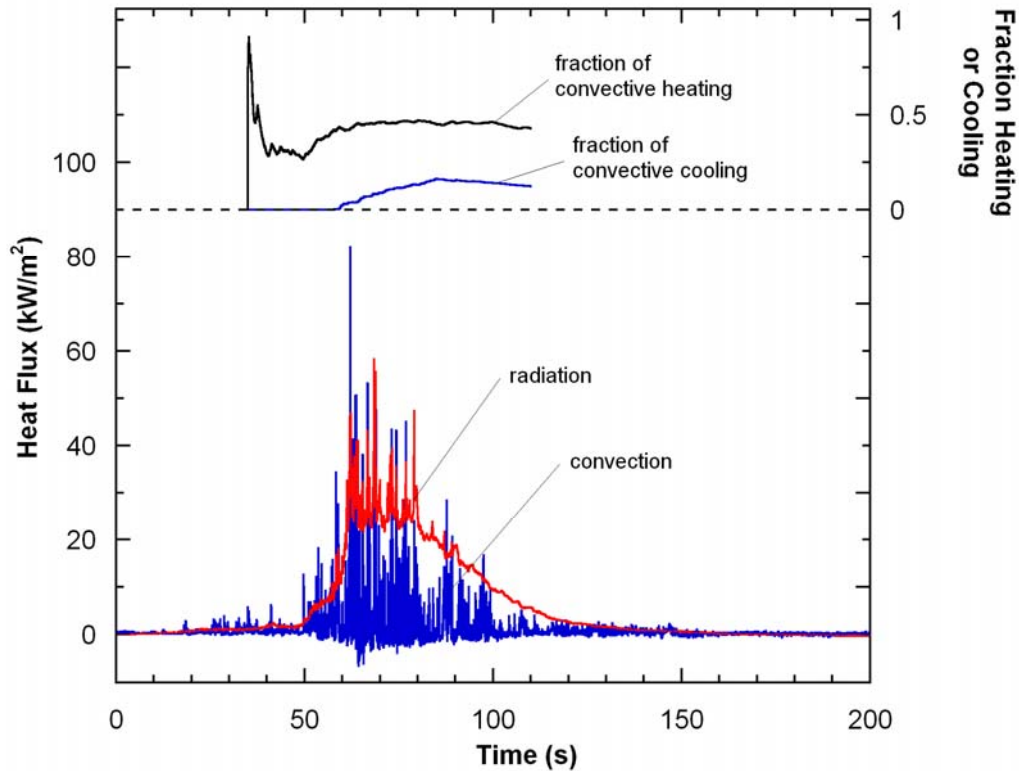


Figure 5.8. Ichauway 6 March 2008 (Burn 2) Wind –none; Slope – 0 deg.; Fuel - grass and longleaf pine (*Pinus palustris*) needle cast, 1 year southern rough, consumed fuel loading unknown.

fraction plots included in Figure 5.8 show that the convection heated 43 percent of the time and cooled 12 percent of the time.

5.4.2. Fires Manifesting Non-frontal Flame Spread

The remainder of data presented come from conditions where the fire did not spread directly toward the sensor package. The top panel of Figure 5.9 shows an instrument package deployment site (N45.67907 W113.74894, 2290 m elevation, southeast aspect, 33 percent (15 degrees) slope) before a crown fire occurring on the Rat Creek Fire approximately 14 miles west of Wisdom, Montana on the afternoon of the 16 August 2007. The fuel was mature Lodgepole Pine (*Pinus contorta*). These data were taken at a

sampling rate of 5 Hz. For safety reasons, no photographic record was made of this burn. As a result, it is impossible to determine which direction from which the fire came.

The sensors for this particular data set were extended to 1.5 m off the ground. The crown fire was violent enough to topple the sensor package. The collected heat flux data are shown in Figure 5.9 (bottom panel). The maximum measured radiation heat flux was 300 kW/m². After this incident all the data are taken 0.3 meters from the ground to avoid damage to sensors. The convection heat flux appears to be low (42 kW/m²) in this data set when compared to the radiation. It is unclear whether this convection profile resulted from the height of the sensor or the fire spread direction relative to the sensor. In either case, these radiation data have a magnitude similar to the data of Butler *et al.* (2004), which were also taken in a crown fire environment.

Convection and radiation heat fluxes were recorded at a fire in the Mill Creek drainage (N46.46460 W113.50946, 1770 m elevation, east aspect, 0-10 percent (0-5 degrees) slope) in Montana on the afternoon of the 30 August 2007. A photograph of the fuel conditions prior to the burn is included in Figure 5.10. The sensors were placed in an area with little or no wind and very little slope. The fuel consisted of mixed grasses and lodge pole pine needle cast with a crown of Lodgepole Pine (*Pinus contorta*) trees. The data were collected at a sampling rate of 5 Hz.

The video confirmed that the fire approached the sensors laterally instead of toward the front. It is interesting to note that these data (shown in the bottom panel of Figure 5.10) show both a ground fire (at 750 s) and a crown fire (at 1600 s) as distinct peaks. The radiation peaked at 26 kW/m² for the ground fire, and 189 kW/m² when the crown

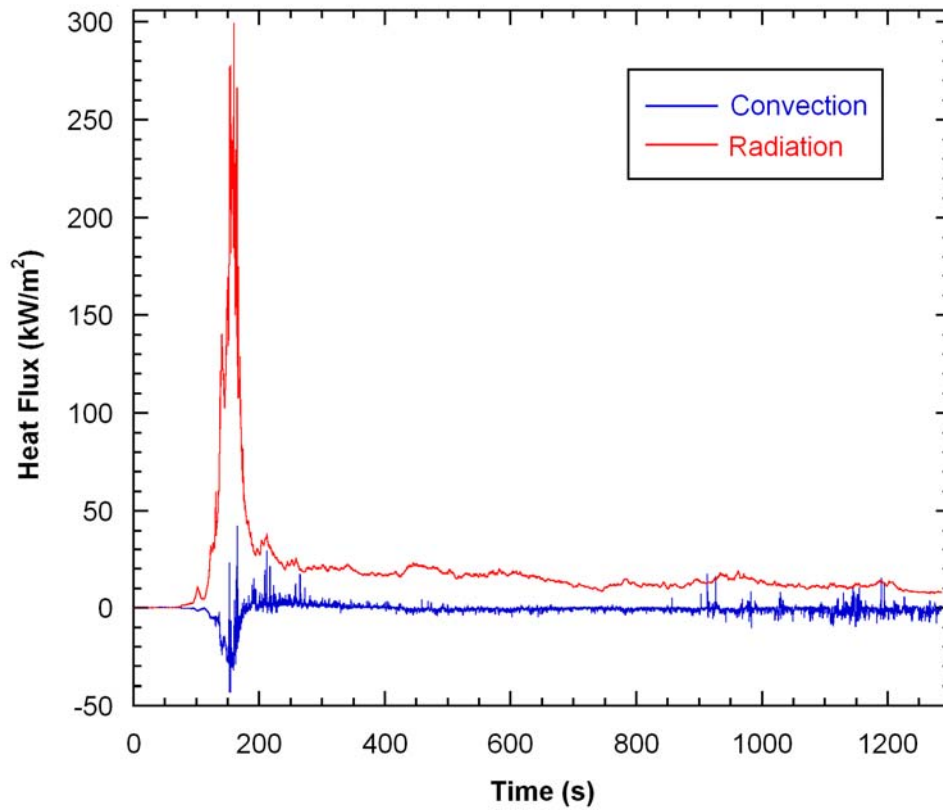


Figure 5.9. Rat Creek Fire 16 August 2007 – Wind –none; Slope - not measured but steep; Fuel - Lodgepole pine (*Pinus contorta*), grass and needle cast (bottom) Heat Flux Data

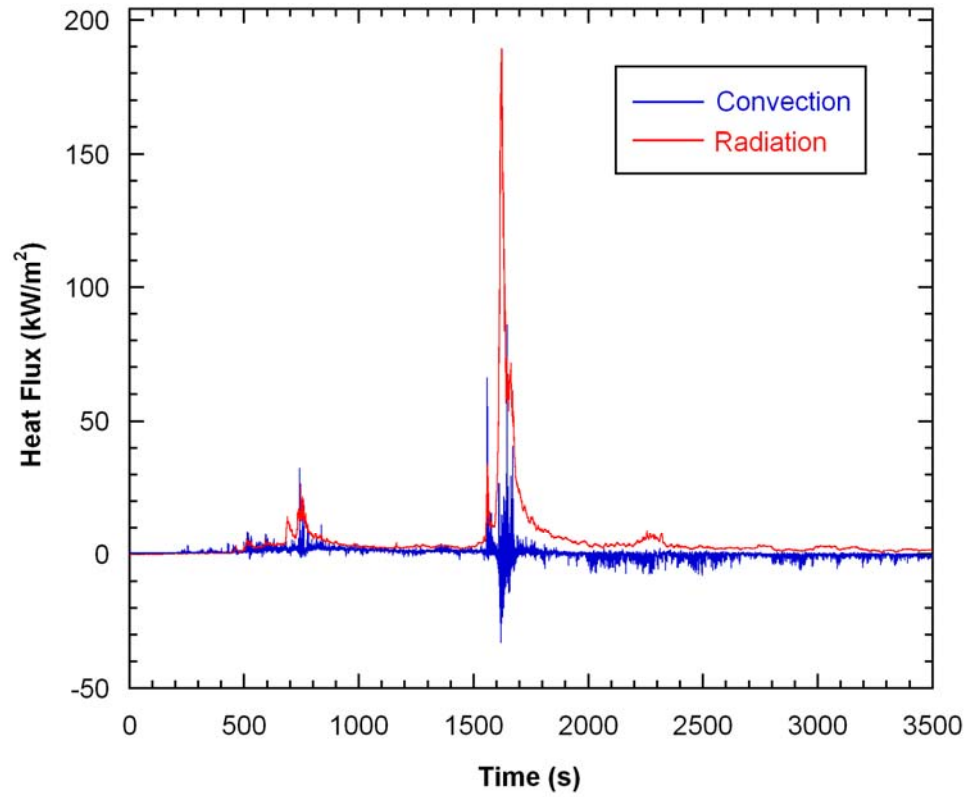


Figure 5.10. Mill creek crown fire 30 August 2007 Wind –none; Slope – 4 deg.; Fuel - Lodgepole pine (*Pinus contorta*), grass and needle cast. (bottom) Heat Flux Data

fire arrived at the sensors. The peak convection heat flux was 32 kW/m² for the ground fire and 86 kW/m² for the crown fire.

A controlled burn on Eglin Air Force Base (N 30.653028°, W 86.288639°, 65 m altitude, slope 0 degrees, 1 year southern rough) was instrumented with heat flux sensors on the morning of the 2 March 2008. These data were collected at 50 Hz and are presented in Figure 5.11. Palmetto plants were present, but the fire was not vigorous enough to ignite them (picture shown in Figure 5.11 - top) and the consumed fuel loading was 0.33 kg/m². There was a 0.5-1 m/s wind blowing toward the sensor face. Furthermore, the flames approached the sensors from behind. The peak heat flux reached 24 kW/m² in radiation and 13 kW/m² in convection.

The two sets of heat flux data near Leadore, Idaho (N44.81833 W113.29324, 2315 m elevation, north aspect, nominally 20 percent (10 degrees) slope) were taken on the morning of May 20, 2008 and are shown in Figure 5.12. These data were collected at 100 Hz. The fuel type was sagebrush (*Artemisia tridentata* subsp. *Wyomingensis*) and mixed grasses. There terrain slope was not measured, and there was a 0.5 - 1.5 m/s wind present that shifted directions intermittently throughout the burn. The fire approached the sensors laterally during the collection of both data sets. This is likely the cause of the extremely low convection peak values (26 kW/m² and 19 kW/m²). The radiation heat flux values peaked at 120 kW/m² and 132 kW/m².

5.4.3. Discussion of Results

The field heat flux data presented here does not lend itself well to comparisons between one condition and another, since the burn conditions vary so widely. Factors

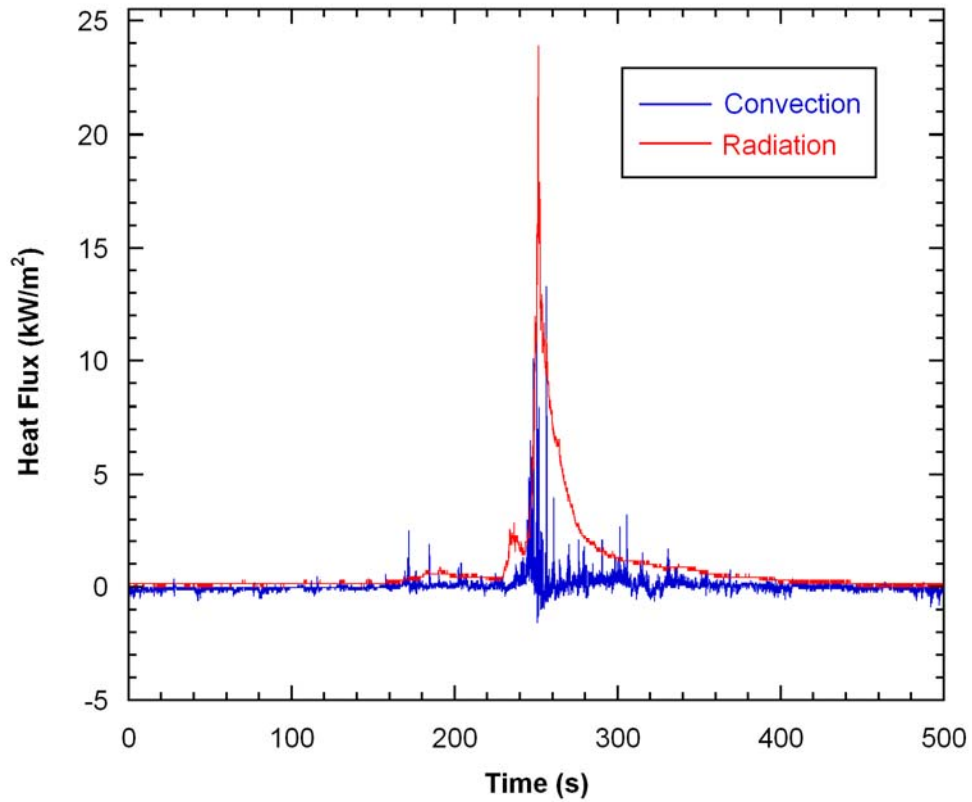


Figure 5.11. Eglin Air Force base 2 March 2008 Wind $-0.5-1.5$ m/s; Slope -0 deg.; Fuel - grass and longleaf pine (*Pinus palustris*) needle cast, 1 year southern rough, consumed fuel loading 0.33 kg/m²

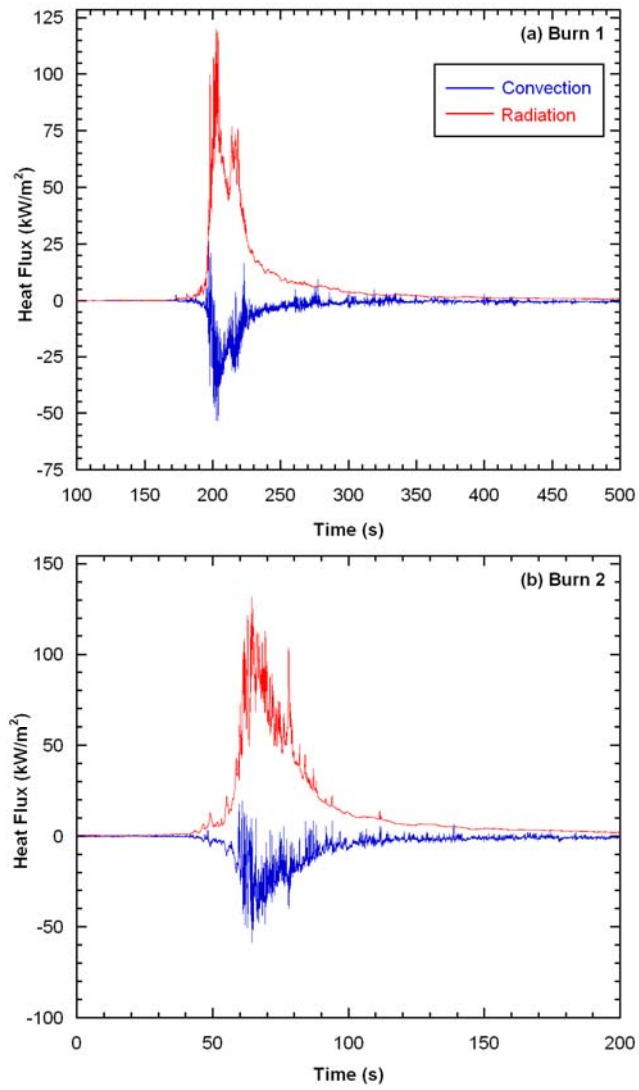


Figure 5.12. Leadore; Wind – 0.5-1.5 m/s; Slope – unmeasured but present; Fuel – Sage brush (*Artemisia tridentata* subsp. *Wyomingensis*) and Grass.

which affect wildfire intensity include, but are not limited to time of day, relative humidity, consumed fuel loading, fuel type, terrain slope and aspect, wind, solar radiation, and fuel geometry/arrangement. Even with the inclusion of these data into the archival literature, the available data are still quite limited and making comparisons between fires is difficult. However, some general comparisons and observations may be offered here.

These temporally resolved radiation and convection heat flux data have been acquired at the highest frequency of any study to date. However, after more closely inspecting these data by the use of a Fast Fourier Transform (FFT) it was observed that the convection heat flux data could not be fully resolved even at a sampling rate of 100 Hz. Radiation transfer data, however, were shown to be fully resolved using sampling frequencies at or above 40 Hz. This had never been previously investigated, and is discussed thoroughly in Chapter 6. This is not to say that these data are not of use. The Vattell sensors used in the collection of the data have a 3000 Hz frequency response (Vatell, 2007). Therefore, while the convection heat flux data were not fully resolved in the time domain, the data captured represents actual values of convective and radiative heat flux in these fires. Therefore, the data as a whole are representative of the conditions existing in the fire with the caveat that radiation (sampled below 40 Hz) or convection (sampled below 200 Hz) heat flux peaks may not be confidently compared because one data set may have faithfully sampled maximum heat flux values and the other may not have. For this reason, convection heat flux data are reported in spite of limitations resulting from sample rates too slow to fully adequately resolve the temporal data. Radiation heat flux, however, is fully resolved in 8 of 12 of the data sets. The remaining 4 data sets, which were sampled at 5 Hz, can be compared to data sampled at higher rates. Chapter six will

show that a 1 second moving average and a cumulative heat flux may be used to compare data sampled at a different rate. The 1 s moving average of radiation heat flux is shown in Figure 5.13 and the 1 s moving average convective heat flux is shown in Figure 5.14.

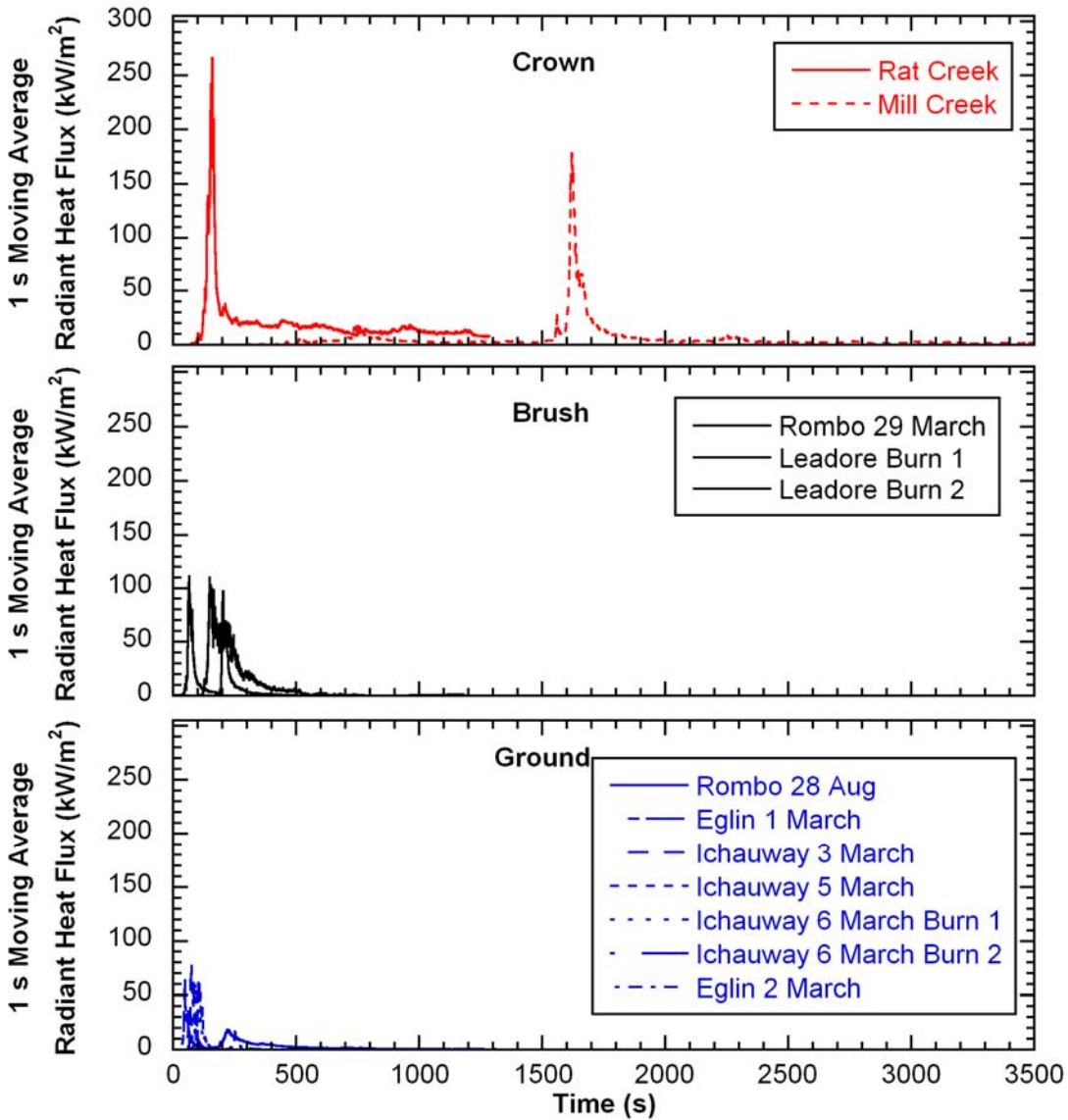


Figure 5.13. 1 s moving average radiant heat flux for all data sets

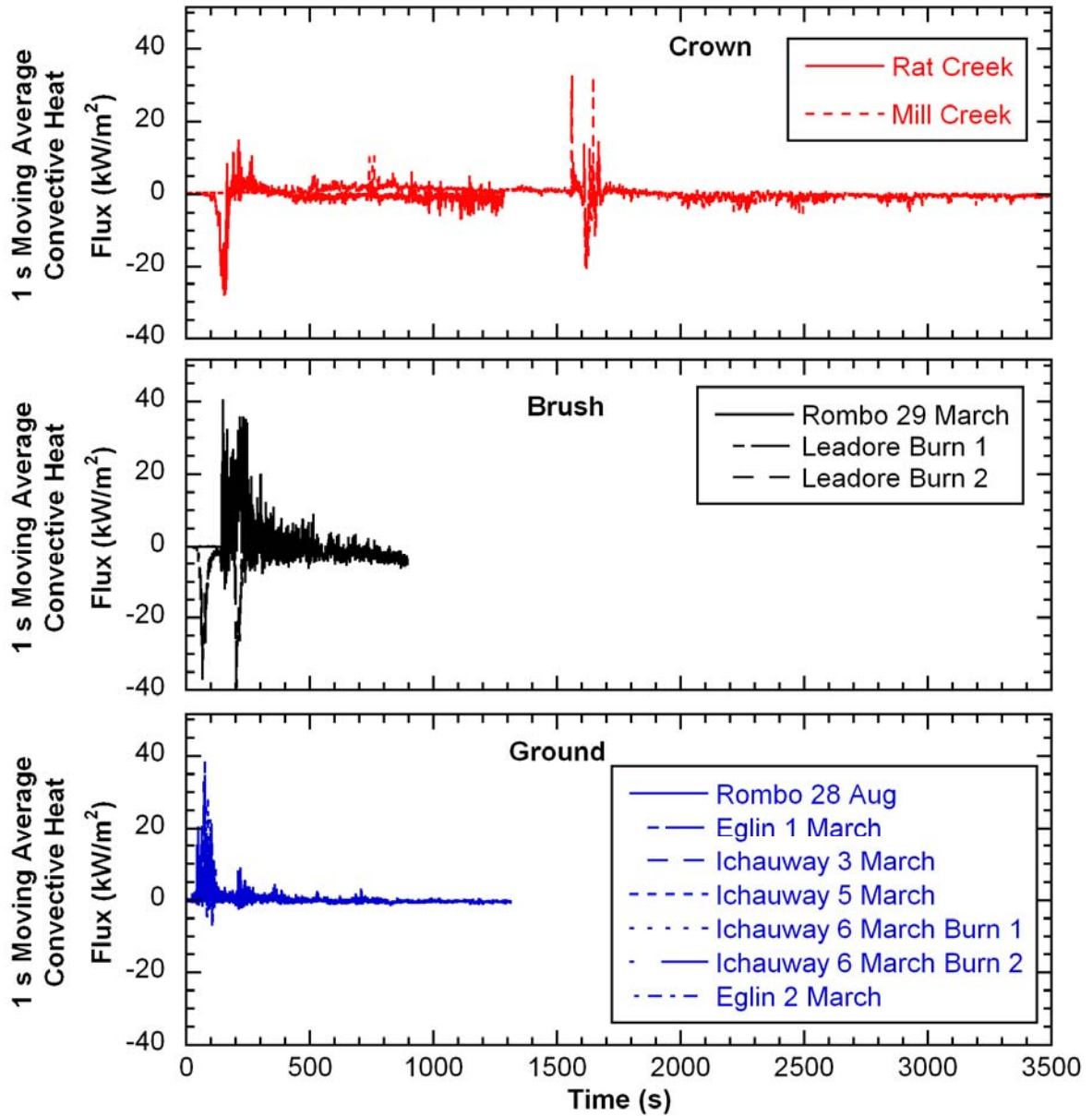


Figure 5.14. 1 s moving average convection heat flux for all data sets

One observation which points to the validity of the data taken is the comparison of the 1 s moving average radiation heat flux between ground, brush, and crown fires. These data reveal that the magnitude of time-averaged radiation heat flux peak for ground fires falls between 18.5 and 77.1 kW/m², brush fires between 97.0 and 110.7 kW/m², and crown fires between 178.9 and 262.8 kW/m². It may thus be concluded that radiation

transfer is intensified as the fuel environment classification proceeds from ground fuels, to brush conditions, and crown/canopy combustion. The moving average of convection heat transfer (Figure 5.14) shows that as the classification of the fire moves from ground to brush to crown, the moving average convective heat flux maximum is only effected slightly while the minimum decreases with increasing fire intensity. This may be explained by the fact that the sensors will heat up more in fires with greater radiant intensity and thus when they come into contact with cooler air, the effect is a lower minimum convective heat flux.

This can be further verified by the use of the instantaneous cumulative radiative and convective heat flux, (again, which will be shown in chapter 6 to be independent of sample rate). The cumulative heat flux quantifies the total radiative and convective heat flux over the combustion event. The cumulative heat flux was calculated by integration, using the trapezoidal rule, of the flux from a time corresponding to its first increase with the start of the combustion event to an arbitrary time t . The cumulative radiant and convective heat flux is shown in the top and bottom of Figure 5.15, respectively. Each plot is divided into ground, brush, and crown fires by color. Further, shaded areas show the respective regimes of ground, brush and crown fires. The cumulative radiant flux is rather well behaved with distinct magnitudes for each fire regime with the exception of one ground fire taken in the Rombo mountain fire on 28 August 2007. This is not surprising as there will be some overlap due to conditions such as wind, fuel loading, and slope which are not exclusive to ground, brush, or crown fires. The cumulative convective flux shows different behavior than does the cumulative radiant heat flux. Each successive increase in fire intensity from ground to brush to crown appears to result in higher or lower

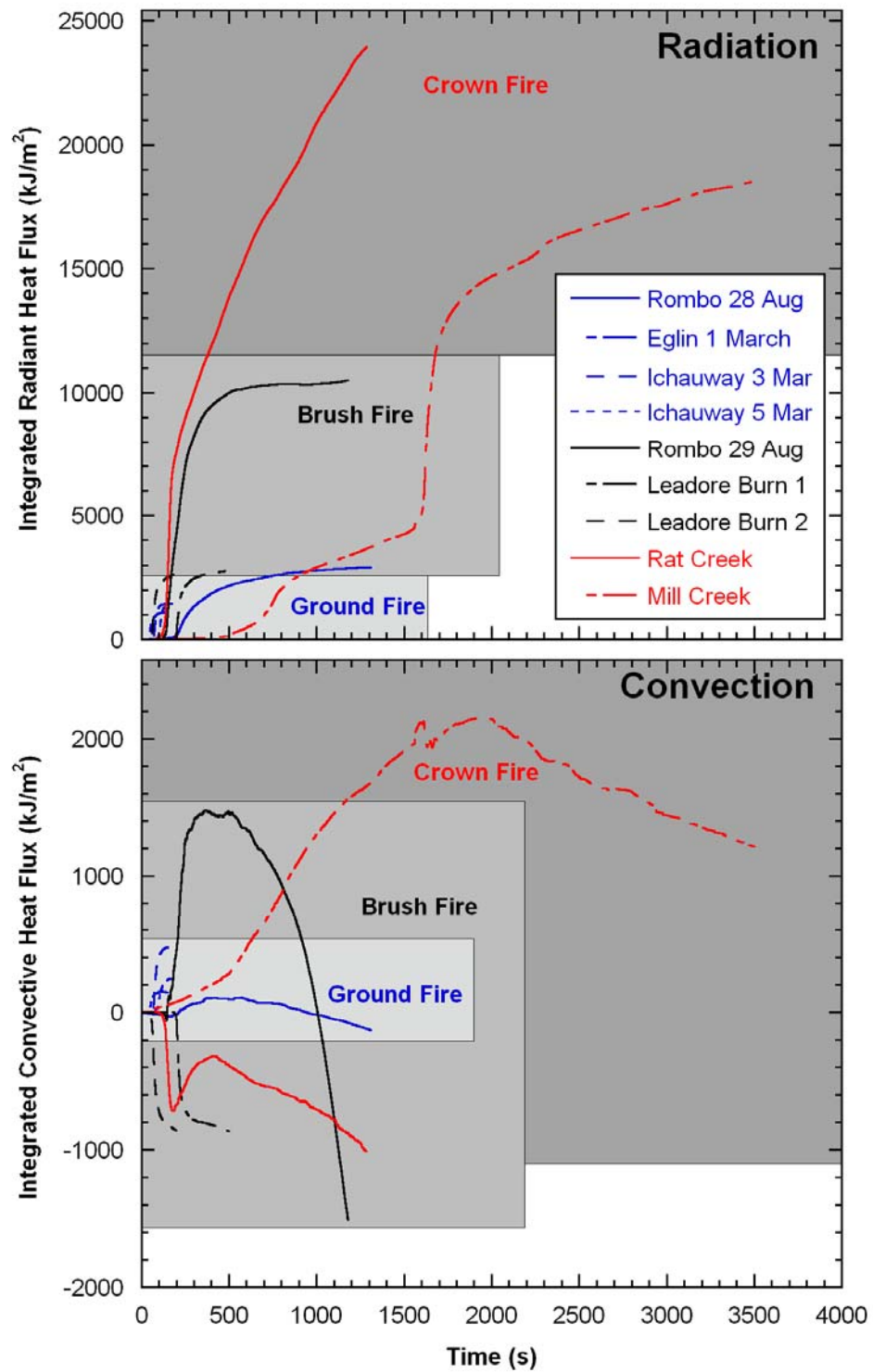


Figure 5.15. Instantaneous cumulative radiation (top) and convection (bottom) heat flux for selected ground fires, brush fires and crown fires.

cumulative convective heat flux. This behavior is explained by increased radiant intensity and the accompaniment of hot combustion products or a relatively cool inflow of air. A fire of greater intensity, such as a crown fire, may produce more and hotter combustion products. However, such a fire also requires more air to complete the combustion process, causing a faster inflow of relatively cool air. Thus, sensors placed in fires of greater intensity may either experience a greater or lesser cumulative convective heat flux than a less intense fire.

5.5. Conclusions

A variety of fuel types, slopes, and fire conditions yield a range of radiation and convection heat fluxes that is necessary for a clearer understanding of fire behavior. Some of the data presented here were collected under conditions where the flame approached the sensor from non-frontal directions. It is likely that the convection heat transfer is affected by these flame spread directions. The radiation heat flux magnitudes, however, may be unaffected. Under ideal flame spread conditions, the data presented here shows that radiation heat fluxes peak between 20 and 130 kW/m². Convective heat fluxes can have the effect of either heating or cooling, and the convection heat flux peaks between 22 and 140 kW/m² (under ideal flame spread conditions). The radiation heat fluxes from crown fires are considerably higher, but these particular crown fires did not spread directly toward the sensors. However, the radiation heat flux magnitudes are supported by data reported in other studies. The convection heat flux is characterized by rapid temporal fluctuation between positive and negative convection values owing to alternating packets of cool air intermingled with hot combustion products.

6. Fuel Response to Rapid Heating Fluctuations in Wildland Fires – Measurement and Analysis

6.1. Abstract

Time-resolved radiation and convection heat flux histories were collected on a controlled wildland burn at a sampling frequency of 500 Hz. The data reveal relatively modest temporal fluctuations in the radiation heat flux. However, short-duration peaks in convective heat flux were observed. Frequency content in the radiant flux as high as 20 Hz and in the convection heat flux up to 100 Hz was revealed by a Fast Fourier Transform of the time-series signals. The effect of sampling frequency on measured convective and radiative heat flux is explored, and it is asserted that traditional sampling frequencies below 50 Hz and 120 Hz, respectively, may be insufficient to fully resolve temporal fluctuations in radiation and convection heat flux. The role of the higher frequency convective content in fuel thermal response is explored using a one-dimensional transient conduction model with a convective boundary condition. It is shown that high-frequency (*i.e.*, short-duration) convective pulses can lead to fine fuel ignition.

6.2. Introduction

Radiation and convection heat transfer play complementary roles in forest fires (Anderson, 1969). The relative contribution of radiation and convection to ignition in

wildland fires is not well understood. Further, understanding of how these heat transfer mechanisms interact and contribute to thermal injury to plant living tissue and subsequent plant mortality is not well-developed (Jones *et al.*, 2004). To better understand these heat transfer phenomena direct measurement in wildfires is necessary. Unfortunately, few heat flux measurements have been reported from field burns. Butler *et al.* (2004) presents temporally resolved radiant heat flux measurements collected at a sampling frequency of 1 Hz from Boreal forest crown fires at various heights. Measured peak radiant heat fluxes averaged 200 kW/m^2 with a peak value of 290 kW/m^2 . It was shown, by comparing thermocouple measurements to narrow angle radiometer measurements, that using thermocouples to calculate heat fluxes is difficult and in many cases impossible. Morandini *et al.* (2006) measured time-resolved radiant heat fluxes at 5, 10 and 15 meters from the flame front on a test fire in south Corsica (France). Radiant heat fluxes measured in this study were between 7 and 8 kW/m^2 . These data were sampled at 100 Hz, and a frequency analysis was performed using a Fast Fourier Transform (FFT). There was no indication of the frequency response of the sensor; therefore it is difficult to interpret the findings. Silvani and Morandini (2009) measured radiant and total heat fluxes on a fire in southern France. These data were sampled at 1 Hz and exhibited peak radiation heat flux values of 50 kW/m^2 and a total (convection + radiation) heat transfer peak of 110 kW/m^2 . These two heat flux measurements and a thermocouple temperature measurement were then used to estimate possible convection coefficients, but measured convection heat flux was never discussed directly.

To the knowledge of the authors, no previous studies have measured time-resolved radiation and convection heat flux in the field. Further, no studies have at-

tempted to characterize fully the temporal fluctuations in convection and radiation heat transfer. This study presents time-resolved radiation and convection heat flux data collected in a wildland fire environment. The spectral content of the radiation and convection heat flux is examined using a Fast Fourier Transform. The time-resolved data are used to determine the effect of sample rate on the measured temporal convective and radiative heat flux, which is accomplished by selectively sampling a reduced number of points from the original data set in order to simulate a reduction in sample rate. Through the FFT and the simulated reduced sample rate, the presence of short duration convective peaks is discovered. The impact of short-duration convective pulses on fuel thermal response time to ignition as a function of the size of the vegetation particle receiving the energy, the intensity of convection heat transfer, and the thermophysical properties of the particle is explored through application of an analytical model. Findings have direct application to fire modeling and fire-induced plant mortality modeling research efforts.

6.3. Measurement and Calibration Procedure

The measurement and calibration procedure is described in detail in chapter 5. Briefly, a sensor package including two thin-film-based thermopile heat flux sensors with corresponding amplifiers and a data logger were placed in the path of a controlled burn. The sensor package was thermally insulated to prevent damage to the amplifiers, data logger and sensors leaving only the sensor faces exposed to the wildfire environment. One sensor was covered by a 0.5 mm diameter sapphire window which limited the collection of the sensor to only radiant energy after some quantified loss in transmission through the window. The second sensor was left exposed to both radiation and convec-

tion. The sensors were Vatell HFM 7 heat flux micro-sensors (Vatell, 2007). These sensors are 6 mm in diameter, coated with a highly absorbent coating ($\varepsilon = 0.94$), and exhibit a 300 μs response time (frequency response > 3000 Hz). They are calibrated to provide radiation and convection heat flux (see chapter 5). An isolated electrical ground system and shielded wiring were used to minimize sensor and datalogger vulnerability to ambient electrical noise. Two battery-powered air pumps provided clean air flow over the windowed sensor to reduce deposition of soot and ash particles on the window during the fire event. Sensor outputs were sampled using a Campbell Scientific CR5000 datalogger which has a 16-bit analog-to-digital converter and a maximum sampling rate of 1667 Hz.

Data were collected on a management-ignited burn conducted on 2 October 2008 near Sula, Montana (location 45.919017N 113.743133W). The site had a southeast aspect, an elevation of 1518 m and a 20 percent (9 degrees) slope. Immediately prior to and during the fire event a 0.5 - 1 m/s wind was blowing uphill. The fuels primarily consisted of mixed grasses and ponderosa pine (*Pinus ponderosa*) needle cast. The sensor package was positioned facing downhill such that the fire would spread directly toward the sensors. The radiation and convection heat flux data were sampled simultaneously at a sampling frequency of 500 Hz.

The error for these experiments was estimated after the data were collected by analyzing 5000 heat flux noise measurements before the controlled burn commenced, and while the sensors were exposed to ambient conditions. A Student's t -confidence interval gives 99 percent probability that the error associated with these measurements is less than 0.32 kW/m². The data taken before the combustion event were also used to establish the

base power spectrum of the sensed signal which is a function of the experimental setup. The noise power spectrum will be discussed in more detail later.

6.4. Heat Flux Data Collection

Two sets of radiation and convection heat flux data, which will be hereafter called Burn 1 and Burn 2. Figure 6.1 is a photograph taken as the fire burned over the sensors during Burn 1.



Figure 6.1. Photograph of flames passing over data collection setup.

The temperature history of the windowed and non-windowed sensors during Burn 1 is shown in Figure 6.2b. The sensors begin to heat as the flame front approaches the sensor package. However, the thermal insulation prevented the sensor temperature from

rising more than 6°C above ambient. This temperature rise results in a radiation error of no more than 0.4 kW/m².

Figure 6.2a shows the radiation and convection heat flux history of Burn 1. Both radiation and convection begin at a value of 0 kW/m². The radiation heat flux exhibits significantly less fluctuation than the convection signal which is characterized by short

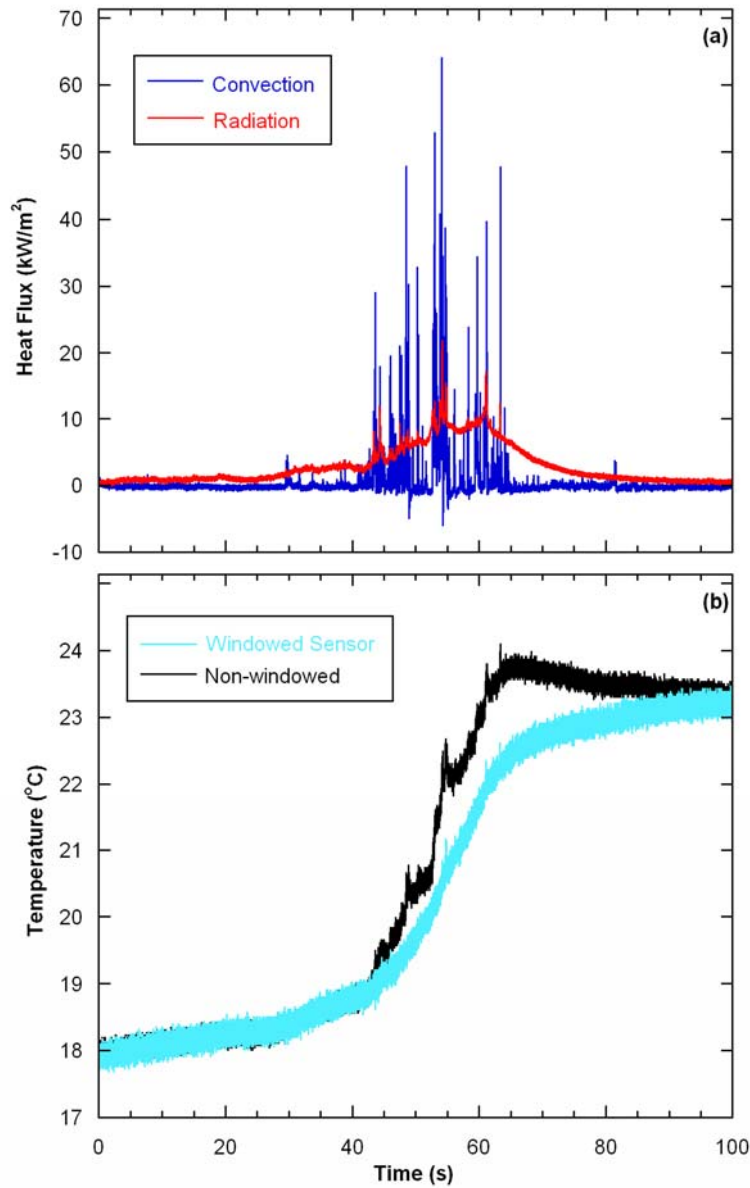


Figure 6.2. Heat flux and sensor temperature history for Sula, MT Burn 1.

duration positive and negative convective pulses. The positive convective heat fluxes are caused by “parcels” of hot air/combustion products passing over the sensor face. Negative convective values are caused by the sensors coming into contact with “parcels” of cool air after the sensors have been heated by radiative and convective heat fluxes.

Figure 6.3a shows the entire Burn 1 event, Figure 6.3b shows all of the major convective events, and c displays a single convective pulse of duration approximately 0.05 s and peak magnitude of 50 kW/m². This pulse is representative of others observed in the time series. The radiation heat flux in this burn event peaks at 22 kW/m² and the convection heat flux peaks at 64 kW/m². Radiation begins to rise almost monotonically at a time of 15 s. Major convection events do not begin until a time of 40 s.

Figure 6.4 shows the radiation and convection heat flux sampled in Burn 2 from a different location. The format of this plot is similar to Figure 6.3; Figure 6.4a shows the entire event, Figure 6.4b shows some of the major convective peaks, and Figure 6.4c highlights a few selected convective heating pulses with various durations and magnitudes. Radiation is seen to rise monotonically, but is detected almost simultaneously with some minor convective peaks. The radiation heat flux in this burn event peaks at 50 kW/m² and the convection heat flux peaks at 110 kW/m².

The overall intensity and duration of Burn 2 (Figure 6.4) is greater than that of Burn 1 (Figure 6.3). However, in spite of the radiation and convection heat flux magnitude differences, rapid convective pulses are present in both events. As mentioned earlier, the presence of these peaks raises questions regarding the sampling rate needed to accurately resolve the temporal fluctuations, the frequency content of the heat flux signal,

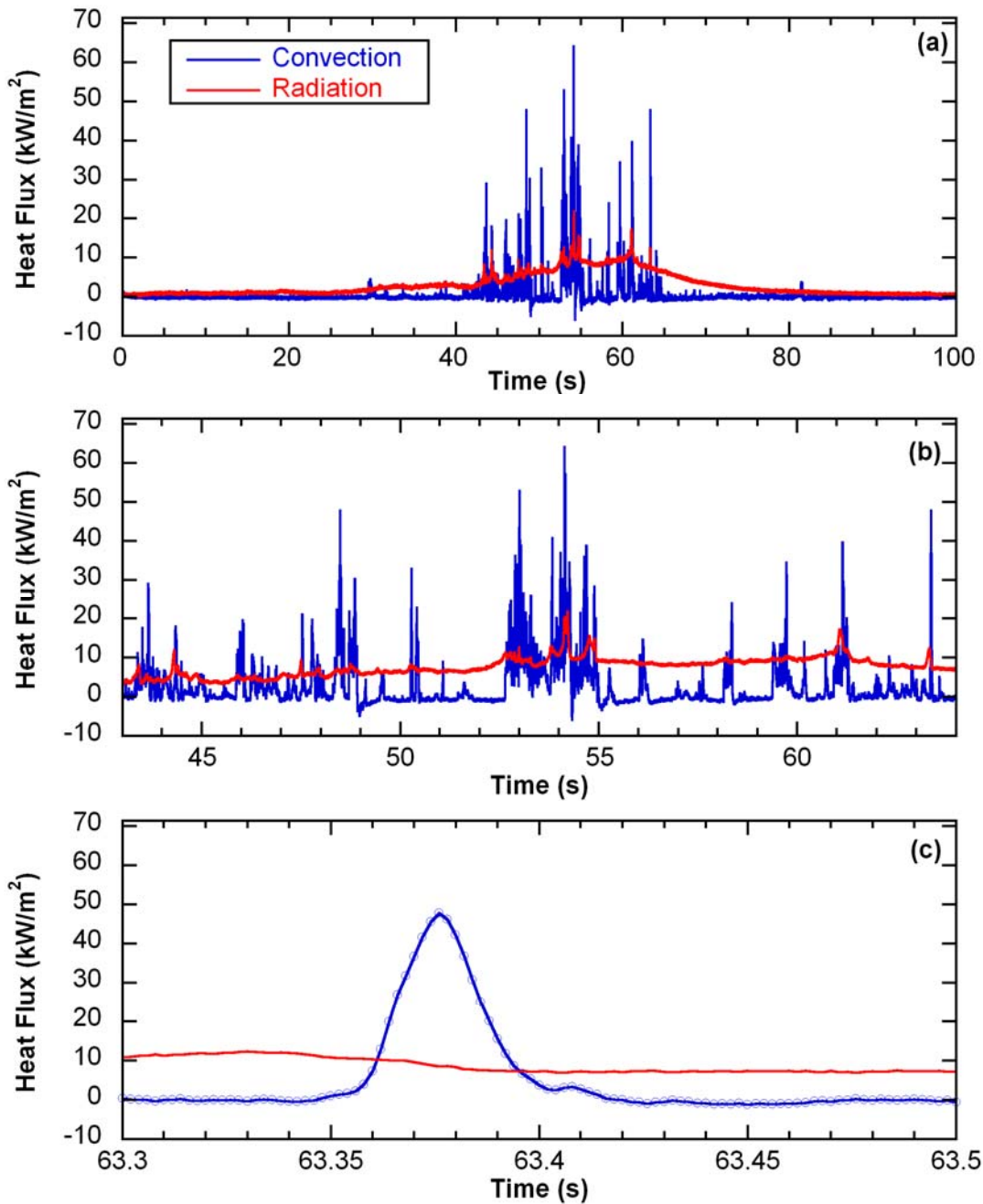


Figure 6.3. Heat flux fluctuations in Sula, MT Burn 1. Figures b and c expand the time scale for one specific segment of the time series.

and the ability of wildland fuels to respond to and potentially ignite from exposure to such rapid fluctuations. The frequency content of the time series convection and radiation heat flux data (Figure 6.4, Figure 6.3a and Figure 6.4a) for both burns was determin-

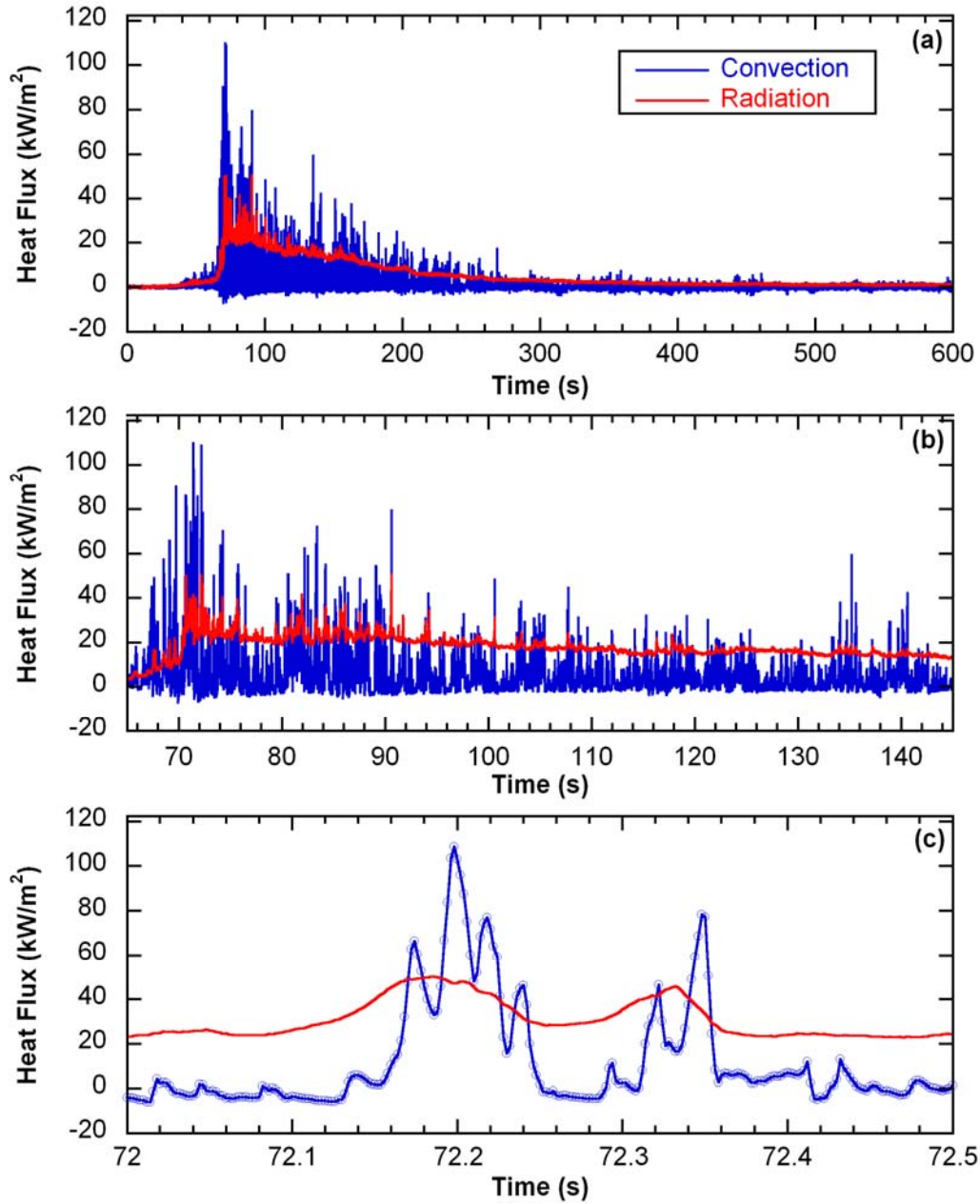


Figure 6.4. Heat flux fluctuations in Sula, MT Burn 2. Figures b and c expand the time scale for one specific segment of the time series.

ed by the use of a Fast Fourier Transform (FFT). Figure 6.5 shows the power spectrum for radiation, convection and the noise floor for both data sets. Again, the noise floor is seen as the frequency at which the power spectrum ceases to change.

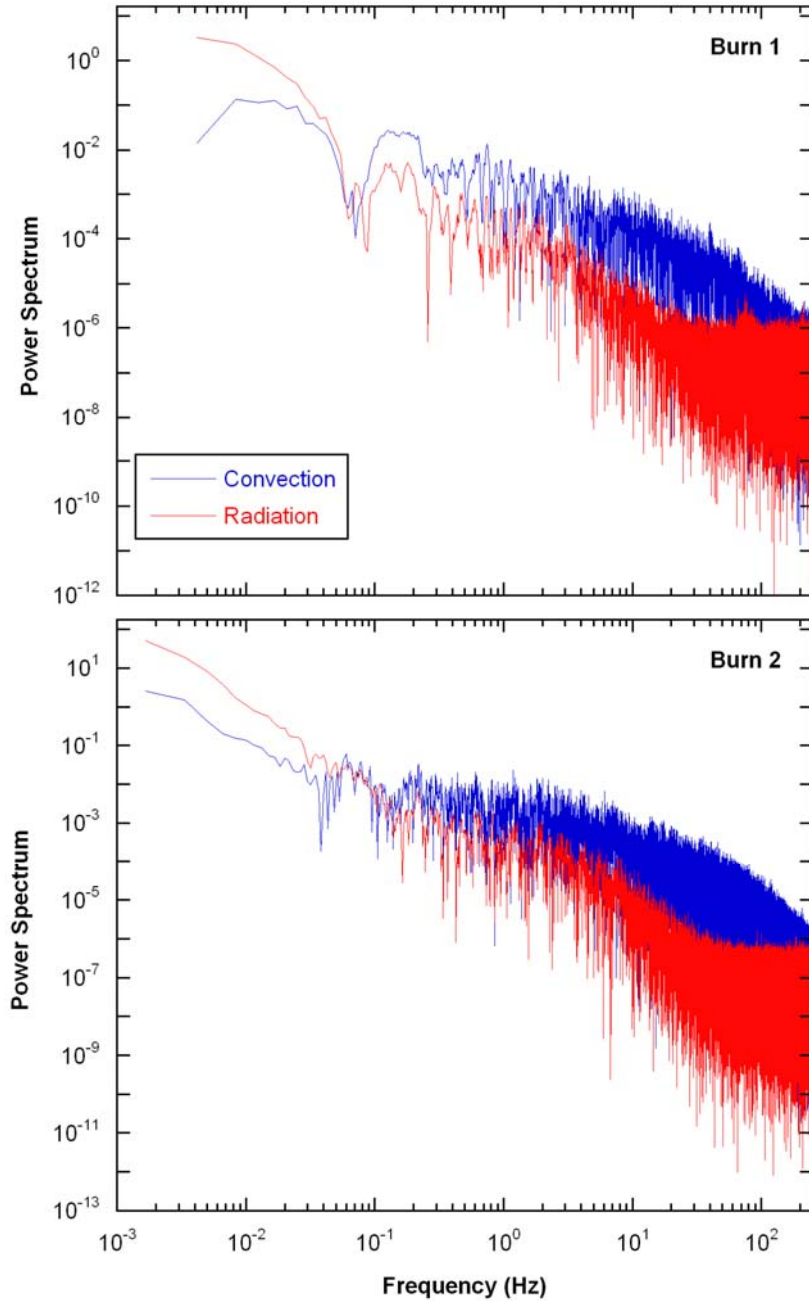


Figure 6.5. Radiation and convection power spectra for both Sula, MT burns.

No anti-alias filtering was employed. The top and bottom panels in Figure 6.5 are the power spectra for Burn 1 and Burn 2, respectively. The noise floor can be identified in the power spectra for radiation in Burns 1 and 2 and the convection in burn 1. Thus, a

sample rate of 500 Hz is sufficient to fully capture all these fluctuations. While the noise floor is not apparent in the power spectrum of the convection heat flux in Burn 2, it appears that the sample rate is sufficiently high to capture the significant temporal fluctuations in the convective flux. It is acknowledged that the magnitude of the noise floor is somewhat a function of the experimental setup used, but, as was mentioned earlier, care was taken to ensure that electrical noise in the signal was kept to a minimum. Although there are considerable fluctuations in the spectra, several observations may be made. There does not appear to be any preferential frequencies contained in either radiation or convection heat flux. The radiation power spectrum shows content above the noise floor beyond a frequency of approximately 10 Hz for both burns. The convection power spectrum shows content between 60 and 80 Hz for Burn 1 and beyond 100 Hz for Burn 2. Recalling that Burn 2 was more intense than Burn 1 it may be suggested that more intense fires have overall higher frequency content, which is supported by chapter 4, wherein laboratory experiments showed higher frequency content for both radiation and convection in wind-aided fires compared to buoyancy-driven fires. The effect of high frequency convective fluctuations on fuel temperature response will be explored later in this work.

The results of Figure 6.2 – Figure 6.5 provide clear evidence of short-duration convective heat flux pulses in wildland fires. In order to determine the effect of sampling rate on measured heat flux, a study was undertaken using the convection flux time series acquired. The time-resolved convection heat flux data, originally sampled at 500 Hz, were intentionally down-sampled to a desired sampling rate. For example, to simulate a 250 Hz sampling rate, every other data point in the 500 Hz series was sampled. Like-

wise, to simulate a 10 Hz sampling rate, every 50th point was sampled. In all cases, the down-sampled time series used the same starting time. This down-sampling study was undertaken for simulated sample rates ranging from the original 500 Hz data down to a simulated sampling rate of 1 Hz, and the results are shown in Figure 6.6 and Figure 6.7 for Burns 1 and 2, respectively. The data for both low- and high-intensity burns in Figure 6.6 and Figure 6.7 reveal little difference in both convective and radiative heat flux between the 500 Hz and down-sampled 250 Hz data. This is not surprising, since the temporal zoom data plotted in Figure 6.3c and Figure 6.4c corresponding to these burns reveals that sampling at 500 Hz provides multiple (a minimum of 10 to 12) data points for each short-duration pulse in the convective heat flux, which is sufficient to resolve the most rapid temporal fluctuations in flux. Down-sampling to 250 Hz still provides sufficient resolution of these convective bursts. At a down-sampled rate of 100 Hz there appears to be some degradation of the convective flux signal. Peak resolved convective heat fluxes are reduced relative to that observed in the original 500 Hz data. The frequency spectra of Figure 6.5 corresponding to the time-resolved convective flux data suggest that significant fluctuations at frequencies as high as 60 - 100 Hz are possible. It might be expected, therefore, that sampling at frequencies lower than approximately 120 – 200 Hz could result in a loss of convective flux signal resolution. It is noted, however, that the radiation flux signal continues to be reproduced with fidelity relative to the original 500 Hz signal at a down-sampling rate of 50 Hz. Again, this is not surprising, since the power spectra of Figure 6.5 for both burns reveal frequency content in the radiation heat flux fluctuations just beyond 10 Hz. Consequently, sampling at 50 Hz is sufficiently fast to capture the lower-frequency fluctuations of the radiation transfer.

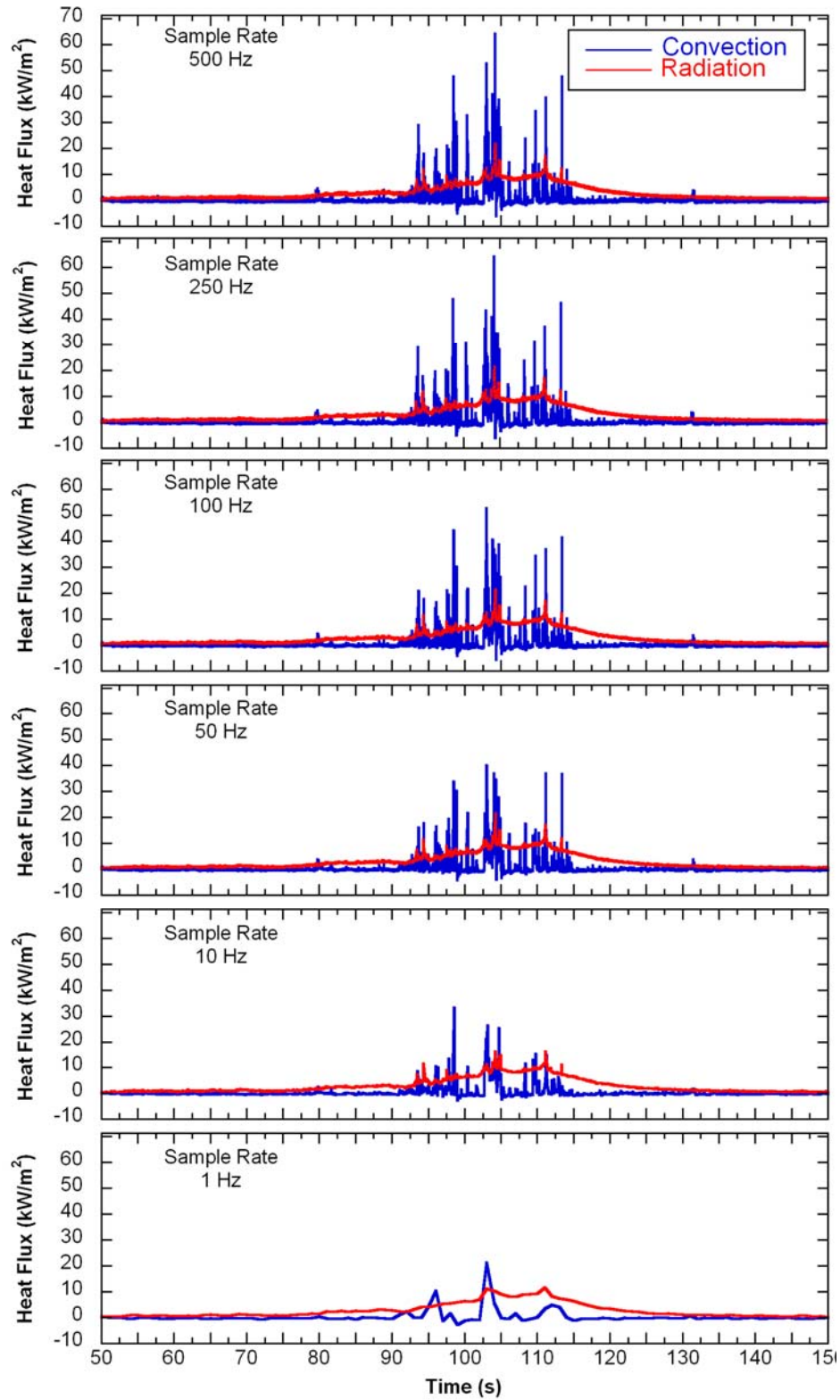


Figure 6.6. The effect of reducing sample rate on measured heat flux, Burn 1.

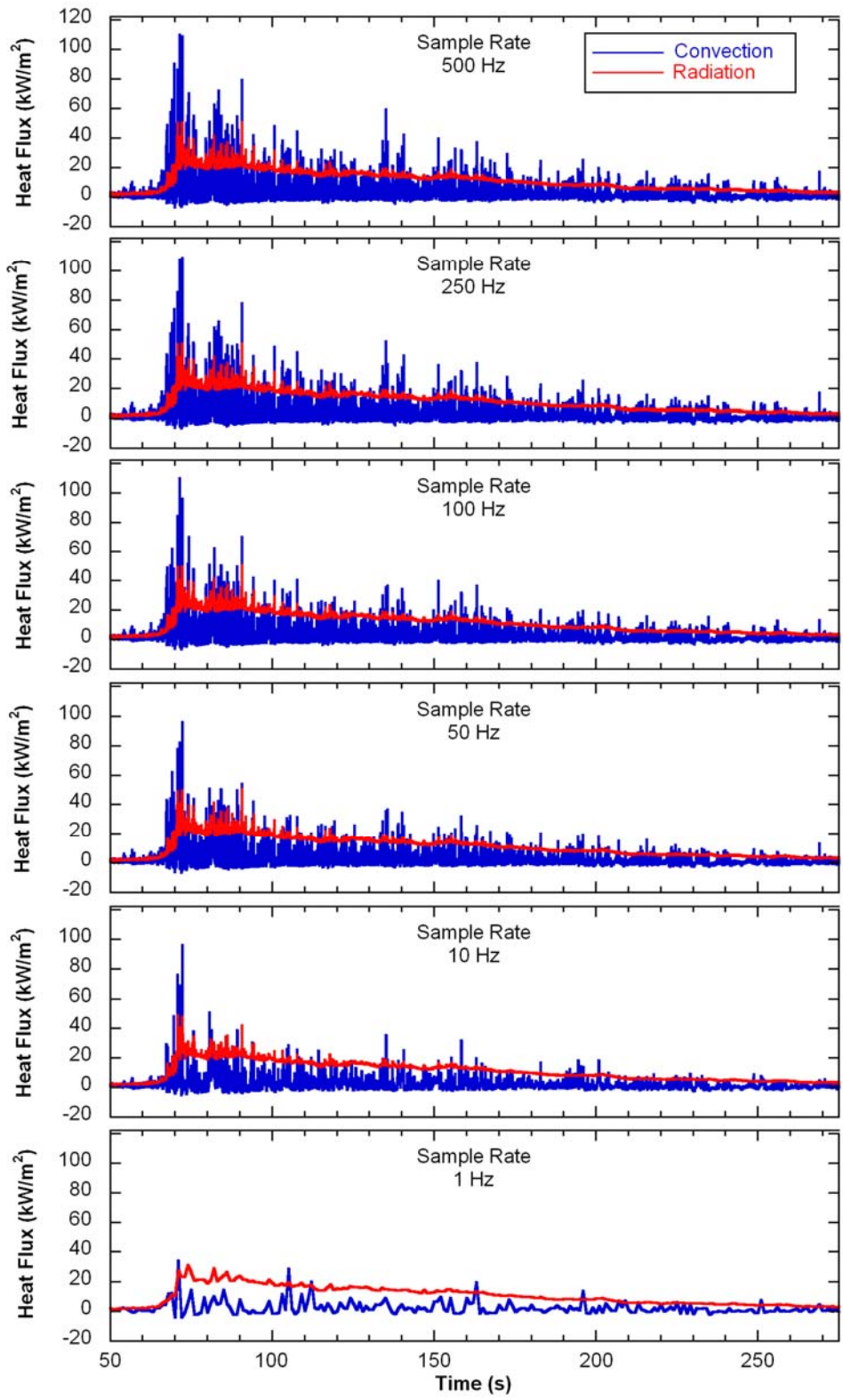


Figure 6.7. The effect of reducing sample rate on measured heat flux, Burn 2.

At a down-sampling frequency of 50 Hz, peak convection fluxes continue to drop, and further, some of the convective pulses are lost. This is even more evident for the 10 Hz data. Moreover, degradation of the radiation heat flux signal is first detectable at a down-sample rate of 10 Hz. Finally, at a down-sample rate of 1 Hz the characteristic rapid fluctuations in the convective heat flux are lost, and moderate loss of radiation flux data is also observed. The data reveal that not only are the peaks resolved poorly as the sampling frequency is reduced, the relative magnitude of the peak radiation and convection heat flux is no longer accurately distinguished. Convective heat flux peaks, which have a greater magnitude in the 500 Hz data, are lost and radiation heat transfer appears to be dominant.

Table 6-1 summarizes quantitatively the variation in maximum radiation heat flux resolved at the various sampling frequencies. The table illustrates the reduction in maximum resolved radiative and convective flux as the sampling frequency is reduced for both burns. The previous observation that lower sampling frequencies (*e.g.*, 50 Hz) are

Table 6-1. Peak radiation and convective heat flux resolved for the two burns as a function of sampling rate.

Sampling Freq (Hz)	Burn 1		Burn 2	
	Peak Radiation Flux (kW/m ²)	Peak Convective Flux (kW/m ²)	Peak Radiation Flux (kW/m ²)	Peak Convective Flux (kW/m ²)
500	21.8	64.1	50.3	109.9
250	20.5	64.1	50.2	108.8
100	21.5	52.8	50.2	109.9
50	21.5	40.1	50.2	96.1
10	16.5	33.4	48.9	96.1
1	11.7	21.2	31	33.8

high enough to accurately capture the radiation signal, is borne out by the data in the table. However, the data reveal that 100 Hz may be insufficient to fully resolve the temporal fluctuations in convective flux. To the knowledge of the authors, no previous investigations measuring time-resolved heat flux in wildland fires have employed sampling frequencies high enough to resolve maximum convective heat fluxes at the levels observed here. Although it must be acknowledged that different wildland environments will likely yield unique combustion characteristics, it seems clear that high-speed data sampling is necessary to fully and accurately resolve temporal fluctuations in the convective heat flux. It is further concluded that fluctuations in the radiation flux signal are characterized by lower frequencies, but that higher speed data sampling than has conventionally been done is probably necessary to capture all fluctuations in convective heat flux. These assertions are supported by Clark and Radke (1999) who show the existence of small turbulent structures within flames using infrared imagery and postulate that these structures influence convection heat transfer. While it appears that higher sampling rates are required to fully capture heat transfer in forest fires. The instantaneous cumulative heat flux and a moving average may be captured at a much lower frequency.

The instantaneous cumulative radiative and convective flux may be determined by integrating the measured flux histories with respect to time. The cumulative flux permits examination of the total convective and radiative heating load over the time period of the combustion event. The cumulative heat flux was calculated by integrating the flux from a time corresponding to its first increase with the start of the combustion event to an arbitrary time t . The integration of the discrete time-series heat flux data was performed

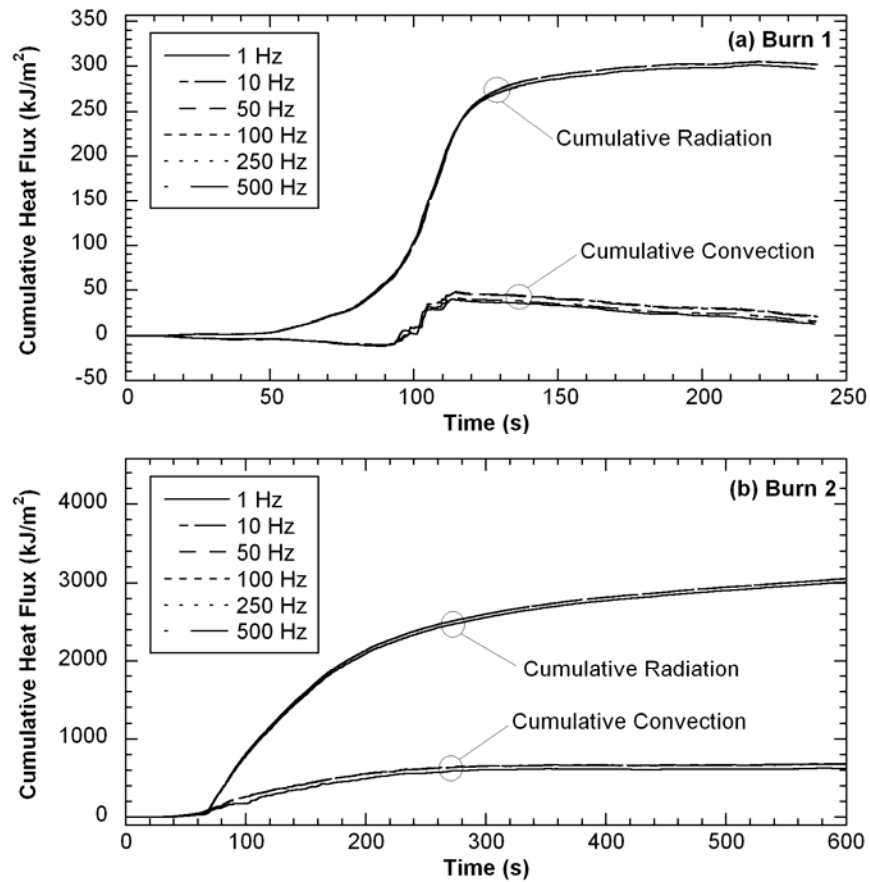


Figure 6.8. Cumulative convective and radiative heat flux histories for Burns 1 and 2 with different sample rates.

numerically using the trapezoidal rule. The results of the integration are shown in Figure 6.8a and Figure 6.8b, respectively for Burn 1 and Burn 2 at all down-sampled frequencies (1, 10, 50, 100, 250 Hz), and the original measurement frequency of 500 Hz).

As expected, the cumulative heat flux begins at zero. As the combustion event commences, the cumulative radiation flux begins to rise first due to the radiative preheating of the heat flux sensor housings by the approaching flame. In Burn 1 the radiant heat flux heats the sensors to a temperature above the cooler ambient air temperature prior to flame arrival such that the sensors are convectively cooled by the air surrounding the sensor package. The result is a negative cumulative flux for the first 100 s of the burn event.

This radiative pre-heating phenomenon is not observed in Burn 2. Aside from the initial radiative pre-heating/convective cooling phase in Burn 1, both the cumulative radiation and convection fluxes rise until the combustion event is over. Comparison of the cumulative flux histories at the down-sampled frequencies reveal that the total heating load on fuel elements may be resolved with little loss in accuracy even at frequencies too low to capture the time-resolved data. In fact, the cumulative heat flux histories corresponding to the different down-sampling frequencies are difficult to distinguish from one another. Thus, while high-frequency sampling is necessary to capture rapid temporal fluctuations in the temporal heat flux data, the cumulative heating load may be satisfactorily measured at considerably lower sampling frequencies.

The moving average heat flux is calculated for every time, t , in a data set. The recorded heat flux corresponding to time t is averaged along with the points ahead of time t in a specified window. The same procedure is followed for all the points in a data set. It is acknowledged that the shape of the moving average is a function of the window over which the average is taken. The window used in this study is chosen to be 1 s long. The moving average radiative and convective heat flux for both burns 1 and 2 is shown in Figure 6.9 at down-sampling rates of 500, 250, 100, 50, and 10 Hz. The moving averages are plotted on a reduced scale which highlights whatever differences exist between the different sample rates.

Comparison of the 1 s moving average at the different sample rates reveal that it can be reproduced with little loss in accuracy at sample rates which are too slow to fully capture radiative and convective heat flux. Indeed, the 1 s moving average heat fluxes corresponding to sampling frequencies between 500 and 50 Hz are difficult to distinguish

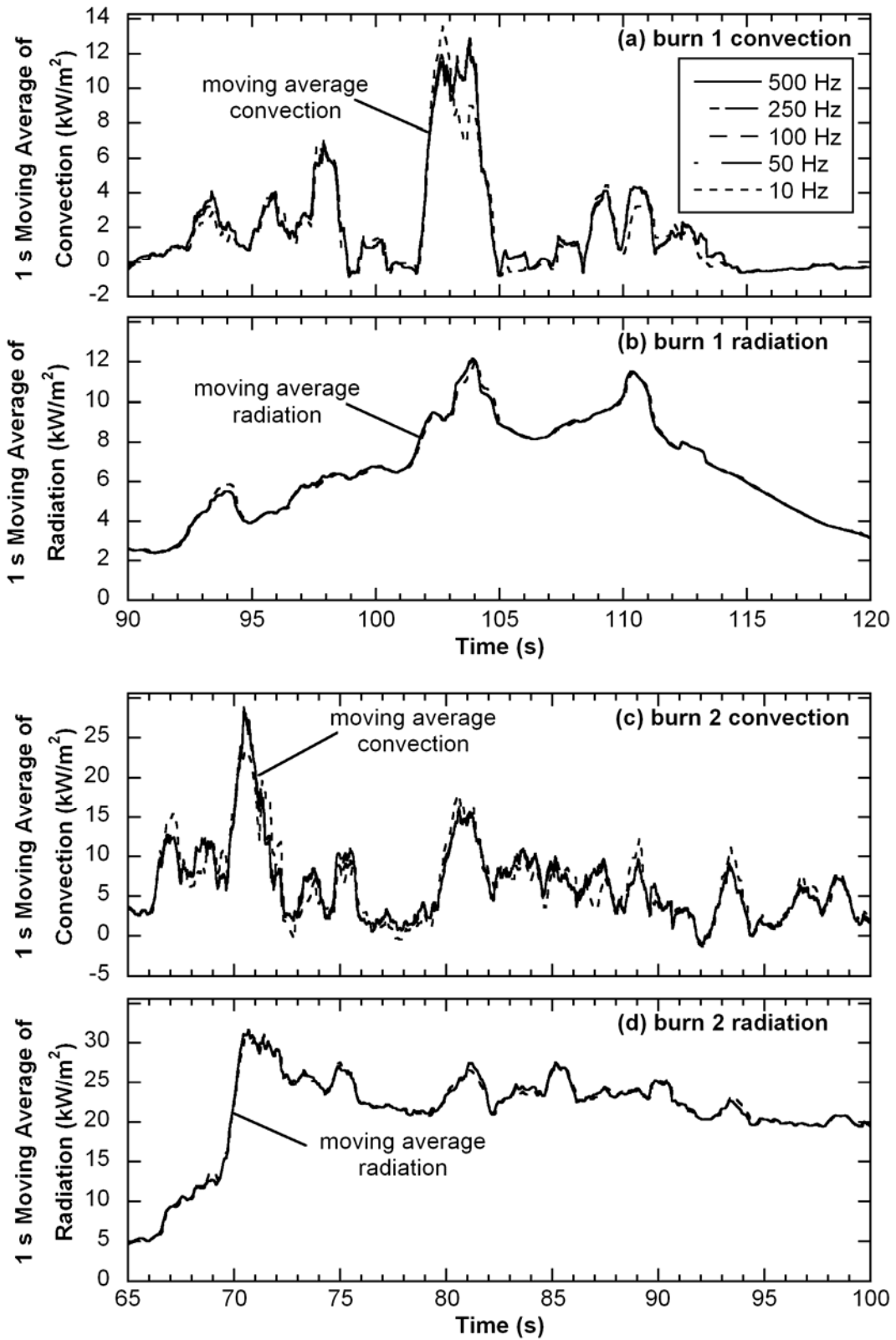


Figure 6.9. 1 s moving average heat flux for Sula burns 1 and 2 radiation and convection

from each other. The 1 s moving average heat flux does depart moderately at a sampling frequency of 10 Hz.

6.5. Model

The foregoing paragraphs illustrate the importance of sufficiently high sampling rate in measurement of time-resolved radiative and convective heat flux in wildland fires. Temporal fluctuations in radiative and convective fluxes corresponding to frequencies as high as 20 Hz and 100 Hz, respectively, have been noted. This prompts the question as to the ability of fuel elements in the wildland fire environment to respond to such high-frequency fluctuations. A one-dimensional transient conduction model for cylindrical fuel elements has been developed for investigating the response of a fuel element to a sudden change in convective environment. The characterization of temporal fluctuations in wildland fire environments presented in the foregoing section guided the analysis by providing information relative to the duration of typical convective heating pulses which might be encountered. Fosberg (1973) investigated a similar problem, albeit with a suddenly imposed step change in boundary temperature on the fuel element. However, a fuel boundary temperature may only change instantaneously when the heat transfer coefficient (h) is infinite. It is asserted here that the more representative boundary condition is one of convective heating, where the particle is subjected convectively to an elevated ambient temperature with physically reasonable convective heat transfer coefficient. The particle surface temperature and local internal temperature then rise in response to the heating.

It should be noted here that the lumped capacitance method has been used previously to solve for the temperature history of small branches and buds (~1 cm) in a previous work (Michaletz and Johnson, 2006). Incropera *et al.* (2007) show a plot compar-

ing the lumped capacitance method to the solution of the heat equation as a function Fourier number (Fo). The data show that for a Biot (Bi) number of 0.1, which is the upper limit below which the lumped capacitance method may be employed (Incropera *et al.*, 2007), $Fo < 10$ will result in error in the dimensionless temperature less than 5 percent and $10 < Fo < 22$ will result in an error or 5-10 percent. While an error of 5-10 percent seems small, this translates to a 65-130 K difference between the lumped capacitance and the actual fuel surface temperature. Greater accuracy is desired for this study. Further, only Bi numbers above 0.1 will be studied in this work, thus applying the lumped capacitance at these Bi numbers would only result in greater error.

Consider a one-dimensional solid cylinder of radius R , and constant density, ρ , thermal conductivity, k , and specific heat, c , as shown schematically in Figure 6.10. The cylinder is initially at uniform temperature T_i . The cylinder is exposed to a convective environment characterized by a constant heat transfer coefficient h , and arbitrary time-varying heating described by the ambient temperature history $T_\infty(t)$. Desiccation and pyr-

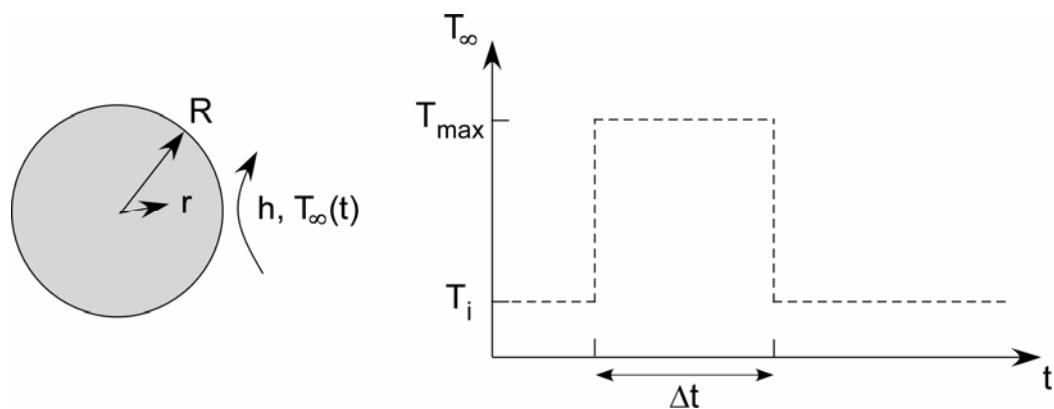


Figure 6.10. Fuel model schematic.

olysis are neglected in the model. Given that these are energy-absorbing mechanisms, their neglect thus provides an upper limit to the predicted temperature response of fine fuels in the scenario described. Introducing the dimensionless coordinate $\eta = r/R$, time $\tau = \alpha t/R^2$ where the thermal diffusivity is $\alpha = k/\rho c$, and temperature $\theta = (T - T_i)/T_i$, the partial differential equation governing the temperature response of the fuel element may be stated as

$$\frac{1}{\eta} \frac{\partial}{\partial \eta} \left(\eta \frac{\partial \theta}{\partial \eta} \right) = \frac{\partial \theta}{\partial \tau} \quad (6-1)$$

The initial condition is

$$\theta(\eta, 0) = 0 \quad (6-2)$$

The centerline symmetry boundary condition and surface boundary condition are

$$\left. \frac{\partial \theta}{\partial \eta} \right|_{\eta=0} = 0 \quad (6-3a)$$

$$\left[\frac{\partial \theta}{\partial \eta} + Bi \theta \right]_{\eta=1} = Bi \theta_{\infty}(\tau) \quad (6-3b)$$

The dimensionless timewise variation in ambient temperature to which the fuel element is subjected during the convective heating is $\theta_{\infty}(\tau) = [T_{\infty}(t) - T_i]/T_i$. The Biot number which appears in the boundary condition, Eq. (6-3b), is defined as $Bi = hR/k$, and is a measure of the ratio of thermal resistance to conduction heat transfer internal to the cylinder, to the convective resistance at the fuel element's boundary. Thus, the higher the Biot number, the greater the internal temperature gradients expected in the fuel element. The heat transfer coefficient, h , is a function primarily of the wind velocity and the fuel

element radius, and depends less strongly on the ambient temperature (Churchill and Bernstein, 1977).

The general solution to Eq. (6-1) for the unsteady, local temperature response of the fuel element subject to the imposed initial and boundary conditions were obtained using the Eigenfunction expansion method (Farlow, 1993) with the assistance of Dr. Matthew Jones (2009), and is stated for arbitrary variation in ambient temperature $\theta_\infty(\tau)$ as

$$\theta(\eta, \tau) = \sum_{n=1}^{\infty} \frac{2 Bi J_o(\lambda_n) J_o(\lambda_n \eta)}{J_o^2(\lambda_n) + J_1^2(\lambda_n)} e^{-\lambda_n^2 \tau} \int_0^\tau e^{\lambda_n^2 \tau'} \theta_\infty(\tau') d\tau' \quad (6-4)$$

A more detailed solution is included in the appendix. The eigenvalues λ_n , $n = 1, 2, \dots, \infty$, which appear in Eq. (6-4) are determined from the eigenfunction relation

$$Bi J_o(\lambda_n) = \lambda_n J_1(\lambda_n) \quad (6-5)$$

Equation (6-4) is the general solution to Eq. (6-1) subject to arbitrary, time-dependent variation in the dimensionless ambient temperature, $\theta_\infty(t)$. For this study the variation in ambient temperature illustrated in Figure 6.10 is imposed. The ambient temperature is suddenly raised from its initial temperature T_i (matching the fuel element initial temperature) to an elevated level T_{max} for a prescribed time interval Δt , then returns to its previous temperature T_i . This particular variation in ambient temperature may be expressed mathematically in dimensionless form as

$$\theta_\infty(\tau) = \theta_{max} [H(\tau) - H(\tau - \Delta\tau)] \quad (6-6)$$

where H is the Heaviside function and θ_{max} is the maximum dimensionless temperature imposed during the heating pulse of arbitrary duration $\Delta\tau = \alpha\Delta t/R^2$. Subject to the pulsed convective heating temperature protocol described by Eq. (6-6), the integral in the general solution of Eq. (6-4) is evaluated as

$$\int_0^\tau e^{\lambda_n^2\tau'} \theta_\infty(\tau') d\tau' = \frac{\theta_{max}}{\lambda_n^2} \left[H(\tau)(e^{\lambda_n^2\tau} - 1) + H(\tau - \Delta\tau)(e^{\lambda_n^2\Delta\tau} - e^{\lambda_n^2\tau}) \right] \quad (6-7)$$

In practice, the infinite series which appears in Eq. (6-4) was summed numerically until additional terms yield no appreciable change in the temperature. For $\Delta\tau \rightarrow \infty$ the problem becomes that of thermal response of the fuel element initially at a uniform initial temperature $\theta(\eta, \tau = 0) = 0$ to a step-change in convective heating temperature with ambient temperature $\theta_\infty = \theta_{max}$. Note further that the thermal response for two fuel particles, one subjected to a pulse of finite duration Δt and the other subjected to a step change in temperature, will be identical for the period of the pulse duration provided the maximum temperature θ_{max} is identical in both cases. Thus, the thermal response of a fuel particle subjected a step change in ambient convective temperature can be used to analyze the early stage heating response of the fuel particle subjected to a short-duration pulse.

The solution of Eq. (6-4) and (6-7) was verified by comparison with two limiting cases, which have been solved analytically. First, as $R \rightarrow \infty$ the problem becomes one of suddenly imposed convective heating on a semi-infinite slab of uniform initial temperature. Second, as $Bi \rightarrow 0$ the temperature gradients internal to the cylinder vanish, and the so-called lumped capacitance condition prevails (Incropera *et al.*, 2007). The transient temperature for this $Bi \rightarrow 0$ (*i.e.*, vanishing cylinder radius or infinitely large thermal

conductivity) case is a function only of time. The analytical solution of Eq. (6-4) agreed with the solutions for both the semi-infinite slab and vanishing- Bi limiting cases to within 0.1 percent.

6.6. Model Predictions

The model solution has the greatest generalized utility in its dimensionless form. In this way the user can select the desired dimensional parameters whose combination yields a given value of the dimensionless variables, and obtain the corresponding solution. The majority of the discussion on the model will therefore be in dimensionless form. However, in an effort to demonstrate utility of the model, a solution for a scenario based on representative dimensional parameters is presented.

Consider a particular case of pulse heating for conditions which might be encountered in a typical crown fire. Two fuel elements of diameter 0.5 and 1.0 mm, respectively, initially at a temperature 300 K, are heated by a 1-s convective pulse. The thermo-physical properties of Douglas-fir (*Pseudotsuga menziesii*) wood are assumed ($k = 0.14$ W/mK, $\alpha = 1.23e-7$ m²/s) (Touloukian and Ho, 1972). It should be noted that live plants may exhibit high moisture content, with resulting higher thermal conductivity. This will yield a decrease in Biot number. However, as this model is developed to explore the possibility of short duration convective pulse fuel ignition, a worst case (high Bi number) scenario is assumed. The maximum temperature of the convective pulse (T_{max}) is 1600 K, as suggested by crown fire measurements reported by Butler *et al.* (2004). Field measurements by Butler (2003) suggest that air velocities of 1 to 10 m/s are common in crown fires with significantly higher transient gusts. In the example presented here a mi-

drange ambient air velocity of 5 m/s is imposed. An empirical correlation by Churchill and Bernstein (1977) describing forced convection heat transfer for cylinders in crossflow is used to determine the Nusselt number ($Nu = hd/k_{air}$), and subsequently the convective heat transfer coefficient h . The thermal conductivity of standard air, required to determine the convection coefficient from the Nusselt number, was evaluated at the initial film temperature of the fuel particle $(T_i + T_{max})/2$ (Vargaftik, 1975). These representative values of problem parameters result in a Biot number of 1.64 for the 1.0 mm fuel particle and 1.20 for the 0.5 mm particle. The results are shown in Figure 6.11 for the two fuel diameters investigated.

The surface temperature responds quickly to the pulse temperature rise. Time is required for the heat to diffuse to the center of the fuel particle and as a result the centerline temperature is delayed in responding to the temperature pulse. The larger fuel particle (1.0 mm) is further delayed due to its larger size. The difference between the surface temperature and the centerline temperature is much larger for the larger (1.0 mm) particle. It is interesting to note that the surface of both fuel elements reach nominal ignition temperature before the centerline temperature shows any significant response. This corresponds to a surface-to-centerline temperature difference of 223 K. Again, it must be acknowledged that the model does not account for desiccation or pyrolysis. However, such a temperature difference predicted even with these idealizations may suggest particle ignition before vaporization of water or pyrolysis on the interior of the particle could begin. The 0.5 mm and 1.0 mm diameter particles reach nominal ignition temperature in 0.035 s and 0.083 s, respectively. The minimum duration of a convective heating pulse needed to bring the particle to ignition temperature thus corresponds to a pulse frequency

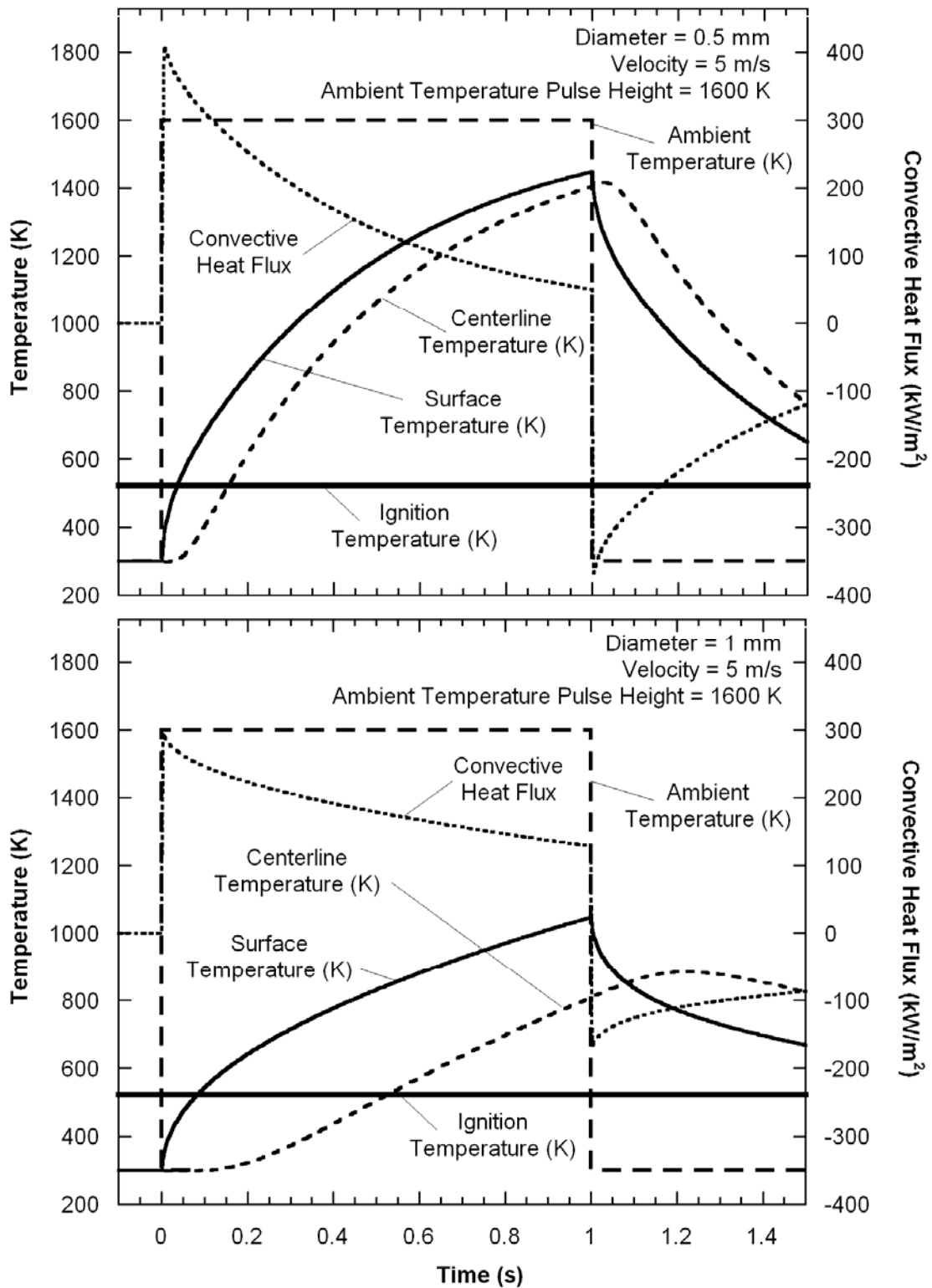


Figure 6.11. Model solution using for $R = 0.5$ and 1.0 mm using the thermophysical properties of fir, $T_{max} = 1600$ K, wind velocity = 5 m/s.

of 29 Hz and 12 Hz for the 0.5 mm and 1.0 mm particles, respectively. While the desiccation and pyrolysis phenomena will result in a slower fuel response, not all of the assumptions made in the formulation of this model would result in an increased ignition time. This model assumes that the fuel begins at a temperature of 300 K when the fuel particle is exposed to the convective pulse. It is likely that the fuel particles would be exposed to radiant heating before the flame arrives, resulting in a higher initial temperature which would significantly decrease the ignition time. In any case, this model shows that it is possible for fuel to respond to higher frequency convective pulses.

The predicted convective heat flux history is also included in Figure 6.11. The maximum convective heat flux for the 0.5 mm particle is just over 400 kW/m² and nearly 300 kW/m² for the 1 mm particle. The highest recorded radiant heat flux measured experimentally was approximately 300 kW/m². The data set which includes this maximum radiant heat flux is shown in Figure 5.9. The gas velocity considered in Figure 6.11 was intentionally chosen to be representative rather than extreme. Given that velocities as high as 10 m/s have been measured in wildfire environments with significantly higher gusts, the potential for a higher convective heat flux does exist.

The dimensionless form of the solution allows the user to explore the effect of any fuel or ambient conditions on particle thermal response. The model results are thus presented here as a function of Biot number and dimensionless ambient temperature regimes (θ_∞). The dimensionless temperature range chosen for this study is based on an initial fuel temperature of 300 K and a maximum ambient temperature (T_{max}) of 1600 K. The smallest value used for θ_{max} is 600 K which is only 77 K over the minimum temperature at which the fuel could ignite (Babrauskas, 2003). These temperatures result in a dimen-

sionless temperature maximum range of 1 to 13/3. The Biot number range is chosen based on average velocities measured by Butler (2003), air properties by Vargaftik (1975) evaluated at the film temperature, fuel diameters as high as 1 cm, and thermal conductivity of cellulosic materials from Stamm (1964). The thermal conductivity of the cellulosic materials is used because to the knowledge of the author, the literature contains no data for the thermal conductivity of fine fuels. It is likely that the Biot number may not extend much past 10 in the field, which is the value the fuel would take on if it were dry wood. However, given that the thermal conductivity of fine fuels appears to be unmeasured, a conservative low value corresponding to the thermal conductivity of Ponderosa bark is used. This results in a Biot number range of interest to wildland fire environments from (0.1) (corresponding to natural convection heating) to a maximum of 30 (corresponding to intense forced convective heating).

Figure 6.12 presents the dimensionless surface and centerline temperatures as a function of dimensionless time for Biot numbers 0.1, 1, and 10. The variation in dimensionless ambient temperature yielding the convective heating of the particle is also illustrated. For the cases shown in Figure 6.12, a maximum dimensionless temperature in the convective heating pulse $\theta_{max} = 13/3$ is imposed. The dimensionless ignition temperature $\theta_{ign} = 0.74$ is also indicated in the figure, taken from the minimum temperature at which cellulosic materials may ignite according to Babrauskas (2003). The dimensionless time $\tau = 0$ corresponds to the initiation of the ambient temperature pulse.

Figure 6.12 shows that the surface temperature, θ_{surf} , responds first as the convective heating pulse is imposed, and it approaches the maximum ambient temperature in the pulse, θ_{max} . As expected, the response of the centerline temperature, θ_{center} , is delayed in

reacting to the heating pulse as a result of the time required for the energy delivered convectively to the particle to diffuse within the material. When the pulse ends the surface temperature decays, again reacting quickly to the change in ambient temperature. The centerline temperature continues to rise owing to the energy still diffusing through the material prior to the end of the pulse. Comparison of the data for varying Biot number reveals that lower Bi results in both delayed thermal response and reduced temperature difference between the surface and centerline (*i.e.*, reduced temperature gradients within the particle). Significant differences in surface and centerline temperature are noted for large Biot number, with those differences decaying with time. It is of note that the fuel element surface reaches the minimum ignition temperature very quickly in the $Bi = 1$ and 10 cases, even before the fuel centerline reacts to the heating pulse. The elapsed dimensionless time for the surface to reach ignition temperature will be discussed in more detail later.

The dimensionless surface (top panel) and centerline (bottom panel) temperature response for a lower range of Biot number, $0.2 < Bi < 0.8$, at the same imposed $\theta_{max} = 13/3$ is shown in Figure 6.13 as a function of dimensionless time τ . Figure 6.14 illustrates similar information for a higher Bi range, $2 < Bi < 30$. The difference between the surface and centerline temperature is also shown as a function of time in the lower panel of both figures.

Again, the dimensionless time $\tau = 0$ corresponds to the initiation of the convective heating pulse. A lower Biot number would arise for smaller particle radius, reduced convective heat transfer coefficient to a lower wind speed (or the onset of natural convection

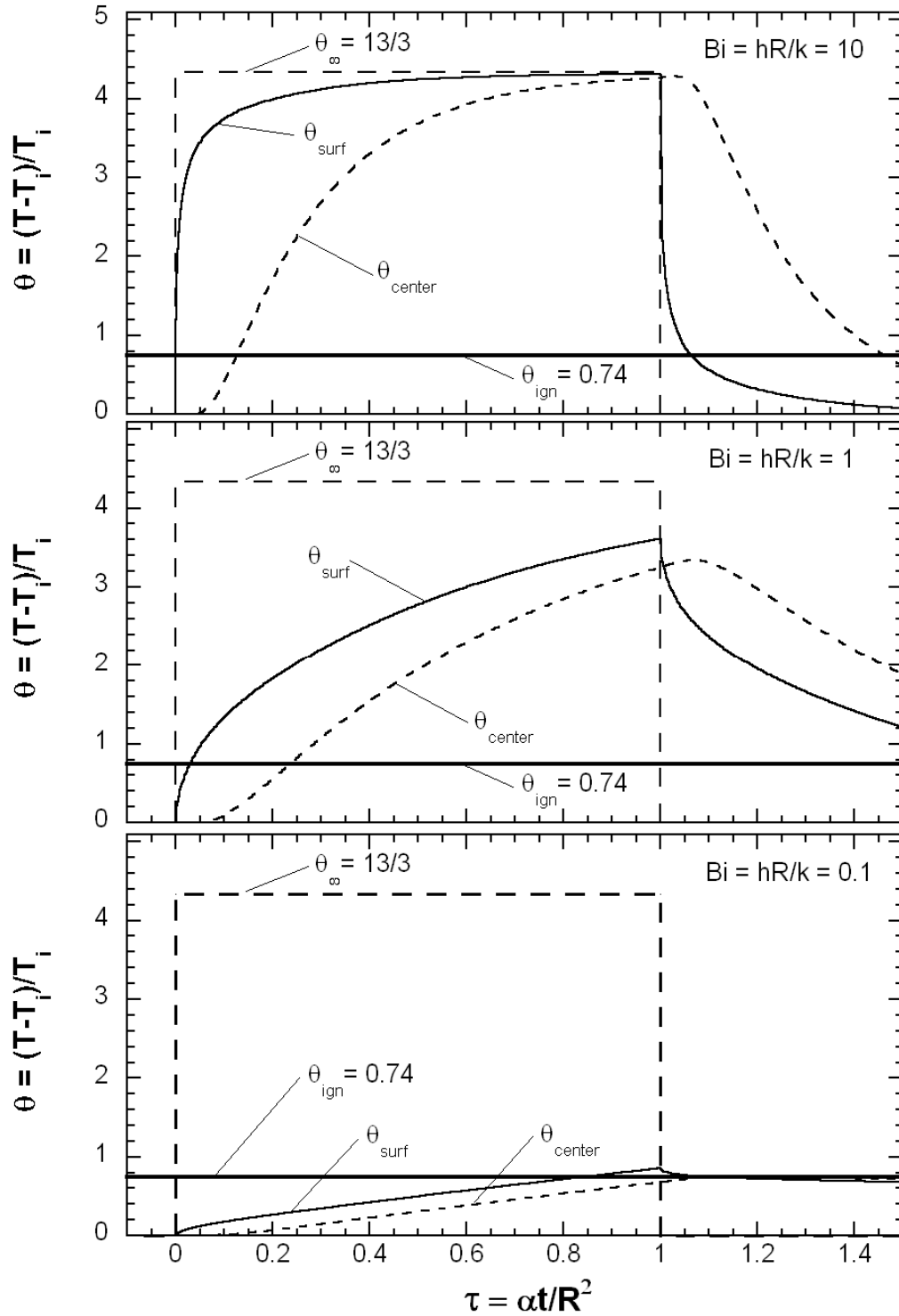


Figure 6.12. Dimensionless predicted surface and centerline temperatures for $Bi = 0.1, 1,$ and 10 .

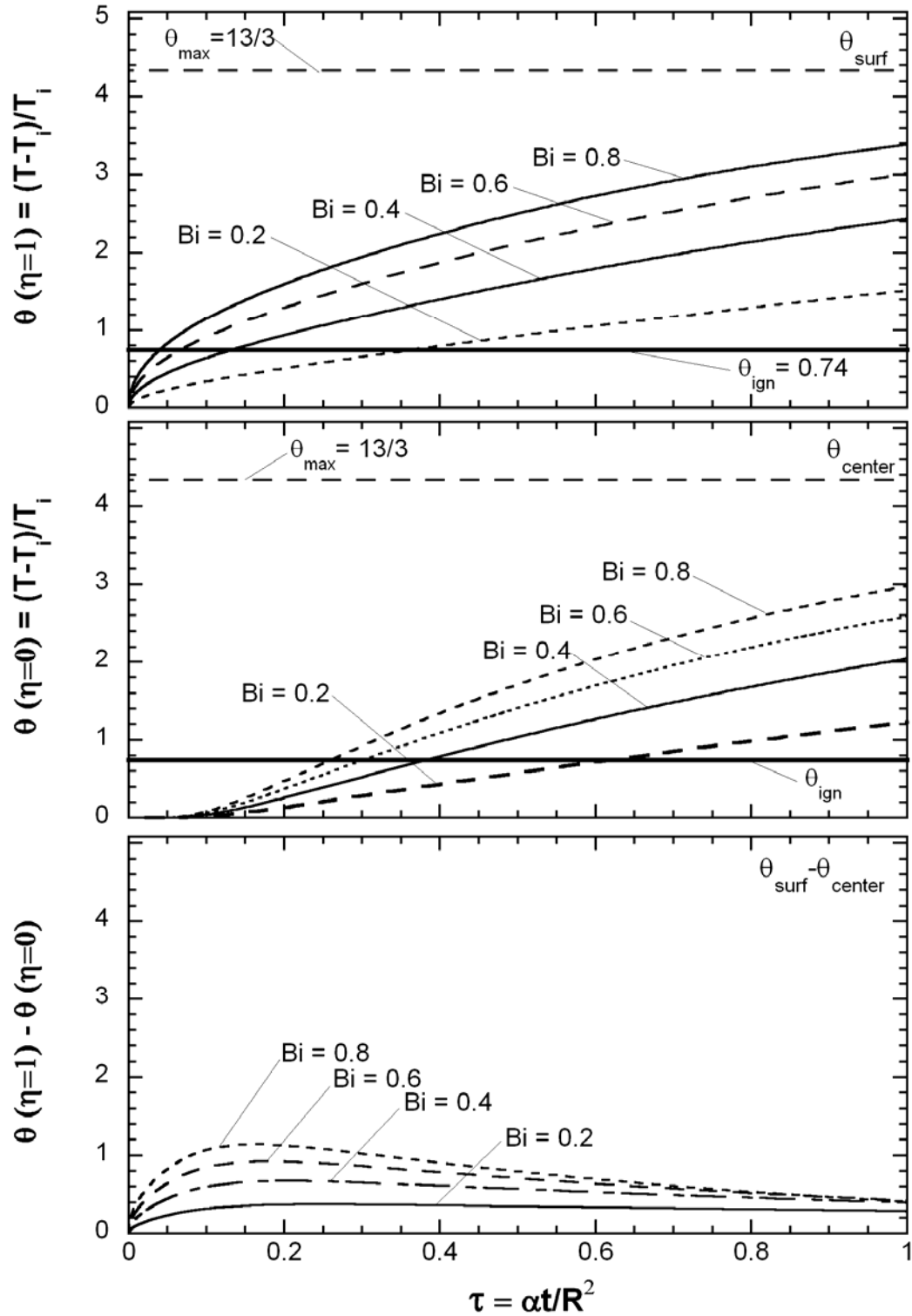


Figure 6.13. Dimensionless predicted surface and centerline temperatures, and temperature differences at $Bi = 0.2, 0.4, 0.6$ and 0.8 .

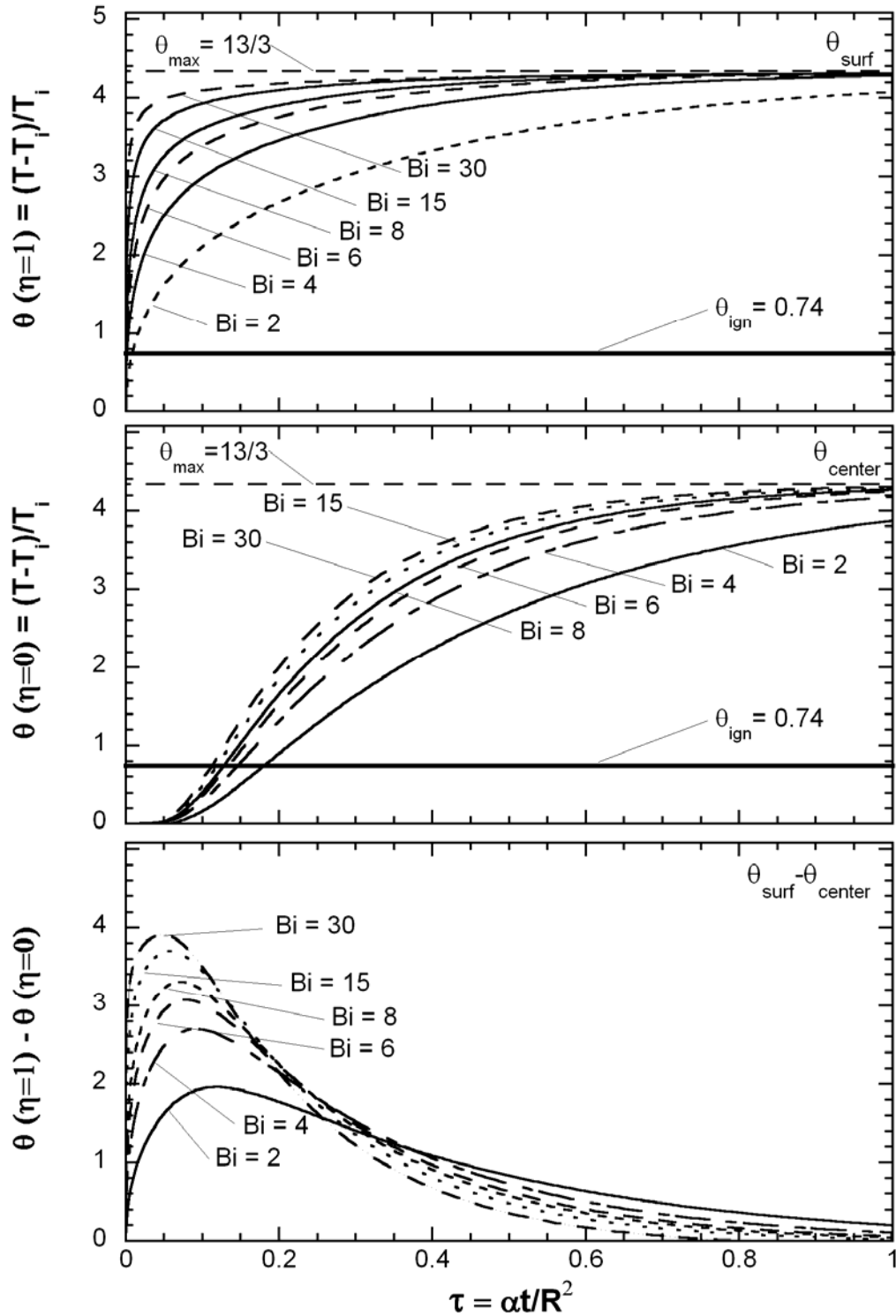


Figure 6.14. Dimensionless predicted surface and centerline temperatures, and temperature differences at $Bi = 2, 4, 6, 8, 15$ and 30 .

heating in the absence of forced flow), and/or increased fuel thermal conductivity. The dimensionless minimum ignition temperature $\theta_{ign} = 0.74$ of cellulosic material identified by Babrauskas (2003) is also shown in the top two panels of both figures. It is again seen that a lower Biot number results in slower response to the sudden heating, and smaller temperature gradients within the fuel element. Except at very low Biot number, the data indicate significant time delay between surface and centerline temperature response. Further, the difference between surface and centerline temperature increases as Bi is increased. The temperature gradient internal to the fuel particle can be quite significant, particularly for high Bi . The $\theta(\eta = 1) - \theta(\eta = 0)$ predictions for $Bi = 0.8$ in Figure 6.13 reveal that the surface-to-center temperature difference, $T_{surf} - T_{center}$, is greater than 300 K for the $\theta_{max} = 13/3$ scenario presented here. For $Bi > 2$ the predictions (of Figure 6.14) reveal that $T_{surf} - T_{center}$ exceeds 600 K (again, for the $\theta_{max} = 13/3$ of this case).

Such internal temperature differences are significant, and may result in explosive desiccation or other physical phenomena not modeled here but observed by others experimentally (Pickett *et al.*, 2007). The predictions reveal that it may not be appropriate to assume that temperature gradients within the fuel are negligible, even for very small fuel elements.

The data of Figure 6.13 and Figure 6.14 also suggest the possibility that particles will reach the minimum ignition temperature at the surface for short-duration convective pulses. However, even if the fuel ignition temperature were definitively known, one may not confidently suggest that a fuel element would ignite when the surface temperature reaches the ignition temperature. The complex phenomena of desiccation and pyrolysis render the prediction of ignition time difficult. The simplified nature of this modeling

exercise is designed to explore the thermal response of idealized fuel elements subjected to short-duration pulses in convective heating.

As mentioned previously, the cases explored thus far correspond to a maximum temperature in the convective heating pulse of $T_{max} = 1600$ K, as reported by Butler *et al.* (2004) for high-intensity crown fires. In order to characterize the thermal response and ignition temperature of fuel elements for other heating environments, the time required for a particle surface to reach the minimum ignition temperature (as defined by Babrauskas, (2003) for a range of maximum temperatures in the convective heating pulse and different Biot numbers was explored. Figure 6.15 presents the results of this study, where the dimensionless ignition time, $\tau_{ign} = \alpha t_{ign}/R^2$, is shown on the ordinate as a function of Bi on the abscissa for maximum temperatures in the convective heating pulse in the range $1 < \theta_{max} < 13/3$. Note that there appear to be two temporal heating regimes, and that the dependence of τ_{ign} on Bi is linear (in log-log space) in both. Transition from one regime to another occurs at $\tau_{ign} \approx 0.2$. The dimensionless time to ignition exhibits greater dependence on Bi for $\tau_{ign} < 0.2$ than for $\tau_{ign} > 0.2$. Not surprisingly, the results of Figure 6.15 reveal generally that for a given Biot number, the time to ignition increases with decreasing θ_{max} . The implication is that for a given particle size and convective heat transfer coefficient, the ignition time will be higher for a lower maximum temperature in the convective heating pulse, T_{max} . Figure 6.15 also shows that as θ_{max} is held constant, the dimensionless time to ignition increases with decreasing Biot number. This, too, is expected, since Bi may be reduced by a drop in heat transfer coefficient (corresponding to lower wind speed), resulting in lower intensity of convective heating of the particle. As noted previously, higher moisture content in the fuel particles will yield higher thermal

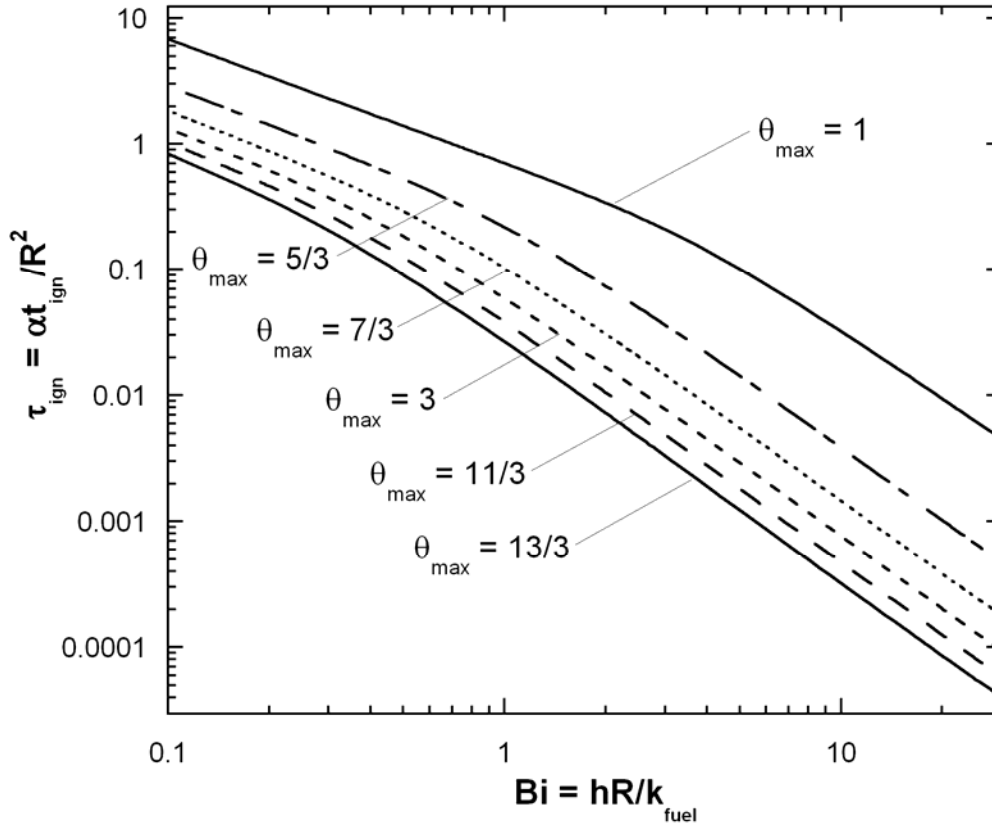


Figure 6.15. Relationship between predicted dimensionless ignition time and Biot number for a range of ambient temperature magnitudes.

conductivity. In the absence of desiccation and/or other physical phenomena as modeled here, higher fuel thermal conductivity would result in a further decrease in the ignition time, t_{ign} , since an increase in k yields a decrease in Bi and an increase in τ_{ign} .

The measured radiation and convection heat flux data from the Sula burns were analyzed previously (Figure 6.5) to illustrate the range of frequencies encountered in both modes of heat transfer. The response of a fuel element to short-duration pulses corresponding to the frequencies observed in the experimentally measured heat flux data may now be investigated using the analytical model. This is done by introduction of a dimensionless ignition frequency, $\phi = R^2 f_{ign} / \alpha$, which may also be expressed as the reciprocal of the dimensionless ignition time, $\phi = R^2 / \alpha t_{ign}$. The dimensionless frequency parameter ϕ

may be viewed as the maximum frequency for the specified Bi and θ_{max} at which the particle may respond thermally and reach the ignition temperature. Thus, a fuel element's susceptibility to ignition from a single ambient temperature pulse of known pulse frequency can be assessed. Figure 6.15 is re-plotted in terms of dimensionless frequency in Figure 6.16. The maximum dimensionless temperature in the convective heating pulse, θ_{max} , again ranges between 1 and $13/3$, and the Biot number ranges from 0.1 to 30. The experimental data of Figure 6.5 revealed that measured fluctuations in convective heat flux were distinguishable from the noise floor at frequencies as high as 100 Hz in Burn 2. Expressed in dimensionless terms, this maximum resolvable frequency measured experimentally thus corresponds to $\phi_{meas,max} \approx 200$ for the thermophysical properties of Douglas-fir (*Pseudotsuga menziesii*) and a fuel element diameter of 1 mm ($R = 0.5$ mm). This limit is indicated in Figure 6.16. The figure shows that, depending on Biot number, the ignition temperature of fuels may be reached for convective heating fluctuations characterized by frequencies lower than $\phi_{meas,max}$ for the full range of maximum temperature in the convective heating pulse, $1 < \theta_{max} < 13/3$. For a given θ_{max} , particles reach the ignition temperature only at higher Biot number (*i.e.*, more intense convective heating) as the pulse frequency increases. For a given pulse frequency, higher Biot number is also required for ignition as the maximum temperature of the convective pulse, θ_{max} , decreases. Finally, the figure reveals that for high but realistic values of θ_{max} and Bi , fuel particles may reach the minimum ignition temperature when exposed to convective fluctuations of significantly higher frequency than that measured experimentally. While frequencies as high as 100 Hz have been measured in this study, it must be acknowledged that these data for a single controlled burn. However, the fluctuations measured experimentally and

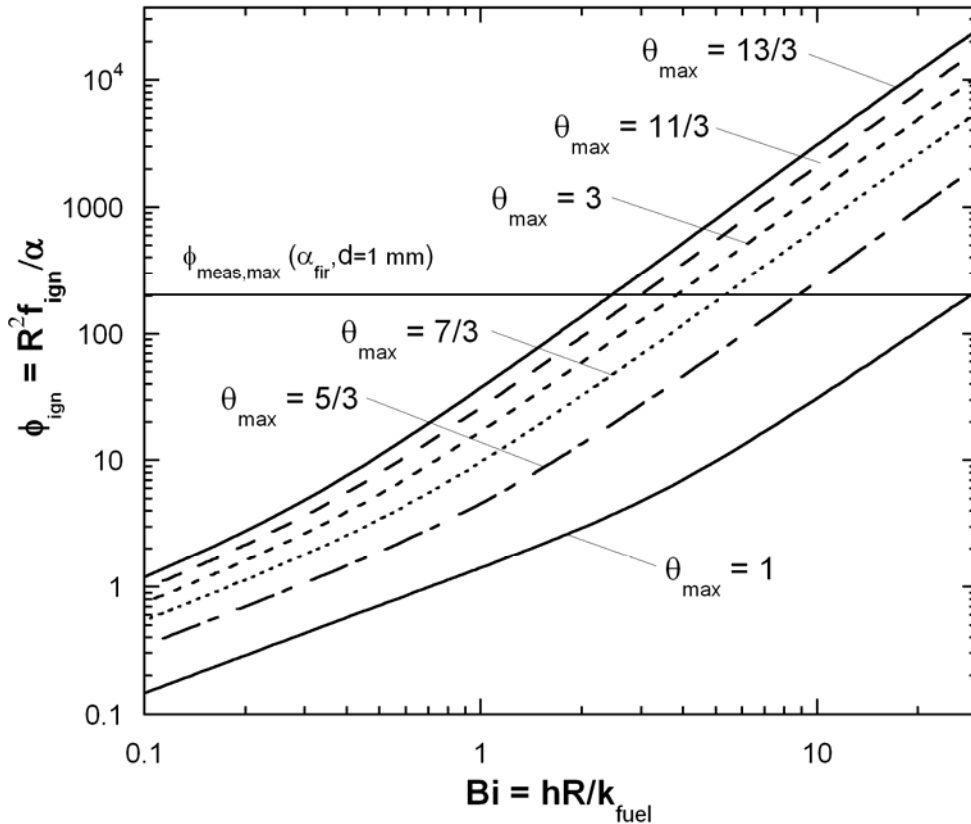


Figure 6.16. Relationship between predicted dimensionless ignition frequency and Biot number for a range of ambient temperature magnitudes.

are reported here for the Sula, Montana controlled burns are not inconsistent with similar measurements made in controlled burns characterized by a range of fuel conditions (crown fires, brush fires, wind-assisted ground fires, *etc.*), as shown in Chapter 5.

While the model has been specifically developed to determine the response of a fuel particle to a convective heat flux, it can be used to predict fuel response to a constant heat flux. This is accomplished by setting the convection coefficient to the desired heat flux, q_{des} , divided by the ambient temperature, T_∞ , as shown in Eq. 6-8.

$$\left[k \frac{\partial T}{\partial r} \right]_{r=R} = h(T_\infty - T(r=R, \tau)) = \frac{q_{des}}{T_\infty} (T_\infty - T(r=R, \tau)) \quad (6-8)$$

As the ambient temperature is artificially increased the heat flux at the boundary approaches the desired heat flux, as shown in Eq. 6-9.

$$\lim_{T_{\infty} \rightarrow \infty} \left[q_{des} \left(1 - \frac{T(r = R, \tau)}{T_{\infty}} \right) \right] = q_{des} \quad (6-9)$$

Thus, the analysis developed for an imposed convective boundary may be used to simulate an imposed constant heat flux pulse. In practice, a very large ambient temperature was chosen (of the order of 10^6 W/m²K), such that the temperature difference $T_{\infty} - T(r = R, \tau)$ was effectively equal to the ambient temperature, T_{∞} , and the resulting actual heat flux was within 1% of the desired heat flux value. The predicted surface and centerline temperature histories for imposed axisymmetric heat fluxes of 100, 200, and 300 kW/m² simulated in this way are shown in Figure 6.17.

The constant imposed heat flux variation of the model has utility in studying the response of fine fuels to fluctuations in radiation heat flux. It provides a worst case scenario in which the fuel particle is exposed to an axisymmetric radiant heat flux with no radiant or convective losses. Thus, if the particle is shown to be unable to react thermally to the frequency of fluctuations measured in the field under the extreme conditions modeled here, the particle is unlikely to react to more realistic conditions which are found in the field. It is emphasized that the constant heat flux boundary condition differs fundamentally from the convective boundary condition in that the convective boundary condition surface heat flux is continually reduced by a factor equal to the difference between ambient temperature and the fuel surface temperature, $T_{\infty} - T(r = R, \tau)$. For an imposed

constant heat flux the surface heating does not change with time and the temperatures in the particle may continue to rise (perhaps to unrealistically high values).

Not surprisingly, Figure 6.17 illustrates behavior qualitatively similar that observed for the convective heating boundary condition. The surface responds quickly to the imposed heat flux, and the response of the centerline is delayed due to the time requ-

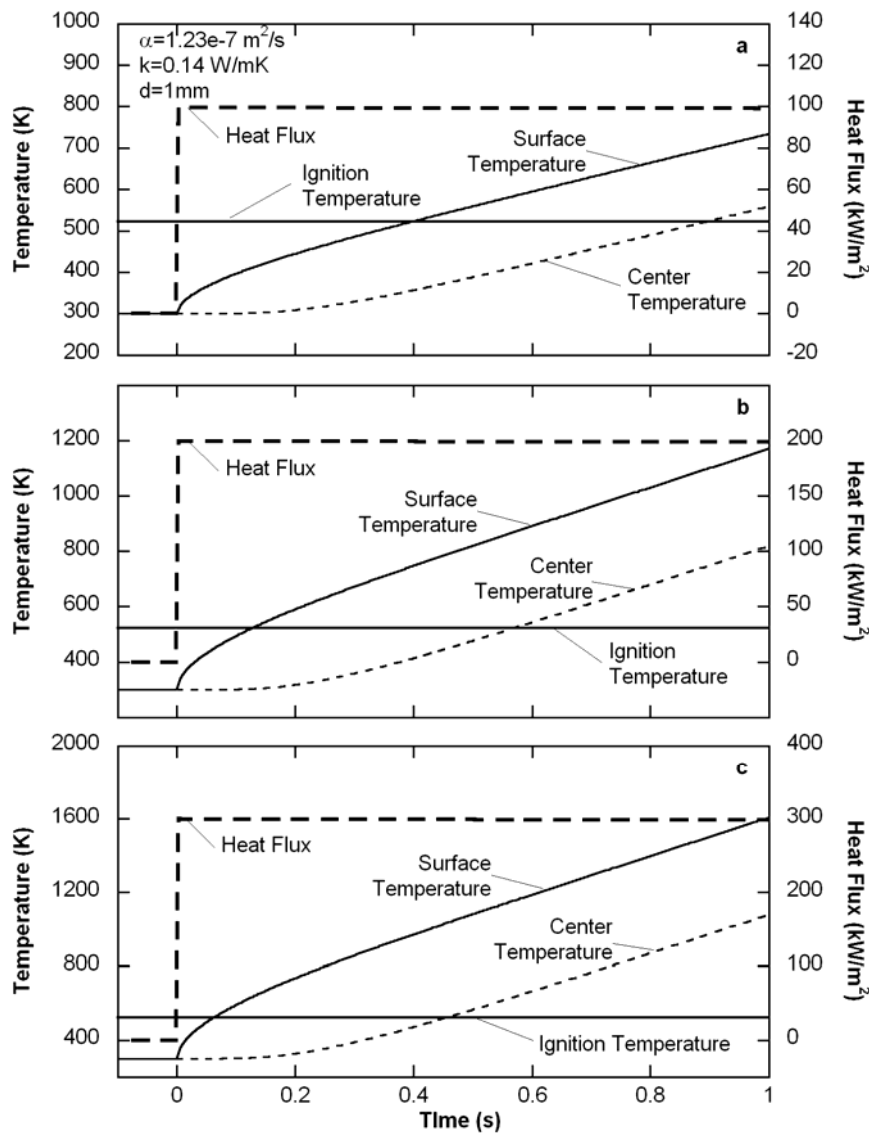


Figure 6.17. Predicted surface and centerline temperature histories of a 1mm Douglas Fir cylindrical particle under 3 imposed heat fluxes a) 100 kW/m² b) 200 kW/m² and c) 300 kW/m².

ired for the heat to diffuse into the material. Figure 6.17 shows that once the centerline responds to the constant heat flux, the centerline and the surface temperatures rise together linearly thereafter, consistent with the constant heating boundary condition. The surface of the fuel element exposed to the 200 and 300 kW/m² constant heat flux magnitude rises to the ignition temperature before the centerline responds to the constant heat flux. Recall that the maximum gas temperature measured in the field is approximately 1600 K (Butler *et al.*, 2004). In order for the fuel to be exposed to an axisymmetric heat flux of 300 kW/m², the fuel must be entirely surrounded by a radiating blackbody at 1516 K. Thus, the likelihood of a particle experiencing such a thermal environment is quite low.

In order to fully explore the response of fine fuels to a constant axisymmetric heat flux, the heat flux is given in its dimensionless form as

$$\left[\frac{\partial \theta}{\partial \eta} \right]_{\eta=1} = \frac{q_{des} R}{k T_i} = q^* \quad (6-10)$$

The dimensionless frequency of fuel ignition is plotted as a function of dimensionless imposed heat flux in Figure 6.18. The highest frequency at which the fuel surface reaches the ignition temperature (defined by Babrauskas (2003)) subject to an imposed dimensionless heat flux is denoted “Ignition Line” in the figure. The properties of Douglas Fir (*Pseudotsuga menziesii*) are used to define the other two lines shown on the plot. The horizontal line corresponds approximately to the highest measured frequency observed experimentally in the radiation heat flux (see Figure 6.5). The vertical line corresponds to the highest radiant heat flux measured in the field of approximately 300 kW/m², reported in Chapter 5 (see Figure 5.9). The predictions reveal that fuel elements exposed to the worst case scenario radiation heat flux pulse (300 kW/m² axisymmetric

heating, imposed without heat losses) can respond thermally reaching the ignition temperature to temporal fluctuations in flux as high as 30 Hz. Thus, it appears unlikely that the fuel can respond to ignition when exposed to the radiant flux fluctuations observed experimentally. This was further verified using properties of Oak, White Pine and Yellow pine.

In addition to predicting particle ignition, it is of interest to understand the temperature-time history of the particle with the objective of determining cambial and foliage

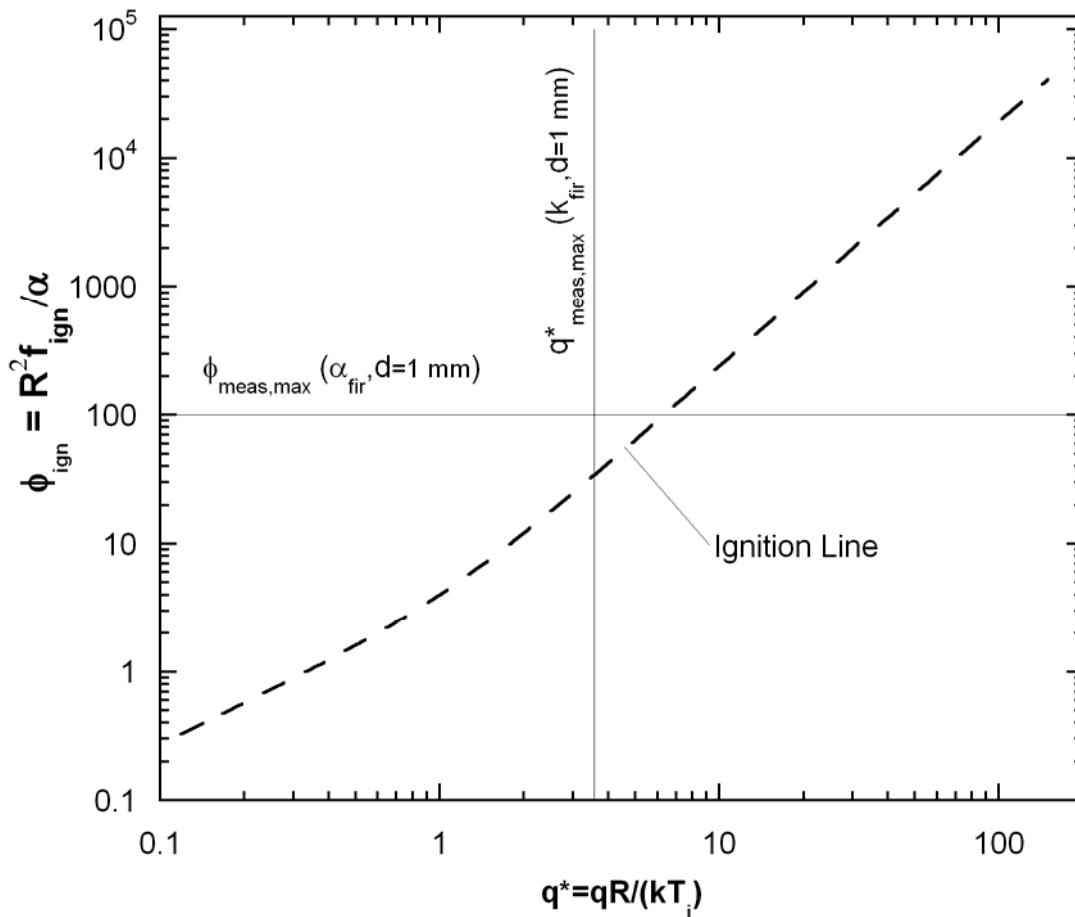


Figure 6.18. Relationship between predicted dimensionless ignition frequency and dimensionless heat flux (q^*).

cell necrosis as a function of heating rate (Jones *et al.*, 2004). No clear consensus exists regarding the best approach for simulating small particle heating, largely due to the lack of detailed understanding of how small particles respond to an imposed heat flux as well as the lack of detailed temporal heating data. Logic supporting both the use of lumped capacitance approach (Michaletz and Johnson, 2006), and a more rigorous multi-dimensional thermal analysis (Jones *et al.*, 2004) have been presented. The analysis presented herein suggests that for small diameter stems, leaves, and needles a significant temperature gradient exists between the exterior surface and interior center of the particle. Further analysis using alternate geometries may reveal additional details and understanding about thermal effects on plant living cells and implications for whole plant mortality.

6.7. Conclusions

The two radiation and convection heat transfer data sets that were taken, reveal the presence of short duration convective peaks. The analysis of the data using an FFT and an artificial down-sampling technique showed that radiation frequency content exists beyond 10 Hz and convection frequency content exists out to 100 Hz. Thus, the 500 Hz sample rate used to collect the radiation and convection heat flux data was sufficient to capture all fluctuations. The down sampling technique also showed substantial loss in convection heat flux content when sampling at 100 Hz or lower. Radiation was not as drastically effected and could be sampled as low as 10 Hz with rather minimal heat flux magnitude loss. Of the two data sets that were collected, the more intense event showed higher frequency content. It was acknowledged that even more intense combustion

events such as brushfires or crown fires may have higher frequency content than that which is represented here.

The one-dimensional transient conduction model developed herein demonstrates the possibility that forest fuels could react thermally to high frequency convective fluctuations. The model also showed that significant temperature gradients could develop in small diameter fuel implying that the lumped capacitance heat transfer solutions may be subject to substantial error.

7. Conclusions

The work reported here has explored the heat transfer characteristics of wildland and simulated wildland fires. This has been done through laboratory and field measurements of temporally resolved radiation and convection heat flux, and through modeling of heat transfer to and within fuel particles. The dissertation adds to the archival literature through its contributions in the following areas: 1) Understanding of attenuation of radiation heat transfer due to water vapor; 2) Radiation heating of particles and their susceptibility to induced ignition; 3) Characterization of the temporally resolved radiation and convective flux in fires, quantifying the partitioning of radiation and convection in the laboratory and the field; and 4) Determination of the convection and radiation heat flux frequency content in flames.

First, predictions were made for radiative transfer from black, isothermal, planar flame to a black fuel bed maintained at 300 K. The effect of flame inclination, flame temperature, and flame length were explored for cases with and without absorption by environmental water vapor in the intervening air (at 300 K). From these simulations it is concluded that depending on the conditions, water vapor has only a modest effect on the radiative transfer from flame to fuel. The effect is more pronounced for larger flames at

higher flame temperatures. The influence of water vapor on attenuation of radiation is reduced for angled flames.

Next, a model was developed to predict the steady-state temperature of fine fuels subject to irradiation from a simulated flame (burner) of known size and temperature. The model was validated by comparison with experimental data gathered for poplar excelsior of two sizes, and Ponderosa pine needles. The model presented accurately predicts the heat transfer of fine fuels with an incident radiant flux while cooled by radiant emission and natural convection. Parametric results with the model suggest that particle ignition by radiant heating alone is unlikely.

Third, experimental measurements of time-resolved convective and radiative heat flux in discrete fuel beds designed to simulate natural fuels present in wildland fires have been made. The influence of fuel row spacing and height on heat transfer characteristics were investigated for both buoyancy and wind-driven flow. The results show the effect of discrete combustion characteristics of fuel rows on radiation preheating. Whereas radiation transfer is felt long before flame arrival, the convective heating occurs only when the combustion engulfs the fuel. Convective cooling is evident during intervals of radiative preheating prior to flame arrival, and during high-amplitude turbulent fluctuations after flame arrival. Turbulent temporal fluctuations in convective flux are more rapid than previously documented, with content at frequencies as high as 70 Hz for buoyancy-driven flames and 150 to 200 Hz for wind-assisted flames. Temporal fluctuations in the radiative flux are confined more principally to low frequencies. Depending on the conditions, total energy contributed by convection seems to be about 25% of that contributed by radiant energy transfer. Successively stronger convective heating pulses are exhibited

immediately prior to ignition in nearly all cases, suggesting that convective energy transport may be critical to the flame “jumping” across discrete fuel gaps. These results have direct application to current efforts within wildland fire science to develop and evaluate new multidimensional numerical models describing the heating, pyrolysis, ignition, and spread of wildland fires.

A variety of fuel types, slopes, and fire conditions yield a range of radiation and convection heat fluxes that is necessary for a clearer understanding of fire behavior. Some of the data presented here were collected under conditions where the flame approached the sensor from non-frontal directions. Under ideal flame spread conditions, the data presented here show that radiation heat fluxes peak between 20 and 130 kW/m² and convective heat fluxes, which can have the effect of either heating or cooling, with peaks between 22 and 140 kW/m². There are much higher radiation heat fluxes from crown fires, but these particular crown fires did not spread directly toward the sensors and thus, the data are difficult to interpret. The convection heat flux is characterized by rapid fluctuation between positive and negative convection values owing to alternating packets of cool air intermingled with hot combustion products.

Finally, two radiation and convection heat transfer data sets were taken at a sampling rate of 500 Hz in the field, and reveal the presence of short-duration convective pulses. The analysis of the data using an FFT and an artificial down-sampling technique reveal that frequency content in the radiation flux extends beyond 10 Hz, and fluctuations in convective flux exist at frequencies as high as 100 Hz. It is demonstrated that the 500 Hz sample rate used to collect the radiation and convection heat flux data was sufficient to capture all fluctuations. The down-sampling technique also showed substantial loss in

convection heat flux signal content when sampling at 100 Hz or lower. Radiation was not as drastically affected and could be sampled as low as 10 Hz with rather minimal loss in heat flux signal. Of the two data sets collected, the more intense burn event showed higher frequency content. It is acknowledged that even more intense combustion events such as brushfires or crown fires may have higher frequency content than that which is represented here.

The one-dimensional transient conduction model developed as part of this study demonstrates the possibility that forest fuels can react thermally to high frequency convective fluctuations. The model also reveals that significant temperature gradients may develop in small-diameter fuel, implying that lumped capacitance-based heat transfer fuel models may be subject to substantial error.

The breadth of this work reveals much concerning the interplay of radiation and convection heat transfer in forest fires. Previous studies are not in agreement regarding the relative contribution of radiation and convection heat transfer. Several models include radiation as the only heat transfer mechanism. This dissertation has demonstrated that ignition by radiation alone is unlikely. Convection heat flux has also been shown to have previously unmeasured higher frequency fluctuations and was demonstrated as a means of fuel ignition. It is clear from this work that the interplay between radiation and convection is dependent on a number of factors.

This work has had as its objective the improvement of understanding of the fundamental heat transport process in the spread of wildland fires. Much of the modeling work done in the past in this area has been based on empirical or semi-empirical methods. Consequently, the models cannot confidently be extended to conditions outside of those

on which their empirical elements were based. Models based on first principles are emerging. This work enables understanding of the fundamental nature of radiation and convective transport, and will guide development of modeling capability. The goal in all of this is the accurate prediction of fire spread, with improved prediction capability in the hands of those whose responsibility is to prevent associated loss of life and property. It is hoped that the work reported here has advanced that effort.

8. References

- Albini, F. A. (1967). *A physical model for fire spread in brush*. Symp. (Int.) Combust., [Proc.], 11, 553-560.
- Albini, F. A. (1985). A model for fire spread in wildland fuels by radiation. *Combust. Sci. Technol.*, 42(5&6), 229-258.
- Albini, F. A. (1986). Wildland fire spread by radiation-a model including fuel cooling by natural convection. *Combust. Sci. Technol.*, 45(1&2), 101-113.
- Albini, F. A. and Stocks, B. J. (1986). Predicted and observed rates of spread of crown fires in immature jack pine. *Combust. Sci. Technol.*, 48(1&2), 65-76.
- Anderson, H. E. (1968). Flame shape and fire spread. *Fire Tech.*(Feb.), 51-58.
- Anderson, H. E. (1969). Heat transfer and fire spread. *USDA Forest Service Research Paper INT*, 69, 1-20.
- Anderson, W. R., Catchpole E.A., and Butler B.W. (2009). In Review. Measuring and modeling convective heat transfer in front of a spreading fire submitted to *International Journal of Wildland Fire February*
- Asensio, M. I. and Ferragut, L. (2002). On a wildland fire model with radiation. *Int. J. Numer. Methods Eng.*, 54, 137-157.
- Babrauskas, V. (2003). *Ignition Handbook*, Fire Science Publishers, Issaquah WA, USA, ISBN 9780972811132.
- Butler, B. W. (1993). *Experimental measurements of radiant heat fluxes from simulated wildfire flames*. 12th International Conference on Fire and Forest Meteorology, Jekyll Island, Georgia, Society of American Foresters, 104-112.
- Butler, B. W. (2003). *Field measurements of radiant energy transfer in full scale wind driven crown fires*. 6th ASME-JSME Thermal Engineering Conference, Hawaii Island, Hawaii, Japan Society of Mechanical Engineers, 6, 347.

- Butler, B. W., Cohen, J., Latham, D. J., Schuette, R. D., Sopko, P., Shannon, K. S., Jimenez, D. and Bradshaw, L. S. (2004). Measurements of radiant emissive power and temperatures in crown fires. *Can. J. For. Res*, 34(8), 1577-1587.
- Catchpole, E. A., Catchpole, W. R. and Rothermel, R. C. (1993). Fire behavior experiments in mixed fuel complexes. *Int. J. Wildland Fire*, 3(1), 45-57.
- Catchpole, W. R., Catchpole, E. A., Butler, B. W., Rothermel, R. C., Morris, G. A. and Latham, D. J. (1998). Rate of spread of free-burning fires in woody fuels in a wind tunnel. *Combust. Sci. Technol.*, 131(1), 1 - 37.
- Cekirge, H. M. (1978). Propagation of fire fronts in forests. *Comp. Math. Appl.*, 4, 325-332.
- Cheney, N. P. and Gould, J. S. (1995). Fire growth in grassland fuels. *Int. J. Wildland Fire*, 5(4), 237-247.
- Churchill, S. W. and Bernstein, M. (1977). Correlating equation for forced convection from gases and liquids to a circular cylinder in crossflow. *J. Heat Transfer*, 99(2), 300-306.
- Churchill, S. W. and Chu, H. S. (1975). Correlating equations for laminar and turbulent free convection from a horizontal cylinder. *Int. J. Heat Mass Transfer*, 18(9), 1049-1053.
- Clark, T. L. and Radke, L. (1999). Analysis of small-scale convective dynamics in a crown fire using infrared video camera imagery. *J. Appl. Meteorol.*, 38(10), 1401.
- De Mestre, J. J., Catchpole, E. A., Anderson, D. H. and Rothermel, R. C. (1989). Uniform propagation of a planar fire front without wind. *Combust. Sci. Technol.*, 65, 231-244.
- Denison, M. K. and Webb, B. W. (1993a). A spectral line-based weighted-sum-of-gray-gases model for arbitrary RTE solvers. *ASME J. Heat Trans.*, 115, 1012.
- Denison, M. K. and Webb, B. W. (1993b). An absorption-line blackbody distribution function for efficient calculation of gas radiative transfer. *J. Quant. Spectrosc. Radiat. Transfer*, 50, 510.
- Dupuy, J. L. (2000). Testing two radiative physical models for fire spread through porous forest fuel beds. *Combust. Sci. Technol.*, 155(1), 149 - 180.
- Emmons, H. (1964). Fire in the forest. *Fire Res. Abs. Rev.*, 5, 163-178.
- Farlow, S. J. (1993). *Partial Differential Equations for Scientists and Engineers*, Dover Publications Inc., New York, ISBN 0-486-67620.

- Fons, W. L. (1946). Analysis of fire spread in light forest fuels. *J. Agr. Res.*, 72(13), 93-121.
- Fosberg, M. A. (1973). Prediction of prepyrolysis temperature rise in dead forest fuels. *Fire Tech.*, 9(3), 182-188.
- GAO. (2009). "Government Accountability Office." Retrieved 23 April, 2009, from <http://www.gao.gov/>.
- Gordon, R. (1960). A transducer for the measurement of heat-flow rate. *J. Heat Transfer*, 82, 396-398.
- Hirano, T. and Sato, K. (1974). *Effect of radiation and convection on gas velocity and temperature profiles of flames spreading over paper*. Symp. (Int.) Combust., [Proc.], 15, 233-241.
- Hottel, H. C. and Sarofim, A. F. (1967). *Radiative Transfer*, McGraw-Hill Book Company, New York, New York, ISBN N/A.
- Hottel, H. C., Williams, G. C. and Steward, F. R. (1965). *The modeling of firespread through a fuel bed*. Symp. (Int.) Combust., [Proc.], The Combustion Institute, 10, 997 - 1007.
- Incropera, F. P., Dewitt, D. P., Bergman, T. L. and Lavine, A. S. (2007). *Fundamentals of Heat and Mass Transfer*, John Wiley & Sons, New York, 6th ed., ISBN 978-0-471-45728-2.
- Jakob, M. (1949). *Heat Transfer*, Wiley, New York,
- Jimenez, D., Forthofer, J. M., Reardon, J. J. and Butler, B. W. (2007). Fire behavior sensor package remote trigger design. *The Fire Environment-innovations, management, and policy*. Butler, B. W. and Cook, W. Destin, FL: 662.
- Jones, J. L., Webb, B. W., Jimenez, D., Reardon, J. and Butler, B. (2004). Development of an advanced one-dimensional stem heating model for application in surface fires. *Can. J. For. Res.*, 34(1), 20-30.
- Jones, M. R. (2009). The eigenfunction expansion method (private conversation). Frankman, D. Provo, UT.
- King, A. R. (1961). Compensating radiometer. *Br. J. Appl. Phys.*(11), 633.
- Knight, I. K. and Sullivan, A. L. (2004). A semi-transparent model of bushfire flames to predict radiant heat flux. *Int. J. Wildland Fire*, 13(2), 201-207.
- Konev, E. V. and Sukhinin, A. I. (1977). The analysis of flame spread through forest fuel. *Combust. Flame*, 28, 217-223.

- Michaletz, S. T. and Johnson, E. A. (2006). A heat transfer model of crown scorch in forest fires. *Can. J. For. Res.*, 36(11), 2839-2851.
- Modest, M. F. (2003). *Radiative Heat transfer*, Academic Press, New York, 2nd Ed., ISBN 0125031637.
- Morandini, F., Silvani, X., Rossi, L., Santoni, P.-A., Simeoni, A., Balbi, J.-H., Louis Rossi, J. and Marcelli, T. (2006). Fire spread experiment across Mediterranean shrub: Influence of wind on flame front properties. *Fire Saf. J.*, 41(3), 229-235.
- Morvan, D., Dupuy, J. L., Porterie, B. and Larini, M. (2000). *Multiphase formulation applied to the modeling of fire spread through a forest fuel bed*, Edinburgh, United Kingdom, Combustion Institute, 28, 2803-2809.
- Munson, B. R., Young, D. F. and Okiishi, T. H. (2002). *Fundamentals of Fluid Mechanics*, John Wiley & Sons, New York, NY, 4th. ISBN 0-471-44250-X.
- NIFC. (2009). "National Interagency Fire Center." Retrieved 23 April, 2009, from <http://www.nifc.gov/>.
- NOAA. (2009). "National Oceanic and Atmospheric Administration." Retrieved 23 April, 2009, from <http://www.noaa.gov/>.
- NWCG. (2009). "National Wildfire Coordinating Group." Retrieved 23 April, 2009, from <http://www.nwcg.gov/>.
- Ostrach, S. (1953). An analysis of laminar free-convection flow and heat transfer about a flat plate parallel to the direction of the generating body force. *NACA Report 1111*.
- Packham, D. and Pompe, A. (1971). Radiation temperatures of forest fires. *Aust. For. Res.*, 5, 1-8.
- Pagni, P. J. (1972). *Flame spread through porous fuels*. Symp. (Int.) Combust., [Proc.], 14, 1099-1107.
- Pickett, B. M., Isackson, C., Wunder, R., Fletcher, T. H., Butler, B. W. and Weise, D. R. (2007). Experimental measurements during combustion of moist individual foliage samples. *Accepted by the International Journal of Wildland Fire*.
- Santoni, P. A., Balbi, J. H. and Dupuy, J. L. (1999). Dynamic modelling of upslope fire growth. *Int. J. Wildland Fire*, 9(4), 285-292.
- Santoni, P. A., Simeoni, A., Rossi, J. L., Bosseur, F., Morandini, F., Silvani, X., Balbi, J. H., Cancellieri, D. and Rossi, L. (2006). Instrumentation of wildland fire: Characterisation of a fire spreading through a Mediterranean shrub. *Fire Saf. J.*, 41(3), 171-184.

- Sardoy, N., Consalvi, J.-L., Porterie, B. and Fernandez-Pello, A. C. (2007). Modeling transport and combustion of firebrands from burning trees. *Combust. Flame*, 150(3), 151-169.
- Siegel, R. and Howell, J. (2002). *Thermal Radiation Heat Transfer*, Taylor & Francis, 4th Ed., ISBN 1560328398.
- Silvani, X. and Morandini, F. (2009). Fire spread experiments in the field: Temperature and heat fluxes measurements. *Fire Saf. J.*, 44(2), 279-285.
- Simms, D. L. (1963). On the pilot ignition of wood by radiation. *Combust. Flame*, 7(3), 253-261.
- Stamm, A. J. (1964). *Wood and Cellulose Science*, Ronald Press Co., New York, ISBN N/A.
- Susott, R. A. (1980). Thermal behavior of conifer needle extractives. *For. Sci.*, 26, 347-360.
- Telisin, H. P. (1973). Flame radiation as a mechanism of fire spread in forests In Afgan, N. H. and Beer, J. M. (Ed.) *Heat Transfer in Flames*. John Wiley, New York, Toronto, London, Vol. 2, pp. 441-449.
- Thomas, P. H. (1967). Some aspects of the growth and spread of fire in the open. *Forestry*, 40(2), 139-164.
- Touloukian, Y. S. and Ho, C. Y., Eds. (1972). *Thermophysical Properties of Matter*. Plenum Press, New York, ISBN 978-0471260479.
- Van Wagner, C. E. (1967). Calculations on forest fire spread by flame radiation. *Special paper for the 6th world forestry conference*: 1-14.
- Vargaftik, N. B. (1975). *Tables of Thermophysical Properties of Liquids and Gases*, Hemisphere Publishing, New York, 2nd ed., ISBN 978-0470903100.
- Vatell. (2007). "Vatell Corporation Web Page." Retrieved 18 October, 2007, from <http://www.vatell.com/hfm.htm>.
- Weber, R. O. (1991). Modeling fire spread through fuel beds. *Prog. Energy Combust. Sci.*, 17(1), 67-82.
- Wotton, B. M., Martin, T. L. and Engel, K. (1996). Vertical flame intensity profile from a surface fire. *13th Fire and Forest Meteorology Conference*. Lorne, Australia, IAWF: 175-182.
- Wotton, B. M., McAlpine, R. S. and Hobbs, M. W. (1999). The effect of fire front width on surface fire behaviour. *Int. J. Wildland Fire*, 9(4), 247-253.

Wykoff, W. R. (2002). Measuring and modeling surface area of ponderosa pine needles. *Can. J. For. Res.*, 32(1), 1-8.

Yedinak, K. M., Forthofer, J. M., Cohen, J. D. and Finney, M. A. (2006). Analysis of the profile of an open flame from a vertical fuel source. *For. Ecol. Manag.*, 234(Supplement 1), S89-S89.

A. Appendix A

A.1. Description

This program is used to calculate one gray gas exchange factor (see chapter 2). It is written in C.

A.2. Code

```
#include <cmath>

#include <fstream>

#include <math.h>

using namespace std;

#define pi 3.1415926536

int main()
{
    /*This program is used to calculate ss - the gray gas exchange factor*/
    /*define Input and Output file names*/
    ofstream outfile ("output.txt");
```

```

ifstream infile ("input.txt");

/*define variable precision*/

double

b,a,xi,xe,Nx,Ny,Nz,Dx,Dy,Dza,Dzb,zb,za,x,y,sum,ss,kappa,conc,wgt,ggn;

int i,j,k,l;

/*define variable values*/

/*b - length of fuel bed and half the length of fire line (extent of z) */

/*a - flame length*/

b=100;

a=10;

/*Nx, Ny and Nz define number of partitions in the strip, y and z respectively
*/

Nx=400;

Ny=400;

Nz=2*400;

Dza=2*b/Nz;

Dzb=2*b/Nz;

Dx=(xe-xi)/Nx;

Dy=a/Ny;

sum=0;

```

```

/*bring in values from input file*/

/* xi and xe define the strip on the fuel bed -
conc=pass through variable for book keeping - ggn=gray gas number -
wgt=gray gas weight - kappa=absorption coefficient
*/

infile >> conc >> ggn >> xi >> xe >> wgt >> kappa;

/*begin for loops (multiple integration) */
for (i=1;i<=Nz;i++)
{
zb=i*Dza-b;
for (j=1;j<=Ny;j++)
{
y=j*Dy;
for (k=1;k<=Nz;k++)
{
za=k*Dza-b;
for (l=1;l<=Nx;l++)
{
x=xi+l*Dx;

```

```

sum=sum+exp(-kappa*sqrt(x*x+y*y+(zb-za)*(zb-
za)))*(x*y*Dx*Dy*Dza*Dzb)/((x*x+y*y+(zb-za)*(zb-za))*(x*x+y*y+(zb-
za)*(zb-za)));
    }
}
}
}
ss=sum/(a*2*b*pi);
outfile << conc << endl << ggn << endl << xi << endl << xe << endl << wgt
<< endl << kappa <<
endl << ss << endl;
/* This program was verified for accuracy against an analytical solution for
the view factor by setting the absorption coefficient (kappa) to 0
*/
}

```

B. Appendix B

B.1. Description

This program is associated with chapter 3. It calculates the steady state temperature of a cylindrical fuel particle exposed to a rectangular radiation source as a function of distance from the burner. Matlab is the programming language.

B.2. Code

```
%This Program solves for the fuel particle temperature as a function of
%distance from the burner

clear

% Read in propertie from Incropera and DeWitt

[ptemp,rho,cp,mu,v,k,alph,pr]=textread('properties.txt','%f %f %f %f %f %f %f
    %f','delimiter','\t');

pi=3.1415926535898;

g=9.80665;

sigma=5.67051e-8;

% Assuming that differential element is  $d=(1\text{mm})^3$ . Right now, for the purpose
% of this model, I am assuming tha the radiation element is a very small
```

```

% plane. The convection model will assume a cylinder.

% Burner dimensions (a by b)

a=0.115;

x=a;

b=0.075;

% d=7.00e-4; % diameter of ponderosa pine is 7.0e-4 meters

% d=1.29e-3; % diameter of large excelsior is 1.29e-3 meters

% d=4.35e-4; % diameter of small excelsior is 4.35e-4 meters

d=8.08e-4; % average of Small excelsior, large excelsior and ponderosa pine

% d=0.005;

% Afr is the projected area of the cylinder (length equal to diameter)

Afr=d^2;

% Afc is the fuel convective area

Afc=pi*d^2;

% Tinf is the far field temperature (temperature the fuel radiates to)

Tinf_far=300;

% plane flame temp

Tb=890; % Black body temp calculated by averageing all flux averages

% Tb=1500;

% Burner area

Ab=4*a*b;

% Maximum distance from burner at which fuel temperature will be calculated

maxdist=1;

```

```

%Number of points between burner and maxdist
N=2000;

% solving for view factor between the burner and fuel
% The expression from siegel and howell for Ffb is for a differential
% element to a plane at the corner of that plane. The 4 was added to assume
% that the differential element was at the center. Note also that a and b
% are only half of the length and width.

for i=1:N

    y(i)=i*maxdist/N;

    A=a/y(i);

    B=b/y(i);

    Ffb(i,1)=4/(2*pi)*(A/((1+A^2)^0.5)*atan(B/((1+A^2)^0.5))+B/((1+B^2)^0.5)
    *atan(A/((1+B^2)^0.5)));

    Fbf(i,1)=Afr/Ab*Ffb(i,1);

end

%diagnostic variables

over=0;

under=0;

check=0;

j=0;

% initial temperature guess

T_d1(N,1)=305;

```

```

%switch to turn on natural convection (turn off forced convection)

natconv=1;

% velocity (m/s) when natconv=0;

forcevel=5.0;

% m loop is for the individual solutions for temperature at each N locations be-
    tween maxdist and burner

for m=0:N-1

    %i loop is used to converge solution

    for i=1:3000

        ycurr=y(N-m);

        Tf(i)=(Tinf_far+T_d1(N-m,1))/2;

%    This loop finds the location of the properties (subject to the film
%    temperature Tf)

        while Tf(i)>check

            j=j+1;

            check=ptemp(j);

        end

        % Define properties

        nu=(Tf(i)-ptemp(j-1))*(v(j)-v(j-1))/(ptemp(j)-ptemp(j-1))+v(j-1);

        alpha=(Tf(i)-ptemp(j-1))*(alph(j)-alph(j-1))/(ptemp(j)-ptemp(j-1))+alph(j-1);

        RaD(N-m)=(2*g*d^3/(nu*alpha))*(T_d1(N-m,1)-Tinf_far)/(T_d1(N-
m,1)+Tinf_far);

        pran=(Tf(i)-ptemp(j-1))*(pr(j)-pr(j-1))/(ptemp(j)-ptemp(j-1))+pr(j-1);

```

```

kk=(Tf(i)-ptemp(j-1))*(k(j)-k(j-1))/(ptemp(j)-ptemp(j-1))+k(j-1);

% Different nusselt numbers for different convection scenarios

% (natural vs forced)

if natconv==1

    NuDb(N-m)=(0.6+(0.387*RaD(N-
m)^(1/6))/((1+(0.559/pran)^(9/16))^(8/27)))^2;

else

    ReD=forcevel*d/nu;

    NuDb(N-
m)=0.3+(0.62*ReD^0.5*pran^(1/3))/((1+(0.4/pran)^(2/3))^0.25)*(1+(ReD/28
2000)^(5/8))^0.8;

end

% Convection coef

h(N-m,1)=kk/d*NuDb(N-m);

% Solve for convective fuel temperature

qfb(N-m,1)=Afr*sigma*(T_d1(N-m,1)^4-Tinf_far^4)+Afr*(1-Ffb(N-
m,1))*sigma*(T_d1(N-m,1)^4-Tinf_far^4);

qff(N-m,1)=Afr*Ffb(N-m,1)*sigma*(T_d1(N-m,1)^4-Tb^4);

T=Tinf_far-(qfb(N-m,1)+qff(N-m,1))/(h(N-m,1)*Afc);

% Quantify heat gain and loss

convloss(N-m,1)=h(N-m,1)*Afc*(T-Tinf_far);

radloss(N-m,1)=Afr*sigma*(T_d1(N-m,1)^4-Tinf_far^4)+Afr*(1-Ffb(N-
m,1))*sigma*(T_d1(N-m,1)^4-Tinf_far^4);

```

```

radgain(N-m,1)=Afr*Ffb(N-m,1)*sigma*(T_d1(N-m,1)^4-Tb^4);

% The next several lines of code are used to sneak up on the
% solution.

if abs(T-T_d1(N-m,1))>100
    if T > T_d1(N-m,1)
        T_d1(N-m,1)=T_d1(N-m,1)+1;
    else
        T_d1(N-m,1)=T_d1(N-m,1)-1;
    end
end

if abs(T-T_d1(N-m,1))>10
    if T > T_d1(N-m,1)
        T_d1(N-m,1)=T_d1(N-m,1)+.1;
    else
        T_d1(N-m,1)=T_d1(N-m,1)-.1;
    end
end

if abs(T-T_d1(N-m,1))>1
    if T > T_d1(N-m,1)
        T_d1(N-m,1)=T_d1(N-m,1)+.01;
    else
        T_d1(N-m,1)=T_d1(N-m,1)-.01;
    end
end

```

```

end
if abs(T-T_d1(N-m,1))>.1
    if T > T_d1(N-m,1)
        T_d1(N-m,1)=T_d1(N-m,1)+.001;
    else
        T_d1(N-m,1)=T_d1(N-m,1)-.001;
    end
end
end
if abs(T-T_d1(N-m,1))>.01
    if T > T_d1(N-m,1)
        T_d1(N-m,1)=T_d1(N-m,1)+.0001;
    else
        T_d1(N-m,1)=T_d1(N-m,1)-.0001;
    end
end
end
if abs(T-T_d1(N-m,1))>.001
    if T > T_d1(N-m,1)
        T_d1(N-m,1)=T_d1(N-m,1)+.00001;
    else
        T_d1(N-m,1)=T_d1(N-m,1)-.00001;
    end
end
end
% once the temperature does not change more than 0.001 the program

```

```

    % moves to the next point

    j=0;

    check=0;

    checkin(i,N-(m))=T-T_d1(N-m,1);

    if abs(checkin(i,N-(m)))<.001

        break

    end

end

if m<N-1

    T_d1(N-(m+1),1)=T_d1(N-m,1);

end

m

end

% Adding experimental values to Plot Values come from Latham work

nonconverged=max(size(checkin))

Edist(1)=0.15;

Edist(2)=0.25;

Edist(3)=0.35;

Edist(4)=0.45;

LE(1)=128.063;

PP(1)=117.44;

SE(1)=90.86;

LE(2)=77.693;

```

```

LE(3)=61.523;
LE(4)=49.993;
SE(2)=57.46;
SE(3)=52.563;
SE(4)=36.98;
PP(2)=77.493;
PP(3)=56.273;
PP(4)=46.26;
SE=SE+273.15;
LE=LE+273.15;
PP=PP+273.15;
% Plot the results
figure (1)
plot(y,T_d1,Edist,SE,'y',Edist,LE,'dg',Edist,PP,'o');
title('Temperature')
xlabel('Distance (m)')
ylabel('Temperature (K)')
legend('Predicted Temperature','Small Excelsior','Large Excelsior','Ponderosa
      Pine Needles',1)
grid on
%Store the data
for i=1:N
      data(i,1)=y(i);

```

```
data(i,2)=T_d1(i);  
data(i,3)=radgain(i,1);  
data(i,4)=radloss(i,1);  
data(i,5)=convloss(i,1);  
end
```

C. Appendix C

C.1. Description

A more detailed solution using the Eigenfunction expansion method to the partial differential equation in chapter 6 is given here.

C.2. Solution

Governing Equation

$$\frac{1}{\eta} \frac{\partial}{\partial \eta} \left(\eta \frac{\partial \theta}{\partial \eta} \right) = \frac{\partial \theta}{\partial \tau} \quad (1)$$

The initial condition is

$$\theta(\eta, 0) = 0 \quad (2)$$

The centerline symmetry boundary condition and surface boundary condition are

$$\left. \frac{\partial \theta}{\partial \eta} \right|_{\eta=0} = 0 \quad (3a)$$

$$\left[\frac{\partial \theta}{\partial \eta} + Bi \theta \right]_{\eta=1} = Bi \theta_{\infty}(\tau) \quad (3b)$$

The Eigenfunction and Eigen condition can be found using the corresponding Sturm Liouville problem, which is shown below.

$$\frac{1}{\eta} \frac{d}{d\eta} \left(\eta \frac{d\phi}{d\eta} \right) = -\lambda_n^2 \phi \quad (4)$$

Subject to Boundary conditions

$$\left[\frac{\partial \phi}{\partial \eta} \right]_{\eta=0} = 0 \quad (5a)$$

$$\left[\frac{\partial \phi}{\partial \eta} + Bi \phi \right]_{\eta=1} = 0 \quad (5b)$$

The solution to equation 4 is

$$\phi(\eta) = c_1 J_0(\lambda_n \eta) + c_2 Y_0(\lambda_n \eta) \quad (6)$$

The derivative of equation 6, which will be required in the application of the equation 5b, is

$$\frac{\partial \phi}{\partial \eta} = -c_1 \lambda_n J_1(\lambda_n \eta) + c_2 \lambda_n Y_1(\lambda_n \eta) \quad (7)$$

Applying equation 5a to the equation 7 yields the Eigenfunction

$$0 = c_1 J_0(0) + c_2 Y_0(0) \longrightarrow c_2 = 0 \longrightarrow \phi = c_1 J_0(\lambda_n \eta) \quad (8)$$

Applying equation 5b results in the Eigen condition

$$\left[\frac{\partial \phi}{\partial \eta} + Bi \phi \right]_{\eta=1} = -c_1 \lambda_n J_1(\lambda_n) + Bi c_1 J_0(\lambda_n) = 0 \longrightarrow Bi J_0(\lambda_n) - \lambda_n J_1(\lambda_n) = 0 \quad (9)$$

We can now guess a solution to the original problem (equations 1-3)

$$\theta(\eta, \tau) = \sum_{n=1}^{\infty} a_n(\tau) J_0(\lambda_n \eta) \quad (10)$$

Use the orthogonal property of the Bessel function and integrate from 0 to 1 to eliminate the summation

$$\begin{aligned} \int_0^1 \eta J_0(\lambda_m \eta) \theta d\eta &= \int_0^1 \sum_{n=1}^{\infty} a_n(\tau) \eta J_0(\lambda_n \eta) J_0(\lambda_m \eta) d\eta \\ &= a_n(\tau) \left[\frac{1}{2} (J_0^2(\lambda_n) + J_1^2(\lambda_n)) \right] \end{aligned} \quad (11)$$

Take the derivative with respect to τ of equation 11

$$\int_0^1 \eta J_0(\lambda_m \eta) \frac{\partial \theta}{\partial \tau} d\eta = \frac{\partial a_n}{\partial \tau} \left[\frac{1}{2} (J_0^2(\lambda_n) + J_1^2(\lambda_n)) \right] \quad (12)$$

Substitute equation 1 into the left half of equation 12

$$\int_0^1 J_0(\lambda_m \eta) \frac{\partial}{\partial \eta} \left(\eta \frac{\partial \theta}{\partial \eta} \right) d\eta = \frac{\partial a_n}{\partial \tau} \left[\frac{1}{2} (J_0^2(\lambda_n) + J_1^2(\lambda_n)) \right] \quad (13)$$

The left side of equation 13 can now be integrated by parts twice. Equation 3a and 3b will be used as well as the Eigen condition. The result is the differential equation below

$$\frac{\partial a_n}{\partial \tau} + \lambda_n^2 a_n = \frac{Bi \theta_{\infty}(\tau) J_0(\lambda_n)}{\left[\frac{1}{2} (J_0^2(\lambda_n) + J_1^2(\lambda_n)) \right]} \quad (14)$$

Equation 14 is solved using an integrating factor and the solution is

$$a_n(\tau) = \frac{Bi J_0(\lambda_n)}{\left[\frac{1}{2} (J_0^2(\lambda_n) + J_1^2(\lambda_n)) \right]} e^{-\lambda_n^2 \tau} \int_0^{\tau} e^{\lambda_n^2 \tau'} \theta_{\infty}(\tau') d\tau' \quad (15)$$

The solution to equation 1, subject to the initial condition (equation 2) and boundary conditions (equations 3a and 3b), is

$$\theta(\eta, \tau) = \sum_{n=1}^{\infty} \frac{2Bi J_0(\lambda_n) J_0(\lambda_n \eta)}{\left[J_0^2(\lambda_n) + J_1^2(\lambda_n) \right]} e^{-\lambda_n^2 \tau} \int_0^{\tau} e^{\lambda_n^2 \tau'} \theta_{\infty}(\tau') d\tau' \quad (16)$$

